The effect of hydrodynamics on the interaction between floating structures and flexible ice floes

A study based on potential theory

Keijdener, Chris

DOI
10.4233/uuid:a66b84b9-6c66-4c9c-a2e1-87163244ae07

Publication date
2019

Document Version
Final published version

Citation (APA)
Keijdener, C. (2019). *The effect of hydrodynamics on the interaction between floating structures and flexible ice floes: A study based on potential theory*. [Dissertation (TU Delft), Delft University of Technology]. https://doi.org/10.4233/uuid:a66b84b9-6c66-4c9c-a2e1-87163244ae07

THE EFFECT OF HYDRODYNAMICS ON THE INTERACTION BETWEEN FLOATING STRUCTURES AND FLEXIBLE ICE FLOES

A STUDY BASED ON POTENTIAL THEORY

THE EFFECT OF HYDRODYNAMICS ON THE INTERACTION BETWEEN FLOATING STRUCTURES AND FLEXIBLE ICE FLOES

A STUDY BASED ON POTENTIAL THEORY

Proefschrift

ter verkrijging van de graad van doctor
aan de Technische Universiteit Delft,
op gezag van de Rector Magnificus prof. dr. ir. T.H.J.J. van der Hagen,
voorzitter van het College voor Promoties,
in het openbaar te verdedigen op vrijdag 6 december 2019 om 10:00 uur

door

Chris KEIJDENER

civiel ingenieur, Technische Universiteit Delft, Nederland
geboren te Heerlen, Nederland.

Dit proefschrift is goedgekeurd door de

promotor: prof. dr. A. Metrikine
copromotor: dr. ir. H. Hendrikse

Samenstelling promotiecommissie:

Rector Magnificus,	voorzitter
Prof. dr. A. V. Metrikine,	Technische Universiteit Delft
Dr. H. Hendrikse,	Technische Universiteit Delft
Onafhankelijke leden:	
Prof. dr. ir. W. Uijttewaal	Technische Universiteit Delft
Prof. dr. ir. K. Vuik	Technische Universiteit Delft
Prof. dr. S. Løset	Norges Teknisk-Naturvitenskapelige Universitet
Prof. dr. Z. Gao	Norges Teknisk-Naturvitenskapelige Universitet
Prof. dr. A. A. Abramian	Institute for Problems of Mechanical Engineering, Russian Academy of Sciences

This thesis was financed by the Research Council of Norway (10382200) through the Center for Research-based Innovation *Sustainable Arctic Marine and Coastal Technology* (SAMCoT, 50049000).

Keywords: Hydrodynamics, Ice-floater interaction, Bending failure, Effective modeling, Ship response.

Printed by: Gildeprint

Cover design: Veryname

ISBN 978-94-6384-070-5

An electronic version of this dissertation is available at
http://repository.tudelft.nl/.

SUMMARY

The Arctic presents a great opportunity for two major industries. First, since the region is expected to contain a significant amount of hydrocarbon reserves, it is very attractive for the oil and gas industry. Second, the receding extent of sea ice is making the region more accessible for shipping and, therefore, an opportunity is emerging for the shipping industry. In order to exploit both economic opportunities in a safe and sustainable manner, a thorough understanding of the interaction between ice and floating structures is needed. The most common method for studying ice-floater interaction (IFI) is via numerical modeling, which the fluid is a major component of. As fluid-ice interaction is challenging to model, a wide range of simplified and sophisticated models are employed to meet the challenge.

A literature study was performed on the usage of fluid models employed in IFI and it was found that they can be divided into four categories: hydrostatic models, models based on potential flow, models based on Reynolds-averaged Navier–Stokes or a similarly advanced method, and effective fluid models. The hydrostatic models are by far the most prevalent despite only accounting for buoyancy. Most IFI models that account for hydrodynamics make use of potential theory. These models account for fluid flow and surface waves, which together alter the dynamic behavior of floating ice, resulting in hydroelastic effects. The surface-wave-based coupling between ice and floater has not been studied before and there are still open questions regarding the effects of hydroelasticity on the bending failure of ice. The advanced fluid models are a recent trend in IFI and, consequently, most of those are still under development. These models are very promising and may be the future of IFI modeling. Finally, the effective models avoid the practical issues associated with hydrodynamic models in terms of development and calculation time by capturing hydrodynamics in an effective manner, employing, for instance, added mass and damping coefficients. While several studies investigated the efficacy of these models, currently no satisfactory effective fluid model exists.

The main goal of this thesis is to further the understanding of how hydrodynamics affects the interaction between ice and a sloping structure and to assess whether it is possible to create an effective model that can replicate the observed effects. The full scope encompasses three smaller studies. First, the surface-wave-based coupling between an elastic ice sheet and nearby floater structure is investigated. This interaction has not been studied before and the solution method that is developed for this problem is also used in the subsequent two studies. Second, a thorough study of the effects of hydrodynamics on the interaction between a sloping structure and level ice is accomplished. This study resulted in the identification of the parameter range wherein hydrostatic models are valid, which is essential given that they constitute the majority of all models. In addition, this study improved the understanding of the effects of hydrodynamics by means of investigating the importance of various components such as the rotational inertia of the ice, axial compression, and the nonlinear hydrodynamic pres-

sure. Furthermore, the relation was analyzed between the temporal development of the contact force and the velocity dependence of the breaking length. Lastly, based on the findings of the second study, an attempt was made to develop an effective fluid model for ice-slope interaction. The efficacy of this model was studied in this thesis for a range of parameters. The main findings of the three studies are summarized next.

Part one In the first part of this thesis, the interaction is investigated between an ice floe and a floater through surface waves. This problem is considered first as the Green's functions that are derived for this problem are required for the subsequent studies on ice-slope interaction. The floater is modeled in-plane as a thin rigid body that floats on the surface of a fluid layer of finite depth. On one side of the floater, an ice floe is present which is modeled as a semi-infinite Kirchhoff-Love plate. The floater is excited by external loads and the resulting motions generate waves. Those waves hitting the ice edge are partly transmitted into the ice floe and partly reflected back towards the floater. The reflected waves exert pressure on the floater, altering its response. The resulting motions of the floater were analyzed, revealing several interesting facts.

The study showed that below a certain onset frequency, the waves are almost fully transmitted into the ice floe and, consequently, the response of the floater is unaffected by the presence of the ice. The susceptibility of a floater to the waves reflected by a nearby ice floe can thus be estimated by checking how much of its open water response occurs above or below the onset frequency. The onset frequency is sensitive to changes of the ice thickness and insensitive to changes of the Young's modulus and water depth.

Above the onset frequency, the waves reflected by the ice have a pronounced effect on the response of the floater. In certain frequency ranges, quasi-standing waves occur within the gap between ice floe and floater. Within these frequency ranges, the response of the floater is significantly altered. Depending on the phasing between the reflected waves and the floater's motions, resonance or anti-resonance can occur which can greatly amplify or reduce the floater's motions when compared to the case when no ice is present. Even when there is no gap between ice and floater, the amplitude of the floater can still be amplified and its natural frequency somewhat increased.

Part two The second study of this thesis focuses on the effect of hydrodynamics on the bending failure of an elastic ice floe due to the interaction with a downward-sloping floater, i.e. the effects of hydrodynamics on ice-slope interaction (ISI). A novel, semi-analytical in-plane ISI model is proposed that is based on potential theory in conjunction with the nonlinear Bernoulli equation to describe the fluid pressure. The ice is modeled as a semi-infinite Kirchhoff-Love plate. The predictions of the hydrodynamic model are compared with those of a hydrostatic ISI model, thereby obtaining a quantitative measure of the effect of hydrodynamics on ISI. The comparison revealed several interesting facts.

First, the importance of several components of the model was investigated to determine which ones are essential for ISI. It was found that the contribution of the rotational inertia of the ice, axial compression and the nonlinear hydrodynamic pressure is insignificant. Being able to ignore the last two components greatly simplifies the modeling of ISI as it removes all sources of spatial nonlinearity. The terms that were found to

be essential for ISI, listed in the order of importance, are: bending of the ice floe, linear hydrodynamic pressure, hydrostatic pressure and the inertia of the ice floe. The contribution of the fluid's inertia is on average four to ten times bigger than that of the inertia of the ice. The study also demonstrated that the effect of wave radiation on ISI is minimal.

Second, the relation between the temporal development of the contact force and the velocity-dependence of the breaking length was studied. The study showed that the breaking length has two regimes which are separated by a transition velocity. When the ice velocity is below the transition velocity, the ice fails during the initial impact. Alternatively, when the ice velocity is above the transition velocity, the ice floe survives the impact and fails with a breaking length that is close to the static breaking length. The transition velocity of the hydrodynamic model is much lower than the transition velocity of the hydrostatic model, 0.0725 m/s compared to 0.275 m/s. This major difference in transition velocity is the primary reason for the limited applicability of the hydrostatic model. The results show that the hydrostatic model should not be used when the ice velocity is higher than 0.6 times the transition velocity of the hydrodynamic model as its predictions will deviate significantly, with errors ranging from 30% to 100%. This upper bound corresponds to values between 0.02 m/s and 0.1 m/s for the parameters considered.

Lastly, this study underlined the stochastic nature of the breaking length of the ice floe. When the floe fails, a relatively large segment of the floe is, in fact, close to failure. A defect in the ice can locally amplify the stresses, causing the ice to fail at the defect rather than at the location predicted by a homogeneous model. This can cause the breaking length to vary by 10% to 30%.

Part three The last part of this thesis builds on the knowledge gained in part two by attempting to create a simple effective fluid model (EFM) that captures the effects of hydrodynamics on ISI as observed in part two. Based on the observations, an EFM is proposed that uses frequency-independent added mass and damping coefficients. This EFM was added to the hydrostatic model, thereby obtaining an ISI model that contains all four essential components of the ISI model. The resulting effective ISI model is very simple and, consequently, its implementation is trivial compared to a true hydrodynamic model such as the one proposed in part two. Its simplicity should help to improve the adoption of hydrodynamics in ISI.

The performance of the effective ISI model is assessed. Investigated are the velocity-dependent breaking length, the maximum contact force that occurred during the interaction, and the contact force as a function of time. The predictions of the effective model are far more accurate than those of the hydrostatic model. The coefficients of the EFM were found to be relatively insensitive to changes in the parameters, allowing the effective model to be used for a fairly broad range of parameters.

SAMENVATTING

Het noordpoolgebied biedt een grote kans voor twee belangrijke industrieën. Ten eerste, omdat de regio naar verwachting een aanzienlijke hoeveelheid koolwaterstofreserves zal bevatten, zeer aantrekkelijk voor de olie- en gasindustrie. Ten tweede wordt de regio toegankelijker voor de scheepvaart door de afnemende hoeveelheid zee-ijs en biedt daarom kansen voor de scheepvaartindustrie. Om beide economische kansen op een veilige en duurzame manier te benutten, is een doortastend begrip van de interactie tussen ijs en drijvende structuren nodig, vanuit het Engels vaak afgekort als floater. De meest gebruikelijke methode voor het bestuderen van ijs-floater-interactie (IFI) is via numerieke modellering, waarvan water een belangrijk component is. Omdat de interactie tussen water en ijs een uitdaging is om te modelleren, wordt een breed scala aan vereenvoudigde en geavanceerde modellen gebruikt om deze uitdaging aan te gaan.

Als eerst is een literatuurstudie uitgevoerd naar het gebruik van vloeistofmodellen die in IFI. De toegepaste modellen kunnen onderverdeeld worden in vier categorieën: hydrostatische modellen, modellen op basis van potentiaalstroming, modellen op basis van Reynolds-averaged Navier-Stokes of een eveneens geavanceerde methode, en effectieve vloeistofmodellen. De hydrostatische modellen zijn verreweg de meest voorkomende, ondanks dat ze alleen rekening houden met het drijfvermogen van het ijs. De meeste IFI-modellen die verantwoordelijk zijn voor hydrodynamica maken gebruik van potentiaalstroming. Deze modellen bevatten vloeistofstroming en oppervlaktegolven, die samen het dynamische gedrag van drijvend ijs veranderen wat resulteert in hydroelastische effecten. De koppeling tussen ijs en floater veroorzaakt door de oppervlaktegolven is nog niet eerder bestudeerd en er zijn nog steeds open vragen over de effecten van hydro-elasticiteit op het falen van ijs in buiging. De geavanceerde vloeistofmodellen zijn een recente trend in IFI en bijgevolg zijn de meeste daarvan nog in ontwikkeling. Deze modellen zijn veelbelovend en zijn mogelijk de toekomst van IFI-modellering. Ten slotte zijn er de effectieve modellen welke de praktische problemen die hydrodynamic met zich mee brengt, zoals in toename in programmeer en berekentijd van het model, vermijden door het hydrodynamisch effect van het water op een effectieve manier mee te nemen, bijvoorbeeld door het gebruik van toegevoegde massa en dempingscoëfficiënten. Hoewel verschillende onderzoeken de werkzaamheid van deze modellen hebben onderzocht, bestaat er momenteel geen bevredigend effectief vloeistofmodel.

Het belangrijkste doel van dit proefschrift is om meer inzicht te krijgen in hoe hydrodynamica de interactie tussen ijs en een hellende structuur beïnvloedt en om te beoordelen of het mogelijk is om een effectief model te maken dat de waargenomen effecten kan repliceren. Deze hoofdvraag is opgesplitst in drie studies. Eerst wordt de koppeling op basis van oppervlaktegolven tussen een elastische ijskap en een nabije floater onderzocht. Deze interactie is nog niet eerder bestudeerd en de oplossingsmethode die voor dit probleem is ontwikkeld, wordt ook in de daarop volgende twee studies gebruikt. In de tweede studie is een grondige onderzoek naar van de effecten van hydrodynamica op de

interactie tussen een hellende structuur en een ijslaag gedaan. Deze studie resulteerde in de identificatie van het parameterbereik waarin hydrostatische modellen geldig zijn, wat essentieel is omdat deze het merendeel van alle modellen vormen. Bovendien verbeterde deze studie het begrip van de effecten van hydrodynamica door middel van het onderzoeken van het belang van verschillende componenten zoals de rotatietraagheid van het ijs, axiale compressie en de niet-lineaire hydrodynamische druk. Verder werd de relatie geanalyseerd tussen de temporele ontwikkeling van de contactkracht en de snelheidsafhankelijkheid van de breeklengte van het ijs. Ten slotte werd, op basis van de bevindingen van de tweede studie, een poging gedaan om een effectief vloeistof model voor ijs-hellinginteractie te ontwikkelen. De werkzaamheid van dit model werd in dit proefschrift bestudeerd voor een reeks parameters. De belangrijkste bevindingen van de drie onderzoeken worden hierna samengevat.

Deel een In het eerste deel van dit proefschrift wordt de interactie onderzocht tussen een ijsschots en een floater door middel van oppervlaktegolven. Dit probleem wordt als eerste beschouwd omdat de Greense functies die voor dit probleem zijn afgeleid, nodig zijn voor de onderzoeken naar interactie tussen ijs en hellingen in deel twee en drie van dit proefschrift. De floater is 2D gemodelleerd als een dun, star lichaam dat op het oppervlak van een vloeistof laag van eindige diepte drijft. Aan de ene kant van de floater is een ijsschots aanwezig die is gemodelleerd als een semi-oneindige Kirchhoff-Love-plaat. De floater wordt geëxciteerd door externe belastingen en de resulterende bewegingen genereren golven. De golven die de ijsrand raken, worden gedeeltelijk doorgelaten in de ijsschots en deels teruggekaatst naar de floater. De gereflecteerde golven oefenen druk uit op de floater, waardoor de respons van de floater verandert. De resulterende bewegingen van de floater werden geanalyseerd, waarbij verschillende interessante feiten werden onthuld.

De studie toonde aan dat beneden een bepaalde beginfrequentie de golven bijna volledig worden doorgelaten in de ijsschots waardoor de reactie van de floater niet wordt beïnvloed door de aanwezigheid van het ijs. De gevoeligheid van een floater voor de golven die wordt weerkaatst door een nabijgelegen ijsschots kan dus worden geschat door na te gaan hoeveel van zijn open waterreactie optreedt boven of onder deze beginfrequentie. De beginfrequentie is gevoelig voor veranderingen van de ijsdikte en ongevoelig voor veranderingen van de Young's modulus en waterdiepte.

Boven de beginfrequentie hebben de golven die door het ijs worden gereflecteerd een merkbaar effect op de reactie van de floater. In bepaalde frequentiegebieden treden quasi-staande golven op binnen de opening tussen de ijsschots en de floater. Binnen deze frequentiegebieden is de respons van de floater aanzienlijk veranderd. Afhankelijk van de fase tussen de gereflecteerde golven en de bewegingen van de floater kan resonantie of antiresonantie optreden wat de bewegingen van de floater aanzienlijk kunnen versterken of verminderen vergeleken met het situate wanneer er geen ijs aanwezig is. Zelfs wanneer er geen opening is tussen ijs en floater, kan de amplitude van de response van de floater nog steeds worden versterkt en de natuurlijke frequentie enigszins worden verhoogd.

Deel twee De tweede studie van dit proefschrift richt zich op het effect van hydrodynamica op het falen in buiging van een elastische ijslaag als gevolg van de interactie met een naar beneden hellende floater, d.w.z. de effecten van hydrodynamica op ijs-slopeinteractie (ISI). Een nieuw, 2D semi-analytisch ISI-model wordt voorgesteld dat gebaseerd is op een potentiaalstroming in combinatie met de niet-lineaire Bernoulli-vergelijking om de vloeistofdruk te beschrijven. Het ijs is gemodelleerd als een semi-oneindige Kirchhoff-Love-plaat. De voorspellingen van het hydrodynamisch model worden vergeleken met die van een hydrostatisch ISI-model, waardoor een kwantitatieve meting van het effect van hydrodynamica op ISI wordt verkregen. De vergelijking onthulde een aantal interessante feiten.

Eerst werd het belang van verschillende componenten van het model onderzocht om te bepalen welke essentieel zijn voor ISI. Er werd gevonden dat de bijdrage van de rotatietraagheid van het ijs, axiale compressie en de niet-lineaire hydrodynamische vloeistof druk niet significant is. Het kunnen negeren van de laatste twee componenten vereenvoudigt de modellering van ISI aanzienlijk, omdat het alle bronnen van ruimtelijke niet-lineariteit verwijdert. De termen die essentieel bleken te zijn voor ISI, opgesomd in de volgorde van belangrijkheid, zijn: buiging van het ijs, lineaire hydrodynamische druk, hydrostatische druk en de massa van de ijsschots. De bijdrage van de traagheid van de vloeistof is gemiddeld vier tot tien keer groter dan de bijdrage van de traagheid van het ijs. De studie toonde ook aan dat het effect van golfstraling op ISI minimaal is.

Als tweede werd de relatie tussen de temporele ontwikkeling van de contactkracht en de snelheidsafhankelijkheid van de breeklengte van het ijs bestudeerd. De studie toonde aan dat de breeklengte twee regimes heeft die gescheiden zijn door een overgangssnelheid. Wanneer de snelheid van het ijs lager is dan de overgangssnelheid, faalt het ijs tijdens de initiële botsing. Wanneer de snelheid van het ijs boven de overgangssnelheid ligt, overleeft de ijsschot deze botsing en faalt met een breeklengte die dichtbij de statische breeklengte ligt. De overgangssnelheid van het hydrodynamische model is veel lager dan de overgangssnelheid van het hydrostatische model, 0,0725 m / s vergeleken met 0,275 m / s. Dit grote verschil in overgangssnelheid is de voornaamste reden voor de beperkte toepasbaarheid van het hydrostatische model. De resultaten laten zien dat het hydrostatische model niet moet worden gebruikt als de ijssnelheid hoger is dan 0,6 maal de overgangssnelheid van het hydrodynamisch model, omdat de voorspellingen dan aanzienlijk zullen afwijken, met fouten van 30% tot 100%. Deze bovengrens komt overeen met waarden tussen 0,02 m / s en 0,1 m / s voor de beschouwde parameters.

Ten slotte onderstreepte deze studie de stochastische aard van de breeklengte van het ijs. Op het moment dat het ijs faalt staat een groot gedeelte van het ijs op het punt om te falen. Een defect in het ijs kan de spanningen lokaal versterken, waardoor het ijs faalt bij het defect in plaats van op de locatie die wordt voorspeld door een homogeen model. Hierdoor kan de breeklengte met 10% tot 30% variëren.

Deel drie Het laatste deel van dit proefschrift bouwt voort op de kennis die is opgedaan in deel twee door te proberen een eenvoudig effectief vloeibaar model (EFM) te creëren dat de effecten van hydrodynamica op ISI kan repliceren, zoals waargenomen in deel twee. Op basis van de waarnemingen wordt een EFM voorgesteld die frequentie-onafhankelijke toegevoegde massa en dempingscoëfficiënten gebruikt. Dit EFM is toe-

gevoegd aan het hydrostatische model, waardoor een ISI-model is verkregen dat alle vier essentiële componenten van het ISI-model bevat. Het resulterende effectieve ISI-model is zeer eenvoudig en bijgevolg is de implementatie ervan triviaal in vergelijking met een echt hydrodynamisch model zoals het model dat in deel twee wordt voorgesteld. De eenvoud ervan moet helpen de acceptatie van hydrodynamica in ISI te verbeteren.

De prestaties van het effectieve ISI-model werden beoordeeld. Onderzocht zijn de snelheidsafhankelijke breeklengte, de maximale contactkracht die optrad tijdens de interactie en de contactkracht als een functie van de tijd. De voorspellingen van het effectieve model zijn veel nauwkeuriger dan die van het hydrostatische model. De coëfficiënten van de EFM bleken relatief ongevoelig te zijn voor veranderingen in de parameters, waardoor het effectieve model voor een redelijk breed bereik van parameters kan worden gebruikt.

CONTENTS

Summary v

Samenvatting ix

1 Introduction 1
- 1.1 Opportunities in the Arctic . . . 1
- 1.2 Numerical modeling of ice-floater interaction (IFI) . . . 2
- 1.3 Fluid modeling in IFI . . . 5
- 1.4 Thesis objectives and scope . . . 6
- 1.5 Thesis outline . . . 8
- References . . . 9

2 Review of IFI studies 13
- 2.1 Hydrostatic models . . . 13
  - 2.1.1 Analytical & Empirical models . . . 14
  - 2.1.2 Edge-tracking models . . . 14
  - 2.1.3 Rigid multibody models without failure . . . 15
  - 2.1.4 Rigid multibody models with analytical or empirical failure . . . 16
  - 2.1.5 Elastic multibody models with stress-based failure . . . 17
- 2.2 Models based on potential theory . . . 18
  - 2.2.1 Contact-based interaction . . . 19
  - 2.2.2 Fluid-based interaction . . . 22
  - 2.2.3 Difficulties associated with incorporating hydrodynamics . . . 22
- 2.3 Advanced fluid models . . . 24
- 2.4 Experimental studies . . . 25
  - 2.4.1 Ice-slope interaction . . . 25
  - 2.4.2 Interaction with ship-shaped structures . . . 26
  - 2.4.3 Interaction with conical structures . . . 27
- 2.5 Summary . . . 28
- 2.6 Conclusions . . . 29
- References . . . 29

3 Ice-floater interaction through surface waves 41
- 3.1 Model description . . . 42
  - 3.1.1 Floater's governing equations . . . 43
  - 3.1.2 Fluid's governing equations . . . 44
- 3.2 Discretization . . . 46
  - 3.2.1 Discretization of the contact pressure . . . 46
  - 3.2.2 Discretization of the kinematic floater-fluid interface condition . . . 47

3.3 Solving the problem . . . 48
3.3.1 Fluid response due to differential surface pressure . . . 48
3.3.2 Resolving the floater-fluid interface . . . 50
3.3.3 Floater's response . . . 51
3.4 Results . . . 52
3.4.1 Excitation by an external force . . . 52
3.4.2 Excitation by an external moment . . . 57
3.4.3 Discussion . . . 58
3.5 Conclusions . . . 58
References . . . 59

4 The effect of hydrodynamics on ice-slope interaction 61
4.1 Model description . . . 62
4.1.1 Mathematical model . . . 63
4.1.2 Solution method . . . 65
4.2 Validation . . . 74
4.2.1 Validation of the time-integration scheme . . . 74
4.2.2 Validation of the ISI model . . . 75
4.3 Results . . . 77
4.3.1 Determining the factors of influence for ISI . . . 77
4.3.2 Balance of forces in the ice floe . . . 79
4.3.3 The relation between contact force and breaking length . . . 81
4.3.4 Limitation of the hydrostatic model . . . 86
4.4 Sensitivity study . . . 87
4.4.1 Variations in physical parameters . . . 87
4.4.2 Variations in numerical parameters and in modeling assumptions . . . 88
4.5 Discussion . . . 88
4.5.1 Stochastic nature of the breaking length . . . 88
4.5.2 Single- versus dual-mode contact model . . . 89
4.5.3 Effect of the solution method . . . 90
4.6 Conclusions . . . 91
References . . . 92

5 An effective fluid model for ice-slope interaction 95
5.1 Description of the effective fluid model . . . 95
5.2 Optimization . . . 96
5.3 Results . . . 97
5.3.1 The effect of each coefficient on the predictions . . . 97
5.3.2 Optimal set of coefficients . . . 102
5.3.3 Sensitivity analysis . . . 102
5.4 Discussion . . . 104
5.5 Conclusions . . . 105
References . . . 105

6 Conclusions **107**

A Derivation of Green's functions **111**
A.1 Green's Function for open water . . . 112
A.1.1 Solution in the (k,z,ω)-domain . . . 114
A.1.2 Solution in the (x,z,ω)-domain . . . 115
A.2 Green's Function for ice-covered fluid layer . . . 117
A.3 Green's Functions for a semi-infinite ice cover . . . 119
A.4 Averaged responses . . . 121
A.5 Root-finding algorithms . . . 125
A.5.1 Roots for the open water region . . . 125
A.5.2 Roots for the ice-covered region . . . 126

B Numerical scheme for evaluating IFTs **129**
B.1 Requirements for the IFT scheme . . . 129
B.2 Selection of the analytical form . . . 130
B.3 Numerical aspects . . . 131
B.4 Validation . . . 137

C Derivation of the static breaking length **141**

D Convergence of the iterative scheme **143**

Acknowledgements **145**

Curriculum Vitæ **147**

List of Publications **149**

1

INTRODUCTION

1.1. OPPORTUNITIES IN THE ARCTIC

The Arctic presents a major opportunity for two industries: the oil and gas industry, and the maritime industry. The region is expected to contain 22% of the worlds unexplored hydrocarbon reserves and of these reserves, 84% is expected to be located offshore [1–3], see Fig. 1.1. For the extraction of offshore hydrocarbons, both bottom-founded and floating production platforms are commonly used. Bottom-founded platforms are limited to shallow waters, making floating platforms essential in gaining access to the reserves located in deeper waters. When floating structures operate in ice-infested waters, they are subject to ice loads that are far greater than the wave loads these structures normally encounter in ice-free waters. It is thus paramount to both understand and be able to predict the interaction between ice and floating structures so that the Arctic offshore hydrocarbons can be extracted in a safe and sustainable manner.

Second, a steady decline in sea ice cover [5, 6] is gradually making the region more accessible to marine activity. The primary benefactor of this trend is the shipping industry, with three new possible routes that cross the Arctic Ocean [7, 8], see Fig. 1.1. Routing vessels through the Arctic region is advantageous as it decreases the sailing distance between many major ports [9], see the bottom right of Fig. 1.1. This results in not only economic but also environmental gains as the shorter distances imply less fuel usage and thus lower emissions (49-78% less, see [10]). Although currently only a handful of vessels make use of these routes, this number is expected to increase, albeit slowly, as the sea ice cover continues to decline [9, 11]. In addition to this increase in shipping, the same trend is also making the Arctic region more accessible for cruise ships, leading to an increase in tourism [12, 13]. In order to take advantage of both opportunities without adversely affecting the region, a thorough understanding of the interaction between ice and floating structures, in this case vessels, is again required.

1

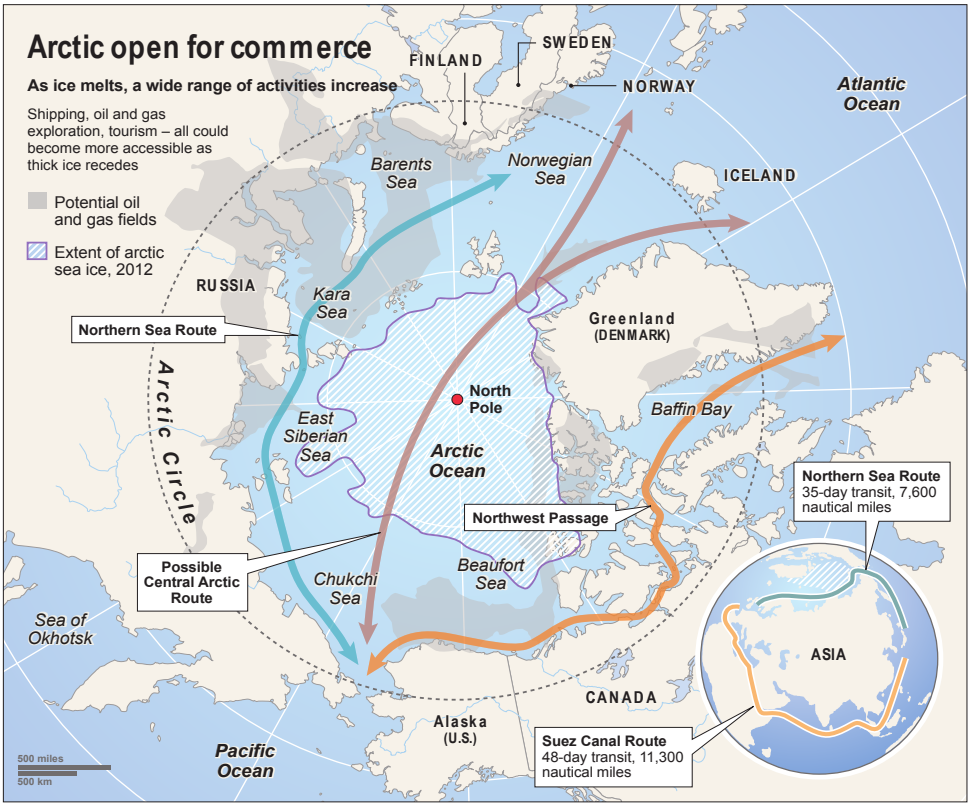

Figure 1.1: A map of the economic opportunities in the Arctic. The regions expected to contain hydrocarbons are highlighted with the gray shading. Three shipping routes that pass through the region are indicated as well. Copyright © 2014 CNA Corporation, www.cna.org. All Rights Reserved.

1.2. NUMERICAL MODELING OF ICE-FLOATER INTERACTION (IFI)

The most common approach for studying ice-floater interaction (IFI) is numerical modeling. A numerical IFI model consists of three major components: the floating structure, often referred to as floater for short, the ice and the fluid. When setting up a numerical IFI model, assumptions have to be made for each of the three components. The assumptions regarding the floater and ice are discussed next. The fluid, which is the main focus of this thesis, is treated separately in Sec. 1.3.

Floater In marine technology, it is common to model floaters as rigid bodies [14]. This assumption is also valid for most IFI studies since the deformations of the hull are small enough to only have a marginal effect on the interaction with the ice. This assumption may become invalid though; for instance, when studying the plastic deformations of the hull due to an impact with an iceberg [15].

Figure 1.2: The HMS Protector of the Royal Navy sailing through pack ice, an ensemble of ice floes, while on her mission to support the work of the Convention for the Conservation of Antarctic Marine Living Resources (CCAMLR). © Crown copyright 2013.

Ice Sea ice can take on many different forms referred to as ice features [16]. The most common features are ice floes (see Fig. 1.2), ice rubble (ice floes with a low length-to-thickness ratio, visible in Fig. 1.2 close to the vessel and in its wake), level ice (an ice floe with an "infinite" length-to-thickness ratio, see Fig. 1.3), ice ridges, icebergs, pack ice (an ensemble of ice floes, see Fig. 1.2), and broken ice (similar to pack ice but created by the interaction with a structure, generally due to an ice management operation). These ice features naturally drift about under the action of wind, current, and waves and may eventually be encountered by a floater. The ice feature and the floater can then interact in two ways: through contact loads or through the fluid. The latter option is discussed in the next section that covers the fluid. As floaters are generally not designed for the contact-based interaction with icebergs or large ridges, interaction with these ice features falls outside the scope of this thesis. Of the remaining ice features, ice floes, ice rubble, and level ice can be viewed as an ice floe with a certain length-to-thickness ratio, while pack ice and broken ice can be viewed as an ensemble of ice floes.

When an ice floe first impacts any structure, the ice at the contact will be crushed, exerting pressure on both the floe and the structure. How the contact-based interaction then continues depends primarily on the inclination of the structure at the interface with the ice floe. When an ice floe interacts with a vertically sided structure, such as the side of a ship or a wind turbine's monopile, the contact pressure is primarily in-plane and, consequently, bending failure will not occur and the interaction is limited to crushing. However, when an ice floe interacts with a slope, such as the bow of a ship, the resulting contact pressure that acts on the edge of the floe has both an in- and out-of-plane component. The latter component will progressively bend the ice as it slides along the

Figure 1.3: Russian icebreaker Krasin leading an American supply ship through level ice during Operation Deepfreeze in 2006. Image courtesy: NSF.

slope, ultimately causing the ice floe to fail in bending with a certain breaking length. When an ice floe is able to fail in bending, the resulting contact loads on the structure are, on average, much lower. Therefore, in order to minimize the ice loads, it is preferable for structures to be sloping at the expected interface with the ice. For this reason, ship-shaped floaters are generally designed to assure that the interaction predominantly takes place at its sloping bow.

Three major processes contribute to the overall load exerted by the ice floe on the floater when the floe interacts with its bow [17–19]. The first process, the bending of the floe ultimately leading to its failure, was described in the previous paragraph. This process results in the repeated bending failure of the ice floe, with each failure generating new pieces of ice rubble. The remainder of the incoming ice floe then pushes the rubble against the hull, causing the individual pieces to rotate and align with the hull. Any fluid present on top of the ice sheet is ejected by the secondary impact [20, 21]. During this process, it is possible for the rubble pieces to fail again in bending, further reducing their size [22]. The rotation and possible secondary bending failure of the rubble is the second major process that contributes to the overall ice load. After the alignment with the hull, the remainder of the ice floe pushes the rubble pieces forward, forcing them to slide along the hull until they end up beside the floater or in its wake. While sliding along the

hull, the rubble exerts traction due to its own inertia and buoyancy and the fluid flowing around the hull of the floater. This is the third and last major process that contributes to the overall ice load experienced by the floater. Although all three processes play an important role, approximately 60 to 80% of the load, is due to the processes at the waterline [23]. The first process, which gradually bends the ice floe and ultimately causes it to fail in bending, plays an important role in this thesis and will be referred to as ice-slope interaction (ISI).

When modeling IFI, and ISI in particular, an ice model is required that can predict bending deformations. Since ice floes have a relatively uniform ice thickness, they are well described by plate models [24]. Larger floes and level ice are often modeled as infinite or semi-infinite plates while ice rubble is often modeled as a collection of rigid bodies as their length-to-thickness ratio is low. Independently of their size, ice floes that are located at some distance from the floater are generally modeled as rigid bodies as these floes are predominantly subjected to contact loads caused by the collision with other nearby floes, which are mainly in-plane.

1.3. FLUID MODELING IN IFI

The third major component of an IFI model is the fluid. In order to accurately predict the motions of fluids, complex models such as the Navies-Strokes equations are often required. However, the complex nature of these equations and other similarly advanced fluid models result in a very long development and calculation time. In order to avoid these practical issues, assumptions are often made regarding the properties of a fluid that allow simpler fluid models to be used, such as potential theory. While these assumptions do decrease the complexity of the resulting fluid model, they also reduce the number of effects it can predict. As a result, the fluid models in use today range from very simple to very complex.

The fluid models used in IFI can be split into three categorized based on their complexity: models that only account for buoyancy and hydrostatic pressure, models based on potential flow, and advanced models based on methods such as Smooth Particle Hydrodynamics (SPH), Lattice Boltzmann Method (LBM), Large Eddy Simulation (LES), or Reynolds-averaged Navier–Stokes (RANS). Additionally, a fourth category of fluid models is used in IFI, namely effective fluid models. The usage of these four categories in IFI is reviewed in Ch. 2. The findings of that review are summarized next.

Hydrostatic fluid models The first category of fluid models only accounts for buoyancy and the resulting hydrostatic pressure and will be referred to as hydrostatic fluid models. The literature study shows that both historically and in recent years, the majority of IFI studies have been done using a hydrostatic IFI model. Presumably, it is the simplicity of hydrostatic fluid models which has led to their widespread use in IFI.

Fluid models based on potential theory The second category of fluid models employed in IFI use the Bernoulli equation to describe the fluid pressure and assume that the fluid is inviscid and irrotational, i.e. potential flow is assumed. The resulting model can predict three fluid effects that cannot be predicted by a hydrostatic model, namely

fluid flow, surface waves, and hydroelasticity. Fluid flow and surface waves both couple the motions of floating bodies. The former type of coupling has been studied previously for IFI [25–27] while the latter form of coupling has not been studied as thoroughly. In particular, the coupling between a floater and nearby level ice has not been studied.

Moreover, both fluid effects alter the bending behavior of ice floes. This so-called hydroelasticity has a strong effect on ISI, changing both the breaking length and the contact force and their velocity dependence [23]. However, as only a very limited number of studies have focused on the effects of hydrodynamics on ISI, many details are not fully understood. For instance, the relationship between the temporal development of the contact force and the dependence of the breaking length on the velocity has not been studied and the relative importance of the linear and nonlinear component of the Bernoulli equation has also not been studied. Moreover, no previous study has presented a direct comparison between a hydrostatic and a hydrodynamic model in the context of ISI. It is, therefore, unknown in which ranges of parameters the hydrostatic models are valid and how the addition of hydrodynamics influences the aforementioned changes in the breaking length and contact force.

Advanced fluid models The third category of fluid models are those based on SPH, LBM, LES, RANS, or other similarly advanced methods. These models give the most accurate predictions and, consequently, are the most general but, at the same time, the most complex. This category can account for additional fluid effects such as large displacements, viscosity, and turbulence. The importance of these fluid effects has not been studied extensively in the context of IFI. Only large displacements have been studied and it has been shown that this leads to backfill and ventilation effects [28]. Overall, it can be concluded that the adoption of advanced fluid models is a recent trend in IFI and most models are still under development.

Effective fluid models When using a hydrodynamic fluid model, the resulting IFI model becomes significantly more complex when compared to a hydrostatic model. In the author's opinion, this is the main reason for the prevalence of hydrostatic IFI models. Effective fluid models can be used to overcome the practical issues associated with hydrodynamics. These models aim to capture the effects that hydrodynamics has on IFI while remaining simple enough to only result in a marginal increase in complexity when compared to a hydrostatic fluid model. Because of this, effective fluid models are a promising approach to increase the adoption rate of hydrodynamics in IFI. However, while there have been several studies that explored the possibility of using effective fluid models for IFI [29–31], all studies concluded that their proposed effective model was not able to give satisfactory predictions of the hydroelastic behavior of the ice over a large range of parameters.

1.4. THESIS OBJECTIVES AND SCOPE

Research question In order to exploit the economic opportunities in the Arctic in a safe and sustainable manner, a thorough understanding of IFI is needed. The main method for studying IFI is numerical modeling and the fluid is a major component of

such a model. Fluids are difficult to model and consequently, a wide range of fluid models are used in IFI. Hydrostatic models are almost exclusively used, despite previous studies showing that hydrodynamics is an essential component of IFI. Since practical issues are likely to be the cause for the prevalence of hydrostatic models, effective fluids models could help to improve the adoption of hydrodynamics in IFI. Based on this reasoning, the following research question is formulated:

> *How does hydrodynamics affect the interaction between an elastic ice floe and a sloping structure and can its effects be captured by an effective fluid model?*

Because ISI is the main contributor to the overall load experienced by a sloping structure, this thesis will focus on ISI rather than on the whole interaction cycle in order to simplify the model. The rotation of the ice rubble and the flow of the rubble pieces around the hull of the vessel are, therefore, not addressed. All studies are carried out in 2D, to keep the models simple. Based on the above-formulated research question, the following three subquestions are defined.

Subquestion 1 This thesis will use potential theory to model the fluid as previous studies have shown that potential theory gives good predictions for ISI. However, while all previous studies on ISI have used discretization techniques such as FEM to obtain the time-domain response, in the thesis a novel approach is used based on integral transforms. In order to assist in the development of this semi-analytical ISI model, a different problem is considered first, which addressed the effect of the presence of a nearby ice floe on the response of a floating body to a sinusoidal excitation. Only very little is known about the surface-wave based coupling between these two bodies, in particular when the ice floe is modeled as an elastic body. The Green's functions that are derived for this problem can then be used for the development of the ISI model. This leads to the first subquestion of this thesis:

> *How does the surface-wave-based coupling between a floater and a nearby elastic ice floe affect the floater's response?*

Subquestion 2 Since most models utilize a hydrostatic fluid model, it is important to understand the limitations of these models. It is, therefore, essential to identify the velocity range wherein hydrostatic models are valid and how this range depends on parameters such as the ice thickness. Next, outside this range, hydrodynamics has to be included. However, since adding hydrodynamics to an existing model is a time-consuming task, it would be desirable to replicate the effects of hydrodynamics by a simple effective model that can be directly incorporated into existing models. For the development of such an effective model, a detailed understanding of the effects of hydrodynamics on ISI is required since the effective model will have to replicate these effects. Moreover, the general understanding of the effects that hydrodynamics has on ISI can still be improved. For instance, the relationship between the temporal development of the contact force and the dependence of the breaking length on the velocity and the relative importance of the linear and nonlinear component of the Bernoulli equation has not been studied. As such, the second subquestion of this thesis reads:

> *What is the effect of hydrodynamics on ice-slope interaction?*

Subquestion 3 The model used to answer the second subquestion is based on potential theory. Nevertheless, the effort required to implement such a model is substantial, again highlighting the difficulties associated with hydrodynamics. In order to facilitate the adoption of hydrodynamics in IFI models, an attempt is made to create an effective fluid model that captures the effects of hydrodynamics on ISI. This leads to the third and last subquestion of this thesis:

> *Can the effect of hydrodynamics on ice-slope interaction be captured by an effective fluid model that gives valid prediction over a wide range of parameters?*

1.5. THESIS OUTLINE

This thesis is composed of a literature review chapter and three chapters that present the novel contributions of this thesis. Each of the latter chapters addresses one of the research subquestions of this thesis.

In Ch. 2 a review is presented of numerical and experimental IFI studies. The review covers each of the four categories of fluid models as listed previously in this introduction. The main findings of this review were used to define the scope of this thesis and to identify available experimental data that can be used to validate the numerical ISI model proposed in this thesis.

In the second chapter of this thesis, Ch. 3, the first research subquestion is addressed. A semi-analytical model is proposed that can predict the frequency-domain response of a floater while including the coupling with a nearby ice floe, modeled as an elastic plate, due to surface waves. The model is used to assess the conditions under which the presence of the ice affects the floater's response and discover the underlying physical processes that cause the ice to affect the floater's response. The Green's functions derived for this problem can then be used for the development of the ISI model.

In Ch. 4 the second research subquestion is addressed. A semi-analytical model is introduced that can predict the time-domain hydroelastic response of an ice floe interacting with a downward-sloping structure. As part of this model, a convolution-based time-integration scheme is introduced to solve the resulting set of coupled, nonlinear integer-differential equations. Using this novel model, the importance of the various components of the model, such as the rotational inertia of the ice and axial compression, is investigated. Following this, the balance of forces in the ice sheet is studied. Thereafter, the relation between the temporal development of the contact force and the dependence of the breaking length on the ice velocity is investigated. Lastly, as all three studies are done using both hydrodynamic and hydrostatic ISI models, the comparison between their predictions allows the limitation of the latter model to be identified.

Based on the understanding gained in Ch. 4, an attempt is made to develop an effective model that captures the effects of hydrodynamics on ISI. This is done in Ch 5. The proposed effective models is based on frequency-independent added mass and added damping coefficients. The optimal value of these unknown coefficients is found by minimizing the error of the predictions of the resulting effective ISI models with the prediction of the hydrodynamic ISI model that was introduced in Ch. 4. The efficacy of the effective ISI models is then assessed over a wide range of parameters.

The main findings of this thesis are summarized in chapter 3. The appendices that follow the conclusions contain detailed derivations that supplement the numerical models used in this thesis. Specifically, in App. A a set of Green's functions are derived for a semi-infinite Euler-Bernoulli beam floating on an infinitely wide fluid layer of finite depth for various types of loading and in App. B the numerical scheme used to evaluate the various inverse Fourier transform that arose in Ch. 4 is explained.

REFERENCES

[1] K. J. Bird, R. R. Charpentier, D. L. Gautier, D. W. Houseknecht, T. R. Klett, J. K. Pitman, T. E. Moore, C. J. Schenk, M. E. Tennyson, and C. J. Wandrey, *Circum-Arctic Resource Appraisal: Estimates of Undiscovered Oil and Gas North of the Arctic Circle,* USGS Fact Sheet 2008-3049 **2008-3049**, 1 (2008).

[2] D. L. Gautier, K. J. Bird, R. R. Charpentier, A. Grantz, D. W. Houseknecht, T. R. Klett, T. E. Moore, J. K. Pitman, C. J. Schenk, J. H. Schuenemeyer, K. Sørensen, M. E. Tennyson, Z. C. Valin, and C. J. Wandrey, *Assessment of Undiscovered Oil and Gas in the Arctic,* Science **324**, 1175 LP (2009).

[3] A. E. Kontorovich, M. I. Epov, L. M. Burshtein, V. D. Kaminskii, A. R. Kurchikov, N. A. Malyshev, O. M. Prischepa, A. F. Safronov, A. V. Stupakova, and O. I. Suprunenko, *Geology and hydrocarbon resources of the continental shelf in Russian Arctic seas and the prospects of their development,* Russian Geology and Geophysics **51**, 3 (2010).

[4] CNA Military Advisory Board, *National Security and the Accelerating Risks of Climate Change*, Tech. Rep. (CNA Corporation, 2014).

[5] O. M. Johannessen, *Satellite Evidence for an Arctic Sea Ice Cover in Transformation,* Science **286**, 1937 (1999).

[6] K. Y. Vinnikov, K. Y. Vinnikov, A. Robock, R. J. Stouffer, J. E. Walsh, C. L. Parkinson, D. J. Cavalieri, J. F. B. Mitchell, D. Garrett, and V. F. Zakharov, *Global Warming and Northern Hemisphere Sea Ice Extent,* Science **286**, 1934 (1999).

[7] N. Melia, K. Haines, and E. Hawkins, *Sea ice decline and 21st century trans-Arctic shipping routes,* Geophysical Research Letters **43**, 9720 (2016).

[8] Y. Aksenov, E. E. Popova, A. Yool, A. J. Nurser, T. D. Williams, L. Bertino, and J. Bergh, *On the future navigability of Arctic sea routes: High-resolution projections of the Arctic Ocean and sea ice,* Marine Policy **75**, 300 (2017).

[9] A. Buixadé Farré, S. R. Stephenson, L. Chen, M. Czub, Y. Dai, D. Demchev, Y. Efimov, P. Graczyk, H. Grythe, K. Keil, N. Kivekäs, N. Kumar, N. Liu, I. Matelenok, M. Myksvoll, D. O'Leary, J. Olsen, S. Pavithran.A.P., E. Petersen, A. Raspotnik, I. Ryzhov, J. Solski, L. Suo, C. Troein, V. Valeeva, J. van Rijckevorsel, and J. Wighting, *Commercial Arctic shipping through the Northeast Passage: routes, resources, governance, technology, and infrastructure,* Polar Geography **37**, 298 (2014).

[10] H. Schøyen and S. Bråthen, *The Northern Sea Route versus the Suez Canal: cases from bulk shipping,* Journal of Transport Geography **19**, 977 (2011).

[11] L. Beveridge, M. Fournier, F. Lasserre, L. Huang, and P. L. Têtu, *Interest of Asian shipping companies in navigating the Arctic*, Polar Science **10**, 404 (2016).

[12] E. J. Stewart, J. Dawson, and D. Draper, *Cruise tourism and residents in Arctic Canada: Development of a resident attitude typology*, Journal of Hospitality and Tourism Management **18**, 95 (2011).

[13] J. McCarthy, *Responsible cruise tourism and regeneration: the case of Nanaimo, British Columbia, Canada*, International Planning Studies **23**, 225 (2018).

[14] J. Journée and W. Massie, *Offshore Hydromechanics*, 1st ed. (2001).

[15] R. E. Gagnon and J. Wang, *Numerical simulations of a tanker collision with a bergy bit incorporating hydrodynamics, a validated ice model and damage to the vessel*, Cold Regions Science and Technology **81**, 26 (2012).

[16] A. Palmer and K. Croasdale, *Arctic offshore engineering* (World Scientific Publishing, 2013).

[17] E. Enkvist, P. Varsta, and K. Riska, *The Ship-Ice Interaction*, in *Proceedings of the 5th Int. Conference on Port and Ocean Engineering under Arctic Conditions* (Trondheim, 1979) pp. 977–1002.

[18] I. Poznyak and B. Ionov, *The division of icebreaker resistance into components*, in *Proceedings of the 6th Ship Technology and Research (STAR) Symposium* (Ottawa., 1981) pp. 249–252.

[19] P. Varsta, *On the mechanics of ice loads on shipsin level ice in the Baltic Sea*, Technical Research Centre of Finland, Publications 11, Espoo (1983).

[20] P. Valanto, *Experimental and theoretical investigation of the icebreaking cycle in two dimensions*, Ph.D. thesis, University of California, Berkeley (1989).

[21] P. Valanto, *Experimental study of the icebreaking cycle in 2-D*, in *Eighth International Conference on Offshore Mechanics and Arctic Engineering (OMAE)* (The Hague, The Netherlands, 1989) pp. 343–349.

[22] W. Lu, R. Lubbad, K. Høyland, and S. Løset, *Physical model and theoretical model study of level ice and wide sloping structure interactions*, Cold Regions Science and Technology **101**, 40 (2014).

[23] P. Valanto, *The icebreaking problem in two dimensions : experiments and theory*, Journal of Ship Research **36**, 299 (1992).

[24] J. P. Dempsey, Z. G. Zhao, and H. Li, *Axisymmetric indentation of an elastic layer supported by a winkler foundation*, International Journal of Solids and Structures **27**, 73 (1991).

[25] A. Tsarau, R. Lubbad, and S. Løset, *A numerical model for simulation of the hydrodynamic interactions between a marine floater and fragmented sea ice*, Cold Regions Science and Technology **103**, 1 (2014).

[26] A. Tsarau and S. Løset, *Modelling the hydrodynamic effects associated with station-keeping in broken ice,* Cold Regions Science and Technology **118**, 76 (2015).

[27] A. Tsarau, R. Lubbad, and S. Løset, *A numerical model for simulating the effect of propeller flow in ice management,* Cold Regions Science and Technology **142**, 139 (2017).

[28] W. Lu, S. Løset, and R. Lubbad, *Ventilation and backfill effect during ice-sloping structure interactions,* in *21st IAHR International Symposium on Ice* (2012) pp. 826–841.

[29] J. P. Dempsey and Z. G. Zhao, *Elastohydrodynamic response of an ice sheet to forced sub-surface uplift,* Journal of the Mechanics and Physics of Solids **41**, 487 (1993).

[30] Z. G. Zhao and J. P. Dempsey, *Planar forcing of floating ice sheets,* International Journal of Solids and Structures **33**, 19 (1996).

[31] R. Lubbad, G. Moe, and S. Løset, *Static and dynamic interaction of floating wedge-shaped ice beams and sloping structures,* in *Proceedings of the 19th IAHR Symposium on Ice, Vancouver, Canada* (2008) pp. 227 – 237

2

REVIEW OF IFI STUDIES

In this chapter, a review of the state of the art in IFI studies is given. Four categories of fluid models were introduced in Ch. 1: hydrostatic, potential-theory based, advanced, and effective fluid models. Correspondingly, this chapter first gives an overview of numerical IFI studies that fall into these four categories of fluid models. Thereafter, experimental studies on IFI are reviewed.

First, an overview is given of studies that employ hydrostatic IFI models in Sec. 2.1. Second, an overview of IFI models based on potential theory is given in Sec. 2.2. Third, advanced IFI models are discussed in Sec. 2.3. As the number of studies that use effective fluid models is very limited, they are addressed as part of the previous three sections. Experimental studies on IFI are then covered in Sec. 2.4. The review is rounded off with a summary in Sec. 2.5 and a conclusion in Sec. 2.6 that substantiates the scope of this thesis as defined in Sec. 1.4.

Note that this review primarily aims to give an overview of the state-of-the-art of the numerical modeling of ice-floater interaction and may, therefore, not be exhaustive. The placement of studies into a certain category as well as the categories themselves are a subjective process and, therefore, some studies may have inadvertently been placed in a category that one or more of the authors of said studies would disagree with. Unless stated otherwise, all cited models were validated against experimental data or against predictions of other validated models and showed good agreement.

2.1. HYDROSTATIC MODELS

A large majority of IFI models make use of hydrostatic fluid models. These models only account for buoyancy, resulting in a very simplistic description of the fluid reaction. Depending on the geometry of the floating body, the hydrostatic pressure is often modeled using a set of linear springs for rigid bodies or a Winkler foundation for elastic bodies. In rare cases, the hydrostatic pressure is accounted for by direct integration of the hydrostatic pressure over the wetted area, resulting in a nonlinear formulation. This approach was used by, for instance, Jensen *et al.* [32] and Dalane *et al.* [33]. In general, however,

most IFI models use a linear description of hydrostatics. As the total number of such studies is rather large, they are split into several groups based on the complexity of the ice model.

2.1.1. ANALYTICAL & EMPIRICAL MODELS

The number of analytical or empirical models used in IFI is relatively small compared to the number of numerical models. Two seminal analytical models are those by Lindqvist [34] and Croasdale *et al.* [35]. The former proposed a method to estimate the ice resistance experienced by floaters while moving through level ice, whereas the latter proposed a method to estimate the load exerted by level ice on a sloping structure. Both models are still commonly used and Croasdale's model is included in the ISO 19906 standard that covers the design of offshore structures in Arctic environments [36]. Other models are by Keinonen *et al.* [37] who, according to Kulaots *et al.* [38], proposed a method to study the performance and efficacy of icebreakers assistance for ships navigating through various ice conditions and by Riska *et al.* [39] who proposed a method to study the performance of icebreakers.

The main advantage of analytical models is their calculation speed and because of this, new analytical models are still occasionally put forward. Aksnes [40] recently proposed a simple analytical model for the interaction between ships and level ice and Lu *et al.* [41] proposed a 2D analytical model for estimating the loading on a downward sloping structure due to the interaction with level ice. This latter model also accounts for a possible secondary bending failure of the ice floe. However, with the advent of faster computers, analytical models have gradually fallen out of favor and nowadays numerical models are the norm. These models can handle more complex geometries and can account for a large variety of physical phenomena. Consequently, this section on hydrostatic models is mainly devoted to numerical models.

2.1.2. EDGE-TRACKING MODELS

While most hydrostatic IFI models are numerical in nature, a great number of them make use of analytical or empirical formulas for one or more of their components. An example of such a hybrid model is the edge-tracking models.

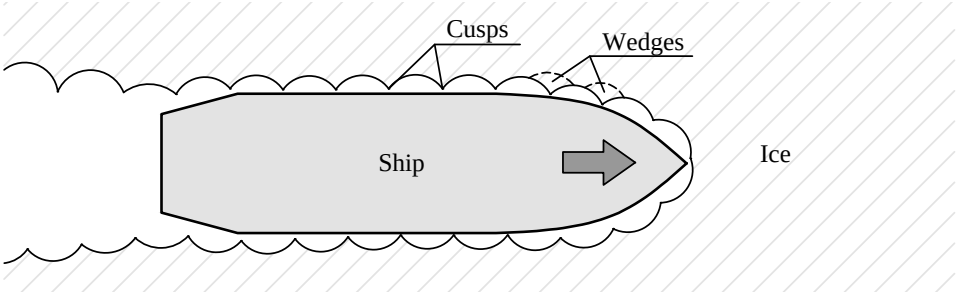

Figure 2.1: As the vessel advances, it mainly interacts with the ice sheet through a series of cusps. Each cusp fails in bending, generating wedges. This process results in an ice edge pattern that is typical for the edge tracking models.

Edge-tracking models were first introduced by Wang [42]. In essence, these models only track the edge of an ice floe and any overlap between the ice edge and the floater is assumed to generate a contact load, the magnitude of which is generally assumed to be proportional to the area of the contact surface. In these models, the interaction between floater and ice edge primarily takes place at a series of cusps, see Fig. 2.1. It is then assumed that the load applied to each cusp causes the associated ice wedges to fail in bending due to a radial crack, breaking off the wedge from the infinite ice sheet. The radius of this crack, as well as the maximum load that can be applied at each cusp before bending failure occurs, are generally calculated using empirical formulas that are based on experimental or full-scale data. Commonly used empirical formulas are those by Nevel [43], Kotras *et al.* [44], Varsta [45], and Lindqvist [34].

Edge-tracking models have been primarily used to estimate the load exerted by level ice on floaters [46–55] and to study the station-keeping of floaters in level ice [56, 57]. Only two studies considered the interaction with broken ice, i.e. with multiple ice floes. Huisman *et al.* [58] used such a model to estimate the ice load experienced by a ship maneuvering through broken ice and Scibilia *et al.* [59] to study the efficacy of an ice management operation. It is important to note that most of the aforementioned studies only [49, 59] include the generated ice rubble as separate bodies, i.e. the clearing loads due to interaction with the ice rubble is either disregarded altogether [47, 48, 58] or captured in an empirical manner [46, 50, 51, 53–57], with the majority using the empirical model by Lindqvist [34].

2.1.3. RIGID MULTIBODY MODELS WITHOUT FAILURE

While most edge-tracking models only account for a single body, namely the floater, multibody models also include the individual ice floes as rigid bodies, see Fig. 2.2. Rigid multibody models that disallow failure of the ice floes are considered first while those that incorporate failure are covered in the next subsection.

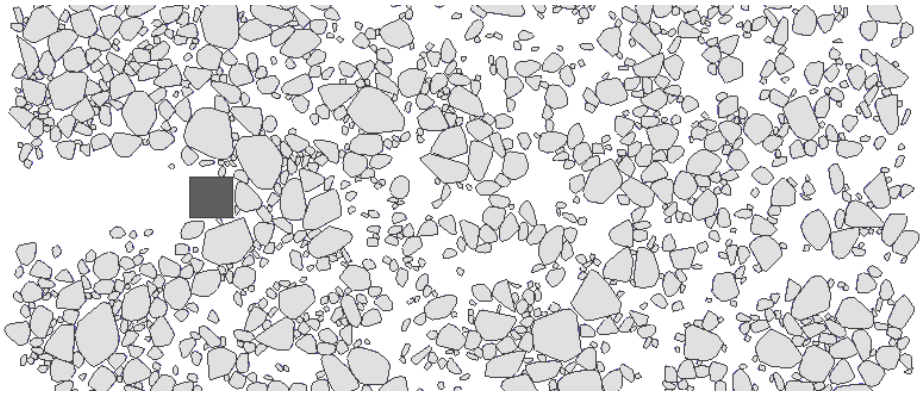

Figure 2.2: A simulation of pack ice flowing around a fixed, rectangular structure, modeled in 2D using rigid bodies without any failure modes. Image Courtesy: Marnix van den Berg.

Rigid multibody models that disallow failure generally consider the interaction between a floater and pack or broken ice in the plane defined by the water surface and,

consequently, the majority of these models are in 2D. One of the earliest of such models was presented by Løset [60]. In this 2D model, the ice floes are assumed to be circular and a smooth contact model is used to resolve the collisions. This model was used to study the ice forces experienced by a boom being pulled through pack ice [61]. Such a rigid, circular multibody model was also used by Dai and Peng [62] to study the station-keeping performance of a vessel using dynamic positioning, by Sayed *et al.* [63] to study the yield condition of an ensemble of ice floes, by Herman [64] to study the influence of ice concentration and floe-size distribution on the formation of broken ice and, lastly, by Daley *et al.* [65, 66] to study the ice loads experienced by a vessel or icebreaker in pack ice.

This last scenario, the performance of a floater moving through or station-keeping in pack ice, is typical for rigid multibody IFI models and was also studied using triangular [67], rectangular [68, 69], parallelepiped [70] and irregular-shaped floes [71–73]. Some of these models make use of event-mechanics in order to solve the problem in a parallel manner using GPUs which greatly improves the calculation time [65, 66, 73]. An extension of the circular shapes to 3D was done by Hopkins and Tuhkuri [74] using disk-shaped elements and this model was used to study the compression of circular ice floes. This approach was also used more recently by Ji [75] to study the performance of an icebreaker in broken ice.

By disallowing failure of the floes, a multibody dynamics problem is obtained for which dedicated software libraries exist, referred to as physics engines. A very thorough overview of available physics engines is given in Janßen *et al.* [76]. Generally, these engines use non-smooth contact models to improve the speed and, in recent times, a number of these engines have been used for IFI. The 2D engine Box2D was used by Yulmetov *et al.* [77] and Yulmetov and Løset [78] to study the drift and towing of icebergs through broken ice. Another numerical framework for floaters in broken ice was proposed by Metrikin *et al.* [79]. It makes use of the Vortex engine that employs a non-smooth contact model and can also handle polygon-shaped ice floes.

2.1.4. RIGID MULTIBODY MODELS WITH ANALYTICAL OR EMPIRICAL FAILURE

The group of studies outlined in the previous sub-section did not account for any failure mode. To enhance the capabilities of these models, one or more failure modes, such as bending, buckling, and splitting, can be incorporated. Since the bodies are still rigid, the stresses, which are required to assess whether and how the floe will fail, are obtained using analytical or empirical formulas.

One of the earliest developments of such a model was by Lubbad and Løset [80]. Their model is able to perform real-time simulations of an icebreaker navigating through broken ice and includes bending failure based on two analytical solutions. The initial interaction between the ice floes and the vessel takes place through a smooth contact model based on the PhysX engine. The resulting stresses in the ice floe are then estimated using the analytical solution for the static response of a semi-infinite plate to a distributed load at its edge. Once failure is detected, a series of radial cracks are instantiated from the contact point. This generates several wedges and the total number of wedges is based on full-scale observations by Nevel [81]. Subsequently, the wedges

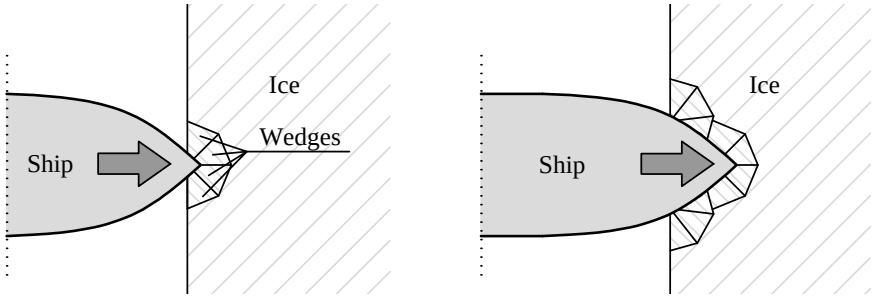

Figure 2.3: An illustration of an analytical failure model that assumes that each interaction point ultimately leads to bending failure, initiating both radial and circumferential cracks, thereby generating an assumed number of wedges. As the vessel advances, the previously generated wedges are pushed below the ship and the failure process repeats itself.

themselves can fail in bending and their failure is based on the stresses estimated using the analytical solution for a static, infinite wedge [82]. This process leads to the failure pattern illustrated in Fig. 2.3. This model makes use of the PhysX engine to perform the collision detection and time integration. A framework with similar functionality is explained in Metrikin [83] and Metrikin *et al.* [84].

A proposal to improve the empirical multibody model by Lubbad and Løset [80] is described in Metrikin *et al.* [85]. Planned improvements were to discretize floes subjected to large forces with FEM, thereby avoiding the need for the empirical bending failure model that was used previously and to include backfill and ventilation. However, this model was never realized. More recently, an improved version of the model by Lubbad and Løset [80] was proposed that also incorporates splitting failure, see Lubbad *et al.* [86]. In this version, the splitting of ice floes is incorporated using analytical solutions based on a geometrical idealization of the floe being considered, see Lu *et al.* [87, 88]. Depending on the estimated stresses, the floe can then fail in either bending or splitting.

Using analytical or empirical formulas to handle the failure of the ice floes has the advantage of improving the computational speed. However, the main disadvantage of this approach is that each state that occurs during the calculation has to be mapped to one of the analytical solutions that are embedded in the model. This mapping introduces an error as the analytical or empirical formulas often have to obey strict assumptions regarding, for instance, the geometry of the floe.

2.1.5. ELASTIC MULTIBODY MODELS WITH STRESS-BASED FAILURE

The only way to truly avoid the mapping issues described in the previous subsection is to resolve failure without making use of analytical or empirical formulas, which can be achieved by using elastic models. Not only does this allow for a more accurate assessment of the stresses in the ice, but the effect of the ice's deformations on the interaction is then also included. Elastic models, therefore, have enhanced capabilities compared to rigid models. However, this increase in accuracy comes with a major downside, namely an increase in the computation time.

A 2D elastic IFI model that has been used for a variety of studies was proposed by

Paavilainen *et al.* [89]. This model considers the interaction between level ice, modeled as a geometrically nonlinear Timoshenko beam, and a rigid, immobile downward sloping structure. The ice moves towards the structure with a constant, far-field velocity and fails in bending or buckling. The resulting rubble pieces are modeled as discrete elements and buoyancy pushes the rubble upwards, affecting the interaction between the incoming ice and the structure. The rubble formation process was studied in several works by the same authors [90–93]. The statistics of this model's predictions were studied by Ranta [94–97]. Lastly, the model was used to perform studies of ridge keel punch through tests in 2D by Polojärvi and Tuhkuri [98] and in 3D [99, 100], after an extension of the model to 3D [101].

The interaction between incoming level ice and a fixed, conical structure has been studied by several authors using an elastic multibody model. Septseault *et al.* [102] presented a 3D model that aims to provide a tool for the optimization of a structure's geometry in order to reduce the ice loads due to level ice. The same scenario was studied by Ji *et al.* [103] using a discrete-element method (DEM) based on spherical elements. The elements are connected to one another using viscoelastic connections that include Mohr-Coulomb friction. The model was used to investigate the ice loading on a sloping structure [103] and for the concept design of an icebreaker's hull by studying its performance in level ice [104]. Such a sphere-based model was also used by Sayed [105] to study the interaction between a fixed structure and floating level ice in a 2D setting. The interaction with a fixed cone was also studied by Lu *et al.* [106] using the cohesive element method. A 3D IFI model was proposed by Jensen *et al.* [32]. While their report lacks details about the numerical model, it is used in conjunction with ice basin measurements for the design of moored floaters. Lau [107] used the commercial DEM package DECICE to study the performance of a vessel moving through ice and van den Berg *et al.* [108] introduced a general purpose 3D nonsmooth multibody model based on Voronoi tessellation.

Lastly, Sayed *et al.* [109] proposed an IFI model based on the particle-in-cell method. In this approach, discrete particles are used to model the advection of the ice. The momentum equations are solved on a Eulerian grid, allowing an implicit time domain solver to be used. The details of this method can be found in [109–111]. This model was employed to study the load exerted by pack ice on the Kulluk vessel [110, 112, 113] and to show the importance of confinement in this scenario [114].

2.2. MODELS BASED ON POTENTIAL THEORY

The next category of numerical IFI models incorporates hydrodynamics by using potential theory to describe the fluid, generally assuming incompressible potential flow. Whereas the hydrostatic models in the previous section only account for buoyancy, models based on incompressible potential flow allow three additional fluid effects to be predicted, namely fluid flow, surface waves, and hydroelasticity. These additional fluid effects influence IFI in several ways.

First, when a body moves through a fluid, for example when an ice floe is deflected downward during ISI, the underlying fluid has to be displaced which generates a flow. The inertia of the mobilized fluid, in turn, exerts a reactive pressure on the body, thereby affecting its response. Moreover, the resulting flow generates a pressure field that can

affect other nearby floating bodies, thereby coupling their motions. An example of when this occurs is when an iceberg passes by a floater [115]. Note that, if the fluid is assumed to be incompressible and the surface assumed to be flat, the fluid flow will instantaneously reach its steady-state velocity in the entire domain. For a compressible fluid, the transient stage will take a finite amount of time. This means that the so-called fluid memory effect is not present when modeling fluid flow under the assumption of incompressible potential flow and a flat surface.

Second, surface waves are radiated when a (partly-)submerged body moves in a fluid that has a free surface. The radiated waves are experienced by the radiating body as a form of energy dissipation, i.e. damping. The excited surface waves propagate in a dispersive manner and can excite motions of other nearby bodies, coupling their motions. However, while the coupling due to fluid flow can be instantaneous if the fluid is assumed to be incompressible and the surface is assumed to be flat, the speed at which surface waves travel is always finite, independently of the compressibility of the fluid. Consequently, when surface waves are included, the effect of hydrodynamics becomes dependent on time, meaning that the fluid memory effect has to be dealt with, which implies that convolution integrals should be dealt with for the time-domain analysis.

Lastly, when ice floes are modeled as elastic bodies, such as a plate, their motions displace the underlying fluid, thereby generating both a flow and waves. The resulting hydroelastic response of the plate thus differs greatly from its hydrostatic response. This has several consequences. First, the plate experiences an increased resistance since it has to mobilize the fluid and, as a result, the combined plate-fluid system has different bending modes than the plate by itself. Second, since surface waves are excited, the combined plate-fluid system has one additional propagating mode compared to the plate by itself. Moreover, if the fluid has a finite depth, countably infinitely many modes are added in addition to the single propagating mode. Lastly, since the plate excites the fluid, it effectively siphons energy from the plate, thereby acting as a source of dissipation from the perspective of the plate.

The overview of this category is split into two parts. First, studies that cover the contact-based interaction between ice and floaters are discussed in Sec. 2.2.1 and, thereafter, studies covering the fluid-based interaction are discussed in Sec. 2.2.2. The, in order to better understand why so few IFI models incorporate hydrodynamics, some of the difficulties associated with incorporating hydrodynamics based on potential theory are discussed in Sec. 2.2.3.

2.2.1. CONTACT-BASED INTERACTION

Contact-based hydrodynamic IFI models are a natural extension of the hydrostatic models discussed in Sec. 2.1. However, the sheer number of hydrostatic studies is in stark contrast to the number of hydrodynamic studies. Moreover, many hydrodynamic studies do not include a floater and instead excite the ice-fluid system by an assumed external force, thereby focusing on the hydroelastic response of the ice-fluid system. While these studies are not IFI in the strict sense, they will be included in this overview.

One of the earliest studies that considered the hydroelastic response of ice is by Kheisin [116]. While it was not possible to find this study, other authors citing this paper [117–119] mention that it considered the vibration of a floating ice sheet, including

hydrodynamics, but did not evaluate the solution. The first study to present the time domain response of a sheet of level ice, including hydrodynamics, was by Nevel [117]. The ice was modeled as an infinite Kirchhoff-Love plate while the fluid layer of finite depth was modeled using incompressible potential flow. The ice was excited by an external time-harmonic load applied over a circle and the response to the axially symmetric problem was obtained using Hankel transforms. Both the free and forced vibrations of the ice sheet are presented by Nevel [117]. The latter solution was used to study the amplification of the stresses in the ice sheet as a function of the excitation frequency. The maximum dynamic amplification was found to be ten percent.

One of the first studies to address ice-slope interaction was accomplished by Sørensen [120]. The presented model uses a semi-infinite Kirchhoff-Love plate that includes in-plane deformations to represent the sheet of incoming level ice. The problem is initially formulated including incompressible potential flow. However, this description is forfeited in favor of an effective model based on a frequency-independent added mass coefficient under the assumption that "the major influence from the water on the deflection of the sheet is the inertia force associated with the acceleration of the water". Its value is based on the added mass of a rotating plate that was obtained by Engelund [121]. The analytical time domain solutions are then obtained using integral transforms. This model was used to study the interaction between level ice and three different structures, namely an infinitely wide sloping structure, a sloping structure of finite width, and several sloping structures at once. The model differentiates between crushing failure of the entire cross-section and dynamic bending failure and presents the velocity-dependent breaking length for the three scenarios considered. Lastly, experiments were performed to validate the analytical model.

The majority of hydrodynamic IFI studies were done in the last two decades. These studies can be split into three groups based on how they choose to excite the ice. One group excited the ice kinematically, a second group assumed an external load and a third group considered the interaction with a sloping structure.

First, the uplift of an ice sheet was studied by Dempsey and Zhao [118, 119, 122]. In their 2D model, an infinite sheet of level ice that floats on a fluid layer of finite depth is kinematically excited by a cylindrical indenter. The ice is modeled as a Kirchhoff-Love plate and the fluid is modeled using incompressible potential flow. The time-domain solution is obtained analytically using Hankel transforms and the resulting convolution integral is evaluated numerically. The sensitivity of the uplift force to various parameters is investigated. It is observed that the fluid underneath the ice increases the mass and damping substantially and that hydrodynamics greatly increases the uplift load. A similar, static problem was also studied by the same authors [123]. In [119, 122] the possibility of using an effective fluid model based on a frequency-independent added mass coefficient is explored. However, both studies showed that the effective model was incapable of capturing the effects of hydroelasticity over a wide range of parameters.

Second, a group of studies focused on the hydroelastic response of level ice excited by an assumed load. The bending failure of a semi-infinite plate subjected to a point load whose magnitude increases linearly in time was studied by Fox [124]. Unfortunately, it was not possible to find the full transcript of this study. A similar study was done by Sawamura *et al.* [125] using the Finite Element Method (FEM). In that paper, it is shown

that the free water surface is important, i.e. that a semi-infinite ice sheet floating on an infinitely wide water layer behaves differently from a semi-infinite ice sheet supported by a semi-infinite water layer. Additionally, they studied the response of a wedge for various wedge angles. The model shows good agreement with the analytical solutions of Fox [124] and Zhao and Dempsey [122]. Fox and Chung [126, 127] presented the Green's function of an infinite, thin plate floating on a fluid layer of both finite and infinite depth in a non-dimensional form and, subsequently, studied the behavior of these functions. The validity of ignoring the mass of the ice sheet is investigated and it is concluded that, while the response is qualitatively the same, quantitatively they are different enough to warrant the inclusion of the ice mass. Kozin and Pogorelova [128] studied the effect of bottom roughness on the response of an infinite ice plate excited by an impulse. The same authors also studied the response to an explosion, i.e. instantaneous load acting on the fluid rather than on the ice itself, see Kozin and Pogorelova [129].

Lastly, true hydrodynamics IFI models are discussed. The seminal works on this topic are by Valanto who studied the loading experienced by icebreakers advancing through level ice. Through a combination of numerical and experimental modeling, Valanto identified hydrodynamics as one of the key components of the bending failure of level ice against a downward-sloping structure.

Valanto created several numerical models. The first was a 2D model in which the fluid is described using unsteady, incompressible potential flow and the ice is modeled as a Euler-Bernoulli beam [130]. The model accounts for the constant forward velocity of the vessel by imposing a steady-state flow of the fluid around the hull of a vessel. The model includes the first two stages of the icebreaking cycle, namely bending failure and rotation of the broken off ice feature. Both fluid and ice are discretized using finite differences and a smooth contact model is employed for the interaction between the advancing vessel and the ice sheet. The prediction of the model shows very good agreement with the experimental results. Based on the prediction of this model, it was found that hydrodynamics greatly affects both the contact load and the breaking length and that it is a defining factor in their velocity dependence, confirming the experimental observation also presented in [130]. In order to improve the computational efficiency of the model, usage of a simplified surface boundary condition was investigated, namely one that does not account for the inertia of the ice sheet. It was found that this simplification is acceptable for modeling the first stage of the icebreaking cycle, i.e. until the ice fails in bending. A similar study was done in 2D by Wang and Poh [131] while also accounting for the edge moment. The results of this study are in agreement with the results by Valanto. Next, the 2D model of Valanto was extended to 3D, resulting in one of the most advanced IFI models to date, named VENICE [132]. This extended model was validated using the full-scale measurements of four different vessels and the model showed good agreement for all four validation cases. VENICE was then used to predict the spatial distribution of the ice loads acting on icebreakers advancing through level ice, including their velocity and ice thickness dependence [133].

Dempsey *et al.* [134] the problem statement for a 2D hydrodynamic IFI model is given. However, no numerical implementation of the model was reported and, consequently, no predictions were presented. Lubbad *et al.* [135] studied ISI with the ice modeled as several adjacent wedge-shaped beams, i.e. it was assumed that radial cracks

have already split the ice sheet into a number of wedges. The model which is based on FEM performed satisfactorily. They also investigated the applicability of an effective fluid model based on a contact added mass coefficient in combination with a Winkler's foundation and a damping term to replicate the effects of hydrodynamics. However, the accuracy of the effective model was lacking when compared to the FEM model.

2.2.2. FLUID-BASED INTERACTION

In addition to contact-based interaction, hydrodynamics opens a second path of interaction, namely coupling due to fluid flow and surface waves. The importance of both fluid flow and surface waves for IFI is discussed next.

The interaction between a floater and nearby ice floes through fluid flow was studied by Tsarau *et al.* [115]. This work is based on incompressible potential flow under the assumption of a flat surface, thereby eliminating surface waves and all fluid memory effects. The proposed model was used to study the interaction between a floater and a nearby piece of ice and was validated against model tests performed in a towing tank. In a follow-up study, the model was extended using the vortex element method to account for the wake generated by the floater and how the wake affects the flow of ice floes around the floater [136]. In a third study, the flow generated by the propellers of a floater was added. The numerical model was calibrated using full-scale data [137]. Similarly, the hydrodynamic interaction between an iceberg and a nearby floater was studies by various authors [138–140].

The importance of surface-wave-based coupling is considered next. Problems that deal with multiple floating bodies which are in close proximity are called multibody hydrodynamic problems and this class of problems has been studied extensively in the field of marine technology under the assumption that all floating bodies are rigid. While this assumption is generally valid for ships, it does not always hold for ice floes since their wavelengths are often comparable to those of the surface waves. It is, therefore, important to understand how the surface-wave-based coupling between a floater and nearby elastic ice affects the response of the floater. However, this type of interaction has not been studied to the best of the author's knowledge.

2.2.3. DIFFICULTIES ASSOCIATED WITH INCORPORATING HYDRODYNAMICS

Looking at the aforementioned hydrodynamics IFI studies, three principal approaches have been used to incorporate hydrodynamics: discretization of the entire fluid domain, analytical approaches based on integral transforms, and the boundary element approach. All three approaches have their own set of challenges and these are discussed next. Note that while other approaches are possible, this subsection merely aims to illustrate the difficulties rather than give a complete overview of possible methods for incorporating hydrodynamics based on potential theory.

The first approach is to discretize the fluid using, for example, the FEM of Finite Differences. This approach was used in [125, 130–133, 135]. The main advantage of this approach is that the fluid equations are reduced to a set of ODEs when dealing with compressible potential flow, or to a set of algebraic equations when dealing with incompressible flow. This allows hydrodynamics to be added to an existing time domain model that already includes the floater and ice as ODEs, which is done in the majority of the

hydrostatic models covered in Sec. 2.1. The major drawback of this approach is that it greatly increases the calculation time of the IFI model. Moreover, the studies that have used this approach all assumed small displacement, eliminating the possibility of drifting objects. Allowing large displacement will further increase the complexity and effort required to utilize this approach.

The second approach is to idealize the geometry of the ice, thereby allowing the problem to be solved using integral methods. In general, this means that the ice is modeled as a (semi-)infinite plate. This approach was used in most of the aforementioned studies [117–119, 122, 124, 126–129, 134]. However, since integral transforms are used, the excitation was generally chosen such that it can be mapped to the frequency domain, allowing the time-domain response to be obtained by evaluating the inverse integral numerically or analytically. Alternatively, the response of the ice can be studied in the frequency domain. However, this limits the study to harmonic excitation at various frequencies. It is important to note that integral transform methods are not easily incorporated into existing ODE-based models and that they are limited to linear problems, again necessitating small displacements.

The third and last approach for incorporating hydrodynamics is to use boundary elements. This approach is commonly used in the field of marine technology to compute the frequency-domain response of vessels. Ultimately, this approach reduces the fluid to a dynamic (frequency dependent) stiffness matrix that acts on- and couples all floating bodies. This approach is based on the Green's function of the supporting fluid layer. Depending on the assumptions used for the surface boundary condition when deriving this Green's function, the resulting dynamic stiffness matrix will capture different phenomena. When the full linear Bernoulli equation is used, both hydrostatic and linear inertial fluid pressure will be included and the resulting Green's function can predict both fluid flow and surface waves. However, the resulting dynamic stiffness will be frequency-dependent. Consequently, in order to obtain the time domain response of the floating bodies, a set of integro-differential equations must be solved. This can be done by directly solving the convolution integrals or by approximating the frequency domain response of the floating bodies, including the frequency-dependent dynamic stiffness of the fluid, with a state-space system, see Keijdener and Metrikine [141]. The former is not easily integrated into an existing ODE-based IFI model and the latter, while it does result in an ODE-based description of the overall problem, is limited to a small number of bodies.

In addition to the issue of converting back to the time domain, another issue arises when using boundary elements, namely, that the geometry of the floating bodies will be embedded in the dynamic stiffness matrix and, therefore, in the frequency domain response of the floating bodies. This means that, unless the floating bodies are limited to small displacement, the frequency domain response function of each body has to be recomputed at every time step, and, consequently, the conversion of each Green's function back to the time domain also has to be redone at every time step. This results in an impractically slow IFI model. This restriction severely limits the applicability of boundary elements for IFI as the floating bodies tend to undergo large relative motions since the ice flows towards and around the floater.

Both of these issues can be overcome by simplifying the surface boundary condition

that the Green's function satisfies by assuming that the surface is flat. The main disadvantage of this assumption is that the Green's function can no longer predict surface waves and is, therefore, limited to fluid flow. The upside of this assumption is that it results in a frequency-independent stiffness matrix. Because of this, the interaction between the bodies is instantaneous and, consequently, results in a set of algebraic equations that must be solved at each time step. This approach was used by [115, 136, 137]. If small displacements are assumed then this set only has to be solved once. This assumption, therefore, makes it easier to incorporate fluid flow into existing time domain models of IFI which only include hydrostatics.

Independently of whether the entire fluid domain is discretized or whether the boundary element method is employed, the calculation time of the IFI model will drastically increase unless severe limitations are imposed, namely the omission of surface waves. Moreover, the complexity and calculation time of the IFI model will increase significantly and incorporating hydrodynamics can be a challenge all by itself, independently of which approach is used. It can be surmised that these are the main reasons for the limited number of hydrodynamic models and the prevalence of hydrostatic models.

2.3. ADVANCED FLUID MODELS

One approach to overcome the aforementioned limitations of hydrodynamic IFI models is to use advanced fluid models based on Smooth Particle Hydrodynamics (SPH), Lattice Boltzmann Method (LBM), Large Eddy Simulation (LES), Reynolds-averaged Navier–Stokes (RANS), or a similar method that can model fluid effects such as turbulence, viscosity, and large displacement. These approaches are becoming more and more accessible with the advent of faster CPUs and GPUs. These methods are common in other fields but have only been used a limited number of times in IFI.

Gagnon [142] studied the impact of an iceberg and a plate-like structure using the Arbitrary Lagrangian–Eulerian (ALE) formulation that is offered by LS-Dyna. The predictions of the model agreed reasonably well with experimental data. In another study by the same author, the impact between an iceberg and a loaded tanker is investigated [143].

A Multi-Material Arbitrary Lagrangian Eulerian (MMALE) formulation was used to model viscous, incompressible flow by Sang-gab and Tuo [144]. The model was used to study the ice resistance experienced by a vessel advancing through level ice. Bihs *et al.* [145] proposed a model wherein the Reynolds-Averaged Navier-Stokes (RANS) equations are solved for the flow. Using this model, the roll motions of a barge are modeled. The predictions show a good agreement with experimental data.

A free surface flow solver based on the Lattice Boltzmann method was proposed by Mierke *et al.* [146] and was used to model a ship advancing through pack ice. The fluid model is coupled to an ODE solver that resolves the time integration of the rigid bodies (the vessel and the floes). The model appears to be under development as the details regarding the interaction between the ice and floater are rather limited. An update on the developments is presented in Janßen *et al.* [76]. This report shows preliminary results of a vessel interacting with nearby ice floes. While this IFI model includes an advanced fluid model, the assumption of rigid bodies for the ice floes limits its applicability.

2.4. EXPERIMENTAL STUDIES

With all four types of numerical IFI models covered, experimental studies on IFI are reviewed next, with a focus on the interaction with sloping structures. The purpose of this section is to identify datasets that can be used for the validation of the numerical ISI models that are proposed in Chs. 4 and 5 and to give a brief overview of the relevant experimental findings.

When looking at the contact-based interaction between ice floes and sloping structures, the geometry of the sloping floaters plays an important role. In 3D, the principle structure types for floaters that are sloping are ship-shaped and conical structures while in 2D most sloping structures can be idealized to an inclined line, i.e. a slope. As most of the findings related to the interaction with slopes also apply to the interaction with ship-shaped and conical structures, these will be reviewed first.

2.4.1. ICE-SLOPE INTERACTION

To the author's knowledge, only very few studies have reported on experiments related to a 2D interaction with a slope. As the numerical model that is proposed in Ch. 4 addresses the interaction with a slope in 2D, the possibility of using these studies for the validation of this model will be discussed next.

A series of experiments were performed by Valanto to investigate the icebreaking cycle in 2D [130, 147, 148]. During these experiments, a downward sloping structure that was shaped like an icebreaker was pushed into sheets of ice using a towing carriage. Two slits were already cut into the ice, ensuring a true 2D experiment. Several observations were made. First, the initial peak in the contact force that is related to the initial impact was mainly caused by the inertia of the ice and the fluid. From this, it was concluded that hydrodynamics plays an important role, even at low velocities. Second, after the ice and fluid have reached their steady-state, the contact force decreased to the level needed to keep the ice piece rotating. This stage is governed by buoyancy, ventilation and the dynamic fluid pressure field around the hull of the advancing vessel. During the third and last stage, the rotating piece of ice impacts against the hull, ejecting any fluid that previously flowed on top of it. This results in a second peak in the contact force. Valanto [130] presents two graphs that can be used for validation, namely the maximum contact force as a function of velocity and the breaking length as a function of velocity. The former shows that the maximum force increases with velocity and the latter that the breaking length decreases with velocity.

Sørensen [120] performed experiments in 2D on the bending failure of level ice. Experiments were done using both model ice and artificial ice. The latter set of tests is not discussed. In this study, a sheet of level ice was pushed against an upward sloping structure. Since the ice sheet was wider than the structure, the interaction with the structure's sides resulted in two parallel slits being cut into the ice sheet and the resulting slab was then pushed up the slope. Consequently, the failure process was slightly different than a true 2D scenario, as was considered by, for instance, Valanto. It was observed that the failure force increase with increasing velocity. The horizontal force was found to increase with an increasing slope angle and friction coefficient while the vertical force was found to be insensitive to these two parameters. The breaking length of the ice was found to increase with an increase in slope angle and friction coefficient and decrease with an

increase in velocity. As this set of experiments did not have precut slits, there may have been 3D effects related to the shearing of the ice that have affected the measurements. Consequently, the data set by Valanto is more suited for validation as it does not suffer from this possible issue.

Aksnes [149] performed 2D measurements on a downward-sloping structure. The structure was pushed into the ice using a towing carriage. The goal of the experiment was to create a synthetic semi-empirical ice force formulations. Unfortunately, very little measurement data is presented, making this set of experiments not usable for validation.

Experiments on the 2D interaction between level ice and a downward slope that transitions into a vertical wall were performed by Lu [41, 150]. It was found that the ice rubble gives a large contribution to the mean vertical load experienced by the structure and that the loading at the waterline gives the largest contribution to the maximum vertical load on the structure. Second, it was found that the ice load decreases gradually after the ice fails in bending, rather than abruptly, due to the rotation of the broken off piece of ice and the submerged rubble. The rubble exerts a pressure on the incoming ice sheet due to its buoyancy which can lead to secondary bending failure of the ice, resulting in rubble with dimensions of about three to eight times its thickness. Another series of experiments that highlight the importance of rubble formation was performed by Timco [151]. Unfortunately, none of these three papers contain data sets that can be used for validation.

2.4.2. INTERACTION WITH SHIP-SHAPED STRUCTURES

The bulk of the experiments with ship-shaped structures focus on the ice resistance experienced by vessels advancing through ice or by vessels performing station keeping in drifting ice [152–154]. In general, the interaction process with ship-shaped structures is similar to the interaction with a slope discussed before. However, the 3D nature of the interaction causes ice failure to generate cusps rather than slabs. Due to this difference and other qualitative differences in the interaction process, experiments on the interaction with ship-shaped structures cannot be used for the validation of the numerical models proposed in this thesis. A very detailed description of ice-ship interaction is given in Valanto [132].

In general, the ice forces increase with an increase in ice thickness, flexural strength, floe size, floe concentration, and velocity [155–158]. However, this last trend was not observed by Kjerstad *et al.* [157] while studying the efficacy of a dynamic positioning in broken ice, nor by Løset *et al.* [159] while assessing the performance of the submerged turret loading concept. They first observed an increase and then a reduction in loading as the velocity increases.

Several studies presented full-scale measurements of vessels advancing through ice. A common approach is to instrument a section of the vessel's bow with strain gauges and infer the ice load through an FE model. This approach was used by Frederking [160] to perform measurements during an icebreaking escort operation in the Gulf of St-Laurent and their data does not show a clear relationship between velocity and contact force. The method was also used by Leira *et al.* [161] to estimate the ice loads on the coast-guard vessel KV Svalbard during the winters of 2007 and 2008 and they concluded that the maximum peak load depends on the ice thickness. However, due to the low mass

of the vessel, it decelerated during the interaction, making it difficult to correlate the ice thickness with the ice action. Another approach to infer the ice loads is to use an inertial measurement unit. This approach was used to infer ice load data of two Swedish icebreakers, Oden and Frej, during a 2013 expedition offshore North-East Greenland. The collected data was used by Scibilia *et al.* [59] and Lubbad *et al.* [86] to validate their numerical codes. Full-scale data was used by Spencer and Jones [162] to identify an increase in ice resistance due to a deteriorating hull of the icebreaker Terry Fox, resulting in an increased hull-ice friction coefficient. This trend was used to recommend maintenance to the hull to reduce the friction. The hull-ice friction coefficient of the same vessel was also identified by Wang and Jones [163] using a non-dimensional method. Lastly, Kim *et al.* [164] reported on the performance of the icebreaker ARAON, including full-scale data.

The effect of different heading on the interaction between a vessel and level ice was studied by Zhou *et al.* [165] and the data set was later on used by Hu and Zhou [52]. The tests showed that for a heading of 0°, there was no rubble accumulation. For a heading of 45° accumulated on the upstream side of the vessel and for 90° severe accumulation was observed at low speeds and much less accumulation at high speeds. Similar observations were made by Izumiyama *et al.* [166] and Kjerstad *et al.* [157]. Metrikin *et al.* [167] showed that a zero degree drift angle causes instability of a vessel on DP and that DP is feasible for high oblique angles.

Model tests on lateral pressure experienced by ships were performed by Hinse *et al.* [168]. It was found that the velocity has a significant impact on the resistance, with faster velocities lowering the resistance. Lastly, a number of papers reported on experiments executed to validate a numerical model and did not draw qualitative conclusions regarding the experiments themselves [51, 67, 71, 169, 170].

2.4.3. INTERACTION WITH CONICAL STRUCTURES

The interaction between ice and a conical structure has much in common with the interaction with a slope. For small diameter structures, the interaction is similar to that of ship-shaped structures, with the resulting fracture patterns often modeled using wedge beam models. For large diameter structures, often circumferential cracks are initiated first that result in breaking off crescent-shaped pieces of ice. Their size depends on the ice thickness, with thicker ice generating cracks that wrap up to 135° around the structure while thinner ice results in cracks that wrap 15-45° [171]. This type of failure occurs more frequently in the central region than at the sides where the effective slope is smaller [172]. If the slope of the conical structure transition into a vertical wall, the ice is deflected backward, which results in an accumulation of ice rubble [93, 172]. As there are many qualitative differences compared to the interaction with a slope, experimental data on the interaction with conical structures cannot be used for validation in this thesis.

For upwards sloping cones many trends are explained by Lau *et al.* [173]. Bending failure dominates at low velocities, low cone angles (10° to 60°), low friction coefficients, and low ice thickness. However, with an increase in friction, thickness, or cone angle the failure mode gradually changes to shear or crushing. An increase in velocity causes the same transition in failure mode but the transition occurs more abruptly. While thin ice

fails with a breaking length that is slightly greater than the characteristic length, thicker ice reduces the breaking length.

Tests on downward sloping cones were performed by Frederking and Schwarz [172]. It was observed that the horizontal force increases with velocity. However, the vertical force rapidly increases up to about 0.3 m/s at which point it starts to decrease again. The effect of vibrations of the cone on the ice loads was studied in the same work. It was found that the loads decrease by up to up to 33% when the structure oscillates vertically, with higher frequency resulting in lower loads, at least up to 2 Hz. Circular vibrations in the plane of the fluid surface are even more effective, reducing the loads by up to 66%. In [173] it was noted that at high velocities, the ice loads are higher for downward-sloping structures as the rubble is subjected to drag and added mass as it pushed into the water rather than into the air.

Model-scale experiments on the Kulluk were done by Matsuishi and Ettema [174]. Experiments on a similarly shaped floater are documented in Keijdener [171]. In both studies, it was found that the floater maintains a constant offset and had a slight trim angle but did not undergo cyclic motions. The global loads increased monotonically as the rubble develops in front of the vessel. After the rubble reached its equilibrium size, the mean loads remained steady. Matsuishi and Ettema [174] found a linear dependence on the ice thickness while Keijdener [171] found a quadratic relation. However, the later model had a gradually increasing effective slope, which meant that as the trim of the vessel or the ice thickness increased, crushing become more dominant as a larger portion of the interaction took place with a part of the hull with a steeper slope. The global loads were found to be independent of the velocity by Matsuishi and Ettema [174] while Keijdener [171] found that the loads increase with velocity. An analysis of full-scale of the Kulluk data was done by Wright [175, 176].

2.5. SUMMARY

The review on IFI is summarized by going over the main findings of each of the four categories of fluid models and those of the experimental studies.

First, the review of hydrostatic IFI models showed that there is a large diversity in these models solely based on the capabilities of the ice model. It is also clear that the more advanced ice models, in particular the elastic models, require significantly more programming time.

Second, the review showed that most contact-based hydrodynamic studies focused on the hydroelastic response of the ice and that the number of studies that considered the contact-based interaction between ice and floater is very limited. While it has been shown that hydrodynamics is a key component of ISI, there are still open questions regarding the effects it has on IFI such as whether the nonlinear term in the Bernoulli equation is important and how the temporal development of the contact force relates to the velocity dependence of the breaking length. The review of studies on the fluid-based interaction between ice and floater showed that existing studies focused on the interaction through fluid flow and did not consider the interaction through surface waves. Therefore, not much is known about this type of interaction. Lastly, an assessment of the difficulties associated with implementing hydrodynamics based on potential theory gave a plausible explanation as to why most models still use hydrostatic fluid modeling.

Third, the usage of advanced fluid models for IFI appears to be a recent trend as the majority of models are still under development. Most of the proposed IFI models are adaptions of previously developed fluid libraries, meaning their ice model are still relatively simple compared to the fluid model. However, this category of models is very promising and may be the future of IFI models.

Fourth, while effective models based on frequency-independent added mass coefficients have been used in several previous studies, currently no satisfactory effective fluid model exists. Nevertheless, they are a promising approach for improving the adaption of hydrodynamics in IFI since effective models do not suffer from the practical issues that plague fluid models based on potential theory or one of the advanced methods.

Lastly, regarding the contact-based interaction, it is concluded that all experimental data on the interaction with ship-shaped and conical structures cannot be used for the validation of the numerical models to be proposed in this thesis as, despite a strong resemblance in observed interaction phenomenon, there are many qualitative differences. The data set most suited for validation is the one by Valanto. This data set will be used throughout this thesis for the validation of the numerical model that is proposed in Ch. 4.

2.6. CONCLUSIONS

Based on the literature review of IFI models, several conclusions can be drawn. First, a simple comparison between the number of studies based on hydrostatic IFI models with those based on hydrodynamic IFI models makes it clear that the majority of IFI research is still being done with hydrostatic models. However, it is not clear for which range of parameters hydrostatic IFI models give valid predictions. Moreover, while it is known that hydrodynamics plays an important role in IFI, there are still open questions and these are addressed in Ch. 4 of this thesis. Lastly, the adoption of hydrodynamics in IFI is, in the author's opinion, mainly held back by practical issues, mainly by an increase in programming time. Effective models offer a promising solution to this issue, but currently, no such model exists. The formulation of an effective model is explained in this thesis in Ch. 5. These conclusions substantiate the scope of this thesis as it was defined in Sec. 1.4.

REFERENCES

[32] A. Jensen, B. Bonnemaire, T. Lundamo, and O. Ravndal, *Efficient Combination of Numerical Simulations and Ice Basin Testing in the Design Process of Moored Structures in Ice,* Proceedings of OTC Arctic Technology Conference **2**, 1071 (2011).

[33] O. Dalane, F. Faye Knudsen, and S. Løset, *Nonlinear Coupled Hydrostatics of Arctic Conical Platforms,* Journal of Offshore Mechanics and Arctic Engineering **134**, 021602 (2012).

[34] G. Lindqvist, *A Straightforward Method for Calculation of Ice Resistance of Ships,* in *Proceedings of the 10th International Conference on Port and Ocean Engineering under Arctic Conditions* (Luleå, Sweden, 1989) pp. 722–735.

[35] K. R. Croasdale, G. Cammaert, and M. Metge, *A Method for the Calculation of Sheet Ice Loads on Sloping Structures,* Iahr **28**, 874 (1994).

[36] International Organization for Standardization, *ISO 19906*, Tech. Rep. (International Organization for Standardization, 2010).

[37] A. Keinonen, Browne R.P., and A. Reynolds, *Ice breaker Characteristics Synthesis,* Report of AKAC Inc. to Transportation Development Centre (1996).

[38] R. Kulaots, P. Kujala, R. v. B. und Polach, and J. Montewka, *Modelling of ship resistance in compressive ice channels Reino,* in *Proceedings of the 22nd International Conference on Port and Ocean Engineering under Arctic Conditions* (2013).

[39] K. Riska, M. Patey, S. Kishi, and K. Kamesaki, *Influence of ice conditions on ship transit times in ice,* in *The International Conference on Port and Ocean Engineering under Arctic Conditions (POAC'01)* (2001) pp. vol. 2, pp. 729–745.

[40] V. Aksnes, *A simplified interaction model for moored ships in level ice,* Cold Regions Science and Technology **63**, 29 (2010).

[41] W. Lu, R. Lubbad, K. Høyland, and S. Løset, *Physical model and theoretical model study of level ice and wide sloping structure interactions,* Cold Regions Science and Technology **101**, 40 (2014).

[42] S. Wang, *A dynamic model for breaking pattern of level ice by conical structures,* Ph.D. thesis, Helsinki University of Technology (2001).

[43] D. E. Nevel, *The ultimate failure of a floating ice sheet,* in *International Association of Hydraulic Research (IAHR), Ice Symposium, Leningrad* (1972) pp. 17–22.

[44] T. Kotras, A. Baird, and J. Naegle, *Predicting Ship Performance in level Ice,* Trans.SNAME **91**, 329 (1983).

[45] P. Varsta, *On the mechanics of ice loads on shipsin level ice in the Baltic Sea,* Technical Research Centre of Finland, Publications 11, Espoo (1983).

[46] J. Liu, M. Lau, and F. M. Williams, *Mathematical modeling of ice-hull interaction for ship maneuvering in ice simulations,* in *Proceedings of the 7th International Conference and Exhibition on Performance of Ships and Structures in Ice, Banff, Alberta.* (2006).

[47] B. Su, K. Riska, and T. Moan, *A numerical method for the prediction of ship performance in level ice,* Cold Regions Science and Technology **60**, 177 (2010).

[48] B. Su, *Numerical predictions of global and local ice loads on ships*, Ph.D. thesis, NTNU (2011).

[49] J. Sawamura, *Numerical Investigation of Ice Bending Failure and Ice Submerging Force for Ship Maneuvering in Level Ice,* 21st IAHR International Symposium on Ice , 1116 (2012).

[50] X. Tan, *Numerical Investigation of Ship's Continuous-Model Icebreaking in Level Ice*, Ph.D. thesis, NTNU (2013).

[51] B. Su, R. Skjetne, and T. E. Berg, *Experimental and numerical investigation of a double-acting offshore vessel performance in level ice,* Modeling, Identification and Control **35**, 317 (2014).

[52] J. Hu and L. Zhou, *Experimental and numerical study on ice resistance for icebreaking vessels,* International Journal of Naval Architecture and Ocean Engineering **7**, 626 (2015).

[53] Q. Zhou, H. Peng, and W. Qiu, *Numerical investigations of ship-ice interaction and maneuvering performance in level ice,* Cold Regions Science and Technology **122**, 36 (2016).

[54] S. Y. Jeong, K. Choi, K. J. Kang, and J. S. Ha, *Prediction of ship resistance in level ice based on empirical approach,* International Journal of Naval Architecture and Ocean Engineering **9**, 613 (2017).

[55] L. Zhou, Z. Chuang, and X. Bai, *Ice forces acting on towed ship in level ice with straight drift. Part II: Numerical simulation,* International Journal of Naval Architecture and Ocean Engineering **10**, 119 (2018).

[56] D. H. Nguyen, D. T. Nguyen, S. T. Quek, and A. J. Sørensen, *Position-moored drilling vessel in level ice by control of riser end angles,* Cold Regions Science and Technology **66**, 65 (2011).

[57] Q. Zhou and H. Peng, *Numerical Simulation of a Dynamically Controlled Ship in Level Ice,* International Journal of Offshore and Polar Engineering **24**, 184 (2014).

[58] M. Huisman, C. Janßen, T. Rung, and S. Ehlers, *Numerical simulation of ship-ice interactions with physics engines under consideration of ice breaking,* Proceedings of the International Offshore and Polar Engineering Conference **2016**, 1174 (2016).

[59] F. Scibilia, I. Metrikin, A. Gürtner, and S. H. Teigen, *Full-Scale Trials and Numerical Modeling of Sea Ice Management in the Greenland Sea,* OTC Arctic Technology Conference , 1 (2014).

[60] S. Løset, *Discrete element modelling of a broken ice field - Part I : model development,* Cold Regions Science and Technology **22**, 339 (1994).

[61] S. Løset, *Discrete element modelling of a broken ice field - Part II: simulation of ice loads on a boom,* Cold Regions Science and Technology **22**, 349 (1994).

[62] J. Dai and H. Peng, *Numerical Modeling for Dynamic Positioning in Pack Ice,* The Twenty-fifth International Offshore and Polar Engineering Conference , 1849 (2015).

[63] M. Sayed, V. R. Neralla, and S. B. Savage, *Yield Conditions of an Assembly of Discrete Ice Floes,* Proceedings of the Fifth International Offshore and Polar Engineering Conference **II**, 330 (1995).

[64] A. Herman, *Influence of ice concentration and floe-size distribution on cluster formation in sea-ice floes,* Central European Journal of Physics **10**, 715 (2012).

[65] C. Daley, D. Peters, B. Quinton, and B. Colbourne, *GPU Modeling of Ship Operations in Pack Ice,* International Conference and Exhibition on Performance of Ships and Structures in Ice, IceTech'12 , 1 (2012).

[66] C. G. Daley, S. Alawneh, D. Peters, and B. Colbourne, *GPU-Event-Mechanics Evaluation of Ice Impact Load Statistics,* Arctic Technology Conference , OTC 24645 (2014).

[67] M. C. Kim, S. K. Lee, W. J. Lee, and J. yong Wang, *Numerical and experimental investigation of the resistance performance of an icebreaking cargo vessel in pack ice conditions,* International Journal of Naval Architecture and Ocean Engineering **5**, 116 (2013).

[68] A. Konno, A. Nakane, and S. Kanamori, *Validation of numerical estimation of brash ice channel resistance with model test,* in *Proceedings of the 22nd International Conference on Port and Ocean Engineering under Arctic Conditions*, 143 (2013).

[69] Ø. K. Kjerstad and R. Skjetne, *Modeling and control for dynamic positioned marine vessels in drifting managed sea ice,* Modeling, Identification and Control **35**, 249 (2014).

[70] A. Konno and T. Mizuki, *Numerical Simulation of Pre-sawn Ice Test of Model Icebreaker Using Physically Based Modeling,* 18th IAHR Simposium on Ice , 17 (2006).

[71] M. Lau and A. J. Simões Ré, *Performance of survival craft in ice environments Performance of Survival Craft in Ice Environments,* NRC- CNRC (2006).

[72] T. H. Amdahl, B. Bjørnsen, O. J. Hagen, and S. R. Søberg, *Numerical simulations of ice loads on an Arctic Floater in managed ice,* Atc , OTC 24549 (2014).

[73] S. Alawneh, R. Dragt, D. Peters, C. Daley, and S. Bruneau, *Hyper-Real-Time Ice Simulation and Modeling Using GPGPU,* IEEE Transactions on Computers **64**, 3475 (2015).

[74] M. A. Hopkins and J. Tuhkuri, *Compression of floating ice fields,* Journal of Geophysical Research: Oceans **104**, 15815 (1999).

[75] S. Ji, *Discrete Element Modeling of Ice Loads on Ship and Offshore Structures,* Acta Oceanologica Sinica **32**, 50 (2013).

[76] C. F. Janßen, D. Mierke, and T. Rung, *On the development of an efficient numerical ice tank for the simulation of fluid-ship-rigid-ice interactions on graphics processing units,* Computers and Fluids **155**, 22 (2017).

[77] R. Yulmetov, R. Lubbad, and S. Løset, *Planar multi-body model of iceberg free drift and towing in broken ice,* Cold Regions Science and Technology **121**, 154 (2016).

[78] R. Yulmetov and S. Løset, *Validation of a numerical model for iceberg towing in broken ice,* Cold Regions Science and Technology **138**, 36 (2017).

[79] I. Metrikin, S. Løset, and S. Loset, *Nonsmooth 3D discrete element simulation of a drillship in discontinuous ice,* Port and Ocean Engineering under Arctic Conditions (2013).

[80] R. Lubbad and S. Løset, *A numerical model for real-time simulation of ship-ice interaction,* Cold Regions Science and Technology **65**, 111 (2011).

[81] D. Nevel, *Ice forces on cones from floes,* in *Proc. 11th IAHR Symposium on Ice* (Banff, Alberta, 1992) pp. 1391–1404.

[82] D. Nevel, *The narrow free infinite wedge on an elastic foundation,* CRREL Research Report 79 , 24 (1961).

[83] I. Metrikin, *A software framework for simulating stationkeeping of a vessel in discontinuous ice,* Modeling, Identification and Control **35**, 211 (2014).

[84] I. Metrikin, A. Gürtner, B. Bonnemaire, X. Tan, A. Fredriksen, and D. Sapelnikov, *SIBIS : A numerical environment for simulating offshore operations in discontinuous ice,* in *Proceedings of the 23rd International Conference on Port and Ocean Engineering under Arctic Conditions* (Trondheim, 2015).

[85] I. Metrikin, W. Lu, R. Lubbad, S. Løset, and M. Kashafutdinovl, *Numerical Simulation of a Floater in a Broken-Ice Field - Part I: Model Description,* in *Proceedings of the ASME 2012 31st International Conference on Ocean, Offshore and Arctic Engineering* (2012) pp. 1–10.

[86] R. Lubbad, S. Løset, W. Lu, A. Tsarau, and M. van den Berg, *An overview of the Oden Arctic Technology Research Cruise 2015 (OATRC2015) and numerical simulations performed with SAMS driven by data collected during the cruise,* Cold Regions Science and Technology , 1 (2018).

[87] W. Lu, R. Lubbad, and S. Løset, *Out-of-plane failure of an ice floe: Radial-crack-initiation-controlled fracture,* Cold Regions Science and Technology **119**, 183 (2015).

[88] W. Lu, R. Lubbad, S. Løset, and M. Kashafutdinov, *Fracture of an ice floe: Local out-of-plane flexural failures versus global in-plane splitting failure,* Cold Regions Science and Technology **123**, 1 (2016).

[89] J. Paavilainen, J. Tuhkuri, and A. Polojärvi, *2D combined finite-discrete element method to model multi-fracture of beam structures,* Engineering Computations **26**, 578 (2009).

[90] J. Paavilainen, J. Tuhkuri, and A. Polojärvi, *Discrete Element Simulation of Ice Pile-Up Against an Inclined Structure,* 18th IAHR International Symposium on Ice , 177 (2006).

[91] J. Paavilainen, J. Tuhkuri, and A. Polojärvi, *2D numerical simulations of ice rubble formation process against an inclined structure,* Cold Regions Science and Technology **68**, 20 (2011).

[92] J. Paavilainen and J. Tuhkuri, *Parameter effects on simulated ice rubbling forces on a wide sloping structure,* Cold Regions Science and Technology **81**, 1 (2012).

[93] J. Paavilainen, *Factors affecting ice loads during the rubbling process using a 2D FE-DE Approach*, Ph.D. thesis, Aalto University (2013).

[94] J. Ranta, A. Polojärvi, and J. Tuhkuri, *The statistical analysis of peak ice loads in a simulated ice-structure interaction process,* Cold Regions Science and Technology **133**, 46 (2017).

[95] J. Ranta, A. Polojärvi, and J. Tuhkuri, *Ice loads on inclined marine structures - Virtual experiments on ice failure process evolution,* Marine Structures **57**, 72 (2018).

[96] J. Ranta, A. Polojärvi, and J. Tuhkuri, *Limit mechanisms for ice loads on inclined structures: Buckling,* Cold Regions Science and Technology **147**, 34 (2018).

[97] J. Ranta, A. Polojärvi, and J. Tuhkuri, *Scatter and error estimates in ice loads – Results from virtual experiments,* Cold Regions Science and Technology **148**, 1 (2018).

[98] A. Polojärvi and J. Tuhkuri, *On modeling cohesive ridge keel punch through tests with a combined finite-discrete element method,* Cold Regions Science and Technology **85**, 191 (2013).

[99] A. Polojärvi, J. Tuhkuri, and O. Korkalo, *Comparison and analysis of experimental and virtual laboratory scale punch through tests,* Cold Regions Science and Technology **81**, 11 (2012).

[100] A. Polojärvi and J. Tuhkuri, *Velocity effects in laboratory scale punch through experiments,* Cold Regions Science and Technology **70**, 81 (2012).

[101] A. Polojärvi and J. Tuhkuri, *3D discrete numerical modelling of ridge keel punch through tests,* Cold Regions Science and Technology **56**, 18 (2009).

[102] C. Septseault, P.-A. Béal, S. L. Yaouanq, A. Dudal, and B. Roberts, *Update on a New Ice Simulation Tool using a Multi-Model Program,* OTC Arctic Technology Conference (2015), 10.4043/25591-MS.

[103] S. Ji, S. Di, and S. Liu, *Analysis of ice load on conical structure with discrete element method,* Engineering Computations (Swansea, Wales) **32**, 1121 (2015).

[104] S.-p. Ji, Z.-l. Li, M.-m. Huang, Y.-h. Wang, Y.-k. Tian, and Z.-g. Li, *Initial Concept Design for a Self-Icebreaking Container Vessel in Ice-Covered Water Region,* 24th International Ocean and Polar Engineering Conference **3**, 1144 (2014).

[105] M. Sayed, *Discrete and lattice models of floating ice covers,* The Seventh International Offshore and Polar Engineering Conference **11**, 428 (1997).

[106] W. Lu, R. Lubbad, and S. Løset, *Simulating Ice-Sloping Structure Interactions With the Cohesive Element Method,* Journal of Offshore Mechanics and Arctic Engineering **136**, 031501 (2014).

[107] M. Lau, *Discrete element modeling of ship manoeuvering in ice,* 18th IAHR International Symposium on Ice , 25 (2006).

[108] M. van den Berg, R. Lubbad, and S. Løset, *An Implicit Time-Stepping Scheme and an Improved Contact Model for Ice-Structure Interaction Simulations,* Cold Regions Science and Technology **155**, 193 (2018).

[109] M. Sayed, R. Frederking, and A. Barker, *Numerical Simulation of Pack Ice Forces on Structures: A Parametric Study,* in *Proceedings of the 10th International Offshore and Polar Engineering Conference (ISOPE 2000)*, Vol 1 (Seattle, USA, 2000) pp. 656–662.

[110] A. Barker, G. Timco, M. Sayed, and B. Wright, *Numerical Simulation of the "Kulluk" in Pack Ice Conditions,* in *15th International Symposium on Ice* (2000) pp. 165–171.

[111] M. Sayed and G. W. Timco, *A numerical model of iceberg scour,* Cold Regions Science and Technology **55**, 103 (2009).

[112] A. Barker, M. Sayed, and G. Timco, *Numerical Simulation of Broken Ice Cover Forces on Structures: a Parametric Study,* Annual Conference of the Canadian Society for Civil Engineering **8**, 8 (2000).

[113] M. Sayed, A. Barker, and C. H. Centre, *Numerical Simulations of Ice Interaction with a Moored Structure,* Arctic Technology Conference , OTC 22101 (2011).

[114] M. Sayed and I. Kubat, *Numerical Simulations of ice forces on the Kulluk: the role of ice confinement, ice pressure and ice management,* Offshore Technology Conference , 1 (2012).

[115] A. Tsarau, R. Lubbad, and S. Løset, *A numerical model for simulation of the hydrodynamic interactions between a marine floater and fragmented sea ice,* Cold Regions Science and Technology **103**, 1 (2014).

[116] D. Kheisin, *Dynamics of the ice cover,* Gigrometeorolicheskoe, Izdatel'stvo, Leningrad (U.S. Technical translation FSTC-HT-458-69) (1967).

[117] D. Nevel, *Vibration of a floating ice sheet,* CRREL Research report 281, Hanover, New Hampshire (1970).

[118] Z. Zhao and J. Dempsey, *A dynamically forced floating beam,* in *IAHR Ice Symposium* (Banff, Alberta, 1992).

[119] J. P. Dempsey and Z. G. Zhao, *Elastohydrodynamic response of an ice sheet to forced sub-surface uplift,* Journal of the Mechanics and Physics of Solids **41**, 487 (1993).

[120] C. Sørensen, *Dynamic response of a semi-infinite plate subjected to steadily increasing boundary force,* ZAMM 58 , T 126 (1978).

[121] F. Engelund, *Added Moment of Inertia for a Rotating Plate* (Coastal Engineering Laboratory, Hydraulic Laboratory, Technical University of Denmark, 1966).

[122] Z. G. Zhao and J. P. Dempsey, *Planar forcing of floating ice sheets,* International Journal of Solids and Structures **33**, 19 (1996).

[123] J. P. Dempsey, Z. G. Zhao, and H. Li, *Axisymmetric indentation of an elastic layer supported by a winkler foundation,* International Journal of Solids and Structures **27**, 73 (1991).

[124] C. Fox, *The response of a floating ice sheet to rapid edge loading,* Ice Mechanics-1993 (ed. Dempsey J.P., Bazant Z.P., Rajapakse Y.D.S., Sunder S.S.) **ASME AMD-V**, 145 (1993).

[125] J. Sawamura, K. Riska, and T. Moan, *Finite element analysis of fluid-ice interaction during ice bending,* in *Proceedings of the 19th IAHR Symposium on Ice, Vancouver, Canada* (2008) pp. 239 – 250.

[126] C. Fox and H. Chung, *Green's function for forcing of a thin floating plate,* Department of Mathematics Research Report Series number 408, The University of Auckland (1998).

[127] C. Fox and H. Chung, *Harmonic deflections of an infinite floating plate,* Mathematics Research Report Series **485** (2002).

[128] V. M. Kozin and A. V. Pogorelova, *Mathematical modeling of shock loading of a solid ice cover,* International Journal of Offshore and Polar Engineering **16**, 1 (2006).

[129] V. M. Kozin and A. V. Pogorelova, *Dynamic Response of an Ice-Covered Fluid to an Impulse Submerged Point Source,* Isope **1**, 568 (2009).

[130] P. Valanto, *The icebreaking problem in two dimensions : experiments and theory,* Journal of Ship Research **36**, 299 (1992).

[131] Y. Wang and L. H. Poh, *Velocity effect on the bending failure of ice sheets against wide sloping structures,* Journal of Offshore Mechanics and Arctic Engineering **139**, 061501 (2017).

[132] P. Valanto, *The resistance of ship in level ice,* Transactions of the Society of Naval Architects and Marine Engineers **109**, 53 (2001).

[133] P. Valanto, *On the Ice Load Distribution on Ship Hulls in Level Ice,* Icetech 2006 , 1 (2006).

[134] J. P. Dempsey, C. Fox, and A. C. Palmer, *Ice-slope interaction: transitions in failure mode,* 18th International Conference on Offshore Mechanics and Arctic Engineering (OMAE) , 225 (1999).

[135] R. Lubbad, G. Moe, and S. Løset, *Static and dynamic interaction of floating wedge-shaped ice beams and sloping structures,* in *Proceedings of the 19th IAHR Symposium on Ice, Vancouver, Canada* (2008) pp. 227 – 237.

[136] A. Tsarau and S. Løset, *Modelling the hydrodynamic effects associated with station-keeping in broken ice,* Cold Regions Science and Technology **118**, 76 (2015).

[137] A. Tsarau, R. Lubbad, and S. Løset, *A numerical model for simulating the effect of propeller flow in ice management,* Cold Regions Science and Technology **142**, 139 (2017).

[138] M. Isaacson and K. A. McTaggart, *Modelling of iceberg drift motions near a large offshore structure,* Cold Regions Science and Technology **19**, 47 (1990).

[139] R. Foschi, M. Isaacson, N. Allyn, and S. Yee, *Combined wave – iceberg loading on offshore structures,* Canadian Journal of Civil Engineering **23**, 1099 (1996).

[140] R. Gagnon, *Physical Model Experiments to Assess the Hydrodynamic Interaction Between Floating Glacial Ice Masses and a Transiting Tanker,* Journal of Offshore Mechanics and Arctic Engineering **126**, 297 (2004).

[141] C. Keijdener and A. Metrikine, *An efficient method for computing the time domain response of a floating ice block including hydrodynamics,* in *Proceedings of the 23nd International Conference on Port and Ocean Engineering under Arctic Conditions* (2015).

[142] R. E. Gagnon, *Results of numerical simulations of growler impact tests,* Cold Regions Science and Technology **49**, 206 (2007).

[143] R. E. Gagnon and J. Wang, *Numerical simulations of a tanker collision with a bergy bit incorporating hydrodynamics, a validated ice model and damage to the vessel,* Cold Regions Science and Technology **81**, 26 (2012).

[144] L. Sang-gab and Z. Tuo, *Ice Resistance Test Simulation of Arctic Cargo Vessel using FSI Analysis Technique,* the Twenty-third (2013) International Offshore and Polar Engineering **9**, 1162 (2013).

[145] H. Bihs, A. Kamath, M. A. Chella, and Ø. A. Arntsen, *CFD Simulations of Roll Motion of a Floating Ice Block in Waves Using REEF3D,* in *Proceedings of the 23th International Conference on Port and Ocean Engineering under Arctic Conditions* (2015).

[146] D. Mierke, C. F. Janßen, T. Rung, Christian F Janßen, and T. Rung, *GPU-accelerated large-eddy simulation of ship-ice interactions,* in *VI International Conference on Computational Methods in Marine Engineering,* July (2015).

[147] P. Valanto, *Experimental and theoretical investigation of the icebreaking cycle in two dimensions,* Ph.D. thesis, University of California, Berkeley (1989).

[148] P. Valanto, *Experimental study of the icebreaking cycle in 2-D,* in *Eighth International Conference on Offshore Mechanics and Arctic Engineering (OMAE)* (The Hague, The Netherlands, 1989) pp. 343–349.

[149] V. Aksnes, *A panel method for modelling level ice actions on moored ships. Part 1: Local ice force formulation,* Cold Regions Science and Technology **65**, 128 (2011).

[150] W. Lu, K. V. Høyland, N. Serre, and K.-U. Evers, *Ice Load Measurement by Tactile Sensor in Model Scale Test in Relation to Rubble Ice Transport on Arctic Offshore Structures (RITAS),* HYDRALAB IV Joint User Meeting , 1 (2014).

[151] G. Timco, *The Vertical Pressure Distribution on Structures Subjected to Rubble-Forming Ice*, Tech. Rep. (National Research Council, 1991).

[152] J. Millan and J. Wang, *Ice force modeling for DP control systems,* in *Dynamic Positioning Conference* (2008).

[153] N. A. Jenssen, T. Hals, P. Jochmann, A. Haase, X. dal Santo, S. Kerkeni, O. Doucy, F. DCNS Research / Srehna, Nantes, A. Gürtner, S. Støle, P. Olav, I. Metrikin, and S. Løset, *DYPIC – A Multi-National R&D Project on DP Technology in Ice by,* in *DYNAMIC POSITIONING CONFERENCE* (2012).

[154] M. Islam, J. Wang, J. Mills, T. Sayeed, B. Gash, M. Lau, D. Millan, and J. Millan, *DP in Ice Environment - Improving Safety and Efficiency of Arctic Operations,* Arctic Technology Conference (2016), 10.4043/27349-MS.

[155] A. D. Derradji-Aouat, *Experimental uncertainty analysis for ship model testing in the ice tank,* in *25th Symposium on Naval Hydrodynamics* (St. John's, Newfoundland and Labrador, Canada, 2004).

[156] R. Gash and J. Millan, *Managed Ice Loads on a Dynamically Positioned Vessel,* Proceedings of OTC Arctic Technology Conference , 3 (2012).

[157] O. K. Kjerstad, I. Metrikin, S. Løset, and R. Skjetne, *Experimental and phenomenological investigation of dynamic positioning in managed ice,* Cold Regions Science and Technology **111**, 67 (2015).

[158] J. Wang, T. Sayeed, D. Millan, R. Gash, M. Islam, and J. Millan, *Ice Model Tests for Dynamic Positioning Vessel in Managed Ice,* in *Arctic Technology Conference* (St. John's, Newfoundland and Labrador, Canada, 2016).

[159] S. Løset, Kanestrøm, and T. Pytte, *Model tests of a submerged turret loading concept in level ice, broken ice and pressure ridges,* Cold Regions Science and Technology **27**, 57 (1998).

[160] R. Frederking, *Ice Loading on a Ship in Discontinuous Ice,* International Offshore and Polar Engineering Conference **7**, 1 (2010).

[161] B. Leira, L. Børsheim, Ø. Espeland, and J. Amdahl, *Ice-load estimation for a ship hull based on continuous response monitoring,* Proceedings of the Institution of Mechanical Engineers Part M: Journal of Engineering for the Maritime Environment **223**, 529 (2009).

[162] D. Spencer and S. J. Jones, *Model-Scale Full-Scale Correlation in Open Water and Ice for Canadian Coast Guard R-Class Icebreakers,* Journal of Ship Research **45**, 249 (2001).

[163] J. Wang and S. Jones, *Resistance and propulsion of CCGS Terry Fox in ice from model tests to full scale correlation,* in *ICETECH 2008* (Banff, Alberta, Canada, 2008).

[164] H. S. Kim, C. J. Lee, K. S. Choi, and M. C. Kim, *Study on icebreaking performance of the Korea icebreaker ARAON in the arctic sea,* International Journal of Naval Architecture and Ocean Engineering **3**, 208 (2011).

[165] L. Zhou, K. Riska, R. von Bock und Polach, T. Moan, and B. Su, *Experiments on level ice loading on an icebreaking tanker with different ice drift angles,* Cold Regions Science and Technology **85**, 79 (2013).

[166] K. Izumiyama, D. Wako, H. Shimoda, and S. Uto, *Ice load measurement on a model ship hull,* Arctic **2**, 635 (2005).

[167] I. Metrikin, S. Kerkeni, P. Jochmann, and S. Løset, *Experimental and Numerical Investigation of Dynamic Positioning in Level Ice,* Journal of Offshore Mechanics and Arctic Engineering **137**, 031501 (2015).

[168] P. Hinse, D. Ehle, and N. Reimer, *Model Tests for Determination of Ship Resistance in Level Ice under Lateral Pressure,* in *Proceedings of the Twenty-third (2013) International Offshore and Polar Engineering*, Vol. 9 (Anchorage, Alaska, USA, 2013) pp. 1156–1161.

[169] M. C. Kim, W.-J. Lee, and Y.-J. Shin, *Comparative study on the resistance performance of an icebreaking cargo vessel according to the variation of waterline angles in pack ice conditions,* International Journal of Naval Architecture and Ocean Engineering **6**, 876 (2014).

[170] B. Su, R. Skjetne, and T. E. Berg, *Numerical assessment of a double-acting offshore vessel's performance in level ice with experimental comparison,* Cold Regions Science and Technology **106-107**, 96 (2014).

[171] C. Keijdener, *Dynamics of JBF Arctic drilling unit moored in ice*, Ph.D. thesis, Delft University of Technology (2012).

[172] R. M. W. Frederking and J. Schwarz, *Model tests of ice forces on fixed and oscillating cones,* Journal of Cold Regions Science and Technology **6**, 61 (1982).

[173] M. Lau, S. J. Jones, R. Phillips, and R. F. McKenna, *Influence of velocity on ice-cone interaction,* in *IUTAM Symposium on Scaling Laws in Ice Mechanics and Ice Dynamics* (Fairbanks, Alaska, 2000).

[174] M. Matsuishi and R. Ettema, *Ice Loads and Motions Experienced By a Floating, Moored Platform in Mushy Ice Rubble*. IIHR Report (Iowa Institute of Hydraulic Research) (1985), IIHR Report No. 295.

[175] B. Wright, *PERD/CHC Report 26-200*, Tech. Rep. (National Research Council of Canada, 1999).

[176] B. Wright, *Full Scale Experience with Kulluk Full Scale Experience with Kulluk Stationkeeping Operations in Pack Ice (With Reference to Grand Banks Developments)*, Tech. Rep. (National Research Council of Canada, 2000)

3

ICE-FLOATER INTERACTION THROUGH SURFACE WAVES

When IFI is studied with a hydrostatic model, ice and structure can only interact with each other through contact forces. This path of interaction is studied in Chs. 4 and 5. However, when hydrodynamics is included, it opens up the possibility for the ice and structure to interact through fluid flow and surface waves. While the interaction through fluid flow has been studied in a series of recent papers [178–180], little is known about the effect of surface waves on ice-floater interaction. This chapter aims to improve the understanding of this type of interaction by answering two fundamental questions.

1) how is the frequency domain response of the floater that is excited by a sinusoidal load affected by the presence of a flexible ice floe located in close proximity of the floater? and 2) under which circumstances can the ice-floater coupling be neglected?

Additionally, a set of Green's functions is derived in this chapter which is also required to construct the ISI model that is introduced in Ch. 4.

Although no previous studies have focused on the effect of surface waves on IFI, a series of related problems have been solved in the field of ocean waves and sea-ice. Studied were the wave propagation in and wave reflection from ice in order to better understand the break up of ice in the marginal ice zone. A review of the earlier studies until 1995 is given by Squire [181] and the subsequent two decades are reviewed in [182]. There is a strong overlap with this research field regarding solution methods and physical phenomena. The main findings of this field relevant to this chapter are briefly discussed below. First, when ocean waves are at normal incidence to an ice edge, at low frequencies most of the energy is transmitted into the ice floe while at high frequencies most of the energy is fully reflected back into the open water, see Fox and Squire [183]. Second, for oblique waves, a critical angle exists beyond which no waves propagate into the ice floe, see Fox and Squire [184]. In both these studies the reflection by the draft of the ice floe was ignored, an assumption of minor consequences as shown in, for instance, by Williams and

Parts of this chapter have been published in Cold Region Science and Technology Keijdener *et al.* [177].

Squire [185]. Lastly, Chung and Linton [186] studied the effect of a gap between two adjacent semi-infinite ice sheets. In this case, the reflection coefficient becomes periodic, having a series of resonance peaks at regular intervals.

In the next section, the mathematical model adopted in this thesis is defined. After this, the solution method is explained in Sec. 3.2 and 3.3. The results are then discussed in Sec. 3.4 and conclusions and recommendations are given in Sec. 3.5. Since the problem is studied in the frequency domain, all equations and figures presented in this chapter have already been transformed into that domain, denoted by a tilde above the field variables. The Fourier transform that is used to relate the time and frequency domains is given by Eq. (A.3). As the problem is in-plane, all parameters are defined per meter.

3.1. MODEL DESCRIPTION

The problem to be solved is depicted in Fig. 3.1. The floater is modeled as a rigid body of length L that floats on the surface of the fluid layer of depth H. The thickness of the floater is assumed to be negligible compared to the water depth. The ice floe is present for $x \leq -l$. The goal is to determine the floater's vertical motion $\tilde{W}(\omega)$ and rotational motion $\tilde{\varphi}(\omega)$ caused by the time harmonic force $F_{\text{ext}}(t) = \tilde{F}_{\text{ext}}(\omega)e^{i\omega t}$ and moment $M_{\text{ext}}(t) = \tilde{M}_{\text{ext}}(\omega)e^{i\omega t}$ acting on it, while accounting for the presence of the ice floe.

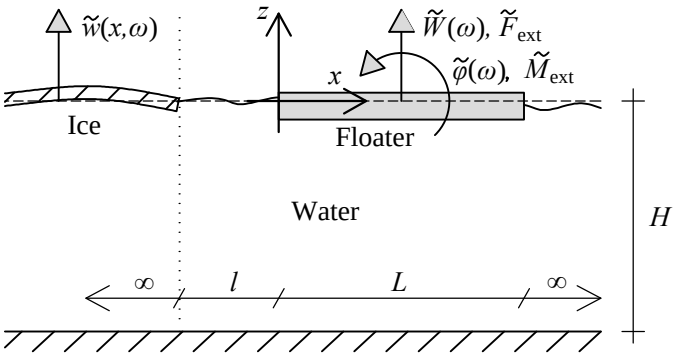

Figure 3.1: The waves generated by the floater's motion reflect at the ice-open water interface indicated by the dashed line. The reflected waves exert a pressure on the floater, altering its response.

The model is assumed to be 2D, which implies that the out-of-plane dimension of the floater is much bigger than the distance l between the ice floe and the floater. This scenario may be representative of the heave and roll motions of barges, tabular icebergs or large ice floes. The extension to 3D would allow for more accurate analysis of other motion types, like pitch and yaw, and would lift the restriction on the out-of-plane dimension of the floater. The extension to embedded bodies (i.e., without ignoring the draft) would enable the analysis of horizontal motions, such as surge and sway, and allow a more complex geometry of the floater to be considered. Although the response in the presence of an ice floe will be quantitatively different for each floater, it is postulated that the phenomena observed and understanding gained from this simple model are applicable to a broad range of floaters.

The floater is excited by two external loads. These push it against the fluid, which in turn offers resistance to its motions. This interaction generates waves at the floater-fluid interface and these waves propagate away from the floater as can be seen in Fig. 3.2 at the right. Waves that propagate to the right, find no heterogeneity and therefore do not

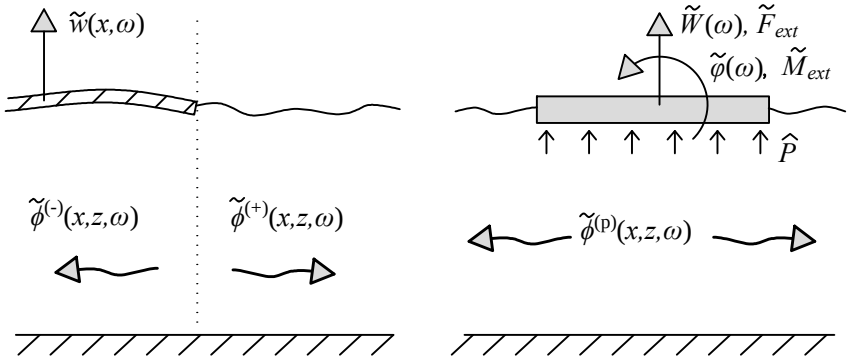

Figure 3.2: Excitation of the floater generates waves (right image) which are party reflected and transmitted by the ice floe (left image)

return to the floater. On the contrary, waves propagating to the left will encounter the ice floe and will be partially transmitted and partially reflected at its edge located at $x = -l$, see the left part of Fig. 3.2. The response of the floater is affected by the reflected wave field. The influence of the reflected waves on the floater's response is the main subject of this chapter. In the ensuing, the mathematical problem is formulated and in the next section, the solution method is discussed.

3.1.1. FLOATER'S GOVERNING EQUATIONS

The loads acting on the floater are the external force $\tilde{F}_{\text{ext}}$ and moment $\tilde{M}_{\text{ext}}$, and the contact pressure $\tilde{P}(x)$ that acts along the interface with the fluid. Therefore, the equation of motion of the floater can be written as:

$$-\omega^2 \begin{bmatrix} m & 0 \\ 0 & J \end{bmatrix} \begin{bmatrix} \tilde{W} \\ \tilde{\varphi} \end{bmatrix} = -\int_0^L \begin{bmatrix} \tilde{P}(x,\omega) \\ (x - C_{\text{x}})\tilde{P}(x,\omega) \end{bmatrix} \mathrm{d}x + \begin{bmatrix} \tilde{F}_{\text{ext}} \\ \tilde{M}_{\text{ext}} \end{bmatrix} \tag{3.1}$$

where m is the floater's mass per meter, J its mass moment of inertia and C_{x} the x-coordinate of its center of gravity. The integral on the right-hand side converts the distributed fluid pressure into an equivalent force and moment with respect to the center of gravity of the floater.

The unknowns of this system of equations are the displacement $\tilde{W}$, rotation $\tilde{\varphi}$ and the contact pressure $\tilde{P}$. On its own, the system is undetermined and must be coupled to the fluid to relate the floater's displacements with the resulting contact pressure $\tilde{P}$. The set of equations governing the fluid are described next.

3.1.2. FLUID'S GOVERNING EQUATIONS

The fluid is assumed to be incompressible, inviscid and irrotational allowing it to be described by the Laplace equation:

$$\nabla^2 \tilde{\phi} = 0 \qquad \forall\ x \in (-\infty, \infty) \cap z \in (-H, 0) \tag{3.2}$$

where parentheses denote an open interval and square brackets, in formulas to follow, a closed one. The displacement potential $\tilde{\phi}(x, z, \omega)$ is defined by:

$$\vec{u} = \nabla \phi \tag{3.3}$$

where $\vec{u}$ contains the horizontal and vertical displacement of the fluid. A displacement potential (see for instance Jensen *et al.* [187]) is used as it results in a clearer and more standard notation from a structural dynamics point of view.

The governing equation of the fluid must be accompanied by proper boundary conditions in order for the system to be determined. At the lower boundary, $z = -H$, the condition prevents penetration of the fluid into the seabed:

$$\frac{\partial \phi(x, -H, t)}{\partial z} = 0 \qquad \forall\ x \in (-\infty, \infty) \tag{3.4}$$

At the upper boundary, $z = 0$, the fluid pressure $\tilde{p}$ must balance with the external pressure. The fluid pressure is calculated according to the linearized Bernoulli equation for unsteady potential flow [188]:

$$\tilde{p}(x, z, \omega) = -\rho_w \left(-\omega^2 \tilde{\phi} + g \left(\frac{\partial \tilde{\phi}}{\partial z} + z \right) \right) \tag{3.5}$$

where ρ_w is the fluid density and g is the gravitational constant. The first term in Eq. (3.5) introduces linear hydrodynamic effects, whereas the second term is responsible for the hydrostatic effects. The nonlinear hydrodynamic pressure term was removed by the linearization.

The external surface pressure acting on the fluid surface is x-dependent. Under the ice floe the fluid pressure must be equal to the pressure imposed by the dynamically flexible ice floe which is modeled as a Kirchhoff-Love plate. Under the rigid floater, the pressure is equal to the contact pressure $\tilde{P}$ that was defined in the previous subsection. Outside these regions the pressure is zero as the atmospheric pressure is ignored. In this way, the fluid pressure $\tilde{p}$ at $z = 0$ is:

$$\tilde{p}(x, 0, \omega) = \begin{cases} -\omega^2 \rho_i A \tilde{w}(x, \omega) + D_i \tilde{w}''''(x, \omega) & \forall\ x \in (-\infty, -l] \\ 0 & \forall\ x \in (-l, 0] \\ \tilde{P}(x, \omega) & \forall\ x \in (0, L] \\ 0 & \forall\ x \in (L, \infty) \end{cases} \tag{3.6}$$

where ρ_i is the density of the ice, h its thickness, $\tilde{w}(x, \omega)$ its transverse displacements and the prime denotes a spatial derivative. The plate's bending stiffness is given by $D_i = E(1 - \nu^2)^{-1} h^3 (12)^{-1}$ where E is the ice's Young's modules and ν its Poisson ratio. Furthermore,

four boundary conditions are required to solve the boundary value problem for the ice plate. Two of them are related to the appropriate behavior at infinity, which means that no energy propagates from infinity and that the plate's deflection is bounded at infinity. The other two are related to the stress-free edge of the ice (free of moments and shear forces):

$$D_\mathrm{i}\frac{\partial^2 \tilde{w}(-l,\omega)}{\partial x^2} = 0 \tag{3.7a}$$

$$D_\mathrm{i}\frac{\partial^3 \tilde{w}(-l,\omega)}{\partial x^3} = 0 \tag{3.7b}$$

To ensure a continuity of vertical displacements of ice and fluid, the following kinematic interface condition applies:

$$\tilde{w}(x,\omega) = \frac{\partial \tilde{\phi}(x,0,\omega)}{\partial z} \qquad \forall\ x \in (-\infty,-l] \tag{3.8}$$

A similar kinematic interface condition applies between floater and fluid. However, since the floater is rigid, its rotation contributes to the vertical displacements and as such has to be accounted for in the continuity condition:

$$\tilde{W}(\omega) + (x - C_\mathrm{x})\tilde{\varphi}(\omega) = \frac{\partial \tilde{\phi}(x,0,\omega)}{\partial z} \qquad \forall\ x \in (0,L] \tag{3.9}$$

For convenience, the fluid is divided into two regions: the ice-covered region, $x \leq -l$, and the open water region, $x > -l$, see Fig. 3.1. In the open water region, two potentials are used: $\tilde{\phi}^{(\mathrm{p})}$ to capture the waves radiated by the floater and $\tilde{\phi}^{(+)}$ to capture the waves that are reflected by the ice. In the ice-covered region, a single potential $\tilde{\phi}^{(\mathrm{i},-)}$ is used to capture those radiated waves that are transmitted into the ice-covered region; all waves in this region either propagate towards negative infinity or, in case of evanescent modes, decay exponentially with the distance from the ice edge. The displacement potential of the fluid $\tilde{\phi}$ is thus composed of three potentials and their spatial dependence is:

$$\tilde{\phi}(x,z,\omega) = \begin{cases} \tilde{\phi}^{(-)}(x,z,\omega) & \forall\ x \in (\infty,-l] \cap z \in [-H,0] \\ \tilde{\phi}^{(\mathrm{p})}(x,z,\omega) + \tilde{\phi}^{(+)}(x,z,\omega) & \forall\ x \in (-l,\infty) \cap z \in [-H,0] \end{cases} \tag{3.10}$$

Based on this definition, the contact pressure $\tilde{P}(x)$ in Eq. (3.6) is accounted for by $\tilde{\phi}^{(\mathrm{p})}$. Consequently, $\tilde{\phi}^{(+)}$ has to satisfy the pressure release condition at its surface, i.e. for all $x > -l$. However, while satisfying the kinematic interface condition between floater and fluid, Eq. (3.8), the summation of both potentials has to be used because both contribute to the vertical displacements at the water surface.

To ensure compatibility and continuity between the two regions, two extra interface conditions need to be satisfied along the full extent of the vertical interface $x = -l$:

$$\tilde{\phi}^{(-)}\big|_{x=-l} = \left(\tilde{\phi}^{(\mathrm{p})} + \tilde{\phi}^{(+)}\right)\big|_{x=-l} \qquad \forall\ z \in [-H,0] \tag{3.11a}$$

$$\frac{\partial \tilde{\phi}^{(-)}}{\partial x}\bigg|_{x=-l} = \left(\frac{\partial \tilde{\phi}^{(\mathrm{p})}}{\partial x} + \frac{\partial \tilde{\phi}^{(+)}}{\partial x}\right)\bigg|_{x=-l} \qquad \forall\ z \in [-H,0] \tag{3.11b}$$

The first one assures continuity of fluid pressure while the second one assures continuity of horizontal displacement.

The methodology used for solving the formulated problem is discussed next.

3.2. DISCRETIZATION

An analytical solution to the problem as defined above is difficult because of the integral in the floater's equation of motion, Eq. (3.1), and the unknown spatial dependence of the interface condition between floater and fluid, Eq. (3.9). To overcome this difficulty, both equations are discretized, starting with the contact pressure. The discretization strategy used in this chapter is similar to the boundary element method.

3.2.1. DISCRETIZATION OF THE CONTACT PRESSURE

The integral in Eq. (3.1) cannot be evaluated directly because the contact pressure $\tilde{P}(x)$ is unknown. The pressure is distributed continuously between $(0, L]$ and so can be seen as working on infinitely many points. This condition is relaxed by approximating the continuous pressure with a summation of elements. To illustrate the discretization procedure, Fig. 3.3 shows a fictitious continuous pressure profile, depicted by the dashed line. This continues profile is approximated by the summation of N_{BEM} elements, anal-

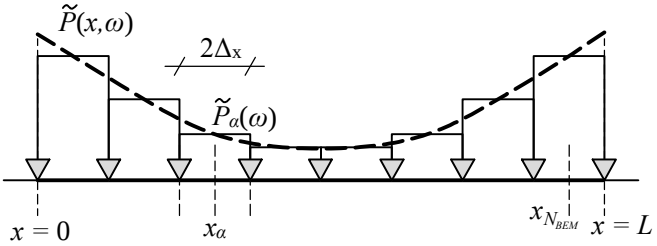

Figure 3.3: The interfacial pressure $\tilde{P}$ is discretized using $N_{\text{BEM}} = 8$ elements. Within each element α the pressure is constant and proportional to $\tilde{P}_\alpha$.

ogous to a Riemann sum. These elements are indexed with α. For convenience, the pressure is assumed invariant within each element. Increasing the number of elements lets the approximation converge to the exact solution.

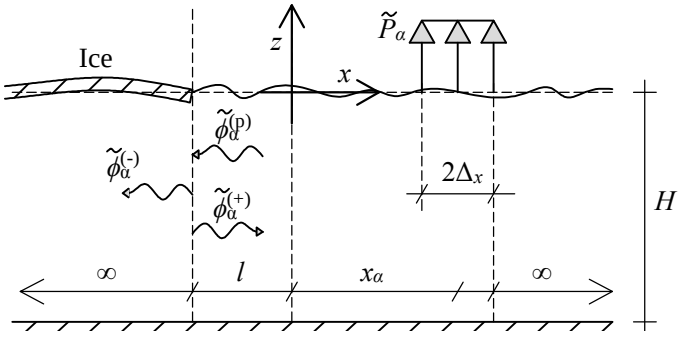

Figure 3.4: The generation of a transmitted potential $\tilde{\phi}_\alpha^{(-)}$ and reflected potential $\tilde{\phi}_\alpha^{(+)}$ due to the presence of the ice.

Fig. 3.4 shows the pressure exerted by a single element on the fluid. The pressure, with complex amplitude $\tilde{P}_\alpha$, is applied within the domain of the element $(x_\alpha^-, x_\alpha^+]$ where $x_\alpha^- = x_\alpha - \Delta_x$ and $x_\alpha^+ = x_\alpha + \Delta_x$. The elements are centered around $x_\alpha = 2\Delta_x(\alpha - 1/2)$ and have a width $2\Delta_x$. The surface pressure of each element excites the fluid, thereby generating waves which are captured by the potential $\tilde{\phi}_\alpha$. Since each element generates its own set of waves, the total fluid response excited by the interface pressure $\tilde{P}$ is given by the combined effect of all N_{BEM} elements:

$$\tilde{\phi}(x,z,\omega) = \sum_{\alpha=1}^{N_{\text{BEM}}} \tilde{\phi}_\alpha(x,z,\omega) \tag{3.12}$$

After discretization, the integrals over the hull of the floater in Eq. (3.1) can be evaluated as:

$$\int_0^L \tilde{P}(x,\omega)\,\mathrm{d}x = 2\Delta_x \sum_{\alpha=1}^{N_{\text{BEM}}} \tilde{P}_\alpha \tag{3.13a}$$

$$\int_0^L (x - C_x)\tilde{P}(x,\omega)\,\mathrm{d}x = 2\Delta_x \sum_{\alpha=1}^{N_{\text{BEM}}} r_\alpha \tilde{P}_\alpha \tag{3.13b}$$

where $r_\alpha = x_\alpha - C_x$.

Approximating the continuous profile with the Riemann sum has reduced the number of unknowns to the N_{BEM} unknown complex amplitudes $\tilde{P}_\alpha$. The goal is now to obtain these amplitudes, allowing the interaction problem to be solved. Doing this requires the fluid response generated by each element: $\tilde{\phi}_\alpha$. These potentials are introduced after the discretization of the interface condition.

3.2.2. DISCRETIZATION OF THE KINEMATIC FLOATER-FLUID INTERFACE CONDITION

The second equation that has to be discretized is the interface condition between floater and fluid, Eq. (3.9). Just like the contact pressure, the interface condition also applies continuously in the interval $(0, L]$. Discretizing the interface condition will result in a finite number of conditions that need to be satisfied.

The discretization of the contact pressure introduced N_{BEM} unknowns. To make the problem solvable, the floater-fluid interface condition is discretized into the same number of elements. This is done by enforcing an equivalent interface condition within the domain of each element. There are multiple ways to do this. In this chapter, the average vertical displacement (AVD) within each element is matched to the AVD of the floater within the element's domain. Using this strategy, the interface condition in Eq. (3.9) is replaced by the following set of N_{BEM} equations, indexed with β:

$$\frac{1}{2\Delta_x}\int_{x_\beta^-}^{x_\beta^+} \left(\tilde{W} + (x - C_x)\tilde{\varphi}\right)\mathrm{d}x = \tag{3.14}$$

$$\frac{1}{2\Delta_x}\int_{x_\beta^-}^{x_\beta^+} \frac{\partial\tilde{\phi}(x,0,\omega)}{\partial z}\,\mathrm{d}x = \tilde{w}_\beta \qquad \forall\ \beta = 1\,..\,N_{\text{BEM}} \tag{3.15}$$

where $x_\beta^- = x_\beta - \Delta_x$, $x_\beta^+ = x_\beta + \Delta_x$ and the symbol $\tilde{w}_\beta$ is given to the fluid's AVD within element β. Due to the discretization of the pressure, the fluid response $\tilde{\phi}$ is given by the superimposed response of all elements (see Eq. (3.12)) and so the interface condition becomes:

$$\tilde{W} + r_\beta \tilde{\varphi} = \frac{1}{2\Delta_x} \sum_{\alpha=1}^{N_{BEM}} \int_{x_\beta^-}^{x_\beta^+} \frac{\partial \tilde{\phi}_\alpha(x,0,\omega)}{\partial z} \, dx = \sum_{\alpha=1}^{N_{BEM}} \tilde{w}_{\alpha,\beta} \qquad \forall\ \beta = 1..N_{BEM} \tag{3.16}$$

where the integral on the left hand side in Eq. (3.14) resulted in the arm $r_\beta = x_\beta - C_x$ and the symbol $\tilde{w}_{\alpha,\beta}$ designates the contribution of element α to the AVD within element β.

In the next section, the discretized problem is solved and the floater's response is obtained.

3.3. SOLVING THE PROBLEM

The discretization performed in the previous section resulted in N_{BEM} discrete potentials $\tilde{\phi}_\alpha$, each one capturing the fluid response generated by the surface pressure of the corresponding element α as depicted in Fig. 3.4. The next step in solving the problem is to find an expression for each $\tilde{\phi}_\alpha$.

3.3.1. FLUID RESPONSE DUE TO DIFFERENTIAL SURFACE PRESSURE

The reflection and transmission processes described before also occur when the waves generated by each element arrive at the ice edge and so each $\tilde{\phi}_\alpha$ also consists of three potentials:

$$\tilde{\phi}_\alpha = \begin{cases} \tilde{\phi}_\alpha^{(-)} & \forall\ x \in (\infty, -l] \ \cap\ z \in [-H, 0] \\ \tilde{\phi}_\alpha^{(p)} + \tilde{\phi}_\alpha^{(+)} & \forall\ x \in (-l, \infty) \ \cap\ z \in [-H, 0] \end{cases} \tag{3.17}$$

Since $\tilde{\phi}_\alpha^{(p)}$ captures the waves radiated by the surface pressure of element α, $\tilde{\phi}_\alpha^{(+)}$ has to satisfy the pressure release condition in the whole region $x \in (-l, \infty)$. The three potentials are depicted in Fig. 3.4. Finding $\tilde{\phi}_\alpha$ therefore implies finding its three constituents. The final form of $\tilde{\phi}_\alpha^{(p)}$ and $\tilde{\phi}_\alpha^{(+)}$ is presented next. Their derivations can be found in App. A. The expression for $\tilde{\phi}_\alpha^{(-)}$ is not presented here as it is not needed, but its derivation can be found in the App. A.2.

The final expression for $\tilde{\phi}_\alpha^{(p)}$ is shown below. The full derivation can be found in App. A.1 with the substitution $P_{GF}^{(+)} = \tilde{P}_\alpha$.

$$\tilde{\phi}_\alpha^{(p)}(x,z,\omega) = -\frac{\tilde{P}_\alpha}{\rho_w g} \sum_{n=0}^{N_k} \gamma_n Q_n^{-1} I_{\alpha,n}(x) Z_n(z) \qquad \forall\ x \in (-l, \infty) \ \cap\ z \in [-H, 0] \tag{3.18}$$

where γ_n is:

$$\gamma_n = \begin{cases} 1/2, & \text{if } n = 0 \\ 1, & \text{if } n > 0 \end{cases} \tag{3.19}$$

Q_n is given by:

$$Q_n = \left(\omega^2/g - k_n \tanh(k_n H)\right) - k_n \left(k_n H \operatorname{sech}^2(k_n H) + \tanh(k_n H)\right) \tag{3.20}$$

The x-dependence is given by $I_{\alpha,n}(x)$:

$$I_{\alpha,n}(x) = \operatorname{sgn}\left(x - x_\alpha^+\right) \mathrm{e}^{\mathrm{i}k_n|x-x_\alpha^+|} - \operatorname{sgn}\left(x - x_\alpha^-\right) \mathrm{e}^{\mathrm{i}k_n|x-x_\alpha^-|} \tag{3.21}$$

The depth eigenfunction $Z_n(z)$ that assures that the solution satisfies the Laplace equation and the boundary condition at the seabed is given by:

$$Z_n(z) = \frac{\cosh(k_n(z+H))}{\cosh(k_n H)} \tag{3.22}$$

The summation is taken over the k_n wavenumbers that satisfy the dispersion relation of the open water region:

$$\omega^2/g - k\tanh(kH) = 0 \tag{3.23}$$

k_n is defined as:

- k_0: 0
- k_1: the negative real pole
- $k_n \ \forall \ n \geq 2$: the positive imaginary poles in ascending order

It is important to note that the sum in Eq. (3.18) is taken over N_k modes. In actual fact, there are infinitely many modes which satisfy the equations governing $\tilde{\phi}_\alpha^{(\mathrm{p})}$ but this infinite set was truncated at N_k for practical reasons.

Next, the general solution for $\tilde{\phi}_\alpha^{(+)}$ is presented. Within the domain of definition of this potential, $x > -l$, the surface boundary condition in Eq. (3.6) simplifies to the pressure release condition, i.e. $\tilde{p}(x,0,\omega) = 0$ (the external forcing from the pressure element has already been accounted for by $\tilde{\phi}_\alpha^{(\mathrm{p})}$). The solution, based on Eq. A.43a, is:

$$\tilde{\phi}_\alpha^{(+)}(x,z,\omega) = \sum_{n=1}^{N_\mathrm{k}} a_{\alpha,n} \mathrm{e}^{\mathrm{i}k_n(x+l)} Z_n(z) \qquad \forall\ x \in [-l,\infty) \cap z \in [-H,0] \tag{3.24}$$

where all amplitudes $a_{\alpha,n}$ are unknown. It is important to note that $\tilde{\phi}_\alpha^{(+)}$ sums over the same modes as $\tilde{\phi}_\alpha^{(\mathrm{p})}$, albeit with different amplitudes, as both potentials satisfy the same surface boundary conditions and consequently the same dispersion relation.

The last step is to resolve the interface condition at $x = -l$. This is done using the eigenfunction matching method [189] which is performed in A.3. During this process, expressions are found for the unknown amplitudes $a_{\alpha,n}$ and these amplitudes become proportional to the unknown $\tilde{P}_\alpha$'s.

The response of the fluid due to each pressure element, including the effects of the ice, has now been obtained in the form of $\tilde{\phi}_\alpha$. The only remaining unknowns are the $\tilde{P}_\alpha$'s and the floater's response. The only remaining equations still to be satisfied are the interface between floater and fluid, Eq. (3.9), and the floater's equation of motion, Eq. (3.1). The remaining unknowns are found in the next subsection.

3.3.2. RESOLVING THE FLOATER-FLUID INTERFACE

Now that an expression has been found for $\tilde{\phi}_\alpha$, the floater-fluid interface condition can be satisfied. This results in an expression for each $\tilde{P}_\alpha$. The last step is then to solve the equation of motion of the floater, thereby obtaining the response of the floater and concluding the derivation.

The floater-fluid interface condition was discretized in Eq. (3.14). This equation states that the fluid's averaged vertical displacement (AVD) within element β's domain, i.e. $\tilde{w}_\beta$, should be equal to the floater's AVD within the same domain. As the fluid response is given by the combined effect of all elements, see Eq. (3.12), the contribution of each element α to the AVD of each interfacial element β is needed, see Eq. (3.16):

$$\tilde{w}_\beta = \sum_{\alpha=1}^{N_{\text{BEM}}} \tilde{w}_{\alpha,\beta} \qquad \forall\ \beta = 1\,..\,N_{\text{BEM}} \tag{3.25}$$

To find an expression for $\tilde{w}_{\alpha,\beta}$, the integral in Eq. (3.16) has to be evaluated. Because the floater is always located to the right of the ice floe, $\tilde{\phi}_\alpha$ in eq. 3.17 reduces to the summation of $\tilde{\phi}_\alpha^{(\text{p})}$ and $\tilde{\phi}_\alpha^{(+)}$ while satisfying the floater-fluid interface. Substituting this into Eq. (3.16) gives:

$$\tilde{w}_{\alpha,\beta} = \tilde{w}_{\alpha,\beta}^{(\text{p})} + \tilde{w}_{\alpha,\beta}^{(+)} = \frac{1}{2\Delta_{\text{x}}} \int_{x_\beta^-}^{x_\beta^+} \left(\frac{\partial \tilde{\phi}_\alpha^{(\text{p})}}{\partial z} + \frac{\partial \tilde{\phi}_\alpha^{(+)}}{\partial z} \right) \Bigg|_{z=0} \mathrm{d}x \tag{3.26}$$

where $x_\beta^- = x_\beta - \Delta_{\text{x}}$, $x_\beta^+ = x_\beta + \Delta_{\text{x}}$. $\tilde{w}_{\alpha,\beta}^{(\text{p})}$ is given by (see Eq. (A.65)):

$$\tilde{w}_{\alpha,\beta}^{(\text{p})} = -\frac{\tilde{P}_\alpha}{\rho_{\text{w}} g} \frac{1}{2\Delta_{\text{x}}} \sum_{n=0}^{N_{\text{k}}} \gamma_n Q_n^{-1} I_{\alpha,\beta,n} \lambda_n \tag{3.27}$$

where $I_{\alpha,\beta,n} = \int_{x_\beta^-}^{x_\beta^+} I_{\alpha,n}(x)\,\mathrm{d}x$ (see Eq. (A.63)) and $\lambda_n = Z_n'(0) = k_n \tanh(k_n H)$. $\tilde{w}_{\alpha,\beta}^{(+)}$ is given by (see Eq. (A.66)):

$$\tilde{w}_{\alpha,\beta}^{(+)} = \frac{1}{\Delta_{\text{x}}} \sum_{n=1}^{N_{\text{k}}} a_n \sinh(\mathrm{i}k_n\Delta_{\text{x}}) \mathrm{e}^{\mathrm{i}k_n(x_\beta + l)} \lambda_n \tag{3.28}$$

As $\tilde{w}_{\alpha,\beta}$ scales linearly with $\tilde{P}_\alpha$, $\tilde{P}_\alpha$ can be factored out to give:

$$\tilde{w}_\beta = \sum_{\alpha=1}^{N_{\text{BEM}}} \tilde{w}_{\alpha,\beta}^{(\text{p})} + \tilde{w}_{\alpha,\beta}^{(+)} = \sum_{\alpha=1}^{N_{\text{BEM}}} \left(\tilde{\Lambda}_{\alpha,\beta}^{(\text{p})} + \tilde{\Lambda}_{\alpha,\beta}^{(+)} \right) \tilde{P}_\alpha \qquad \forall\ \beta = 1\,..\,N_{\text{BEM}} \tag{3.29}$$

All N_{BEM} equations are now combined into a matrix equation:

$$\tilde{\mathbf{w}} = \left(\tilde{\mathbf{\Lambda}}^{(\text{p})} + \tilde{\mathbf{\Lambda}}^{(+)} \right) \tilde{\mathbf{P}} = \tilde{\mathbf{\Lambda}} \tilde{\mathbf{P}} \tag{3.30}$$

where $\tilde{\mathbf{w}}$ and $\tilde{\mathbf{P}}$ are $N_{\text{BEM}} \times 1$ vectors containing the AVD and pressure of each element and $\tilde{\mathbf{\Lambda}}^{(\text{p})}$, $\tilde{\mathbf{\Lambda}}^{(+)}$ and $\tilde{\mathbf{\Lambda}}$ are $N_{\text{BEM}} \times N_{\text{BEM}}$ matrices relating the two.

The interface condition given in Eq. (3.16) can be written in a matrix form:

$$\mathbf{1}\tilde{W} + \mathbf{r}\tilde{\varphi} = \tilde{\mathbf{w}} \tag{3.31}$$

where $\mathbf{1}$ and $\mathbf{r}$ are $N_{\text{BEM}} \times 1$ vectors, the former filled with 1's and the latter containing all N_{BEM} arms r_β. Combining this equation with Eq. (3.30) and solving for $\tilde{\mathbf{P}}$ one obtains a dependence between the contact pressure and the motions:

$$\tilde{\mathbf{P}} = \tilde{\mathbf{\Lambda}}^{-1}(\mathbf{1}\tilde{W} + \mathbf{r}\tilde{\varphi}) = \tilde{\boldsymbol{\kappa}}\tilde{W} + \tilde{\boldsymbol{\kappa}}_\varphi\tilde{\varphi} \tag{3.32}$$

where the $N_{\text{BEM}} \times 1$ vectors $\tilde{\boldsymbol{\kappa}}$ and $\tilde{\boldsymbol{\kappa}}_\varphi$ represent the frequency dependent effective heave and pitch stiffnesses of the fluid layer.

The last step in obtaining the coupled response is to solve Eq. (3.32) together with the equation of motion of the floater. This is done in the next subsection.

3.3.3. FLOATER'S RESPONSE

Now that a relation between the amplitudes $\tilde{P}_\alpha$ and the floater's motions has been found, the equations of motion of the floater can be solved. The integrals in the equation of motion (Eq. (3.2)) were evaluated in Eqs. (3.13) which can be rewritten in matrix form:

$$2\Delta_x \sum_{\alpha=1}^{N_{\text{BEM}}} \tilde{P}_\alpha = 2\Delta_x(\tilde{\mathbf{P}} \cdot \mathbf{1}) \tag{3.33a}$$

$$2\Delta_x \sum_{\alpha=1}^{N_{\text{BEM}}} \tilde{P}_\alpha r_\alpha = 2\Delta_x(\tilde{\mathbf{P}} \cdot \mathbf{r}) \tag{3.33b}$$

where $\cdot$ represent the dot product. Substituting these solutions into the equation of motion of the floater (Eq. (3.1)) yields:

$$-\omega^2 \begin{bmatrix} m & 0 \\ 0 & J \end{bmatrix} \begin{bmatrix} \tilde{W} \\ \tilde{\varphi} \end{bmatrix} = 2\Delta_x \begin{bmatrix} \tilde{\mathbf{P}} \cdot \mathbf{1} \\ \tilde{\mathbf{P}} \cdot \mathbf{r} \end{bmatrix} + \begin{bmatrix} \tilde{F}_{\text{ext}} \\ \tilde{M}_{\text{ext}} \end{bmatrix} \tag{3.34}$$

Rewriting the interaction forces in terms of the effective stiffnesses introduced in Eq. (3.32) gives:

$$-\omega^2 \begin{bmatrix} m & 0 \\ 0 & J \end{bmatrix} \begin{bmatrix} \tilde{W} \\ \tilde{\varphi} \end{bmatrix} = 2\Delta_x \begin{bmatrix} \tilde{\boldsymbol{\kappa}} \cdot \mathbf{1} & \tilde{\boldsymbol{\kappa}}_\varphi \cdot \mathbf{1} \\ \tilde{\boldsymbol{\kappa}} \cdot \mathbf{r} & \tilde{\boldsymbol{\kappa}}_\varphi \cdot \mathbf{r} \end{bmatrix} \begin{bmatrix} \tilde{W} \\ \tilde{\varphi} \end{bmatrix} + \begin{bmatrix} \tilde{F}_{\text{ext}} \\ \tilde{M}_{\text{ext}} \end{bmatrix} \tag{3.35}$$

Solving this set of equations for the unknown amplitudes results in the frequency response function of the heave and rotational motion:.

$$\begin{bmatrix} \tilde{W} \\ \tilde{\varphi} \end{bmatrix} = \left(-\omega^2 \begin{bmatrix} m & 0 \\ 0 & J \end{bmatrix} - 2\Delta_x \begin{bmatrix} \tilde{\boldsymbol{\kappa}} \cdot \mathbf{1} & \tilde{\boldsymbol{\kappa}}_\varphi \cdot \mathbf{1} \\ \tilde{\boldsymbol{\kappa}} \cdot \mathbf{r} & \tilde{\boldsymbol{\kappa}}_\varphi \cdot \mathbf{r} \end{bmatrix} \right)^{-1} \begin{bmatrix} \tilde{F}_{\text{ext}} \\ \tilde{M}_{\text{ext}} \end{bmatrix} \tag{3.36}$$

The obtained frequency response function includes both the effect of the immediate fluid response through $\tilde{\mathbf{\Lambda}}^{(\text{p})}$ and the effect of the waves reflected by the ice through $\tilde{\mathbf{\Lambda}}^{(+)}$, see Eq. (3.30). By replacing $\tilde{\mathbf{\Lambda}}$ by $\tilde{\mathbf{\Lambda}}^{(\text{p})}$ in Eq (3.32), the ice effect can be removed and the response of the floater in open water can be obtained. This allows for easy comparison between the cases when ice is present and when it is not. In the next section, the effect of the level ice on the floater's response is studied by comparing these two cases.

3.4. RESULTS

The goal of this chapter is to study the changes in the frequency domain response of the floater due to the presence of the level ice. In this section, these changes are studied by comparing the floater's response in the presence of level ice with its response in open water. The difference between the two scenarios will be referred to as the *ice effect*.

The frequency response matrix (given by Eq. (3.36)) is complex-valued and frequency dependent. It contains information on both the amplitude of the floater's vibration and the phase lag of the floater's response with respect to the harmonic loading. In this chapter, only the amplitude of the response is studied.

As the ice is only present on one side of the floater, the problem is not symmetric with respect to the floater. The reflected waves only come from the left side and therefore exert an asymmetric pressure on the floater that integrates to a non-zero moment. This implies that even if the floater is only excited in heave, after some time the reflected waves will also cause a rotational motion. The ice thus couples the heave and rotational motion of the floater.

The floater is acted upon by two loads: an external vertical force $\tilde{F}_{\text{ext}}$ and moment $\tilde{M}_{\text{ext}}$. These loads excite the heave motion $\tilde{W}$ and rotation $\tilde{\varphi}$. Consequently, there are three items to discuss; 1) the heave response due to the external force, given the symbol $\tilde{W}_F$, 2) the rotation due to the external moment, $\tilde{\varphi}_M$ and 3) the coupling terms $\tilde{W}_M = \tilde{\varphi}_F$.

For convenience, the magnitude of the loads is chosen such that the resulting quasi-static responses of $\tilde{W}_F$ and $\tilde{\varphi}_M$ are of unit amplitude:

$$\tilde{F}_{\text{ext}} = \rho_{\text{w}} g L \qquad \rightarrow \lim_{\omega \to 0} |\tilde{W}_F| = 1 \text{ [m]} \tag{3.37a}$$

$$\tilde{M}_{\text{ext}} = \frac{\rho_{\text{w}} g L^3}{12} \qquad \rightarrow \lim_{\omega \to 0} |\tilde{\varphi}_M| = 1 \text{ [rad]} \tag{3.37b}$$

For computing the results, the following parameters are used unless specified otherwise: $g = 9.81$ m/s^2, $h = 1$ m, $\nu = 0.3$, $\rho_{\text{i}} = 925$ kg/m^3, $E = 5$ GPa, $H = 100$ m, $\rho_{\text{w}} = 1025$ kg/m^3, $l = 15$ m, $C_{\text{x}} = L/2$, $m = 1\text{E}5$ kg/m and $L = 30$ m. The thickness of the floater is assumed to be negligible and so $J = m/12L^2$. The default values of the environmental parameters (h, ρ_{i}, E and H) were set to the mean values observed in nature. For the remaining parameters it is more difficult to set a default value. For this reason, parametric studies are done to investigate their influence over a range that was deemed realistic.

Lastly, based on the convergence of the results, $N_{\text{k}} = 1000$ modes and the number of elements N_{BEM} is set to $N_{\text{BEM}} = \Delta_L L$ where Δ_L is set to 4 elements per meter. Based on numerical tests, it was established that this is sufficiently dense to guarantee a converged response of the floater for the cases addressed in this chapter. Because an element density is used rather than a fixed number, the error is independent of L and so the numerical error remains of constant order of magnitude when performing sensitivity study on L.

First, the floater's response is studied to the force and then to the moment.

3.4.1. EXCITATION BY AN EXTERNAL FORCE

The amplitudes of the heave $\tilde{W}_F$ and rotational $\tilde{\varphi}_F$ motion induced by the harmonic force $\tilde{F}_{\text{ext}}$ are shown in Fig. 3.5. The superscript i denotes the response of the floater

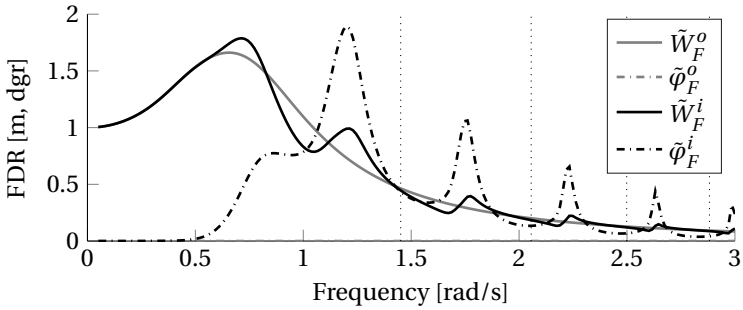

Figure 3.5: The vertical lines are related to the recurrence rate of the peaks and is discussed later. $\tilde{\varphi}_F^o$ is zero as the problem is symmetric when no ice is present.

in the presence of ice and the superscript o denotes its response in open water. The difference between the two is due to the ice effect. The floater itself is symmetric and so $\tilde{\varphi}_F^o$ is zero for all frequencies when no ice is present.

Two things stand out when looking at this figure: 1) below a certain frequency, the ice has a negligible effect and 2) above this frequency, the ice has a significant effect and results in a series of resonance peaks. These observations are explained sequentially.

No ice effect at low frequencies The reason for the floater to remain unaffected at low frequencies lies in the reflection and transmission of the waves incident to the ice edge. Fox and Squire [183] concluded that when waves are at normal incidence to the ice edge, at low frequencies nearly all energy is transmitted into the sheet and almost fully reflected back into the sea at high frequencies.

A corresponding type of behavior can also be seen in Fig. 3.5. Below a frequency of roughly 0.5 [rad/s] almost no waves are reflected and, consequently, the floater is not affected by the ice. The frequency at which the ice effect becomes perceptible is defined as the onset frequency Ω_{of}. Ω_{of} is defined as the frequency at which the reflection coefficient of the incoming propagating surface wave first exceeds 1%. The evanescent modes decay very rapidly in space and so their effect on the response of the floater is assumed to be negligible. Because of this, only the propagating surface wave is considered. This is indeed the same definition of the reflection coefficient as given in [183].

Of all the environmental parameters in this model, only the ice thickness, its Young's modulus and the water depth have a large natural variance. Fig. 3.6 shows that of these three, only the ice thickness has a significant influence on Ω_{of}. This behavior is consistent with that found in [183]. The following power functions give an accurate fit of the dependence of Ω_{of} on the ice thickness for the two cases where $H = 200$ m:

$$\omega_{\text{of}} = \begin{cases} 0.46898h^{-0.3811} - 0.0531 & \text{if} \quad E = 5 \text{ GPa} \\ 0.4183h^{-0.3882} - 0.0391 & \text{if} \quad E = 10 \text{ GPa} \end{cases} \tag{3.38}$$

with an RMS of 0.0026 and 0.0017 [rad/s] respectively.

Two conclusions can be drawn related to Ω_{of}. Firstly, up to Ω_{of} the floater is unaffected by the ice as seen in Fig. 3.5. This implies that if a floater has a low natural

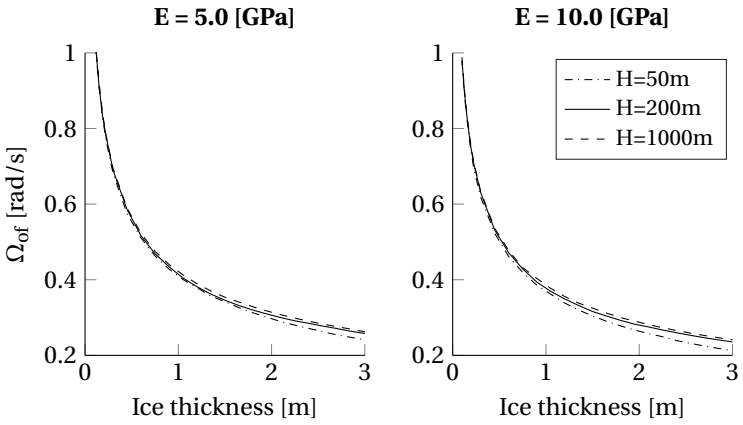

Figure 3.6: Ω_{of} for a range of ice parameters.

frequency, most of its response occurs at frequencies below Ω_{of} and, consequently, the ice effect will be minimal. This is further enhanced by thin ice as this greatly increases Ω_{of}. Second, the ice effect is proportional to the amplitude of the floater's vibration in open water, see Fig. 3.5. If the amplitude of the floater's response is small at frequencies higher than Ω_{of}, the ice effect will be small as well. Fig. 3.6 can thus be used to estimate whether a particular floater is susceptible to ice effects based on its open water response.

It is important to note that the 2D nature of the model in combination with the simplistic geometry of the floater mean that the above-formulated results should only be viewed as a first step towards understanding the hydrodynamic coupling between ice and floater through surface waves. It should also be noted that when the gap between ice and floater becomes very small, evanescent modes might affect the response of the floater which will affect Ω_{of}.

To conclude, Ω_{of}, in combination with a floater's open water response, can be used to estimate the susceptibility of that floater to the ice effect. Only the ice thickness has a significant effect on Ω_{of}.

The ice effect above the onset frequency In the frequency band above Ω_{of}, the ice effect starts to have a pronounced effect on the response of the floater. The most interesting effect is the appearance of the resonance peaks, see Fig. 3.5, at a series of frequencies. The periodicity of these peaks is characterized by the following equation:

$$2l = \lambda_1(\omega)\, j \qquad \forall\ j = 1\,..\,\infty \tag{3.39}$$

where $\lambda_1(\omega) = 2\pi/|k_1(\omega)|$ is the wavelength of the propagating surface wave. The frequencies that satisfy Eq. (3.39) are shown in Figs. 3.5 and 3.7 with the dotted vertical lines.

Fig. 3.5 shows that there are well-defined frequency bands wherein the response is altered by the reflected waves. When the floater oscillates, it loses energy in the form of radiated waves and some of this energy is trapped in the gap between the floater and

ice in the form of a standing wave. Within these frequency bands, the amount of energy trapped is significantly increased due to the gap resonance.

These quasi-standing waves, of which the nodes oscillate slightly about the positions that can be devised based on Eq. (3.39), are visualized in Fig. 3.7. The frequencies at which the amplitudes of the waves increase coincide with the frequencies at which the resonance amplification of the response is seen in Fig. 3.5. Standing waves are characterized by the quasi-sinusoidal patterns seen in Fig. 3.7 at some frequencies. Propagating waves are characterized by a constant color in the same figure.

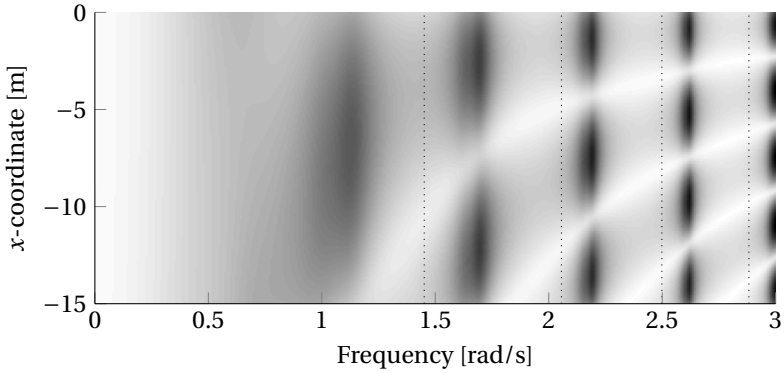

Figure 3.7: The surface amplitude within the gap for different frequencies. White represents a small amplitude, while black represents a large one.

In addition to the standing waves, the phasing of the reflected waves is also important. When the reflected waves are in-phase with the vertical motions of the floater, resonance occurs and the floater's response increases. If the reflected waves are in anti-phase with the floater, anti-resonance occurs and its response lowers.

The combined effect of standing waves and (anti-)resonance results in the alterations seen in Fig. 3.5. When standing waves occur, the rotational motions are greatly amplified because the standing waves occur only on one side of the floater and are thus asymmetric in space, exerting a moment and causing the floater to rock. For the heave motions, (anti-)resonance can be seen when the standing waves occur.

Influence of the floater's mass The influence of the floater's mass per meter on the ice effect is studied next and is shown in Fig. 3.8. Although the range of masses shown in the figure goes into the unphysical regime, as they would cause the floater to sink, it is interesting to check what effect these high masses have. To reduce the ice effect to a single value, the root mean squared (RMS) over the frequency range of [0,3] rad/s is used.

Fig. 3.8 clearly shows that increasing the mass lowers the ice effect. As the mass of the floater increases while the fluid pressure exerted by the reflected waves remain the same, their overall influence on the response of the floater lowers. Increasing the mass reduces the magnitude of the peaks but the frequencies at which they occur remain unaltered. This is supported by Eq. (3.39).

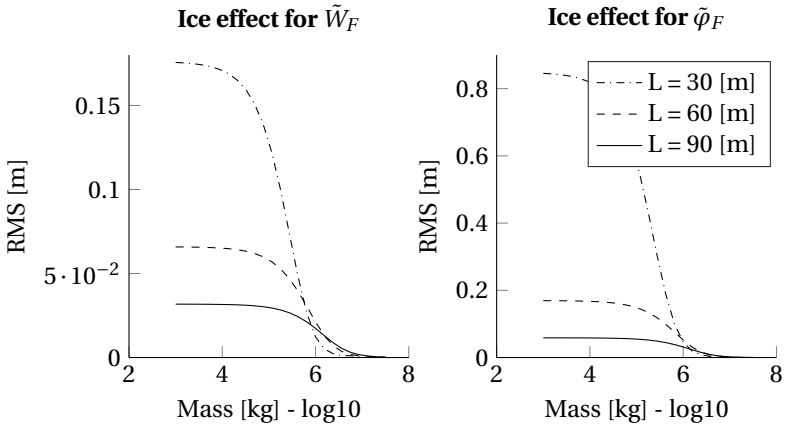

Figure 3.8: The effect of the floater's mass on the ice effect.

Influence of the gap length The last parameter whose effect will be investigated herein is the gap length l. The range that will be checked is $[0, L]$. The larger the ratio l/L, the more important 3D effects become, making the results of this 2D model less accurate. For this reason, an upper bound of $l = L$ is used. Special attention is given to the case when ice and floater are almost in contact, i.e. $l \to 0$. Fig. 3.9 shows the influence of l on the ice effect.

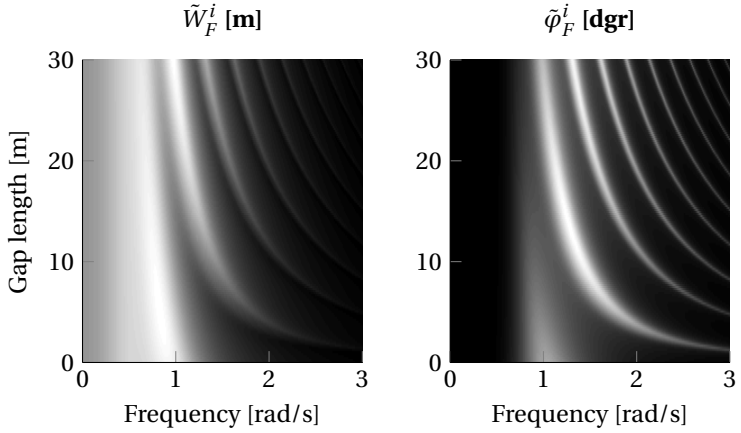

Figure 3.9: The effect of the gap length l on the response with nearby ice. White is a large amplitude and black a small.

Two things stand out in the figure. First, increasing l reduces the spacing between the peaks and introduces more of them. This is consistent with Eq. (3.39). Second, the floater's response is affected by the ice when $l = 0$ as shown in Fig. 3.10.

Although no standing waves can occur at this gap length, the phasing of the reflected

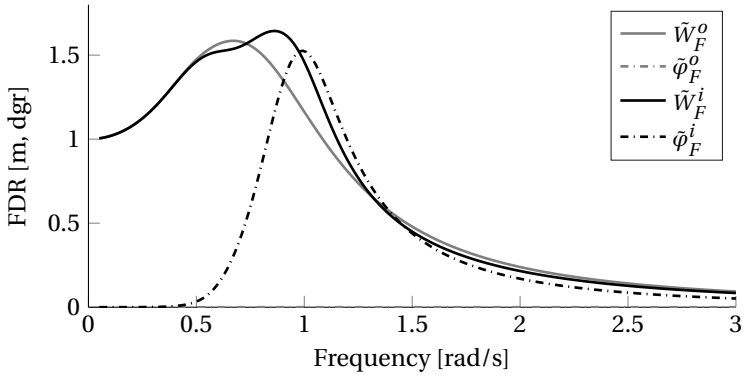

Figure 3.10: The main peak of the FDR is amplified when $l = 0$.

wave still results in (anti-)resonance. The resulting peak is slightly higher than the one in open water and is shifted to a higher frequency.

With this, the analysis of the floater's response excited by the harmonic force is concluded.

3.4.2. EXCITATION BY AN EXTERNAL MOMENT

Next the response caused by the external moment is studied. Because the coupling terms are the same ($\tilde{\varphi}_F = \tilde{W}_M$) and since $\tilde{W}_M$ was already discussed, see Fig. 3.5, $\tilde{\varphi}_F$ will not be discussed in this subsection. The analysis in this subsection is, therefore, limited to $\tilde{\varphi}_M$. $\tilde{\varphi}_M$ is shown in Fig. 3.11 using the default set of parameters.

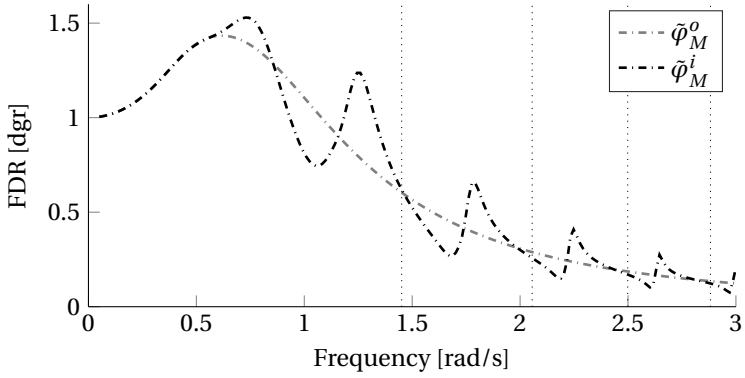

Figure 3.11: $\tilde{\varphi}_M$ for the default parameters.

$\tilde{\varphi}_M$ looks qualitatively the same as $\tilde{W}_F$ studied before. The Ω_{of} is independent of the floater so it also applies to excitation by the moment. The peaks and troughs are again caused by the standing waves in combination with (anti-)resonance. For very small gap lengths, the same effects occur as seen in Fig. 3.10. The behavior of $\tilde{\varphi}_M$ is qualitatively the same as $\tilde{W}_F$ so no further studies are done.

3.4.3. DISCUSSION

As this study is theoretical, a comparison with relevant model tests is desired. In particular, a critical look must be given to the assumption of linearity as model tests have shown that nonlinearities can play an important role in this type of interaction.

Toffoli *et al.* [190], Nelli *et al.* [191] studied the interaction between a floating elastic plate and incoming monochromatic waves in a two-dimensional wave basin experimental campaign. During these experiments, it was observed that for steep waves water can wash on top of the ice floes, a process called overwash [192]. Overwash acts as an amplitude-dependent wave energy dissipation mechanism. A comparison between their theoretical model, also based on linear theory, and their experimental results show that the linear model correctly predicts the transmitted amplitudes for low incident steepness. As the steepness increases, overwash starts to play an increasingly important role and, consequently, the transmitted amplitudes are overpredicted.

As the model presented in this chapter is also linear, overwash is not accounted for. Estimating whether it would occur is not possible because the magnitude of the external loads are not based on a physical process and so no quantitative statements can be made about the steepness of the waves. Despite this, some reservations are in order based on the findings of the previously cited papers. Particularly, the amplified response of the fluid within the gap at the resonance frequencies will be especially susceptible to overwash. As overwash acts as a limiting mechanism on the amplitudes of these waves, they might not reach the amplitudes predicted by the linear model. This, in turn, implies that the amplification of the floater's response at these frequencies will be lower than those predicted as overwash dissipates energy.

Additionally, when overwash occurs, energy can shift to higher harmonics in the reflected wave field and cause it to ultimately become irregular all together [191, 192]. This effect also disrupts the resonance build-ups observed in this chapter. The qualitative results presented in this chapter are thus only valid for waves with a low steepness and, consequently, for relatively small motions of the floater.

Lastly, [191] shows that significant drift of the ice plate can occur. Drift forces are not included in the linear model presented in this chapter. As the body in this model represents a floater, it would normally have a station-keeping system that would counteract these forces. In any case, the second order wave drift forces act additive to the first order forces studied in this chapter and, consequently, the qualitative results on the effect of the first order forces remain valid.

3.5. CONCLUSIONS

In this chapter, the effects of a nearby ice floe on the frequency domain response of a floater was investigated. Once subjected to an external sinusoidal excitation, the floater starts to generate waves that propagate away from it. Those waves falling on ice edge are partly transmitted into the ice floe and partly reflected back towards the floater. The reflected waves interact with the floater, altering its response. How the presence of the ice floe affects the floater's response, i.e. the ice effect, was studied in this chapter using a 2D model. Based on the numerical results presented, the following conclusions can be drawn.

Below a certain onset frequency the waves reflected by the ice floe are negligible and,

consequently, the floater does not feel the presence of the ice floe. Above the onset frequency, the ice effect is proportional to the response of the floater in open water. The susceptibility of a floater to the ice effect can thus be estimated by checking how much of its open water response occurs above or below the onset frequency.

Above the onset frequency, the waves reflected by the ice have a pronounced effect on the response of the floater. In certain frequency ranges, quasi-standing waves can occur within the gap between ice floe and floater. Within these frequency ranges, of which there are infinitely many, half the wavelength of the propagating surface wave of the water layer is approximately an integer multiple of the gap length, causing the amplitude of these standing waves to be greatly amplified. Increasing the gap length reduces the spacing (in frequency) of these ranges, i.e. the spectral density of the resonance frequencies increases

Within these ranges, the response of the floater is significantly altered. Depending on the phasing between the reflected waves and the floater's motions, resonance or anti-resonance can occur. Even when there is no gap between ice and floater, the amplitude of the floater can still be amplified and its natural frequency somewhat increased.

Ice thickness has a significant influence on the onset frequency, while the Young's modulus of the ice and the water depth do not. Lower thicknesses correspond to a higher onset frequency. Increasing the mass of the floater reduces the ice effect.

Lastly, a set of Green's functions were derived as part of this chapter. These functions give the response of a semi-infinite sheet of ice floating on a fluid layer of finite depth. The response of this system to three types of loading was considered, namely a point load and moment acting on the edge of the ice sheet and a distributed vertical load acting on either the surface of the ice or the fluid. This set of Green's function is used in the subsequent chapter to study the effects of hydrodynamics on ISI.

REFERENCES

[177] C. Keijdener, J. M. de Oliveira Barbosa, and A. Metrikine, *The influence of level ice on the frequency domain response of floaters,* Cold Regions Science and Technology **143**, 112 (2017).

[178] A. Tsarau, R. Lubbad, and S. Løset, *A numerical model for simulation of the hydrodynamic interactions between a marine floater and fragmented sea ice,* Cold Regions Science and Technology **103**, 1 (2014).

[179] A. Tsarau and S. Løset, *Modelling the hydrodynamic effects associated with station-keeping in broken ice,* Cold Regions Science and Technology **118**, 76 (2015).

[180] A. Tsarau, R. Lubbad, and S. Løset, *A numerical model for simulating the effect of propeller flow in ice management,* Cold Regions Science and Technology **142**, 139 (2017).

[181] V. Squire, *Of Ocean Waves and Sea Ice,* Annual Review of Fluid Mechanics **27**, 115 (1995).

[182] V. Squire, *Of ocean waves and sea-ice revisited,* Cold Regions Science and Technology **49**, 110 (2007).

[183] C. Fox and V. A. Squire, *Reflection and transmission characteristics at the edge of shore fast sea ice,* Journal of Geophysical Research **95**, 11629 (1990).

[184] C. Fox and V. A. Squire, *On the oblique reflexion and transmission of ocean waves at shore fast sea ice,* Philosophical Transactions of the Royal Society A **347**, 185 (1994).

[185] T. D. Williams and V. A. Squire, *The effect of submergence on wave scattering across a transition between two floating flexible plates,* Wave Motion **45**, 361 (2008).

[186] H. Chung and C. M. Linton, *Reflection and transmission of waves across a gap between two semi-infinite elastic plates on water,* Quarterly Journal of Mechanics and Applied Mathematics **58**, 1 (2005).

[187] F. B. Jensen, W. A. Kuperman, M. B. Porter, and H. Schmidt, *Computational Ocean Acoustics* (Springer New York, New York, NY, 2011) p. 793.

[188] J. J. Stoker, *Water Waves* (John Wiley & Sons, Inc., Hoboken, NJ, USA, 1992).

[189] F. Montiel, L. G. Bennetts, and V. A. Squire, *The transient response of floating elastic plates to wavemaker forcing in two dimensions,* Journal of Fluids and Structures **28**, 416 (2012).

[190] A. Toffoli, L. G. Bennetts, M. H. Meylan, C. Cavaliere, A. Alberello, J. Elsnab, and J. P. Monty, *Sea ice floes dissipate the energy of steep ocean waves,* Geophysical Research Letters **42**, 8547 (2015), arXiv:1502.06040 .

[191] F. Nelli, L. G. Bennetts, D. M. Skene, J. P. Monty, J. H. Lee, M. H. Meylan, and A. Toffoli, *Reflection and transmission of regular water waves by a thin, floating plate,* Wave Motion **70**, 209 (2017).

[192] L. G. Bennetts, A. Alberello, M. H. Meylan, C. Cavaliere, A. V. Babanin, and A. Toffoli, *An idealised experimental model of ocean surface wave transmission by an ice floe,* Ocean Modelling **96**, 85 (2015), arXiv:1402.1555

4

THE EFFECT OF HYDRODYNAMICS ON ICE-SLOPE INTERACTION

In this chapter, the effects of hydrodynamics on the bending failure of an ice floe due to the interaction with a downward-sloping structure, i.e. the effects on ice-slope interaction (ISI), is studied. This chapter has two goals. The first goal is to improve the understanding of the effects that hydrodynamics has on ISI and the second goal is to identify the parameter ranges wherein the assumption of ignoring hydrodynamics is valid.

In order to achieve the first goal, three research question are specified that are addressed in this chapter. Firstly, the pressure of an ideal, incompressible fluid is given by the Bernoulli equation. This nonlinear equation contains three terms but it is still unclear whether the nonlinear term that captures the dynamic pressure is important for ISI. Likewise, the importance of various other factors, such as rotational inertia and axial compression, has not been studied before. Therefore, the first goal is to determine the factors of influence for ISI. Second, it is unclear how the various factors form a balance and how hydrodynamics affects this balance. Studying the balance is the second goal. Third, no detailed study has been done in the past on the relation between the contact load and the breaking length and how hydrodynamics affects this relation. Elucidating this relation is the last goal.

Answering these three questions requires two ISI models: a hydrodynamic ISI model and a hydrostatic ISI model. The limitations of the hydrostatic IFI model are then readily identified by assessing when the predictions of the hydrostatic model start to deviate significantly from those of the hydrodynamic model. Based on this analysis, the second goal of this chapter can be achieved.

This chapter is structured as follows. First, the two ISI models are introduced in Sec. 4.1 and validated in Sec. 4.2. Following this, the factors of influence for ISI are determined in Sec. 4.3.1. Thereafter, these factors are studied to determine how they form a balance of forces in the ice in Sec. 4.3.2. Next, the influence of hydrodynamics on

Parts of this chapter have been published in Cold Region Science and Technology Keijdener *et al.* [193].

the relation between contact load and breaking length is studied in Sec. 4.3.3. In order to compare the predictions of the hydrodynamic model with those of the hydrostatic model, all computations are done using both models. Results from the comparison are used to identify the limitations of hydrostatic models in Sec. 4.3.4. The sensitivity of the results to the choice of model parameters is assessed in Sec. 4.4. A discussion follows in Sec. 4.5 and conclusions are given in Sec. 4.6.

4.1. MODEL DESCRIPTION

The studies to be done in this chapter require two ISI models. The hydrodynamic IFI models will be referred to as $\mathcal{M}_{\text{HD}}$ and the hydrostatic model as $\mathcal{M}_{\text{HS}}$. A sketch of $\mathcal{M}_{\text{HD}}$ is given in Fig. 4.1. $\mathcal{M}_{\text{HS}}$ can be obtained from $\mathcal{M}_{\text{HD}}$ by setting certain parameters, to be specified later, to zero. The ice, located at $x \leq 0$, is modeled as a semi-infinite Kirchhoff-

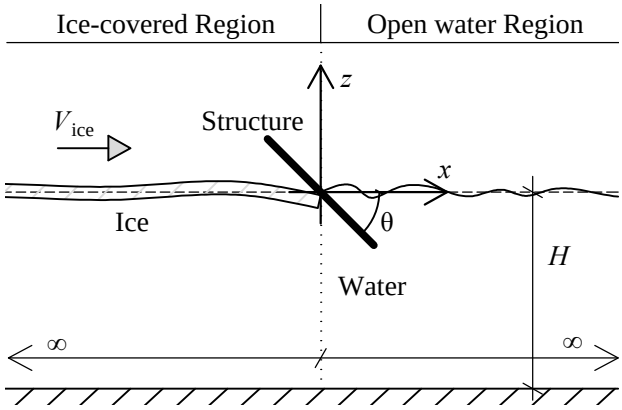

Figure 4.1: A sketch of the 2D semi-analytical ISI model $\mathcal{M}_{\text{HD}}$ that includes hydrodynamics. The region $x \leq 0$ is referred to as the ice-covered region and the region $x > 0$ as the open water region.

Love plate that includes rotational inertia and axial compression. A semi-infinite plate is used as this eliminates far field boundary effects and simplifies the model. The ice floats on a fluid layer with depth H. As the ice is not present for $x > 0$, the fluid has a free surface in this region.

It is assumed that the ice moves towards the structure with a constant horizontal velocity V_{ice}. The structure is assumed to be rigid (as the deformations of the floater are negligible) and immovable to limit the dependency of the results on the parameters of the floater. For the interaction with the fluid, the geometry of the structure is ignored. Therefore, the structure does not affect the model of the fluid. The validity of this assumption is assessed in Sec. 4.4.2. As the ice moves forward, it interacts with the structure, see Fig. 4.1. This interaction generates loads on the edge of the ice floe that cause it to slide down along the structure until it fails in bending. For the interaction with the ice floe, the structure is reduced to a sloping line passing through $x = z = 0$ with a hull angle θ with respect to the x-axis.

In the next subsection, the mathematical model is described. Following this, the solution method is explained.

4.1.1. MATHEMATICAL MODEL

Fluid The fluid is assumed to be incompressible, inviscid and irrotational, i.e. incompressible potential flow is adopted, and is therefore governed by the Laplace equation:

$$\Delta\dot{\phi}(x,z,t) = 0 \qquad \forall\ x \in (-\infty,\infty) \cap z \in (-H,0) \tag{4.1}$$

where $\phi(x,z,t)$ is the displacement potential of the fluid [194], the dot denotes derivatives with respect to time, round brackets denote an open interval while square brackets, in the equations to follow, denote a closed interval. The boundary condition at the seabed prevents penetration of the fluid into the seabed:

$$\frac{\partial\phi(x,-H,t)}{\partial z} = 0 \qquad \forall\ x \in (-\infty,\infty) \tag{4.2}$$

The fluid pressure is calculated according to the Bernoulli equation for unsteady, incompressible potential flow [195]:

$$p(x,z,t) = -\rho_{\mathrm{w}}\left(\ddot{\phi} + \frac{1}{2}v^2 + g\frac{\partial\phi}{\partial z}\right) \tag{4.3}$$

where $p(x,z,t)$ is the fluid pressure, ρ_{w} is the fluid density, g is the gravitational constant and the squared fluid speed is given by $v^2 = \left(\partial\dot{\phi}/\partial x\right)^2 + \left(\partial\dot{\phi}/\partial z\right)^2$. The fluid pressure is thus composed of three terms. From left to right these three terms will be referred to as the linear hydrodynamic, nonlinear hydrodynamic, and hydrostatic pressure, abbreviated as p_{HD}, p_{NLHD}, and p_{HS} respectively. The first two terms together comprise the hydrodynamic effect and, by disabling them, $\mathcal{M}_{\mathrm{HS}}$ is obtained. For $x > 0$, no ice is present and therefore the pressure release condition is imposed. For $x \leq 0$, the ice floe is present at the surface of the fluid and so its surface boundary condition in this region contains equation of motion of the plate. As the draft of the ice floe can be ignored, as was shown by Williams and Squire [196], the boundary condition of the fluid can be formulated at $z = 0$:

$$p(x,0,t) = \begin{cases} \rho_{\mathrm{i}} h\ddot{w} + \rho_{\mathrm{i}}\frac{h^3}{12}\ddot{w}'' + D_{\mathrm{i}}w'''' + F_{\mathrm{ct,x}}(t,w,w',\dot{w},\dot{w}')w'' & \forall\ x \in (-\infty,0) \\ 0 & \forall\ x \in (0,\infty) \end{cases} \tag{4.4}$$

where ρ_{i} is the density of the ice floe, h its thickness, $w(x,t)$ its vertical displacement and the prime denotes a spatial derivative. $D_{\mathrm{i}} = E(1-\nu^2)^{-1}h^3(12)^{-1}$ is the floe's bending stiffness, where E is the ice's Young's modulus and ν its Poisson ratio. Note that D_{i} aims to capture the bending behavior of the ice floe, including any variation of temperature, stiffness or other property across its thickness, in an effective manner, similar to what is done for functionally graded materials, see Kerr and Palmer [197]. This approach is assumed to be valid given that only very long wavelengths are excited in the ice floe. Moreover, the ice is assumed to be linearly elastic with brittle failure since the strain rate during ISI is sufficiently high [198]. The axial compression in the ice floe is assumed to be constant in space and equal to the horizontal component of the contact force $F_{\mathrm{ct,x}}(t,w,w',\dot{w},\dot{w}')$, see Fig. 4.2. These contact loads are calculated with the contact model described in Keijdener and Metrikine [199]. This contact model is piecewise

linear as it switches between two linear modes of interaction. As the moment of transition between the two modes is not known in advance, the contact model is nonlinear in time. A qualitative description of the contact model is given in Sec. 4.3.3. Lastly, it is assumed that water does not flood the submerged plate, i.e. that it remains ventilated [200].

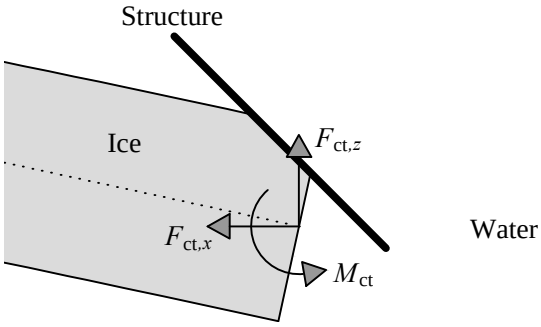

Figure 4.2: The decomposition of the contact force F_{ct}.

Ice As cavitation is not accounted for, continuity between ice and fluid dictates that their vertical displacements must be the same along their interface:

$$w(x,t) = \frac{\partial \phi(x,0,t)}{\partial z} \qquad \forall\ x \in (\infty, 0] \tag{4.5}$$

To complete the description of the ice floe, two boundary conditions are needed at $x = 0$. The contact pressure generated by the interaction with the structure acts on the edge of the plate. This pressure is integrated and translated to the neutral axis of the plate, resulting in a horizontal force $F_{ct,x}$, vertical force $F_{ct,z}$ and moment M_{ct}, see Fig. 4.2. These three loads are assumed to act on the edge of the plate and, therefore, enter its boundary conditions located at $x = 0$. These boundary conditions enforce a balance of forces and moments at the edge of the plate:

$$D_i \frac{\partial^3 w(0,t)}{\partial x^3} + \left(F_{ct,x}(t, w, w', \dot{w}, \dot{w}')w'\right)\Big|_{x=0} = \left(F_{ct,z}(t, w, w', \dot{w}, \dot{w}')\right)\Big|_{x=0} \tag{4.6a}$$

$$D_i \frac{\partial^2 w(0,t)}{\partial x^2} + \left(F_{ct,x}(t, w, w', \dot{w}, \dot{w}')w\right)\Big|_{x=0} = \left(M_{ct}(t, w, w', \dot{w}, \dot{w}')\right)\Big|_{x=0} \tag{4.6b}$$

where the first term in both equations is due to the bending stiffness of the plate and the second term is due to axial compression. As the loads act on the edge of the plate, they are per unit meter. The dependencies of the contact loads on the state of the edge of the plate will be omitted in the remainder of this chapter for brevity.

The ice continues to slide down the structure until it fails in bending. Failure takes place at the moment in time t_{fail} when the maximum axial stresses in the ice first exceed the ice's flexural strength σ_{fl}. Although axial deformations are not included in this

model, the contribution of the axial force to the axial compression is included in the failure criterion:

$$\sigma_{\max}(x,t) = \left| \frac{Eh}{2(1-\nu^2)} w''(x,t) \right| - \frac{F_{\text{ct,x}}}{h} \leq \sigma_{\text{fl}} \tag{4.7}$$

where the max-subscript implies the maximum stress within the cross-section of the ice floe.

4.1.2. SOLUTION METHOD

The approach used to solve the above-formulated dynamical problem is discussed next. The problem is nonlinear due to (i) the nonlinear dynamic pressure in Eq. (4.3), (ii) the state-dependent axial compression in the plate, Eq. (4.4), and (iii) the state-dependent contact force and moment, Eqs. (4.6). The problem is solved using the framework of the pseudo-force approach [201]. In accordance with this approach, the solution procedure is based on the solution of the linear part of the problem, which is expressed in terms of Green's functions. The steps of the procedure are as follows. At each time step, the system is assumed to be linear and the nonlinear components of $\mathcal{M}_{\text{HD}}$ are accounted for by means of pseudo forces. Basically, the nonlinear terms are moved to the right-hand side of the equations of motion and the resulting implicit equations are solved in an iterative manner. In order to deal with the distributed nonlinear loads (the dynamic pressure and the axial compression), these are approximated by piecewise constant functions of the spatial coordinate. The steps of the procedure are presented in detail below.

Green's functions Three frequency domain Green's functions are presented first, neglecting all nonlinearities in the problem statement. These Green's functions, computed for the system and loads shown in Fig. 4.3, represent the response of the system to (i) the force $F_{\text{GF}}\delta(t)$ applied at the edge of the plate, (ii) the moment $M_{\text{GF}}\delta(t)$ applied at the edge of the plate, (iii) a uniformly distributed vertical force $P_{\text{GF}}\delta(t)$ applied to a segment of the plate. The segment has a width of $2\Delta_{\text{x}}$ and is centered around x_α:

$$x_\alpha = 2\Delta_{\text{x}}(\alpha + 1/2) \tag{4.8}$$

where α identifies the location of the segment. The frequency domain response of the system to all three loads is captured in a single fluid potential $\tilde{\phi}_\alpha(x,z,\omega)$. The final form of the potential was derived in Ch. 3 and is shown below. The complete derivation can be found in App. A. Starting from Eq. (A.42), substituting $l = 0$ and using the fact that $\alpha \leq -1$, the expression for $\tilde{\phi}_\alpha$ simplifies to:

$$\tilde{\phi}_\alpha(x,z,\omega) = \begin{cases} \tilde{\phi}_\alpha^{(\text{p})}(x,z,\omega) + \tilde{\phi}_\alpha^{(\text{-})}(x,z,\omega) & \forall\ x \in (-\infty,0]\ \cap\ z \in [-H,0] \\ \tilde{\phi}_\alpha^{(+)}(x,z,\omega) & \forall\ x \in (0,\infty)\ \cap\ z \in [-H,0] \end{cases} \tag{4.9}$$

where the superscripts have been renamed for clarity. The waves excited by the distributed force $P_{\text{GF}}^{(-)}\delta(t)$ are captured in $\tilde{\phi}_\alpha^{(\text{p})}$. These waves are transmitted and reflected by the inhomogeneity at $x = 0$, resulting in a second set of waves that propagate horizontally away from $x = 0$. In addition, a third set of waves are generated by the contact

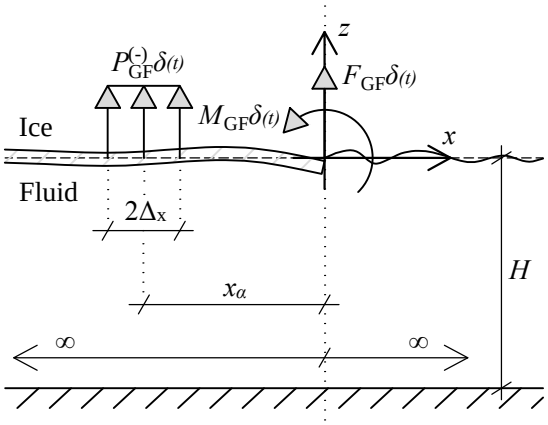

Figure 4.3: The problem definition for $\tilde{\phi}_\alpha(x,z,\omega)$ on which the three Green's functions of the system are based.

loads $F_{GF}\delta(t)$ and $M_{GF}\delta(t)$ that also propagate away from $x=0$. The waves of the second and third set that propagate towards $-\infty$ are captured in $\tilde{\phi}_\alpha^{(-)}$ while those propagating towards $+\infty$ are captured in $\tilde{\phi}_\alpha^{(+)}$. As the response in the open-water region, $x\in(0,\infty)$, is not needed for the analyses performed in this chapter, the expression of $\tilde{\phi}_\alpha^{(+)}$ is not presented here but can be found in App. A, see Eq. (A.43a).

The expressions for the two remaining potentials are given next, starting with $\tilde{\phi}_\alpha^{(\mathrm{p})}$. The final form is presented below. For the complete derivation, see the equations leading to Eq. (A.40).

$$\tilde{\phi}_\alpha^{(\mathrm{p})}(x,z,\omega) = -\frac{P_{GF}^{(-)}}{\rho_w g}\sum_{n=0}^{N_k+2}\gamma_n \bar{Q}_n^{-1}\bar{I}_{\alpha,n}(x)\bar{Z}_n(z) \tag{4.10}$$

where the minus superscript of $P_{GF}^{(-)} = P_{GF}$ indicates that the distributed vertical force acts on the ice-covered region, the overbar differentiates terms related to the ice-covered region from those related to the open water region and the infinite summation was truncated at N_k+2. The solution is a superposition of the modes of the ice-covered region. The shape of these modes is defined by the vertical wavenumbers $\bar{k}_n$ of the system. The wavenumbers are given by the roots of $k\bar{\mathfrak{D}}(k)=0$, where $\bar{\mathfrak{D}}(k)=0$ is the dispersion relation of the ice-covered region:

$$\bar{\mathfrak{D}}(k) = \delta k^4 + 1 - a(\gamma + \lambda^{-1}(k)) \tag{4.11}$$

where k is the wavenumber, $a=\omega^2/g$, ω is frequency, $\gamma = h\rho_i/\rho_w$, $\delta = D_i/(\rho_w g)$ and $\lambda(k) = k\tanh(kH)$. The roots are collected in the set $\bar{k}_n$ which is defined as follows:

- $\bar{k}_0 = 0$,
- $\bar{k}_1$: the complex root in the first quadrant of $\bar{\mathfrak{D}}(k)=0$,
- $\bar{k}_2$: the complex root in the second quadrant of $\bar{\mathfrak{D}}(k)=0$,

- $\bar{k}_3$: the negative real root of $\bar{\mathfrak{D}}(k) = 0$,
- $\bar{k}_n \; \forall \; n \geq 4$: the positive imaginary roots of $\bar{\mathfrak{D}}(k) = 0$ in ascending order.

$\bar{Q}_n$ and γ_n in Eq. (4.10) are given by:

$$\gamma_n = \begin{cases} 1/2, & \text{if } n = 0 \\ 1, & \text{if } n > 0 \end{cases} \tag{4.12}$$

$$\bar{Q}_n = \bar{\mathfrak{D}}_n \left(2\bar{\lambda}_n + H(\bar{k}_n^2 - \bar{\lambda}_n^2)\right) + 4\delta \bar{k}_n^4 \bar{\lambda}_n + a\left(1 + \frac{H(\bar{k}_n^2 - \bar{\lambda}_n^2)}{\bar{\lambda}_n}\right) \tag{4.13}$$

where $\bar{\mathfrak{D}}_n = \bar{\mathfrak{D}}(\bar{k}_n)$ and $\bar{\lambda}_n = \lambda(\bar{k}_n) = Z'(\bar{k}_n, 0) = \bar{k}_n \tanh(\bar{k}_n H)$. The depth eigenfunction $Z(k,z)$ is given by:

$$Z(k,z) = \frac{\cosh(k(z+H))}{\cosh(kH)} \tag{4.14}$$

The x-dependency of $\tilde{\phi}_\alpha$ is captured in $\bar{I}_{\alpha,n}(x)$:

$$\bar{I}_{\alpha,n}(x) = \operatorname{sgn}\left(x - x_\alpha^+\right) \mathrm{e}^{\mathrm{i}\bar{k}_n |x - x_\alpha^+|} - \operatorname{sgn}\left(x - x_\alpha^-\right) \mathrm{e}^{\mathrm{i}\bar{k}_n |x - x_\alpha^-|} \tag{4.15}$$

where $x_\alpha^+ = x_\alpha + \Delta_\mathrm{x}$, $x_\alpha^- = x_\alpha - \Delta_\mathrm{x}$ and $\mathrm{i} = \sqrt{-1}$.

Continuing with the second potential, the final form of $\tilde{\phi}_\alpha^{(-)}(x,z,\omega)$ is presented below. For the full derivation, see the equations leading to Eq. (A.43b).

$$\tilde{\phi}_\alpha^{(-)}(x,z,\omega) = \sum_{n=1}^{N_\mathrm{k}+2} \bar{a}_{\alpha,n} \mathrm{e}^{-\mathrm{i}\bar{k}_n x} \bar{Z}_n(z) \tag{4.16}$$

The amplitudes $\bar{a}_{\alpha,n}$ are obtained by solving a set of $N_\mathrm{k}+2$ equations defined below. The set was established through the eigenfunction matching procedure performed in App. A.3. The first two equations assure that the linearized version of the boundary conditions for the plate in Eq. (4.6) are satisfied. The remaining set of N_k equations assure that the fluid's pressure and displacements are continuous for $x = 0 \cap z \in (-H, 0)$:

$$\sum_{n=1}^{N_\mathrm{k}+2} \bar{a}_{\alpha,n} \bar{k}_n^2 \bar{\lambda}_n = -\frac{M_\mathrm{GF}}{D_\mathrm{i}} + \frac{P_\mathrm{GF}^{(-)}}{\rho_\mathrm{w} g} \sum_{n=1}^{N_\mathrm{k}+2} \bar{Q}_n^{-1} \bar{k}_n^2 \bar{I}''_{\alpha,n}(0) \bar{\lambda}_n \tag{4.17a}$$

$$\sum_{n=1}^{N_\mathrm{k}+2} \bar{a}_{\alpha,n} k_n^3 \bar{\lambda}_n = \frac{F_\mathrm{GF}}{\mathrm{i} D_\mathrm{i}} - \frac{P_\mathrm{GF}^{(-)}}{\rho_\mathrm{w} g} \sum_{n=1}^{N_\mathrm{k}+2} \bar{Q}_n^{-1} \bar{k}_n^3 \bar{I}'''_{\alpha,n}(0) \bar{\lambda}_n \tag{4.17b}$$

$$\sum_{n=1}^{N_\mathrm{k}+2} \bar{a}_{\alpha,n} \frac{\bar{\lambda}_n - \lambda_j}{\bar{k}_n - k_j} = -\frac{P_\mathrm{GF}^{(-)}}{\rho_\mathrm{w} g} \sum_{n=1}^{N_\mathrm{k}+2} \bar{Q}_n^{-1} \left(\bar{k}_n \bar{I}'_{\alpha,n}(0) - k_j I_{\alpha,n}(0)\right) \frac{\bar{\lambda}_n - \lambda_j}{\bar{k}_n^2 - k_j^2}$$

$$\forall \; j = 1 \,..\, N_\mathrm{k} \tag{4.17c}$$

where the summations start at $n = 1$ because $\bar{k}_0$ does not contribute to the response at $x = 0$, which also means that $\gamma_n = 1$. $\lambda_j = \lambda(k_j)$ and k_j is the set of roots of the dispersion relation of the open water region:

$$\mathfrak{D}(k) = a - \lambda(k) = 0 \tag{4.18}$$

which is defined as:

- k_1: the negative real pole of $\mathfrak{D}(k) = 0$,
- $k_j \ \forall \ j \geq 2$: the positive imaginary roots of $\mathfrak{D}(k) = 0$ in ascending order.

Discretization of the distributed nonlinear forces Two distributed nonlinear forces act on the ice, see Eq. (4.4), namely the axial compression and the dynamic pressure p_{NLHD} (the second term on the right-hand side of Eq. (4.3)). The axial compression is present $\forall\ x \in (-\infty, 0]$ while p_{NLHD} is present $\forall\ x \in (-\infty, \infty)$. It is assumed that p_{NLHD} can be ignored in the open water region and, consequently, the distributed nonlinear forces are only present in $x \in (-\infty, 0]$. This assumption is validated in Sec. 4.4.2. These loads are discretized as sketched in Fig. 4.4. The magnitude of these nonlinear loads decreases with the distance from the contact point ($x = 0$). Therefore, only a finite length segment of the ice adjacent to the contact is discretized. The truncation is done at

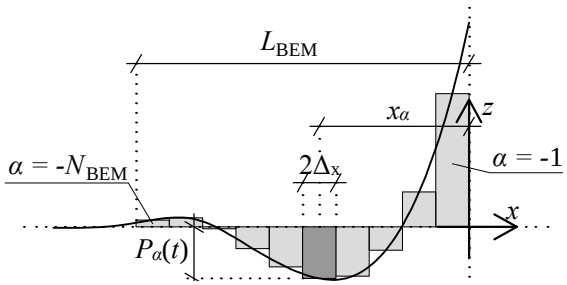

Figure 4.4: The distributed nonlinear loads, depicted with the solid curve, are approximated using a piecewise constant function. Note that $\forall\ x > 0$ the dynamic pressure is not accounted for.

$L_{\text{BEM}} = c_1 l_{\text{br,s}} \mid c_1 \geq 1$, where $l_{\text{br,s}}$ is the static breaking length of the plate that corresponds to the used contact model. $l_{\text{br,s}}$ is derived in App. C and is given by:

$$l_{\text{br,s}} = \sqrt{2} l \operatorname{atan}\left(\frac{\sqrt{2} l}{\sqrt{2} l - h \tan(\alpha)}\right) \tag{4.19}$$

where $l = \sqrt[4]{D_{\text{i}}/(\rho_{\text{w}} g)}$. The resulting line segment of length L_{BEM} is discretized into N_{BEM} elements, each with a width of $2\Delta_{\text{x}} = L_{\text{BEM}}/N_{\text{BEM}}$, see Fig. 4.4. Within each element a constant, time-dependent distributed force $P_\alpha(t)$ applies. The elements are indexed with $\alpha = -N_{\text{BEM}} \,..\, -1$ and are centered around x_α, defined in Eq. (4.8). This discretization assures that each element α corresponds with the excitation of the Green's function $\tilde{\phi}_\alpha$ by the vertical distributed force $P_{\text{GF}}\delta(t)$. How each element's $P_\alpha(t)$ is calculated is explained after the time-integration scheme has been introduced.

Time-integration In order to perform the time-integration numerically, time is discretized using a constant time step Δ_{t}. Within each time step, the loads acting on the system, i.e. the pseudo-forces, are assumed to vary linearly with time. All the nonlinear loads are thus approximated as piecewise linear functions of time, see Fig. 4.5. A state-dependent load $F(t, q(t))$ that depends on the state $q(t)$ (displacement, velocity, etc.) is

thus approximated as:

$$F(t,q(t)) \approx \sum_{\hat{n}=1}^{N_{\text{time}}} \hat{F}_{\hat{n}}(t,q_{\hat{n}})$$
$$= \sum_{\hat{n}=1}^{N_{\text{time}}} \big(\mathcal{H}(t-t_{\hat{n}-1}) - \mathcal{H}(t-t_{\hat{n}})\big)\left(\frac{F_{\hat{n}}(q_{\hat{n}}) - F_{\hat{n}-1}(q_{\hat{n}-1})}{\Delta_t}(t-t_{\hat{n}-1}) + F_{\hat{n}-1}(q_{\hat{n}-1})\right) \tag{4.20}$$

where $\mathcal{H}(t)$ is the Heaviside function, $N_{\text{time}} = T_{\text{sim}}/\Delta_t$ is the total number of time steps with T_{sim} being the simulation time, $t_{\hat{n}} = \Delta_t \hat{n}$ and all $\hat{n}$-subscripts indicate evaluations at $t_{\hat{n}}$. The loading applied within time step $\hat{n}$, $\hat{F}_{\hat{n}}(t,q_{\hat{n}})$, is now decomposed into two

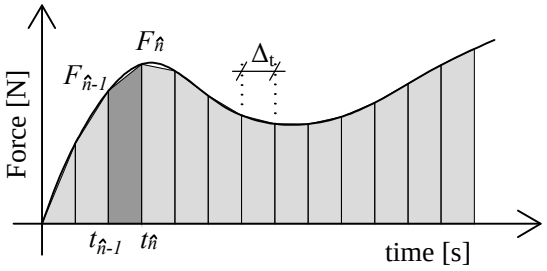

Figure 4.5: All loads are approximated as piecewise linear functions of time. The loading applied within time step $\hat{n}$, $\hat{F}_{\hat{n}}$, is highlighted.

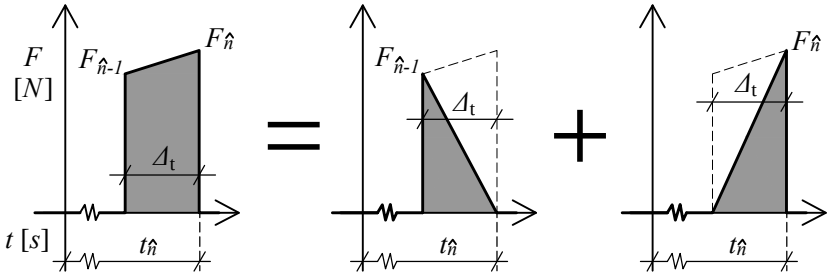

Figure 4.6: The loading applied within a single time-step $\hat{F}_{\hat{n}}(t,q_{\hat{n}})$ is decomposed into two parts: one proportional to $F_{\hat{n}-1}$ and the other proportional to $F_{\hat{n}}$.

parts, one proportional to $F_{\hat{n}-1}(q_{\hat{n}-1})$ and one proportional to $F_{\hat{n}}(q_{\hat{n}})$, see Fig. 4.6:

$$\hat{F}_{\hat{n}}(t,q_{\hat{n}}) = F_{\hat{n}-1}(q_{\hat{n}-1})\hat{\mathcal{L}}_{\hat{n}}(t) + F_{\hat{n}}(q_{\hat{n}})\hat{\mathcal{R}}_{\hat{n}}(t) \tag{4.21}$$

where $\hat{\mathcal{L}}_{\hat{n}}(t)$ and $\hat{\mathcal{R}}_{\hat{n}}(t)$ are given by:

$$\hat{\mathcal{L}}_{\hat{n}}(t) = \big(\mathcal{H}(t-t_{\hat{n}-1}) - \mathcal{H}(t-t_{\hat{n}})\big)F_{\hat{n}-1}\left(1 - \frac{t-t_{\hat{n}-1}}{\Delta_t}\right) \tag{4.22a}$$

$$\hat{\mathcal{R}}_{\hat{n}}(t) = \big(\mathcal{H}(t-t_{\hat{n}-1}) - \mathcal{H}(t-t_{\hat{n}})\big)F_{\hat{n}}\frac{t-t_{\hat{n}-1}}{\Delta_t} \tag{4.22b}$$

The state $q(t)$ at $t = t_{\hat{n}}$ due to the loading applied within a single time step $\hat{F}_{\hat{n}}(t, q_{\hat{n}})$ is thus computed as:

$$q_{\hat{n}} = F_{\hat{n}-1}(q_{\hat{n}-1})\mathcal{L}_{\hat{n}}|_{\hat{n}=0} + F_{\hat{n}}(q_{\hat{n}})\mathcal{R}_{\hat{n}}|_{\hat{n}=0} \tag{4.23}$$

where $\mathcal{L}_{\hat{n}}$ and $\mathcal{R}_{\hat{n}}$ are given by the following inverse Fourier transforms (IFT):

$$\mathcal{L}_n = \frac{1}{2\pi}\int_{-\infty}^{\infty} \tilde{\mathcal{G}}(\omega)\tilde{\mathcal{L}}(\omega)\mathrm{e}^{\mathrm{i}\omega\Delta_\mathrm{t} n}\,\mathrm{d}\omega \tag{4.24a}$$

$$\mathcal{R}_n = \frac{1}{2\pi}\int_{-\infty}^{\infty} \tilde{\mathcal{G}}(\omega)\tilde{\mathcal{R}}(\omega)\mathrm{e}^{\mathrm{i}\omega\Delta_\mathrm{t} n}\,\mathrm{d}\omega \tag{4.24b}$$

and where $\tilde{\mathcal{G}}(\omega)$ is the frequency domain Green's function corresponding to the state $q(t)$ and the load $F(t, q(t))$, and $\tilde{\mathcal{L}}_{\hat{n}}(\omega)$ and $\tilde{\mathcal{R}}_{\hat{n}}(\omega)$ are given by:

$$\tilde{\mathcal{L}}(\omega) = \frac{1}{\omega^2\Delta_\mathrm{t}}\left(\mathrm{e}^{\mathrm{i}\omega\Delta_\mathrm{t}}(1 - \mathrm{i}\omega\Delta_\mathrm{t}) - 1\right) \tag{4.25a}$$

$$\tilde{\mathcal{R}}(\omega) = \frac{1}{\omega^2\Delta_\mathrm{t}}\left(1 + \mathrm{i}\omega\Delta_\mathrm{t} - \mathrm{e}^{\mathrm{i}\omega\Delta_\mathrm{t}}\right) \tag{4.25b}$$

The inverse Fourier transforms in Eqs. (4.24) are evaluated numerically using a quadratic, nested, adaptive integration scheme. The scheme observes a global error criterion that assures the time domain error of $\mathcal{L}_n$ and $\mathcal{R}_n$ is below a specified tolerances for all $t \in [0, T_\mathrm{sim}]$. A detailed description of the scheme can be found in App. B.

Eq. (4.23) only accounts for the response to the loading that was applied during the current time step. The state q_n that is the response at $t = t_n = \Delta_\mathrm{t} n$ due to the load $F(t, q(t))$ that has acted on the system for all $t \in [0, t_n]$ is then approximated as:

$$q_n \approx \sum_{\hat{n}=1}^{n} F_{\hat{n}-1}(q_{\hat{n}-1})\mathcal{L}_{n-\hat{n}} + F_{\hat{n}}(q_{\hat{n}})\mathcal{R}_{n-\hat{n}} \tag{4.26}$$

This implicit equation is solved at each time step and can be viewed as a discretized convolution integral. The iterative scheme used will be explained next, but first Eq. (4.26) is optimized to improve the computational speed and then generalized so it can account for more state components and more pseudo forces.

Eq. (4.26) sums over two terms due to the decomposition visualized in Fig. 4.6. This sum can be rewritten to improve the computation speed. Consider the response at the second time step, $n = 2$:

$$\begin{aligned} q_2 &\approx \left(F_{\hat{n}-1}(q_{\hat{n}-1})\mathcal{L}_{n-\hat{n}} + F_{\hat{n}}(q_{\hat{n}})\mathcal{R}_{n-\hat{n}}\right)\Big|_{\hat{n}=1} + \left(F_{\hat{n}-1}(q_{\hat{n}-1})\mathcal{L}_{n-\hat{n}} + F_{\hat{n}}(q_{\hat{n}})\mathcal{R}_{n-\hat{n}}\right)\Big|_{\hat{n}=2} \\ &= \left(F_0(q_0)\mathcal{L}_1 + F_1(q_1)\mathcal{R}_1\right) + \left(F_1(q_1)\mathcal{L}_0 + F_2(q_2)\mathcal{R}_0\right) \end{aligned} \tag{4.27}$$

Collecting all the loading proportional to F_0, F_1 and F_2 gives:

$$q_2 \approx F_0(q_0)\mathcal{L}_1 + F_1(q_1)\left(\mathcal{R}_1 + \mathcal{L}_0\right) + F_2(q_2)\mathcal{R}_0 \tag{4.28}$$

Since causality dictates that the response comes after the load, $\mathcal{L}_{-1} = 0$. By adding this term to Eq. (4.28):

$$q_2 \approx F_0(q_0)\mathcal{L}_1 + F_1(q_1)\left(\mathcal{R}_1 + \mathcal{L}_0\right) + F_2(q_2)\left(\mathcal{R}_0 + \mathcal{L}_{-1}\right) \tag{4.29}$$

it can be rewritten into the following generalized form:

$$q_n \approx F_0(q_0)\mathcal{L}_{n-1} + \sum_{\hat{n}=1}^{n} F_{\hat{n}}(q_{\hat{n}})\mathcal{T}_{n-\hat{n}} \tag{4.30}$$

where $\mathcal{T}_n$ is defined as (using Eqs. (4.24)):

$$\mathcal{T}_n = \mathcal{R}_n + \mathcal{L}_{n-1} = \frac{1}{2\pi}\int_{-\infty}^{\infty} \tilde{\mathcal{G}}(\omega)\tilde{\mathcal{T}}(\omega)\mathrm{e}^{\mathrm{i}\omega\Delta_\mathrm{t} n}\,\mathrm{d}\omega \tag{4.31}$$

and with $\tilde{\mathcal{T}}$ defined as:

$$\tilde{\mathcal{T}} = \frac{2}{\omega^2\Delta_\mathrm{t}}(1 - \mathrm{i}\sin(\omega\Delta_\mathrm{t})) \tag{4.32}$$

The advantage of Eq. (4.30) over Eq. (4.26) is that the addition has been removed, thereby improving the computational speed. Moreover, if no loading is present at $t = 0$, the IFT related to $\mathcal{L}$ does not have to be computed, which further improves the speed.

Eq. (4.30) only accounts for a single pseudo-force and, therefore, only a single nonlinear load $F(t, q(t))$, while the scheme has to be able to account for multiple nonlinear loads. Likewise, only a single state-component $q(t)$ was considered while multiple are needed. Now, let $\mathbf{q}(t)$ be the state-vector of length N_q that contains all the required state-components, the value of each state-component is then obtained by superimposing the contributions of all pseudo-forces:

$$\mathbf{q}_n \approx \sum_{i=1}^{N_\mathrm{F}} F_0^{(i)}(\mathbf{q}_0)\boldsymbol{\mathcal{L}}_{n-1}^{(i)} + \sum_{\hat{n}=1}^{n}\sum_{i=1}^{N_\mathrm{F}} F_{\hat{n}}^{(i)}(\mathbf{q}_{\hat{n}})\boldsymbol{\mathcal{T}}_{n-\hat{n}}^{(i)} \tag{4.33}$$

where i is the identifier of the pseudo-forces, N_F is the total number of pseudo-forces, $\boldsymbol{\mathcal{L}}_n^{(i)}$ and $\boldsymbol{\mathcal{T}}_n^{(i)}$ are based on Eq. (4.24) and Eq. (4.31) but now using the set of N_q Green's functions $\tilde{\boldsymbol{\mathcal{G}}}_i(\omega)$ that contain the frequency domain response of each state-component in $\mathbf{q}_n$ excited by the i^{th} pseudo-force.

In order to advance to the next time step, Eq. (4.33) is solved for $\mathbf{q}_n$. In agreement with the pseudo-force approach, this is done using an iterative scheme. The scheme is defined by the following recursive relation that starts at $j = 0$:

$$\mathbf{q}_n^{[j+1]} \approx \mathbf{q}_n^{[0]} + \sum_{i=1}^{N_\mathrm{F}} F_n^{(i)}(\mathbf{q}_n^{[j]})\boldsymbol{\mathcal{T}}_0^{(i)} \tag{4.34}$$

where the state-vector $\mathbf{q}_n^{[0]}$ contains the response at t_n due to the loading at all previous time steps:

$$\mathbf{q}_n^{[0]} = \sum_{i=1}^{N_\mathrm{F}} F_0^{(i)}(\mathbf{q}_0)\boldsymbol{\mathcal{L}}_{n-1}^{(i)} + \sum_{\hat{n}=1}^{n-1}\sum_{i=1}^{N_\mathrm{F}} F_{\hat{n}}^{(i)}(\mathbf{q}_{\hat{n}})\boldsymbol{\mathcal{T}}_{n-\hat{n}}^{(i)} \tag{4.35}$$

The rate of convergence of this iterative scheme is $\boldsymbol{\mathcal{T}}_0^{(i)}$, see App. D. Iterations continue until the specified tolerances are met for all entries of the state-vector $\mathbf{q}_n$. The scheme converges in two to five iterations depending on the tolerances used. No convergence problems were encountered while computing the results of this thesis.

Applying the time-integration scheme The time-integration scheme is now used to calculate the time domain response of $\mathcal{M}_{\text{HD}}$ as defined in Sec. 4.1.1.

For $\mathcal{M}_{\text{HD}}$ the set of pseudo-forces $F^{(i)}(t,\mathbf{q}(t))$ contains a total of $N_{\text{F}} = N_{\text{BEM}}+2$ forces:

$$F^{(i)}(t) = P_\alpha(t) = -\frac{\rho_{\text{w}}}{2}\left(\left(\frac{\partial\dot{\phi}^{(-i)}}{\partial x}\right)^2 + \left(\frac{\partial\dot{\phi}^{(-i)}}{\partial z}\right)^2\right) + F_{\text{ct,x}}\frac{\partial^2 w^{(-i)}}{\partial x^2}$$

$$\forall\ i = 1\,..\,N_{\text{BEM}} \tag{4.36a}$$

$$F^{(N_{\text{BEM}}+1)}(t) = F_{\text{ct,z}}\big|_{x=0} - \left(F_{\text{ct,x}}w'\right)\big|_{x=0} \tag{4.36b}$$

$$F^{(N_{\text{BEM}}+2)}(t) = M_{\text{ct}}\big|_{x=0} - \left(F_{\text{ct,x}}w\right)\big|_{x=0} \tag{4.36c}$$

where the superposition of the first N_{BEM} pseudo-forces results in the piecewise approximation of the nonlinear distributed forces, see Fig. 4.4, and the last two pseudo-forces account for the state-dependent loading at the contact, see Eq. (4.6). Because the distributed forces vary within each element, a representative force must be used for each element. This is computed using the average response within the i^{th} element, indicated with the superscript (i).

The state-dependent pseudo-forces $F^{(\alpha)}(t,\mathbf{q}(t))$ depend on several state-component. These are collected in the state-vector $\mathbf{q}(t)$ of length $N_{\text{q}} = 4+3N_{\text{BEM}}$:

$$\mathbf{q}(t) = \Bigg[w, w', \dot{w}, \dot{w}', \frac{\partial\dot{\phi}^{(-N_{\text{BEM}})}}{\partial x}\,..\,\frac{\partial\dot{\phi}^{(-1)}}{\partial x}, \frac{\partial\dot{\phi}^{(-N_{\text{BEM}})}}{\partial z}\,..\,\frac{\partial\dot{\phi}^{(-1)}}{\partial z}, \frac{\partial^2 w^{(-N_{\text{BEM}})}}{\partial x^2}\,..\,\frac{\partial^2 w^{(-1)}}{\partial x^2}\Bigg]^T \tag{4.37}$$

where w, w', $\dot{w}$, and $\dot{w}'$ are used to evaluate the pseudo-forces related to the contact loads, see Eqs. (4.36b) and (4.36c), and the average responses $\frac{\partial\dot{\phi}^{(\beta)}}{\partial x}$, $\frac{\partial\dot{\phi}^{(\beta)}}{\partial z}$ and $\frac{\partial^2 w^{(\beta)}}{\partial x^2}$ are needed to evaluate the N_{BEM} pseudo-forces related to the discretized nonlinear distributed forces, Eq. (4.36a).

All derivatives in $\mathbf{q}(t)$ are computed using finite differences of the corresponding (averaged) displacements. This is done because the IFT of the displacements converges significantly faster than the IFT of the derivatives. In particular, for the velocities a backward finite difference scheme is used. The order of the scheme starts at one and increases up to four as t_n increases. For the slope w' and for the curvature w'' a second order central difference scheme is used. Using finite differences to compute the derivatives increases the errors present in the displacements. Therefore, $\mathcal{L}_n^{(i)}$ and $\mathcal{T}_n^{(i)}$ need to be computed using strict tolerances and Δ_{t} and Δ_{x} need to be sufficiently small. Since all derivatives are computed using finite differences, these state-components no longer have to be computed using the convolution that is embedded in Eq. (4.34). Consequently, the following reduced state-vector of length $\hat{N}_\beta$ is introduced that excludes these state-components:

$$\hat{\mathbf{q}}(t) = \left[w, \frac{\partial\phi^{(-N_{\text{BEM}})}}{\partial x}\,..\,\frac{\partial\phi^{(-1)}}{\partial x}, \frac{\partial\phi^{(-N_{\text{BEM}})}}{\partial z}\,..\,\frac{\partial\phi^{(-1)}}{\partial z}\right]^T \tag{4.38}$$

The full state-vector $\mathbf{q}_n$ can then be computed from $\hat{\mathbf{q}}_n$ using the relevant finite difference relations. Eq. (4.34) is updated accordingly:

$$\begin{aligned}
&\text{Starting at } j = 0: \\
&1.\ \mathbf{q}_n^{[j]} \approx \mathbf{D}(\hat{\mathbf{q}}_n^{[j]}, \hat{\mathbf{q}}_{n-1}^{[j]} \,..\, \hat{\mathbf{q}}_{n-d}^{[j]}) && \text{(4.39a)} \\
&2.\ \hat{\mathbf{q}}_n^{[j+1]} \approx \hat{\mathbf{q}}_n^{[0]} + \sum_{i=1}^{N_\mathrm{F}} F_n^{(i)}(\mathbf{q}_n^{[j]}) \boldsymbol{\mathcal{T}}_0^{(i)} && \text{(4.39b)}
\end{aligned}$$

where the finite difference operator $\mathbf{D}$ computes $\mathbf{q}_n^{[j]}$ based on the current as well as the last d reduced state-vectors. d starts at 0 for $n = 1$ and increases up to 4 in order to have enough data points to evaluate the fourth order finite difference scheme used for computing the velocities.

For each state-component $q(t)$, the contribution of all pseudo-forces must be superimposed. This means that a total of $\hat{N}_\beta \times N_\mathrm{F}$ frequency domain Green's functions are needed to relate all pseudo-forces in $F^{(i)}(t, \mathbf{q}(t))$ with all state-components in $\hat{\mathbf{q}}(t)$. These Green's functions are based on $\tilde{\phi}_\alpha$, given by Eq. (4.9):

$$\begin{aligned}
\tilde{\boldsymbol{\mathcal{G}}}_i(\omega) = \Big[&\tilde{\phi}_{-i}(0,0,\omega), \frac{\partial \tilde{\phi}_{-i}^{(-N_\mathrm{BEM})}(0,\omega)}{\partial x} \,..\, \frac{\partial \tilde{\phi}_{-i}^{(-1)}(0,\omega)}{\partial x}, \\
&\frac{\partial \tilde{\phi}_{-i}^{(-N_\mathrm{BEM})}(0,\omega)}{\partial z} \,..\, \frac{\partial \tilde{\phi}_{-i}^{(-1)}(0,\omega)}{\partial z} \Big]^T \quad \forall\ i = 1 \,..\, N_\mathrm{F}
\end{aligned} \tag{4.40}$$

$\tilde{\phi}_\alpha(x,z,\omega)$ is a superposition of the response to three generalized forces: P_GF, F_GF and M_GF. For each specific value of i, only one of these three forces is activated, according to the following definition:

$$\begin{aligned}
&\text{for } i = 1 \,..\, N_\mathrm{BEM}, \quad P_\mathrm{GF}^{(-)} = 1, F_\mathrm{GF} = 0, M_\mathrm{GF} = 0 \\
&\text{for } i = N_\mathrm{BEM} + 1, \quad P_\mathrm{GF}^{(-)} = 0, F_\mathrm{GF} = 1, M_\mathrm{GF} = 0 \\
&\text{for } i = N_\mathrm{BEM} + 2, \quad P_\mathrm{GF}^{(-)} = 0, F_\mathrm{GF} = 0, M_\mathrm{GF} = 1
\end{aligned} \tag{4.41}$$

and the Green's function of the mean horizontal displacement of the fluid's surface within element $\beta = -\infty \,..\, 0$ is computed using (see Eq. (A.55)):

$$\begin{aligned}
\frac{\partial \tilde{\phi}_\alpha^{(\beta)}(0,\omega)}{\partial x} &= \frac{1}{2\Delta_\mathrm{x}} \int_{x_\beta^-}^{x_\beta^+} \frac{\partial \tilde{\phi}_\alpha(x,0,\omega)}{\partial x} \,\mathrm{d}x \qquad \text{(4.42)} \\
&= -\frac{P_\mathrm{GF}^{(-)}}{\rho_\mathrm{w} g} \frac{1}{2\Delta_\mathrm{x}} \sum_{n=0}^{N_\mathrm{k}+2} \gamma_n \bar{Q}_n^{-1} \bar{I}'_{\alpha,\beta,n} \bar{Z}_n(0) - \frac{\mathrm{i}}{\Delta_\mathrm{x}} \sum_{n=1}^{N_\mathrm{k}+2} \bar{a}_{\alpha,n} \sin(\bar{k}_n \Delta_\mathrm{x}) \mathrm{e}^{-\mathrm{i}\bar{k}_n x_\beta} \bar{Z}_n(0)
\end{aligned}$$

where $x_\beta^- = x_\beta - \Delta_\mathrm{x}$, $x_\beta^+ = x_\beta + \Delta_\mathrm{x}$ and $\bar{I}'_{\alpha,\beta,n}$ is given by (see Eq. (A.57)):

$$\bar{I}'_{\alpha,\beta,n} = \int_{x_\beta^-}^{x_\beta^+} \frac{\partial \bar{I}'_{\alpha,n}(x)}{\partial x} \,\mathrm{d}x = \begin{cases} 2\,\mathrm{sgn}(\beta - \alpha)(1 - \cos(2\bar{k}_n \Delta_\mathrm{x}))\mathrm{e}^{\mathrm{i}\bar{k}_n |x_\beta - x_\alpha|}, & \text{if } \beta \neq \alpha \\ 0, & \text{if } \beta = \alpha \end{cases} \tag{4.43}$$

The Green's function of the mean vertical displacement of both the ice and the fluid's surface within element β is computed using (see Eq. (A.62)):

$$\begin{aligned}\frac{\partial\tilde{\phi}_\alpha^{(\beta)}(0,\omega)}{\partial z} &= \frac{1}{2\Delta_x}\int_{x_\beta^-}^{x_\beta^+}\frac{\partial\tilde{\phi}_\alpha(0,\omega)}{\partial z}\,\mathrm{d}x \\ &= -\frac{P_{\mathrm{GF}}^{(-)}}{\rho_w g}\frac{1}{2\Delta_x}\sum_{n=0}^{N_k+2}\gamma_n\bar{Q}_n^{-1}\bar{I}_{\alpha,\beta,n}\bar{Z}_n'(0)+\frac{1}{\Delta_x}\sum_{n=1}^{N_k+2}\bar{a}_{\alpha,n}\frac{\sin(\bar{k}_n\Delta_x)}{\bar{k}_n\Delta_x}\mathrm{e}^{-\mathrm{i}\bar{k}_n x_\beta}\bar{Z}_n'(0)\end{aligned} \tag{4.44}$$

where $\bar{I}_{\alpha,\beta,n}$ is given by (see Eq. (A.63)):

$$\bar{I}_{\alpha,\beta,n}=\int_{x_\beta^-}^{x_\beta^+}I_{\alpha,n}(x)\,\mathrm{d}x=\frac{-4}{\bar{k}_n\Delta_x}\begin{cases}\sin(\Delta_x\bar{k}_n)\mathrm{e}^{\mathrm{i}\Delta_x\bar{k}_n}, & \text{if } \alpha=\beta\\ \mathrm{i}\sin^2(\Delta_x\bar{k}_n)\mathrm{e}^{2\mathrm{i}\Delta_x\bar{k}_n|\alpha-\beta|}, & \text{if } \alpha\neq\beta\end{cases} \tag{4.45}$$

Employing the above-described procedure, the breaking length of the ice floe, which is a key output the chapter focuses upon, is computed using cubic spline interpolation of the axial stress of each element.

4.2. VALIDATION

The validation of the time-integration scheme is addressed first, followed by a validation of $\mathcal{M}_{\mathrm{HD}}$, the proposed hydrodynamic ISI model.

4.2.1. VALIDATION OF THE TIME-INTEGRATION SCHEME

In order to validate the time-integration scheme, the analytical time-domain solution of a floating plate obtained by Zhao and Dempsey [202] is chosen as a benchmark. They considered, in a 2D context, the response of an infinite ice floe floating on a finite depth fluid layer to the load $F(t)=\delta(x)\mathcal{H}(t)$. The ice floe is modeled as a Kirchhoff-Love plate, the fluid is described by the Laplace equation and its pressure on the ice by the linearized Bernoulli equation.

The approach presented in the current chapter was applied to the same model. The following set of parameters was used for this validation case: $h=1$ m, $\rho_i=925$ kg/m^3, $E=(10h)^4\rho_w g/(h^3/12)$ Pa, $\nu=0.3$, $\rho_w=1025$ kg/m^3, $g=9.81$ m/s^2, $H=4l$ where $l=\sqrt[4]{\delta}=\sqrt[4]{D/(\rho_w g)}$, $N_{\mathrm{BEM}}=40$, $2\Delta_x=4l/N_{\mathrm{BEM}}$, $\Delta_t=10^{-3}$ s and $N_k=500$. The value of all numerical parameters are based on extensive convergence studies.

Application of the procedure introduced in this chapter results in a single state-independent pseudo-force: $F^{(1)}(t)=\mathcal{H}(t)$. The state-vector $\mathbf{q}(t)$ contains the response of the plate as a function of $\bar{x}=x/l$ with l defined in Eq. (4.19), at the values shown in Fig. 4.7. The corresponding Green functions are approximated by taking $\tilde{\phi}_\alpha^{(\mathrm{p})}$, given by Eq. (4.10), letting Δ_x approach zero and evaluating this function at the relevant values of $\bar{x}$:

$$\tilde{\mathcal{G}}(\bar{x},\omega)=\lim_{\Delta_x\to 0}\tilde{\phi}_{-1/2}^{(\mathrm{p})}(\bar{x},0,\omega) \tag{4.46}$$

where the evaluation at $\alpha=-1/2$ assures that the load is applied at $\bar{x}=0$.

Fig. 2.a of Zhao and Dempsey [202] has been reproduced in Fig. 4.7. This figure shows the time domain response of the plate at several locations and moments in time. The figure shows that the results of both approaches agree very well.

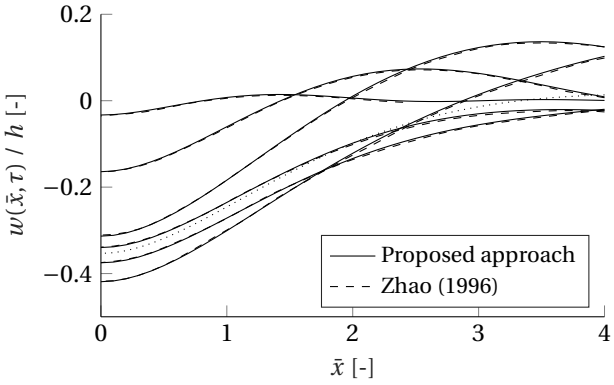

Figure 4.7: The normalized, transient, vertical response of the ice floe. The solid lines show the response of the proposed model and the dashed lines are the results from Zhao and Dempsey [202]. The lines, from top to bottom at $\bar{x} = 0$, are evaluations at $\tau = t\sqrt{g/l} = \{0.25, 1, 2, 8, 6, 4\}$ respectively. The dotted line shows the static response.

4.2.2. VALIDATION OF THE ISI MODEL

In order to validate $\mathcal{M}_{\text{HD}}$, its predictions are compared with the experimental work done by Valanto [203]. In Valanto's experimental campaign, the 2D interaction between level ice and a downward-sloping plate was studied for a range of ice velocities. The measurements of interest are the maximum horizontal contact force as a function of the ice velocity $F_{\max}(V_{\text{ice}})$ and the breaking length as a function of the ice velocity $l_{\text{br}}(V_{\text{ice}})$.

In correspondence with the experiments, the following parameters were used in the numerical procedure (see also [204]): $h = 1/33.33$ m, $\rho_{\text{i}} = 916$ kg/m^3, $\rho_{\text{w}} = 1025$ kg/m^3, $g = 9.81$ m/s^2, $H = 1$ m, $E = 140 \times 10^6$ Pa, $\nu = 0.3$, $\sigma_{\text{c}} = 11 \times 10^3$ Pa, $\sigma_{\text{fl}} = 25 \times 10^3$ Pa, ice-steel friction coefficient $\xi = 0.1$ [–], width $b = 0.340$ m, $\theta = 15°$ and $V_{\text{ice}} = [0, 0.5]$ m/s. $N_{\text{BEM}} = 60$, $c_1 = 1.25$, $\Delta_{\text{t}} = 5 \times 10^{-4}$ s and $N_{\text{k}} = 250$.

In the experimental setup of Valanto, the geometry of the icebreaker was accounted for while in the proposed model it is not. To mimic the structure's presence, a semi-infinite problem is considered, see Fig. 4.8. This approach was also adopted by other researchers who used this case for validation [203, 204]. All equations presented in Sec. 4.1 remain valid with one exception. The set of N_{k} equations Eq. (4.17c) that assures the continuity of the fluid's displacement and pressure at $x = 0$ has to be replaced by the following set of equations:

$$\sum_{n=1}^{N_{\text{k}}+2} -a_{\alpha,n} k_n \frac{\lambda_n - \bar{\lambda}_j}{k_n - \bar{k}_j} = \frac{P_{\text{GF}}}{\rho_{\text{w}} g} \sum_{n=1}^{N_{\text{k}}+2} Q_n^{-1} k_n I'_{\alpha,n}(0) \frac{\lambda_n - \bar{\lambda}_j}{k_n^2 - \bar{k}_j^2}$$
$$\forall\ j = 1 \,..\, N_{\text{k}} \tag{4.47}$$

This set assures that the horizontal displacement of the fluid is zero at $x = 0 \cap z \in (-H, 0)$.

Breaking length In Fig. 4.9, the breaking length as a function of ice velocity $l_{\text{br}}(V_{\text{ice}})$ as predicted by the semi-infinite version of the proposed ISI model is compared with the measurements by Valanto [203].

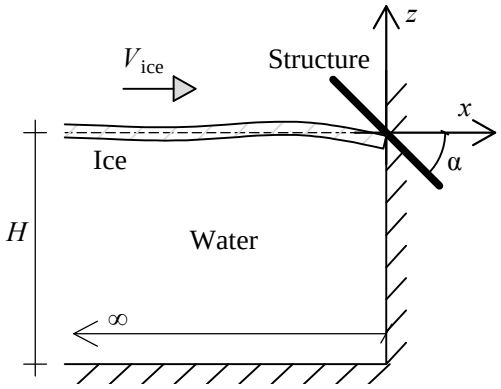

Figure 4.8: For validation a semi-infinite model is considered.

Overall, the predictions of $\mathcal{M}_{\text{HD}}$ agree well with the experimental data. At high velocities, $\mathcal{M}_{\text{HD}}$ predicts slightly smaller breaking lengths. A possible explanation for this discrepancy could be that during the experiments the ice slab, which was 334 to 340 mm wide, had two slits running alongside it, each with a width of 5-8 mm. As fluid can flow into these slits, their presence alleviates the build-up of fluid pressure under the ice. This phenomenon is discussed in Valanto [203]. Reducing the hydrodynamic pressure means that the ice experiences less resistance as it deflects downwards, thereby reducing the bending stresses generated. This, in turn, causes the ice to fail later during the interaction process, thereby increasing the breaking length.

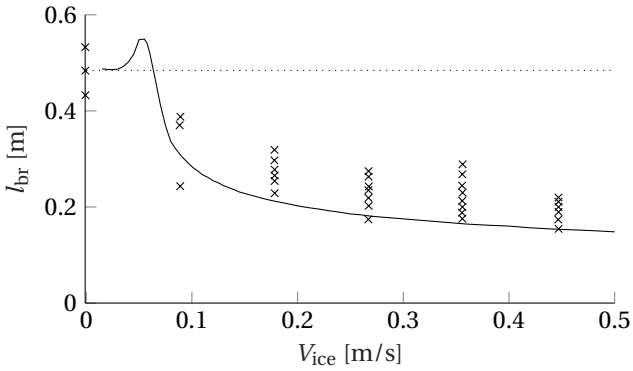

Figure 4.9: The breaking length as a function of the ice velocity $l_{\text{br}}(V_{\text{ice}})$. The crosses represent the experimental data. The curve shows the values predicted by the proposed model. The dotted line is the static breaking length.

At low velocities, $\mathcal{M}_{\text{HD}}$ predicts a velocity range wherein the ice fails statically. No experiments were done in this range and so this phenomenon cannot be validated. The transition from quasi-static to dynamic failure around 0.07 m/s in Fig. 4.9 is studied in detail in the next section.

Maximum horizontal contact force The maximum horizontal contact force $F_{\max}(V_{\text{ice}})$ as a function of ice velocity predicted by the proposed model is compared against the experimental data by Valanto [203] in Fig. 4.10. At lower velocities, the $F_{\max}$ predicted by the proposed model agrees well with the measured ones but as the ice velocity increases, the model increasingly underpredicts $F_{\max}$. A possible explanation for this could be that the horizontal component of the fluid pressure due to the stationary flow around the hull is not accounted for in the proposed model.

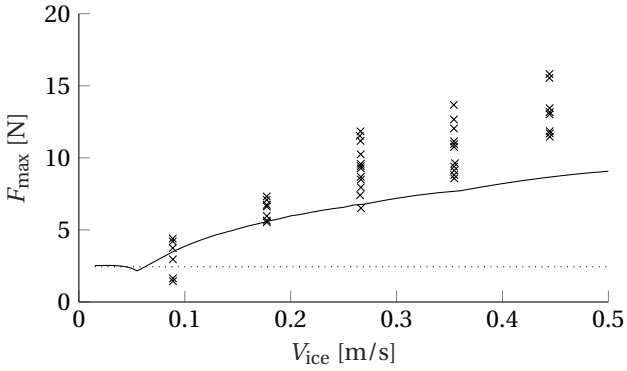

Figure 4.10: $F_{\max}$ for a range of ice velocities. The crosses show the experimental data. The values predicted by the proposed model are shown by the curve. The dotted line is the static $F_{\max}$.

4.3. RESULTS

In this section, the results based on the predictions of $\mathcal{M}_{\text{HS}}$ and $\mathcal{M}_{\text{HD}}$ are presented. The focus is first placed on assessing the relative importance of the various forces that act on the ice. Thereafter, the interdependence of the temporal development of the contact force and the dependence of the breaking length on the ice velocity l_{br} is studied. Finally, the limitations of $\mathcal{M}_{\text{HS}}$ are addressed.

The results presented in this section have been computed using the following set of full-scale parameters [205]: $h = 1$ m, $\rho_{\text{i}} = 925$ kg/m^3, $\rho_{\text{w}} = 1025$ kg/m^3, $g = 9.81$ m/s^2, $H = 100$ m, $E = 5$ GPa, $\nu = 0.3$, $\sigma_{\text{c}} = 600$ kPa, $\sigma_{\text{fl}} = 500$ kPa, ice-steel friction coefficient $\xi = 0.1$ [–], hull angle $\theta = 45°$ and $V_{\text{ice}} = [0, 0.5]$ m/s. The value of all numerical parameters are based on extensive convergence studies and are: $N_{\text{BEM}} = 60$, $c_1 = 1.25$, $\Delta_{\text{t}} = 10^{-3}$ s, $N_{\text{k}} = 250$.

4.3.1. DETERMINING THE FACTORS OF INFLUENCE FOR ISI

In this model, there are a total of seven forces that affect the dynamic equilibrium of the ice floe. The terms representing these forces together form the equation of motion of the ice floe, Eq. (4.4), and are related to: the inertia of the ice floe, the rotational inertia of the ice floe, bending of the ice floe, axial compression, hydrostatic pressure p_{HS}, linear hydrodynamic pressure p_{HD} and nonlinear hydrodynamic pressure p_{NLHD}.

In order to determine the relative importance of the above-mentioned forces, the contribution of each of the seven terms to the balance of forces is studied. This is done

by using the following measure:

$$R_j = \frac{\int_0^{t_{\text{fail}}} \int_{-L_{\text{BEM}}}^{0} |p_j(x,0,t)| \, \mathrm{d}x \, \mathrm{d}t}{\sum_{i=1}^{7} \int_0^{t_{\text{fail}}} \int_{-L_{\text{BEM}}}^{0} |p_i(x,0,t)| \, \mathrm{d}x \, \mathrm{d}t} \tag{4.48}$$

where i and j imply indexing over the seven terms listed before. The absolute magnitude of each term is averaged in both space, for $x \in [-L_{\text{BEM}}, 0]$, and in time, starting from $t = 0$ until the ice fails in bending at $t = t_{\text{fail}}$. This average contribution is then normalized, thereby characterizing the significance of each term relative to all the other terms. The left graph in Fig. 4.11 shows the relative importance R_j of each of the seven terms.

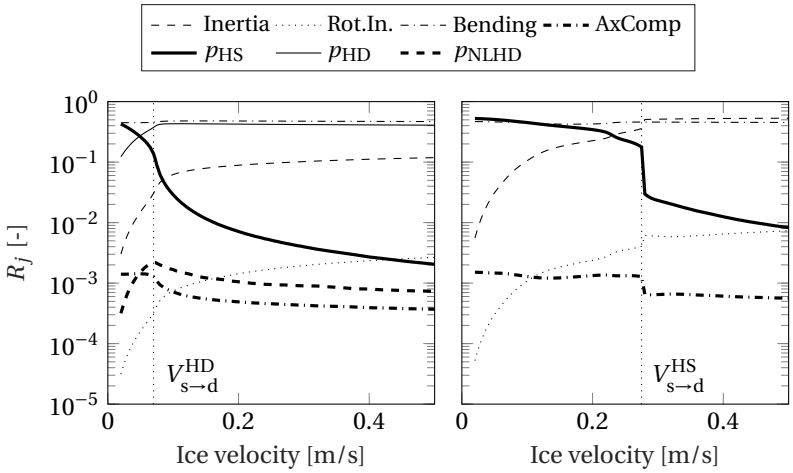

Figure 4.11: The relative importance R_j of all seven terms. Left: $\mathcal{M}_{\text{HD}}$. Right: $\mathcal{M}_{\text{HS}}$. The vertical dotted lines indicate the transition velocity $V_{\text{s}\to\text{d}}$ that separates the quasi-static and dynamic interactions. $V_{\text{s}\to\text{d}}$ is discussed in detail in Sec. 4.3.3.

The pressure that the fluid exerts on the ice floe is described by three terms forming the right-hand side of Eq. (4.3). The hydrodynamic component of this pressure is given by two of these terms: $p_{\text{HD}} = -\rho_{\text{w}}\dot{\phi}$ and $p_{\text{NLHD}} = -\rho_{\text{w}}\frac{1}{2}v^2$. The left graph in Fig. 4.11 shows that the relative importance of p_{NLHD} is about thousand times smaller than the relative importance of p_{HD}. All of the hydrodynamic effects can thus be attributed to p_{HD}. From this, it can be concluded that p_{NLHD} is not a factor of influence for ISI. Since p_{NLHD} incurs a significant calculation cost, it is ignored in the remainder of this thesis.

Of the four terms related to the internal forces in the ice floe, two have a marginal contribution, namely; the rotational inertia of the ice floe and the axial compression. The insignificance of rotational inertia was also found previously by Fox and Squire [206] when studying the transmission of surface waves into a semi-infinite ice sheet. These two terms are also ignored in the remainder of this chapter.

Based on these findings, it can be concluded that of the seven terms studied, only four terms are important for ISI. Listed in the order of importance, the factors of influence for ISI are thus: bending of the ice floe, the linear hydrodynamic pressure p_{HD}, the

hydrostatic pressure p_{HS} and the inertia of the ice floe. This confirms the qualitative findings by Valanto [203].

4.3.2. BALANCE OF FORCES IN THE ICE FLOE

Four factors of significant influence were identified in the previous subsection. It is still to understand, however, how these four terms form a balance of forces in the ice floe and how hydrodynamics affects the balance. The balance of forces is first studied by reexamining the relative importance in Fig. 4.11. Thereafter, the variation of the balance in space and time is studied.

Balance of forces: averages. The left graph in Fig. 4.11 was computed with $\mathcal{M}_{\mathrm{HD}}$ while the graph on the right was computed with $\mathcal{M}_{\mathrm{HS}}$ that was obtained by disabling p_{HD} and p_{NLHD}. The dotted vertical lines indicate the transition velocity $V_{\mathrm{s}\to\mathrm{d}}$. Interactions with an ice velocity $V_{\mathrm{ice}} < V_{\mathrm{s}\to\mathrm{d}}$ are classified as quasi-static while those with $V_{\mathrm{ice}} > V_{\mathrm{s}\to\mathrm{d}}$ are classified as dynamic. The transition velocity $V_{\mathrm{s}\to\mathrm{d}}$ is studied in Sec. 4.3.3.

First, consider $\mathcal{M}_{\mathrm{HD}}$ shown in the left graph. At the ice velocity $V_{\mathrm{ice}} = 0$, the balance is mainly between bending and p_{HS}. As V_{ice} increases, the importance of p_{HS} quickly reduces while the importance of p_{HD}, i.e. the inertia of the fluid, increases. In the dynamic regime, the balance is mainly between p_{HD} and bending. Together they account for nearly the complete force balance. The inertia of the ice plays only a minor role, contributing 10% or less with its maximum contribution at high velocities.

Next, consider the predictions of $\mathcal{M}_{\mathrm{HS}}$ shown on the right. Although the graph appears different, the trends are in fact similar. At low velocities, bending is again balanced by p_{HS} and at high velocities, it is again balanced by inertia. However, as the inertia of the fluid is not accounted for, bending is now balanced by the inertia of the ice floe. In addition, the transition from quasi-static to dynamic interaction occurs at a much higher velocity, $V^{\mathrm{HD}}_{\mathrm{s}\to\mathrm{d}} = 0.275$ m/s while $V^{\mathrm{HS}}_{\mathrm{s}\to\mathrm{d}} = 0.07$ m/s. From this, it can be concluded that p_{HD} adds a significant amount of inertia to the ice.

Balance of forces: temporal and spatial variation. The balance of pressure is studied again but now as a function of space and time. In the previous subsection, two nonlinear terms, namely p_{NLHD} and axial compression, were found to be insignificant. The only remaining nonlinearity is the contact model, which is piecewise linear in time. Despite the presence of the latter nonlinearity, all four significant forces show to be almost perfectly proportional to the ice velocity. This property was also taken advantage of by Wang and Poh [204] with their Rapid Analysis Strategy.

The proportionality of the four significant forces to the ice velocity allows them to be visualized for a range of ice velocities in a single figure. This is done in Fig. 4.12, which shows the dependence of the normalized by the ice velocity forces on time. For each ice velocity, the graphs are valid until the time t_{fail} at which failure of the ice occurs. The relation between t_{fail} and the ice velocity is shown in Fig. 4.13.

The response of $\mathcal{M}_{\mathrm{HD}}$ is shown in Fig. 4.12 on the left. Initially, the balance is between bending and inertia. The inertia of the fluid contributes significantly more, up to ten times as much as the inertia of the ice. This minor contribution of the ice's inertia was

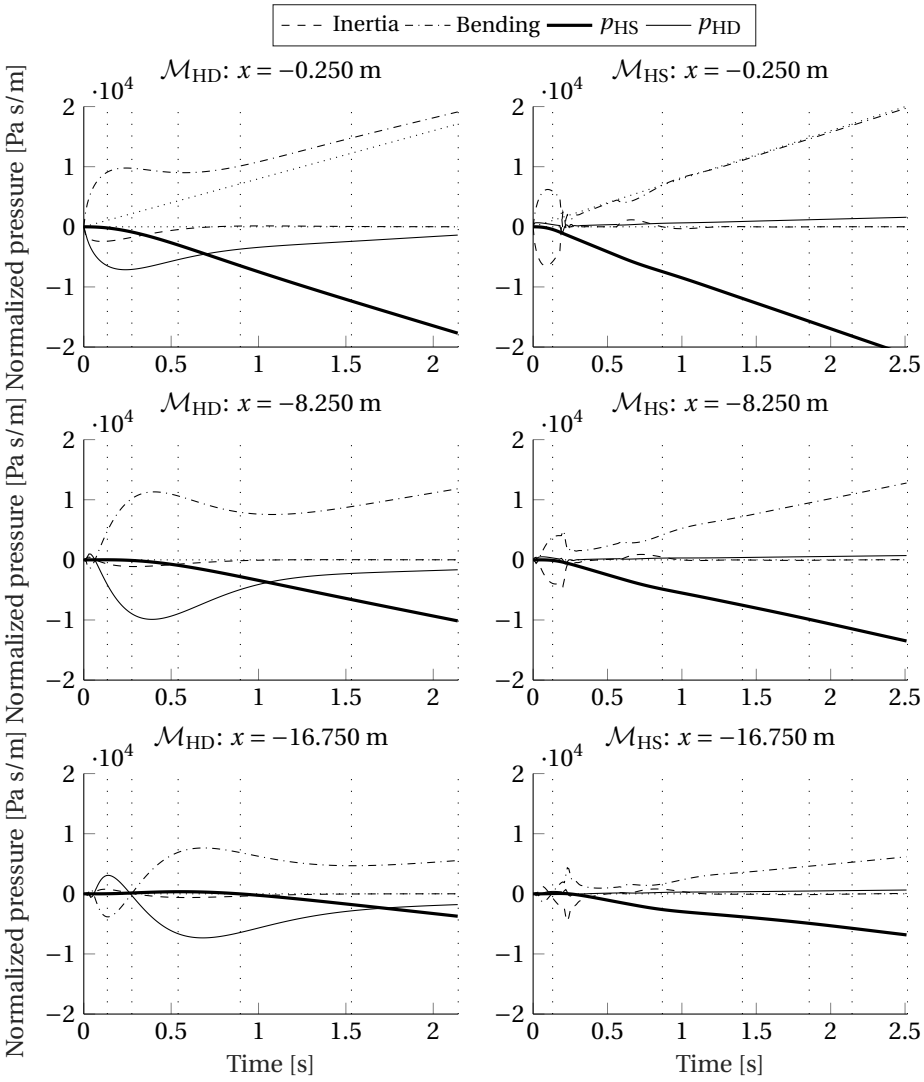

Figure 4.12: The four important factors that act on the ice floe at three locations, normalized by the ice velocity. A zero-line and the static bending pressure are included for reference with the dotted sloped lines. The vertical loosely dotted lines indicate the failure time t_{fail} at the following ice velocities (from left to right): 0.5, 0.2, 0.1, 0.08, 0.07 and 0.06 m/s.

also observed by other authors [203, 207, 208]. p_{HS} does not contribute during the transient phase of the interaction and is only relevant in the steady-state regime, in which the normalized forces increase quasi-linearly in time. It is interesting to note that the bending stresses have a local maximum in the transient interaction phase. The maximum is followed by a local minimum as the system transitions into the steady-state regime. Similarly, p_{HD} also peaks during the transient interaction phase and then slowly decays

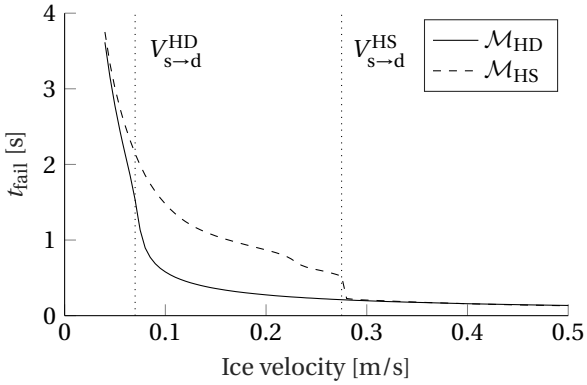

Figure 4.13: The failure time t_{fail} of both models. The vertical dotted lines indicate the transition velocity $V_{\text{s}\to\text{d}}$.

back to zero, indicating that the action p_{HD} is of the added damping type. This was also observed by Zhao and Dempsey [202]. This effective damping is due to the energy being radiated in the form of flexural-gravity waves.

Comparing the graphs of $\mathcal{M}_{\text{HS}}$ (the right part of Fig. 4.12) and $\mathcal{M}_{\text{HD}}$ one can observe markedly different behavior. Although the graphs of $\mathcal{M}_{\text{HS}}$ contain some noise introduced at the transient phase of the interaction, the trends are very clear. The transient phase of $\mathcal{M}_{\text{HD}}$ lasts significantly longer and the bending stresses experienced during this phase are also much larger. Both effects imply that p_{HD} adds a significant amount of inertia to the ice. The drop in the bending stress after the peak is also more abrupt for $\mathcal{M}_{\text{HS}}$.

Lastly, two observations can be made from the times of failure t_{fail} of both models shown in Fig. 4.13. Firstly, as V_{ice} increases, the duration of the interaction decreases, meaning that the role of the transient interaction phase becomes more and more significant as the ice velocity increases. This is in agreement with the trends seen in Fig. 4.11. Second, as the bending stresses generated during the transient interaction phase are much lower for $\mathcal{M}_{\text{HS}}$, even at high ice velocities the ice fails statically.

4.3.3. THE RELATION BETWEEN CONTACT FORCE AND BREAKING LENGTH

Understanding the relation between the temporal development of the contact force $F_{\text{ct}}(t)$ and velocity-dependence of the breaking length $l_{\text{br}}(V_{\text{ice}})$ requires a thorough understanding of the evolution of the contact force and the interaction process. Because of this, a detailed study on the temporal development of the contact force is carried out first. Following this, the effect of hydrodynamics on the contact force F_{ct} is studied. Lastly, $l_{\text{br}}(V_{\text{ice}})$ is studied as well as how it is related to the contact force and how it is affected by hydrodynamics.

The temporal development of the contact force. A typical profile of the contact force $F_{\text{ct}}(t)$ is shown in Fig. 4.14. This figure shows two transitions, depicted by the dashed vertical lines. At these transitions, the contact model switches between its two modes.

In the crushing mode M_{cr} the ice crushes at the contact with the floater and in the sliding mode M_{sl} the ice slides along the hull of the floater without crushing:

$$F_{\mathrm{ct}}(t) = \begin{cases} \sigma_{\mathrm{c}} A_{\mathrm{ct}}(t) & \text{when crushing } (\mathsf{M}_{\mathrm{cr}}) \\ \sigma_{\mathrm{ct}}(t) A^*_{\mathrm{ct}} & \text{when sliding } (\mathsf{M}_{\mathrm{sl}}) \end{cases} \tag{4.49}$$

where $F_{\mathrm{ct}}(t) = \sqrt{(F_{\mathrm{ct,x}}(t))^2 + (F_{\mathrm{ct,z}}(t))^2}$, σ_{c} is the representative crushing strength of the ice, $A_{\mathrm{ct}}(t)$ is the variable contact area between ice and floater in the crushing mode, $\sigma_{\mathrm{ct}}(t)$ is the variable contact stress while sliding and A^*_{ct} is the fixed contact area in sliding.

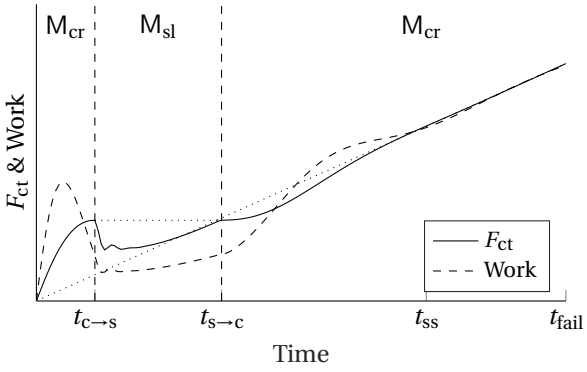

Figure 4.14: An illustration of how the contact force F_{ct}, depicted with the solid curve, develops during a typical interaction. The work done by the contact force is shown by the dashed curve. Both signals are normalized. The contact force based on a static equilibrium is depicted with the dotted diagonal line. The dashed vertical lines delimit the two modes of the contact model.

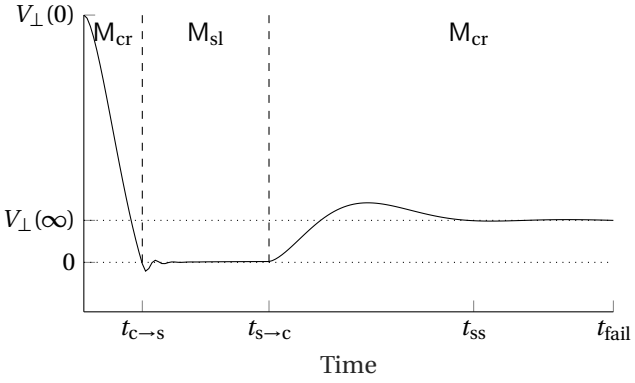

Figure 4.15: The speed at which the ice penetrates into the structure $V_{\mathrm{pen}}(t)$ during a typical interaction. The steady-state penetration speed $V_{\mathrm{pen}}(\infty)$ and a zero line are included for reference. The dashed vertical lines delimit the two modes of the contact model.

At the start of the interaction, the contact area is very small which means that even a

relatively small contact force causes crushing of the ice. During the transient interaction phase $t \in [0, t_{c\to s}]$, a large amount of work has to be performed to align the ice's tip-velocity with the structure's hull. This work is performed by the contact force during this transient phase and results in a peak in the force prior to $t_{c\to s}$ (see Fig. 4.14). Therefore, most of this work transfers to the kinetic energy in both ice floe and fluid. Starting from $t_{c\to s}$, the floe's edge velocity has aligned itself with the structure and the required work drops. Consequently, the contact force drops as well. After this moment in time, most of the work done by the contact force is used to increase the potential energy of the ice and fluid, namely by increasing the curvature of the ice floe (bending) and by increasing the hydrostatic draft of the ice floe.

The alignment of the floe's edge velocity with the structure is illustrated in Fig. 4.15. This figure shows the normal to the structure component $V_\perp(t)$ of the velocity of the edge of the ice floe. The interaction begins with $V_\perp(t)$ that is dictated by the initial conditions: $V_\perp(0) = V_{ice}\sin(\theta)$. Immediately after, $V_\perp(t)$ experiences a rapid drop and reaches zero at $t_{c\to s}$ as can be seen in Fig. 4.14. At this moment, the contact force starts to decrease and, consequently, the contact model experiences transition into the sliding mode M_{sl}. While in this mode, the contact area remains constant at $A^*_{ct} = A_{ct}(t_{c\to s})$ and the contact stress $\sigma_{ct}(t)$ becomes variable: $\sigma_{ct}(t) \in [0, \sigma_c)$. $\sigma_{ct}(t)$ is ideally computed using Lagrangian Multipliers but this approach gave numerical issues. To avoid these, a very stiff contact spring was used to approximate a rigid contact. This finite stiffness results in $V_\perp(t)$ becoming slightly negative just after $t_{c\to s}$.

The contact model remains in M_{sl} until $\sigma_{ct}(t) = \sigma_c$. This happens at $t_{s\to c}$ and results in a second transient stage. After this, the ice transitions into the steady-state regime. It is important to note that $V_\perp(t)$ converges to a constant value rather than to zero. This is because the contact force has to continue to grow in order to balance with the increasing bending and hydrostatic forces, as shown in Fig. 4.14.

Hydrodynamic influence on the contact force. Fig. 4.16 shows a comparison between the contact force F_{ct} predicted by $\mathcal{M}_{HS}$ and $\mathcal{M}_{HD}$. On the left, $F_{ct}(t)$ of both models is shown and on the right $V_\perp(t)$.

Both graphs show that hydrodynamics greatly increases the resistance provided by the water against the bending of the ice floe. Analyzing the contact force shown in Fig. 4.16 on the left, this is apparent in two ways. Firstly, the force peak during the transient interaction phase is greatly increased by hydrodynamics, which is indicative of increased inertia. Second, the ensuing transition to the steady-state equilibrium is much slower for $\mathcal{M}_{HD}$, which is indicative of increased damping. Both effects can also be observed in Figs. 4.11 and 4.12.

Looking at $V_\perp(t)$ on the right in the same figure, similar conclusions can be drawn. $V_\perp$ of $\mathcal{M}_{HS}$ overshoots the static equilibrium and predicts sliding (M_{sl} regime) for $t \in [0.18, 0.57]$ s. $V_\perp$ of $\mathcal{M}_{HD}$ changes much slower, again indicative of increased inertia and never enters M_{sl}. Within $\mathcal{M}_{HD}$, $V_\perp$ does overshoot $V_\perp(\infty)$ but does so only a little. This is similar to a system with significant, but less than critical, damping. This is in stark contrast to $\mathcal{M}_{HS}$ that exhibits a lightly damped response.

To conclude, hydrodynamics adds a significant amount of resistance to the ice floe in the form of added mass and damping. This increases the contact force during the

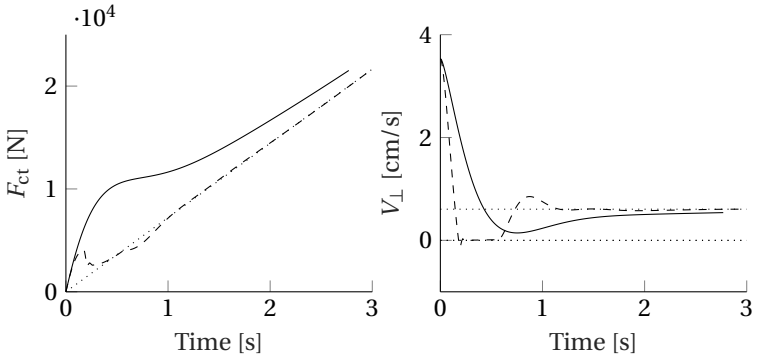

Figure 4.16: $F_{ct}(t)$ (left) and $V_{\perp}(t)$ (right) for $\mathcal{M}_{HS}$ (dashed) and $\mathcal{M}_{HD}$ (solid). The dotted line on the left shows the static contact force. On the right a zero line and $V_{\perp}(\infty)$ are included for reference. V_{ice} was set to 0.05 m/s for this figure.

transient interaction phase and results in a highly damped behavior of the ice floe.

The relation between breaking length and contact force. Next, the breaking length as a function of ice velocity $l_{br}(V_{ice})$ is analyzed in order to understand its relationship with the temporal development of the contact force $F_{ct}(t)$ studied previously. Special attention is again given to the effect of hydrodynamics on this relation. $l_{br}(V_{ice})$ is shown in Fig. 4.17 for both $\mathcal{M}_{HD}$ and $\mathcal{M}_{HS}$.

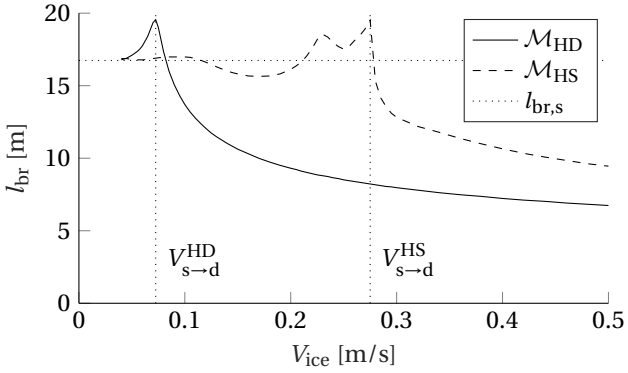

Figure 4.17: $l_{br}(V_{ice})$ as predicted by both models. $l_{br,s} = l_{br}(0)$ was computed using Eq. (4.19). The dotted vertical lines indicate $V_{s\to d}$ of each model.

Fig. 4.17 reveals three interesting features. Firstly, it is clear that for both models $l_{br}(V_{ice})$ behaves distinctly different at lower and higher ice velocities. The transition between the two regimes occurs at the transition velocity $V_{s\to d}$, indicated in Fig. 4.17 for each model with the vertical dotted line. Second, the figure shows that $V^{HD}_{s\to d}$ is much smaller than $V^{HS}_{s\to d}$. Lastly, the breaking length of both models changes very abruptly at velocities close to the transition velocity $V_{s\to d}$. These three features are explained next.

Firstly, in order to understand the existence of the two regimes, consider that the initial peaks in the contact forces of both models, as seen in Fig. 4.16 on the left, are caused by the initial impact between ice and structure. The magnitude of both peaks scales with the ice velocity V_{ice}. Therefore, it makes sense for a certain ice velocity $V_{s\to d}$ to exist, above which the impact is so strong that the ice fails during the transient interaction phase, i.e. for $t_{fail} < t_{c\to s}$. These interactions, for which $V_{ice} > V_{s\to d}$, are classified as dynamic. The magnitude of the peak in the contact force continues to grow as V_{ice} increases, which causes the ice to fail earlier and closer to the contact point. This can be observed in Figs. 4.13 and 4.17 for both models.

Alternatively, if the impact is not strong enough, the ice will survive the peak force that occurs during the transient stage of the interaction ($t < t_{c\to s}$ in Fig. 4.14). This occurs if $V_{ice} < V_{s\to d}$. In this regime, the ice will fail with a breaking length that is approximately equal to the static breaking length $l_{br,s}$.

Second, it is important to note that $V^{HD}_{s\to d}$ is much lower than $V^{HS}_{s\to d}$. The left graph in Fig. 4.16 shows that the initial peak in the contact force of $\mathcal{M}_{HD}$ is significantly larger than the same peak of $\mathcal{M}_{HS}$ for any given ice velocity due to the inertia of the fluid. Consequently, $\mathcal{M}_{HD}$ predicts dynamic failure of the ice at much lower ice velocities.

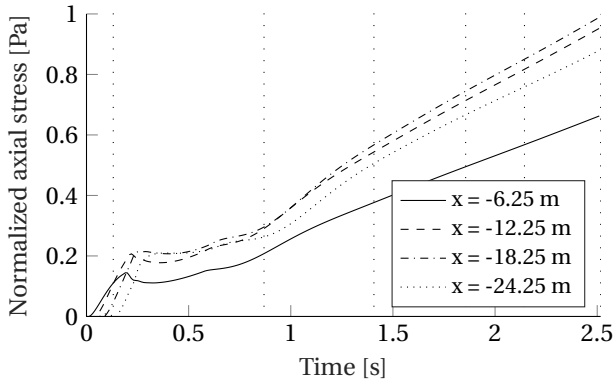

Figure 4.18: The axial stress due to bending of $\mathcal{M}_{HS}$ normalized by the flexural yield stress σ_{fl} as a function of time at four locations. For this figure V_{ice} = 0.06 m/s. The vertical loosely dotted lines indicate the failure time t_{fail} at the following ice velocities (from left to right): 0.5, 0.2, 0.1, 0.08, 0.07 and 0.06 m/s.

Lastly, the breaking length of both models changes abruptly at ice velocities close to the transition velocity $V_{s\to d}$, i.e. while transitioning from the quasi-static to the dynamic regime. This behavior will first be explained for $\mathcal{M}_{HS}$. Fig. 4.14, which corresponds to $\mathcal{M}_{HS}$, and the left graph of Fig. 4.16 both show that, for $t \in [t_{c\to s}, t_{s\to c}]$, the contact force is lower than during the transient interaction phase ($t \in [0, t_{c\to s}]$). The reduction of the contact force during this relaxation period results in a similar drop in the axial stress due to bending (the contribution of the axial compression in Eq. (4.7) is negligible), see Fig. 4.18. During the relaxation period, the ice cannot fail as the maximum bending moment in the ice is lower than experienced previously. Consequently, if the ice survives the transient interaction phase, the duration of the interaction will increase by approximately the duration of the relaxation period. This behavior can be observed in Fig. 4.13 as a

jump in the failure time t_{fail} around $V_{\text{s}\to\text{d}}^{\text{HS}}$. Fig. 4.18 shows that after the relaxation period the stresses in the ice are very close to their steady-state values. Because of this, the ice will fail with a breaking length that is very close to the static one. Therefore, whether the ice survives the transient interaction phase has a drastic effect on the breaking length of $\mathcal{M}_{\text{HS}}$. This behavior is also reflected in Fig. 4.17 as the breaking length decreases abruptly by about four meters at $V_{\text{s}\to\text{d}}^{\text{HS}}$.

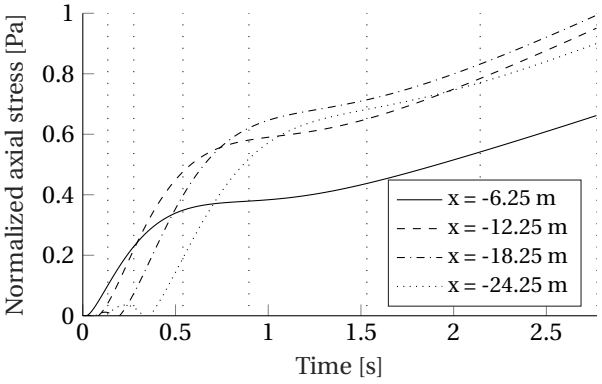

Figure 4.19: The axial stress of $\mathcal{M}_{\text{HD}}$ normalized by the flexural yield stress σ_{fl} as a function of time at four locations. For this figure $V_{\text{ice}} = 0.05$ m/s. The vertical dotted lines indicate the failure time t_{fail} at the following ice velocities (from left to right): 0.5, 0.2, 0.1, 0.08, 0.07, 0.06 and 0.05 m/s.

The abrupt behavior of the breaking length at ice velocities close to $V_{\text{s}\to\text{d}}^{\text{HD}}$ is analyzed next. Fig. 4.19 shows that the stresses predicted by $\mathcal{M}_{\text{HD}}$ always increase in time. However, between approximately 0.5 and 1.5 seconds, the stresses grow at a very slow pace. This corresponds to the period wherein $0 < V_{\perp}(t) < V_{\perp}(\infty)$ in Fig. 4.16 on the right. The reduced growth rate of the contact force makes it easier for the ice to survive this quasi-relaxation period. This is reflected in Fig. 4.13 by the rapid reduction failure time around $V_{\text{s}\to\text{d}}$ and in Fig. 4.17 by the rapid decrease of the breaking length after $V_{\text{s}\to\text{d}}$. Note that, since the axial stress is always increasing, there is no jump in the failure time of $\mathcal{M}_{\text{HD}}$, i.e. it is a smooth function.

4.3.4. LIMITATION OF THE HYDROSTATIC MODEL

Based on the above discussion, it is clear that the results of $\mathcal{M}_{\text{HD}}$ and $\mathcal{M}_{\text{HS}}$ start to differ, both qualitatively and quantitatively, when $V_{\text{ice}} \approx V_{\text{s}\to\text{d}}^{\text{HD}}$. The difference remains significant for all higher ice velocities. The two main characteristics of ice-slope interaction, namely $l_{\text{br}}(V_{\text{ice}})$ and $F_{\max}(V_{\text{ice}})$, as predicted by both models, are compared in order to assess the validity range of $\mathcal{M}_{\text{HS}}$.

First, $\mathcal{M}_{\text{HS}}$ starts to predict the breaking lengths wrongly at $V_{\text{ice}} \approx 0.6 V_{\text{s}\to\text{d}}^{\text{HD}}$, see Fig. 4.17. With the parameter set used, $V_{\text{s}\to\text{d}}^{\text{HD}}$ is approximately 0.0725 m/s and so $\mathcal{M}_{\text{HS}}$ correctly predicts the breaking length up to approximately 0.05 m/s. For interactions with a higher ice velocity, the relative error in the predicted breaking length can be as much as 100%. Second, $F_{\max}(V_{\text{ice}})$ of both models is compared in Fig. 4.20. The predictions of both models again start to deviate around $0.6 V_{\text{s}\to\text{d}}^{\text{HD}}$ with the relative error increasing up

to 40%.

From these two comparisons it can be concluded that if $\mathcal{M}_{HS}$ is used to predict l_{br} or F_{max}, the range of ice velocities wherein the predictions are valid is very limited. An approximate upper bound for the maximum ice velocity of $\mathcal{M}_{HS}$ is $0.6V_{s\to d}^{HD}$.

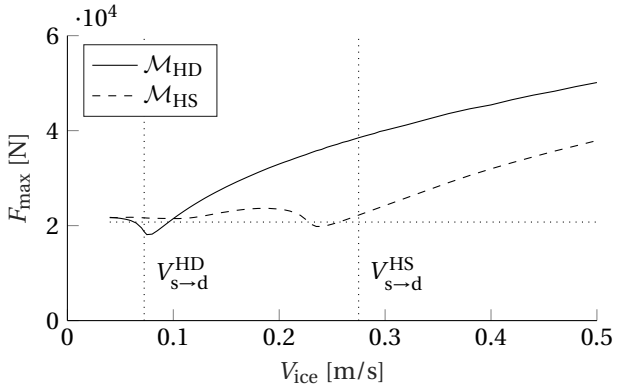

Figure 4.20: $F_{max}(V_{ice})$ of both models. The static force is included for reference as is depicted with the dotted horizontal line.

4.4. SENSITIVITY STUDY

The sensitivity of the results to changes in the parameter set is studied next. The focus is mainly on how the transition velocity $V_{s\to d}$ is affected by these changes as the applicability of $\mathcal{M}_{HS}$ is directly linked to $V_{s\to d}$. The parameters that have a large variance are the ice thickness h, Young's modulus E, flexural strength σ_{fl}, crushing strength, σ_c the water depth H and the hull angle θ. The effect of the semi-infinite model in Fig. 4.8 is also studied. Lastly, the sensitivity of the model to the number of modes N_{modes} is studied.

The default values for the transition velocity $V_{s\to d}$ are: $V_{s\to d}^{HD} = 0.0725$ m/s and $V_{s\to d}^{HS} = 0.275$ m/s.

4.4.1. VARIATIONS IN PHYSICAL PARAMETERS

Ice thickness. Halving h to 0.5 m causes $\mathcal{M}_{HS}$ to be in the sliding mode M_{sl} for a total of 0.2 s (compared to 0.45 s for $\mathcal{M}_{HS}$) and reduces $V_{s\to d}^{HD}$ to 0.065 m/s. Doubling h to 2 m increases $V_{s\to d}^{HD}$ to 0.08 m/s.

Young's modulus. $V_{s\to d}$ is relatively sensitive to changes in E. Halving E to 2.5×10^9 Pa increases $V_{s\to d}^{HD}$ to 0.11 m/s and $V_{s\to d}^{HS}$ to 0.38 m/s. When E is doubled to 10^{10} Pa, $V_{s\to d}$ decreases considerably for both models, to 0.045 m/s and 0.19 m/s respectively.

Flexural strength. σ_{fl} has a strong effect on $V_{s\to d}$. When halved to 2.5×10^5 Pa, $V_{s\to d}^{HD}$ lowers to roughly 0.03 m/s and $V_{s\to d}^{HS}$ to 0.135 m/s. Doubling σ_{fl} to 10^6 Pa has the opposite effect, increasing the $V_{s\to d}^{HD}$ to about 0.145 m/s and $V_{s\to d}^{HS}$ to more than 0.5 m/s.

Crushing strength. When σ_c is doubled to 1.2×10^6 Pa, $\mathcal{M}_{HS}$ is in the sliding mode M_{sl} for a total of 0.45 s, compared to 0.55 s for $\mathcal{M}_{HS}$. The overall contact force increases while the overall interaction quickens. Halving σ_c has the opposite effect. It appears that both effects cancel each other out as neither the breaking length nor $V_{s\to d}$ is significantly affected by changes in σ_c.

Water depth. The influence of H is negligible. Values as low as 30 m and as high as 200 m were tested but these did not affect the breaking length, nor $V^{HD}_{s\to d}$.

Hull angle. θ affects $V_\perp(0) = V_{ice}\sin(\theta)$ as well as the ratio between the horizontal and vertical contact forces. Increasing θ to 60° lowers $V^{HD}_{s\to d}$ to 0.045 m/s and $V^{HS}_{s\to d}$ to 0.16 m/s. The contribution of the axial compression to the dynamic equilibrium of the ice sheet studied in Sec. 4.3.1 is not significantly affected by the steeper hull angle. Lowering θ to 30° increases $V^{HD}_{s\to d}$ to 0.12 m/s and $V^{HS}_{s\to d}$ to 0.46 m/s and causes $\mathcal{M}_{HD}$ to enter the sliding mode M_{sl} for a total of 0.3 s compared to 0.55 s for $\mathcal{M}_{HS}$.

4.4.2. VARIATIONS IN NUMERICAL PARAMETERS AND IN MODELING ASSUMPTIONS

Number of modes. The Green's functions in Sec. 4.1.2 used to describe the response of $\mathcal{M}_{HD}$ in the ice-covered region are a superposition of the infinite modes of the system. The infinite number of modes was truncated at N_k. The truncation introduces an error that manifests itself at $x = 0$ as a discontinuity in the displacements and pressure of the fluid along the entire water column. The discontinuity is largest just below the surface. The two regions merge as the number of modes increases.

N_k is gradually lowered to study how it affects the ISI. While values of N_k as low as ten have only minor effects on the $l_{br}(V_{ice})$ and $F_{max}(V_{ice})$, such a low number of modes causes very large discontinuities in the displacements and pressure of the fluid along the interface at $x = 0$.

Modeling the structure. Next, the effect of reducing the infinite problem shown in Fig. 4.1 to the semi-infinite problem shown in Fig. 4.8 is studied. This change has only a minor effect, reducing $V^{HD}_{s\to d}$ from 0.0725 m/s to 0.05 m/s. The average breaking length is lowered by approximately 7%. The effect on the maximum horizontal contact force is just as minor. This result is somewhat different from the findings of Sawamura *et al.* [209] who found that semi- versus infinite does have a fairly significant effect. However, their model was based on FEM.

4.5. DISCUSSION

4.5.1. STOCHASTIC NATURE OF THE BREAKING LENGTH

When analyzing the breaking length it is common to present it as a deterministic value, similar to Fig. 4.17. However, even the deterministic models used in this chapter underline the stochastic nature of the breaking length.

Thus far in this chapter, the breaking length has been defined as the x-coordinate at which the axial stress in the cross-section of the ice plate first exceeds the flexural

strength σ_{fl} of the ice. However, this definition does not account for the fact that at t_{fail}, which is the moment the ice fails, a large segment of the ice is very close to failure. This was also noted by Valanto [203]. If in this segment a local defect is present, for instance, a lower ice thickness, the resulting stress-peak could cause the ice to fail at the location of the defect rather than at the location predicted by a homogeneous model. The sensitivity of the breaking length to such defects is shown in Fig. 4.21. The sensitivity is quantified using the axial stress, see Eq. (4.7), at t_{fail} normalized by the flexural yield stress: $\sigma_{\text{norm}}(x) = |\sigma_{\text{max}}(x, t_{\text{fail}})/\sigma_{\text{fl}}|$.

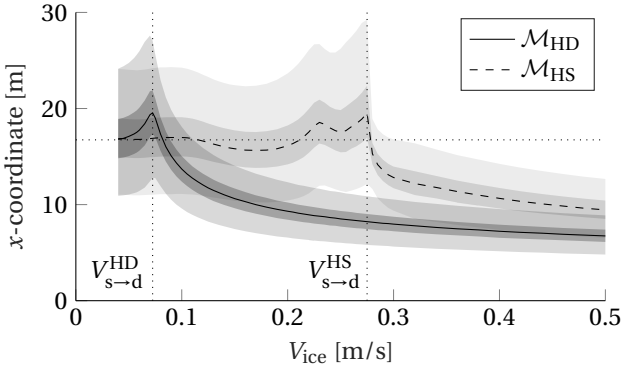

Figure 4.21: The sensitivity of $l_{\text{br}}(V_{\text{ice}})$ to defects for both models. The solid and dashed line indicate the location of the deterministic breaking lengths as previously shown in Fig. 4.17. Therefore, on these lines $\sigma_{\text{norm}}(l_{\text{br}}(V_{\text{ice}})) = 1$. The dark grey shading indicates the segment of the ice wherein $\sigma_{\text{norm}}(x) \geq 0.99$ and light gray $\sigma_{\text{norm}}(x) \geq 0.90$ for both models. The horizontal dotted line indicates the static breaking length $l_{\text{br,s}}$ computed with Eq. (4.19).

Given that ice is very inhomogeneous material [205], spatial variations in the ice thickness h, Young's modulus E or flexural yield stress σ_{fl} of several percentages are more than realistic. Fig. 4.21 shows that even such small variations can have a large effect on the breaking length. A spatial variation of 1% can change the breaking length by as much as 10% while a 10% variation can change the breaking length by as much as 30%. Fig. 4.21 thus shows that even a deterministic model underlines the stochastic nature of the breaking length. Therefore, presenting the breaking length as a deterministic property does not seem to be desirable.

4.5.2. SINGLE- VERSUS DUAL-MODE CONTACT MODEL

The contact model used in this chapter has two modes: a crushing mode M_{cr} and a sliding mode M_{sl}. The sliding mode is triggered when $V_{\perp}$ becomes zero (see Fig. 4.15) at $t_{\text{c}\to\text{s}}$ (see Fig. 4.14) and assures that the ice slides along the structure without crushing.

However, it is not uncommon for ice-structure interaction models to use a single-mode contact model that only accounts for crushing. Such a model will work fine as long as $V_{\perp} > 0$. However, in this work, this assumption would not have been valid. Fig. 4.16 shows that $\mathcal{M}_{\text{HS}}$ enters the sliding mode and certain parameters choices also cause $\mathcal{M}_{\text{HD}}$ to enter the sliding mode, see Sec. 4.4.1. Therefore, a single-mode contact model would not suffice for the studies done in this chapter. If such a contact model were used,

it would affect $l_{br}(V_{ice})$ around $V_{s\to d}$ and the contact force just after $t_{c\to s}$. In general, when a single-mode contact model is used in an ISI model, the underlying assumption that $V_\perp$ is assumed to be larger than zero should be more explicitly mentioned and the validity of this assumption should be asserted throughout the study.

4.5.3. EFFECT OF THE SOLUTION METHOD

To the author's knowledge, only two other works have studied ISI in 2D using a numerical model that includes hydrodynamics: Valanto [203] and Wang and Poh [204]. The $l_{br}(V_{ice})$ as predicted by all three models is shown in Fig. 4.22. At high velocities, all three models predict comparable breaking lengths. At low velocities, the model introduced in this chapter predicts a quasi-static regime. The $l_{br}(V_{ice})$ predicted by Valanto [203] does not predict a quasi-static regime and Wang and Poh [204] did not do any calculations in this regime.

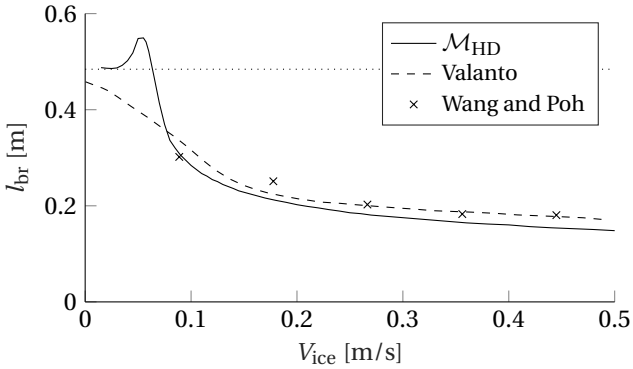

Figure 4.22: $l_{br}(V_{ice})$ as predicted by all three models. The horizontal dotted line is the static breaking length computed with Eq. (4.19).

It can be shown that by introducing a large amount of damping to $\mathcal{M}_{HS}$, a $l_{br}(V_{ice})$ that is similar to the one predicted by Valanto [203] can be obtained (see Ch. 5.3). For such a model, $V_\perp(t) > V_\perp(\infty)\ \forall\ t \in [0, t_{fail}]$ and, consequently, in the course of ISI, $V_\perp(t)$ decreases monotonically to its steady-state value. This kind of behavior of $V_\perp$ can also be seen in Wang and Poh [204]. Therefore, it is likely that both other models predict a stronger hydrodynamic effect than the model introduced in this chapter.

This difference is likely caused by the different assumptions and solution method adopted by the models. Valanto [203] uses finite difference for the discretization of both the fluid and the ice and considers the steady-state velocity of the fluid around the structure. Wang and Poh [204] use FEM for the discretization, adopt a single-stage contact model, and do not include the steady-state velocity.

$\mathcal{M}_{HD}$ thus differs in three ways from the two other two models. Firstly, the effect of a single stage contact model versus a two-stage contact model only affects the behavior near the transition velocity $V_{s\to d}$, as explained in Sec. 4.5.2, and therefore cannot explain the different results. Second, the effect of the steady-state velocity of the fluid around the structure can be inferred by comparing Wang and Poh [204] and Valanto [203]. As

there is still a discrepancy between $\mathcal{M}_{\text{HD}}$ and Wang and Poh [204], this can only explain part of the difference in the results. The adopted solution method thus appears to be the most likely source of the discrepancy. However, as the available data is lacking and both models are not publicly available, a detailed study on the effect of the solution method is not possible.

4.6. CONCLUSIONS

In this chapter, the effects of hydrodynamics on ISI was studied. This study was done by comparing the results of a model that includes both hydrostatics and hydrodynamics, $\mathcal{M}_{\text{HD}}$, with one that includes only hydrostatics, $\mathcal{M}_{\text{HS}}$. The conclusions of this study are presented next.

The factors of influence for ISI Seven forces were accounted for in the dynamic equilibrium of the ice. The contribution of the rotational inertia, the axial compression and the nonlinear hydrodynamic pressure p_{NLHD} to the dynamic equilibrium were found to be less than 1%. These three terms can thus be ignored without significantly affecting the results of an ISI model. Being able to ignore the axial compression and p_{NLHD} greatly simplifies the modeling of ISI as it removes all sources of spatial nonlinearity. Note that only the nonlinear contribution of the axial compression to the dynamic equilibrium of the ice can be ignored. Its linear contribution to the axial stresses was not studied and so no conclusion can be drawn regarding this.

The remaining four terms are essential for an accurate description of ISI. These terms, listed in the order of importance, are: bending of the ice floe, the linear hydrodynamic pressure p_{HD}, hydrostatic pressure p_{HS} and the inertia of the ice floe.

The effect of hydrodynamics on ISI is given by the combined effect of p_{HD} and p_{NLHD}. The relative importance of these two terms had not been studied before. However, from this work, it can be concluded that the entirety of the hydrodynamic effect can be attributed to the linear hydrodynamic pressure p_{HD}.

The relation between the contact force and the breaking length. A detailed study on the relation between the velocity-dependency of the breaking length $l_{\text{br}}(V_{\text{ice}})$ and the temporal development of the contact force revealed two interesting features.

Firstly, $l_{\text{br}}(V_{\text{ice}})$ has two regimes that are separated by the transition velocity $V_{\text{s}\to\text{d}}$: a quasi-static regime when the ice velocity $V_{\text{ice}} < V_{\text{s}\to\text{d}}$ and a dynamic regime when $V_{\text{ice}} > V_{\text{s}\to\text{d}}$. In the dynamic regime, the ice fails during the transient interaction phase. The breaking length is significantly smaller than the static breaking length and decreases as the ice velocity increases. Alternatively, if the ice does not fail in the transient regime, it often reaches the steady-state regime and will fail with a breaking length that is close to the static breaking length.

Second, the transition velocity of $\mathcal{M}_{\text{HD}}$, $V^{\text{HD}}_{\text{s}\to\text{d}}$ is much lower than the transition velocity of $\mathcal{M}_{\text{HS}}$, 0.0725 m/s compared to 0.275 m/s. $V^{\text{HD}}_{\text{s}\to\text{d}}$ decreases as the Young's modulus or hull angle is increased and increases as the flexural strength of the ice is increased. Other parameters such as the ice thickness, crushing strength and water depth have a negligible effect on the transition velocity.

The balance of forces. For interactions with $V_{\text{ice}} < V_{\text{s}\to\text{d}}$, bending is balanced by hydrostatics. For interactions with $V_{\text{ice}} > V_{\text{s}\to\text{d}}$ bending is balanced by the two inertia terms. The contribution of the inertia of the fluid is on average four to ten times bigger than that of the inertia of the ice.

The limitations of a hydrostatic model. The contact force and breaking length predicted by $\mathcal{M}_{\text{HS}}$ start to diverge rapidly from those predicted by $\mathcal{M}_{\text{HD}}$ for $V_{\text{ice}} > 0.6V_{\text{s}\to\text{d}}$. The error ranges from 30% to 100%. As such it is not recommended to use hydrostatic models for interactions with ice velocities above approximately 0.02 to 0.1 m/s, depending on the parameter being used.

The importance of wave radiation. Truncating the computation domain from infinite to semi-infinite had only minor effects on the breaking length and the contact force. This shows that the energy loss due to the radiation of surface waves in the open water region has only minor effects on ISI.

The stochastic nature of the breaking length. Lastly, when the ice fails, a relatively large segment of the ice is close to failure. Defects in the ice can amplify the stresses in this segment and can cause the ice to fail at the defect rather than at the expected location. This can easily cause the breaking length to vary by 10% to 30%.

The results of this chapter are used to create an effective fluid model for ISI in the next chapter.

REFERENCES

[193] C. Keijdener, H. Hendrikse, and A. Metrikine, *The effect of hydrodynamics on the bending failure of level ice,* Cold Regions Science and Technology **153**, 106 (2018).

[194] F. B. Jensen, W. A. Kuperman, M. B. Porter, and H. Schmidt, *Computational Ocean Acoustics* (Springer New York, New York, NY, 2011) p. 793.

[195] J. J. Stoker, *Water Waves* (John Wiley & Sons, Inc., Hoboken, NJ, USA, 1992).

[196] T. D. Williams and V. A. Squire, *The effect of submergence on wave scattering across a transition between two floating flexible plates,* Wave Motion **45**, 361 (2008).

[197] A. D. Kerr and W. T. Palmer, *The deformations and stresses in floating ice plates,* Acta Mechanica **15**, 57 (1972).

[198] E. Enkvist, P. Varsta, and K. Riska, *The Ship-Ice Interaction,* in *Proceedings of the 5th Int. Conference on Port and Ocean Engineering under Arctic Conditions* (Trondheim, 1979) pp. 977–1002.

[199] C. Keijdener and A. Metrikine, *The effect of ice velocity on the breaking length of level ice failing in downward bending,* Proceedings of 22nd IAHR International Symposium on Ice (2014), 10.3850/978-981-09-0750-1 1262.

[200] P. Valanto, *The resistance of ship in level ice,* Transactions of the Society of Naval Architects and Marine Engineers **109**, 53 (2001).

[201] A. Aprile, A. Benedetti, and T. L. Trombetti, *On non-linear dynamic analysis in the frequency domain: Algorithms and applications,* Earthquake Engineering & Structural Dynamics **23**, 363 (1994).

[202] Z. G. Zhao and J. P. Dempsey, *Planar forcing of floating ice sheets,* International Journal of Solids and Structures **33**, 19 (1996).

[203] P. Valanto, *The icebreaking problem in two dimensions : experiments and theory,* Journal of Ship Research **36**, 299 (1992).

[204] Y. Wang and L. H. Poh, *Velocity effect on the bending failure of ice sheets against wide sloping structures,* Journal of Offshore Mechanics and Arctic Engineering **139**, 061501 (2017).

[205] G. W. Timco and W. F. Weeks, *A review of the engineering properties of sea ice,* Cold Regions Science and Technology **60**, 107 (2010).

[206] C. Fox and V. A. Squire, *Coupling between the ocean and an ice shelf,* Annals of Glaciology **15**, 101 (1991).

[207] J. P. Dempsey and Z. G. Zhao, *Elastohydrodynamic response of an ice sheet to forced sub-surface uplift,* Journal of the Mechanics and Physics of Solids **41**, 487 (1993).

[208] C. Fox and H. Chung, *Harmonic deflections of an infinite floating plate,* Mathematics Research Report Series **485** (2002).

[209] J. Sawamura, K. Riska, and T. Moan, *Finite element analysis of fluid-ice interaction during ice bending,* in *Proceedings of the 19th IAHR Symposium on Ice, Vancouver, Canada* (2008) pp. 239 – 250

5

AN EFFECTIVE FLUID MODEL FOR ICE-SLOPE INTERACTION

In the previous chapter, it was shown that the predictions of the hydrostatic ice-slope interaction (ISI) model $\mathcal{M}_{\text{HS}}$ start to deviate significantly from the predictions of the hydrodynamic ISI model $\mathcal{M}_{\text{HD}}$ when the ice velocity $V_{\text{ice}} > 0.6V_{\text{s}\to\text{d}}^{\text{HD}}$ (see Sec. 4.3.4), which evaluates to approximately 0.02 – 0.1 m/s depending on the parameters used (see Sec. 4.4.1). Moreover, implementing a hydrodynamic model is no trivial task (see, for example, Sec. 4.1.2)) which, in the author's opinion, is the main reason for the prevalence of hydrostatic ISI models. These two observations are the motivation for this chapter in which an attempt is made to create a simple effective fluid model (EFM) that can capture the effects that hydrodynamics has on ISI as observed in Sec. 4.3.

The EFM is introduced in the next section and the optimization of its coefficients is done in section 5.2. Thereafter, the results are presented in Sec. 5.3, including a sensitivity study in Sec. 5.3.3. A dicussion follows in Sec. 5.4 and lastly, the conclusion is given in Sec. 5.5.

5.1. DESCRIPTION OF THE EFFECTIVE FLUID MODEL

The results in Sec. 4.3, as well as findings of [210, 211], show that the effect of hydrodynamics on ISI is of the added mass and added damping type. For this reason, the EFM proposed in this chapter is based on a frequency-independent added mass and a frequency-independent added damping coefficient. By constructing the EFM in this manner, it is trivial to add it to an existing ice-slope interaction model that only accounts for hydrostatics. In this chapter, the EFM is added to $\mathcal{M}_{\text{HS}}$. By augmenting $\mathcal{M}_{\text{HS}}$ with this EFM, an ice-slope interaction model is obtained that includes all four essential components as identified in Sec. 4.3.1, namely bending, hydrodynamics, the inertia of the ice, and hydrostatics. The resulting effective ice-slope interaction model will be referred to as $\mathcal{M}_{\text{eHD}}$. Based on its definition, the equation of motion of $\mathcal{M}_{\text{eHD}}$ can be expressed

as:

$$\rho_i h(1+C_m)\ddot{w} + 2\xi_d C_{crit}\dot{w} + D_i w'''' + \rho_w g w = 0 \tag{5.1}$$

where ρ_i is the density of the ice, h its thickness, $w(x,t)$ its vertical displacement, $D_i = E/(1-\nu^2)h^3/12$ its bending stiffness, $C_{crit} = \sqrt{\rho_i h \rho_w g}$, ρ_w the density of the fluid and g the gravitational constant. C_m and ξ_d are the unknown dimensionless added mass and added damping coefficients, where the latter is expressed in terms of critical damping, analogous to a damped harmonic oscillator. The optimal value of both coefficients is determined in the next section.

$\mathcal{M}_{eHD}$ has two unknown coefficients, namely C_m and ξ_d. To further improve the efficacy of the EFM, a dashpot is added at the boundary of the ice that is located at $x = 0$. This dashpot could capture the radiation of energy into the open-water region through surface waves. However, the importance of wave radiation on the ice-slope interaction is unclear as in Sec. 4.4.2 it is concluded that radiation damping does not have a significant impact on the interaction while Sawamura *et al.* [212] found a 40% reduction in the displacements of the ice when disabling wave radiation. Despite lacking a clear physical substantiation for this dashpot, its addition does not significantly affect the computational efficiency of the EFM and is, therefore, an efficient way to improve its efficacy. Eqs. (5.2) are updated accordingly:

$$D_i \frac{\partial^3 w(0,t)}{\partial x^3} + C_{bc} C_{crit}\dot{w}(0,t) = \left(F_{ct,z}(t,w,w',\dot{w},\dot{w}')\right)\Big|_{x=0} \tag{5.2a}$$

$$D_i \frac{\partial^2 w(0,t)}{\partial x^2} = \left(M_{ct}(t,w,w',\dot{w},\dot{w}')\right)\Big|_{x=0} \tag{5.2b}$$

where C_{bc} is the damping coefficient of the dashpot with dimensions m^2. As the addition of the dashpot may not be desirable from a physical point of view, the optimization of the EFM's coefficients will be done twice, once with $C_{bc} = 0$ and once with $C_{bc} \neq 0$.

5.2. OPTIMIZATION

The optimal value of the coefficients of the EFM, C_m, ξ_d and C_{bc}, are found through an optimization process. The goal of this process is to find the set of coefficients that results in the smallest discrepancy between the predictions of $\mathcal{M}_{eHD}$ and the predictions of the hydrodynamic model $\mathcal{M}_{HD}$ that was introduced in Sec. 4.1. The predictions that will be considered are the breaking length as a function of ice velocity $l_{br}(V_{ice})$ and the maximum contact force that occurred during the interaction as a function of ice velocity $F_{max}(V_{ice})$ as these are important aspects of ice-slope interaction. Based on these two predictions, the discrepancy is quantified using the error ϵ that is defined as:

$$\epsilon = \text{rms}\left(\frac{l_{br}(V_{ice}) - l_{br}^{HD}(V_{ice})}{l_{br}^{HD}(V_{ice})}\right) + \text{rms}\left(\frac{F_{max}(V_{ice}) - F_{max}^{HD}(V_{ice})}{F_{max}^{HD}(V_{ice})}\right) \tag{5.3}$$

where the four terms with the HD superscript are the predictions of $\mathcal{M}_{HD}$ and the remaining two terms are the predictions of $\mathcal{M}_{eHD}$.

The following bounds are used for the parametric space wherein the optimal values are being sought: $0 \leq C_m \leq 12$, $0 \leq \xi_d \leq 4.5$ and $0 \leq C_{bc} \leq 12 \times 10^{-6}$ m^2. These bounds

were chosen to assure that the optimal set of coefficients falls within the search space. The volume is discretized using a step size of 2, 0.5 and 2×10^{-6} m^2 respectively, resulting in 420 grid points. Spline interpolation is then used to interpolate between the grid points to find the set of two (or three) coefficients that leads to the smallest error ϵ.

5.3. RESULTS

The results are presented next. First, the effect of each coefficient on the predictions of $\mathcal{M}_{\text{eHD}}$ is studied. Thereafter, the optimization is done for the set of default parameters of the system that is listed below. Noting that the optimal value of the coefficients will change depending on the physical parameter of the system used, the sensitivity of the coefficients to changes in these physical parameters is studied.

The results presented in this chapter have been computed using the same set of parameters as used in the previous chapter. This parameter set will be referred to as the default set of parameters. The set is repeated here for convenience: $h = 1$ m, $\rho_{\text{i}} = 925$ kg/m^3, $\rho_{\text{w}} = 1025$ kg/m^3, $g = 9.81$ m/s^2, $H = 100$ m, $E = 5$ GPa, $\nu = 0.3$, $\sigma_{\text{c}} = 600$ kPa, $\sigma_{\text{fl}} = 500$ kPa, ice-steel friction coefficient 0.1 [–], hull angle $\theta = 45°$, $V_{\text{ice}} = [0, 0.5]$ m/s, $N_{\text{BEM}} = 60$, $c_1 = 1.25$, $\Delta_{\text{t}} = 10^{-3}$ s and $N_{\text{k}} = 250$. The numerical parameters were adaptively refined to assure convergence for all cases considered in this chapter.

5.3.1. THE EFFECT OF EACH COEFFICIENT ON THE PREDICTIONS

The effective fluid model has three coefficients. The effect of each coefficient on the predictions of $\mathcal{M}_{\text{eHD}}$ is presented next.

Effect of C_{m} The effect of C_{m} on the predictions of $\mathcal{M}_{\text{eHD}}$ is shown in Fig. 5.1. The additional mass increases the magnitude of the peak in the contact force that occurs during the initial impact, as can be seen in the bottom graph. This increase in peak force is also reflected in the middle graph by an increase in $F_{\text{max}}(V_{\text{ice}})$ and causes the ice floe to fail dynamically at lower ice velocities, thereby reducing the transition velocity $V_{\text{s}\to\text{d}}$ that marks the transition from static to dynamic failure. This trend can be observed in the top graph which shows that as C_{m} increases, $V_{\text{s}\to\text{d}}$ of $\mathcal{M}_{\text{eHD}}$, $V_{\text{s}\to\text{d}}^{\text{eHD}}$, decreases and approaches that of the reference model $V_{\text{s}\to\text{d}}^{\text{HD}}$.

Effect of ξ_{d} The effect of ξ_{d} on the predictions of $\mathcal{M}_{\text{eHD}}$ is shown in Fig. 5.2. First, the bottom graph shows that increasing ξ_{d} smoothens $F_{\text{ct}}(t)$, leading to a reduction in the duration and intensity of the relaxation period. This, in turn, has a smoothening effect on $F_{\text{max}}(V_{\text{ice}})$ and $l_{\text{br}}(V_{\text{ice}})$ when $V_{\text{ice}} \approx V_{\text{s}\to\text{d}}^{\text{eHD}}$, as is evident from the top and middle graph. Second, the added damping results in a slight increase in $F_{\text{ct}}(t)$, resulting in a slight increase in $F_{\text{max}}(V_{\text{ice}})$ and a shorter $l_{\text{br}}(V_{\text{ice}})$. These trends were also observed in Sec. 4.3.3.

Effect of C_{bc} The effect of C_{bc} on the predictions of $\mathcal{M}_{\text{eHD}}$ is shown in Fig. 5.3. The bottom graph shows that increasing C_{bc} has a smoothing effect on $F_{\text{ct}}(t)$, similar to ξ_{d}. However, as the dashpot is only present at $x = 0$ whereas ξ_{d} is present $\forall\ x \leq 0$, it has a strong effect on $F_{\text{max}}(V_{\text{ice}})$ and only a weak effect on $l_{\text{br}}(V_{\text{ice}})$. Its effects on $l_{\text{br}}(V_{\text{ice}})$ are

limited as the breakage of the ice is more driven by the distributed terms, i.e. C_m and ξ_d, as shown previously.

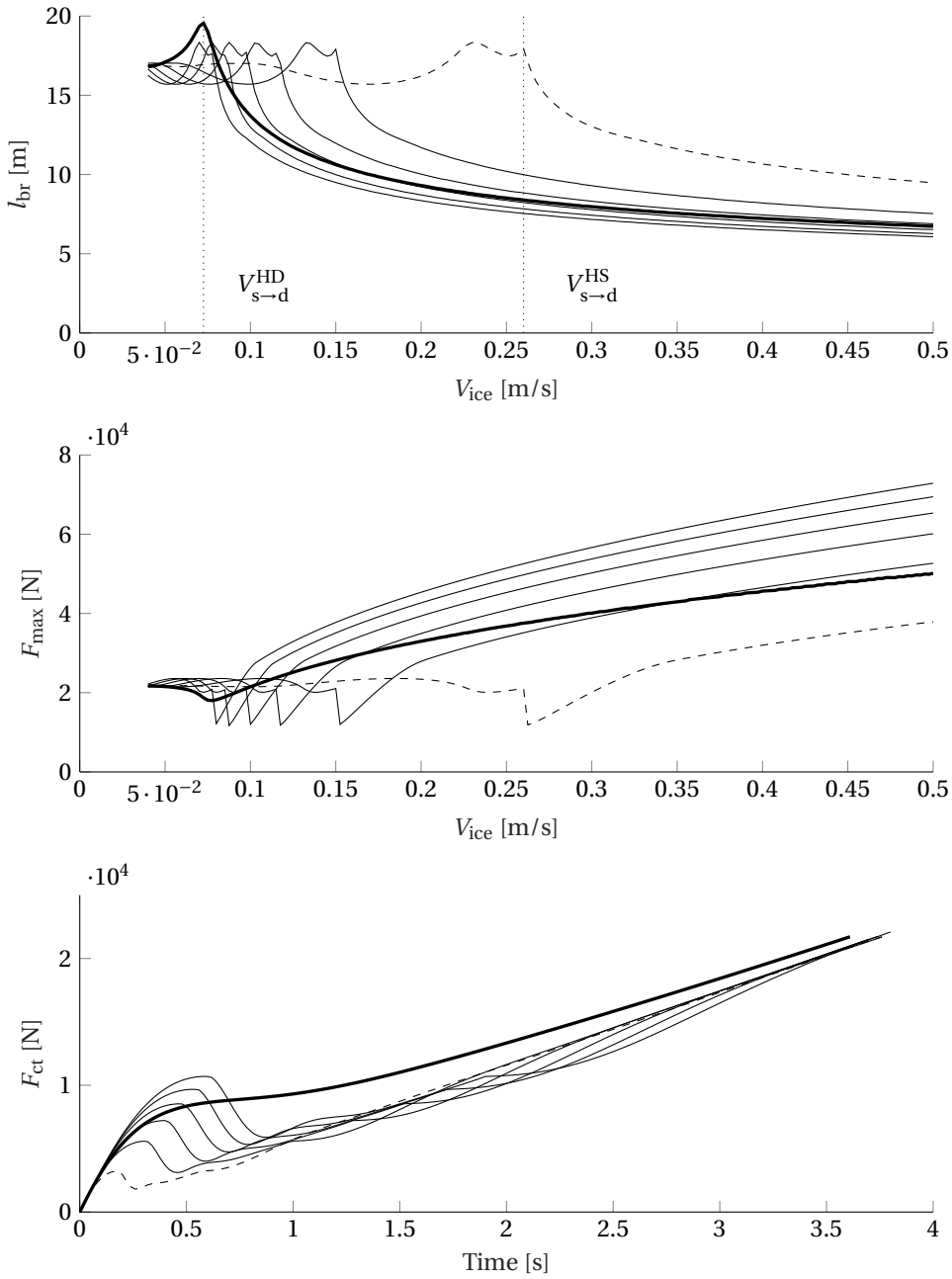

Figure 5.1: The effect of C_m on the predictions of $\mathcal{M}_{eHD}$. The bold curve is $\mathcal{M}_{HD}$. The dashed curve shows $\mathcal{M}_{eHD}(\xi_d = C_{bc} = C_m = 0) = \mathcal{M}_{HS}$. All subsequent solid curves are evaluations at $C_m = \{2,4,6,8,10\}$ respectively. For the bottom graph $V_{ice} = 0.04$ m/s.

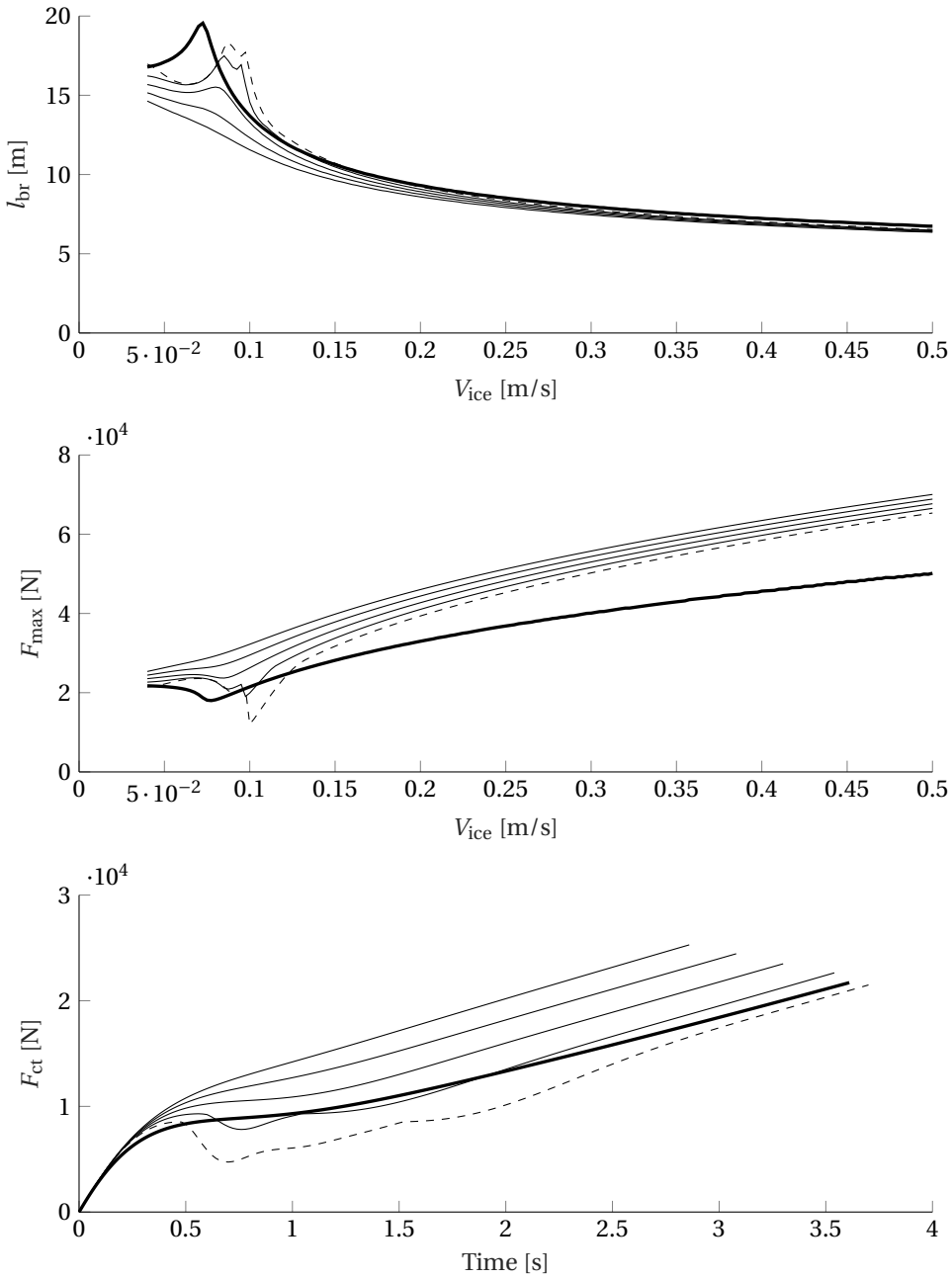

Figure 5.2: The effect of ξ_d on the predictions of $\mathcal{M}_{eHD}$. The bold curve is $\mathcal{M}_{HD}$. The dashed curve shows $\mathcal{M}_{eHD}(\{C_m = 6.26, \xi_d = C_{bc} = 0\}) \neq \mathcal{M}_{HS}$. All subsequent solid curves are evaluations at $\xi_d = \{1,2,3,4\}$ respectively. For the bottom graph $V_{ice} = 0.04$ m/s.

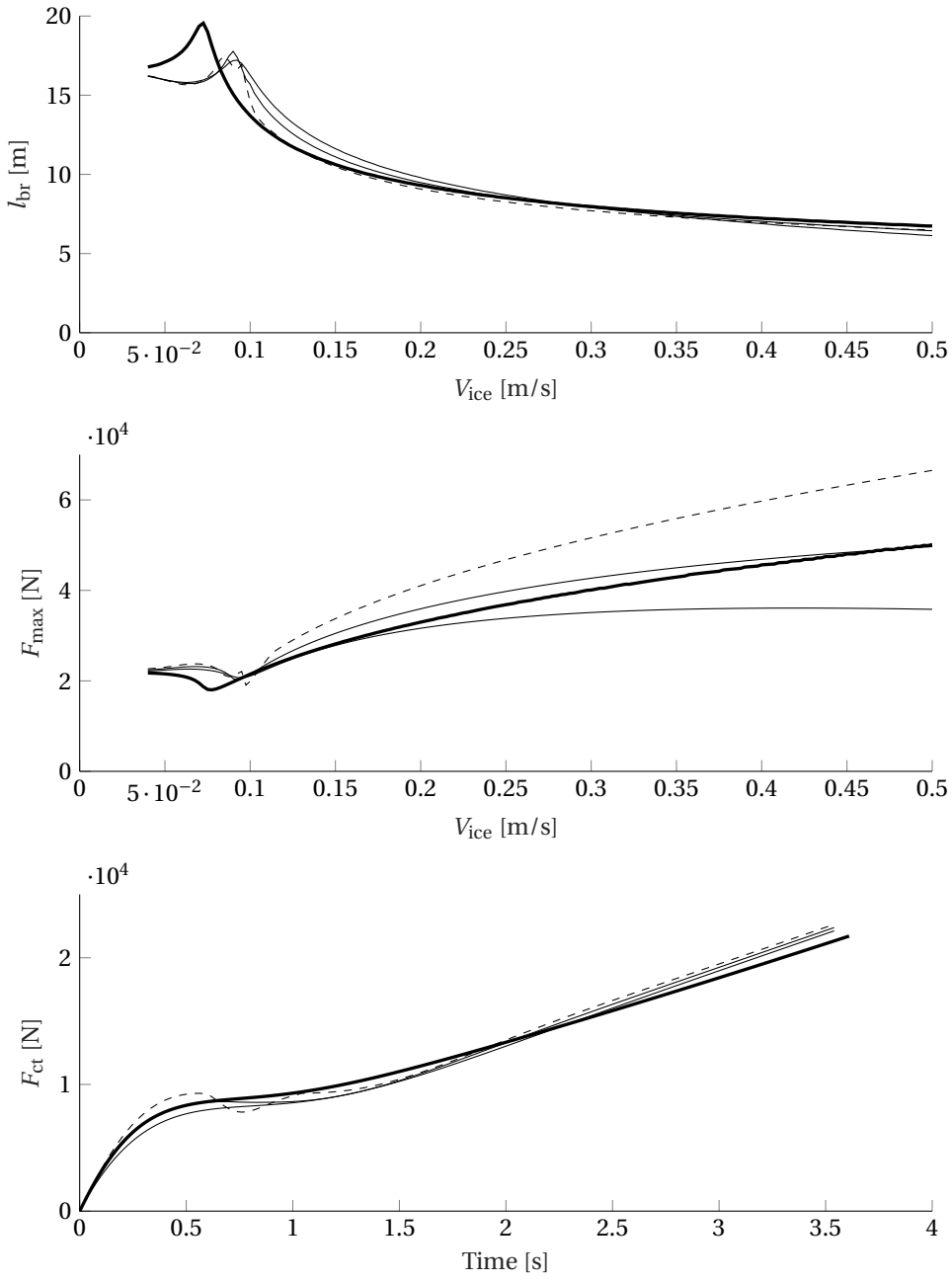

Figure 5.3: The effect of C_{bc} on the predictions of $\mathcal{M}_{eHD}$. The bold curve is $\mathcal{M}_{HD}$. The dashed curve shows $\mathcal{M}_{eHD}(\{C_m = 6.26, \xi_d = 1.06, C_{bc} = 0\}) \neq \mathcal{M}_{HS}$. All subsequent solid curves are evaluations at $C_{bc} = \{4, 8\} \times 10^{-6}$ m^2 respectively. For the bottom graph $V_{ice} = 0.04$ m/s.

5.3.2. OPTIMAL SET OF COEFFICIENTS

Based on the optimization process described above the optimal sets of coefficients were determined. The optimal set with $C_{bc} = 0$ will be referred to as $\mathcal{P}$ while the optimal one with $C_{bc} \neq 0$ will be referred to as $\mathcal{P}^*$. The optimization was done for the default set of parameters, leading to the following optimal sets: $\mathcal{P}_{def} = \{C_m = 2.83,\ \xi_d = 1.46,\ C_{bc} = 0\ m^2\}$ and $\mathcal{P}^*_{def} = \{C_m = 6.26,\ \xi_d = 1.06,\ C_{bc} = 4.85 \times 10^{-6}\ m^2\}$. The performance of $\mathcal{M}_{eHD}(\mathcal{P}_{def})$ and $\mathcal{M}_{eHD}(\mathcal{P}^*_{def})$ is shown in Fig. 5.4. The figure shows that the prediction of $\mathcal{M}_{eHD}(\mathcal{P}_{def})$ are significantly better than those of $\mathcal{M}_{HS}$ and that the predictions of $\mathcal{M}_{eHD}(\mathcal{P}^*_{def})$ are slightly better still.

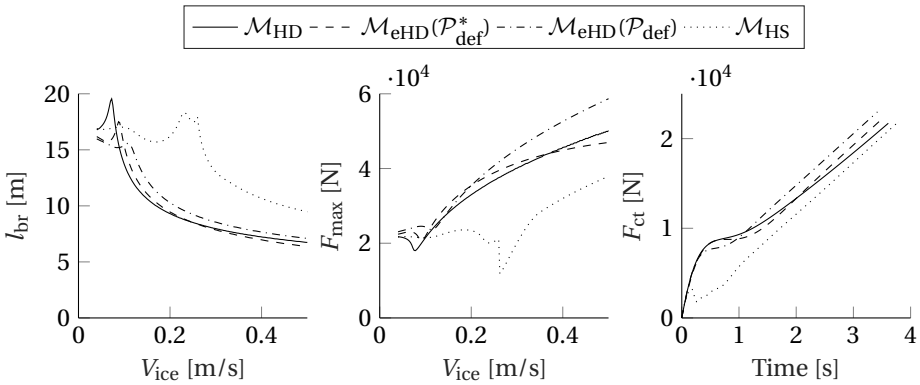

Figure 5.4: The performance of $\mathcal{M}_{eHD}(\mathcal{P}_{def})$ and $\mathcal{M}_{eHD}(\mathcal{P}^*_{def})$. For the right graph $V_{ice} = 0.04$ m/s.

5.3.3. SENSITIVITY ANALYSIS

As the predictions of the reference model $\mathcal{M}_{HD}$ depend on the physical parameters of the system, the optimal set of coefficients will be different depending on the set of physical parameters used. However, as having parameter-dependent coefficients is impractical, the option of using $\mathcal{M}_{eHD}(\mathcal{P}_{def})$ and $\mathcal{M}_{eHD}(\mathcal{P}^*_{def})$ independently of changes to the physical parameter is explored. Since these two sets become suboptimal when the physical parameters of the system are changed, the error ϵ of both models will increase. This increase in error is shown in Table 5.1. All parameters were set to their default values except for the parameter listed in the left column, which was set to the specified value.

Table 5.1 shows that the performance of $\mathcal{M}_{eHD}(\mathcal{P}_{def})$ is insensitive to change in Young's modulus E, flexural strength σ_{fl} and water depth H. Changes in the ice thickness h, crushing strength σ_{cr} and hull angle θ result in a medium increase in error. Overall it can be concluded that $\mathcal{M}_{eHD}(\mathcal{P}_{def})$ is fairly insensitive to changes in the parameter set and is, therefore, quite robust.

Next, the performance of $\mathcal{M}_{eHD}(\mathcal{P}^*_{def})$ is also insensitive to changes in the water depth H, mildly sensitive to changes in ice thickness h, Young's modulus E, hull angle θ, and very sensitive to changes in flexural strength σ_{fl}, crushing strength σ_{cr}. It is also important to note that despite the larger relative increase in error, the error of $\mathcal{M}_{eHD}(\mathcal{P}^*_{def})$ is smaller than the error of $\mathcal{M}_{eHD}(\mathcal{P}_{def})$ for all cases considered.

In order to visualize what the increase in error mean in terms of deterioration of the

Increase in error when using $\mathcal{P}_{\text{def}}$ and $\mathcal{P}^*_{\text{def}}$				
	$\mathcal{P}$		$\mathcal{P}^*$	
	ϵ	Incr.	ϵ	Incr.
Default	0.24	+0%	0.12	+0%
$h = 0.5$ m	0.29	+21%	0.16	+33%
$h = 2.0$ m	0.22	-9%	0.11	-9%
$E = 2.5$ GPa	0.25	+4%	0.14	+17%
$E = 10$ GPa	0.24	+0%	0.13	+8%
$\sigma_{\text{fl}} = 250$ kPa	0.25	+4%	0.22	+83%
$\sigma_{\text{fl}} = 1$ MPa	0.25	+4%	0.16	+33%
$\sigma_{\text{cr}} = 300$ kPa	0.22	-9%	0.12	+0%
$\sigma_{\text{cr}} = 1.2$ MPa	0.29	+21%	0.21	+75%
$H = 50$ m	0.24	+0%	0.12	+0%
$H = 200$ m	0.25	+4%	0.12	+0%
$\theta = 30°$	0.29	+21%	0.17	+42%
$\theta = 60°$	0.25	+4%	0.13	+8%

Table 5.1: The increase in the error ϵ when using $\mathcal{P}_{\text{def}}$ and $\mathcal{P}^*_{\text{def}}$ independently of changes in the physical parameters of the system. The column with header 'ϵ' lists the error for the listed change in parameter. The column with header 'Incr.' lists the increase in error relative to the error for the default set of parameters which is 0.24 and 0.12, respectively.

prediction of both models, their predictions for one the worst cases, namely when σ_{fl} is set to 250 kPa, are shown in Fig. 5.5. Despite this increase in error, both models still perform significantly better than $\mathcal{M}_{\text{HS}}$.

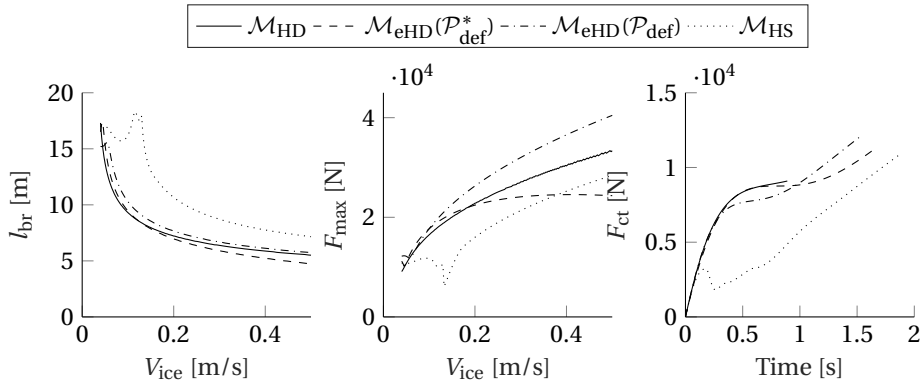

Figure 5.5: The performance of $\mathcal{M}_{\text{eHD}}(\mathcal{P}_{\text{def}})$ and $\mathcal{M}^*_{\text{eHD}}(\mathcal{P}_{\text{def}})^*$ when σ_{fl} is changed to 250 kPa. For the right graph $V_{\text{ice}} = 0.04$ m/s.

Even though $\mathcal{M}_{\text{eHD}}$ is a fairly robust model as shown by Table 5.1, there might be situations in which changing the parameters is desirable in order to minimize the error. As such, the optimization process was redone for each change in parameter, resulting in the sets of coefficients listed in Table 5.2. The table shows that when the optimization

Optimal sets of coefficients							
	$\mathcal{P}$			$\mathcal{P}^*$			
	C_m [-]	ξ_d [-]	ϵ [-]	C_m [-]	ξ_d [-]	C_{bc} 10^{-6} [m^2]	ϵ [-]
Default	2.83	1.46	0.24	6.26	1.06	4.85	0.12
$h = 0.5$ m	2.73	2.19	0.27	6.16	1.56	4.36	0.15
$h = 2.0$ m	2.83	0.96	0.21	6.16	0.56	4.36	0.09
$E = 2.5$ GPa	3.03	1.33	0.25	6.46	0.92	6.18	0.12
$E = 10$ GPa	2.73	1.60	0.24	6.16	1.19	4.00	0.11
$\sigma_{fl} = 250$ kPa	2.83	1.65	0.24	3.84	1.51	2.06	0.11
$\sigma_{fl} = 1$ MPa	4.55	1.10	0.24	9.19	0.69	9.82	0.10
$\sigma_{cr} = 300$ kPa	3.03	1.06	0.21	6.57	0.69	6.55	0.09
$\sigma_{cr} = 1.2$ Mpa	2.53	2.10	0.28	6.26	1.37	3.64	0.15
$H = 50$ m	2.83	1.46	0.24	6.16	1.06	4.73	0.12
$H = 200$ m	2.73	1.46	0.25	6.26	1.10	5.09	0.12
$\theta = 30°$	3.33	1.87	0.27	8.69	0.01	7.27	0.14
$\theta = 60°$	2.42	1.01	0.23	6.26	0.78	3.88	0.10

Table 5.2: The sets of optimal coefficients for a range of system parameters and the resulting error.

is redone when the physical parameters are changed, the error of both $\mathcal{M}_{eHD}(\mathcal{P}_{def})$ and $\mathcal{M}_{eHD}(\mathcal{P}^*_{def})$ remains of the same order of magnitude.

5.4. DISCUSSION

Two other studies have investigated using EFM in the context of the hydrodynamic response of elastic ice as mentioned in the introduction. It is interesting to compare those models with the EFM proposed in this paper.

First, the possibility of using a frequency-independent added mass coefficient for the dynamical uplift of level ice was investigated by Dempsey and Zhao [211, 213, 214]. All three studies concluded that this approach cannot reproduce the effects of hydrodynamics because the wave motion is fundamentally different when hydrodynamics is included. Although these studies do not consider ice-slope interaction, it is interesting to assess how the proposed EFM performs when only an added mass coefficient is used, i.e. when $\xi_d = C_{bc} = 0$. The optimal value of C_m for the default set of parameters is 4.44 [-]. In the papers by Dempsey and Zhao papers, the main prediction that was studied was $F_{ct}(t)$. Fig. 5.6 shows that $F_{ct}(t)$ is also poorly predicted by the proposed EFM when $\xi_d = C_{bc} =$. From this, it can be concluded that added damping is an essential component of the EFM, a finding that is supported by the observations regarding the effects of hydrodynamics on ice-slope interaction.

Second, Lubbad *et al.* [215] studied using a frequency-independent added mass and damping coefficient for ice-slope interaction. However, the difference with the proposed EFM is that the added damping term was multiplied with the squared fluid velocity. They found that this damping term had a marginal influence on the response of the ice. There-

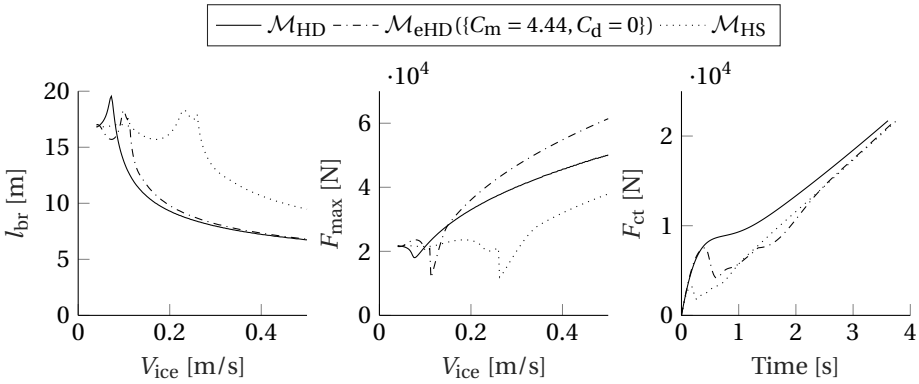

Figure 5.6: The performance of $\mathcal{M}_{\text{eHD}}(\{C_{\text{m}} = 4.44, \xi_{\text{d}} = C_{\text{bc}} = 0\})$ for the default set of parameters. For the right graph $V_{\text{ice}} = 0.04$ m/s.

fore, this model also only considered added mass and it is, therefore, likely that this is the reasons for the unsatisfactory agreement with their hydrodynamic reference model.

Applicability of the proposed effective fluid models Although the proposed effective fluid models greatly improve the predictions of $\mathcal{M}_{\text{HS}}$, some reservations are in order. Firstly, in this study, only the interaction with a sloping structure was considered. The applicability of the EFM to other cases, like the uplift scenarios considered in Dempsey and Zhao [211], Zhao and Dempsey [214] or interaction between individual ice floes, has to be investigated. Moreover, as the current models are 2D, their applicability for ice-slope interaction in 3D is unknown.

5.5. CONCLUSIONS

In this chapter, an effective fluid model was presented that can reproduce the effects that hydrodynamics has on ice-slope interaction. This fluid model can be added to existing ice-sloping interaction model that only includes hydrostatics with minimal effort. The resulting effective ice-slope interaction model is very simple but its predictions are significantly better than a hydrostatic model. The model is also fairly robust in that its prediction remain accurate even when the physical parameters of the system are changed. While the applicability of the proposed fluid model to a wider range of IFI problems remains to be investigated, the proposed approach is very promising.

REFERENCES

[210] P. Valanto, *The icebreaking problem in two dimensions : experiments and theory*, Journal of Ship Research **36**, 299 (1992).

[211] J. P. Dempsey and Z. G. Zhao, *Elastohydrodynamic response of an ice sheet to forced sub-surface uplift*, Journal of the Mechanics and Physics of Solids **41**, 487 (1993).

[212] J. Sawamura, K. Riska, and T. Moan, *Finite element analysis of fluid-ice interaction*

during ice bending, in *Proceedings of the 19th IAHR Symposium on Ice, Vancouver, Canada* (2008) pp. 239 – 250.

[213] Z. Zhao and J. Dempsey, *A dynamically forced floating beam,* in *IAHR Ice Symposium* (Banff, Alberta, 1992).

[214] Z. G. Zhao and J. P. Dempsey, *Planar forcing of floating ice sheets,* International Journal of Solids and Structures **33**, 19 (1996).

[215] R. Lubbad, G. Moe, and S. Løset, *Static and dynamic interaction of floating wedge-shaped ice beams and sloping structures,* in *Proceedings of the 19th IAHR Symposium on Ice, Vancouver, Canada* (2008) pp. 227 – 237

6

CONCLUSIONS

The goal of this thesis is to define how hydrodynamics affects the interaction between an elastic ice floe and a sloping structure. A literature review on ice-floater interaction (Ch. 2) has shown that the majority of numerical studies on this topic are performed with a hydrostatic model. Furthermore, the effects of hydrodynamics on ice-floater interaction are not fully understood and the adoption of hydrodynamics in numerical studies of ice-floater interaction is mainly held back by the challenges associated with implementation. An effective fluid model offers a solution to overcome such challenges. The secondary goal of this thesis is, therefore, to develop an effective fluid model which can capture the hydrodynamic effects during the interaction between ice and a sloping structure.

To achieve these goals three research questions were defined, each addressed in one of the chapters of this thesis. In Ch. 3, the question of how the surface-wave-based coupling between a floater and a nearby elastic ice floe affects the floater's response has been addressed. In Ch. 4, the effect of hydrodynamics on ice-slope interaction has been investigated. Lastly, in Ch. 5, the development of an effective fluid model that can capture the effect of hydrodynamics on ice-slope interaction has been presented. The main conclusions related to each question are as follows.

The interaction between an ice floe and a floater through surface waves has been investigated in Ch. 3. The floater was modeled in 2D as a thin rigid body that floats on the surface of a fluid layer of finite depth. On one side of the floater, an ice floe was assumed, modeled as a semi-infinite Kirchhoff-Love plate. The floater in the presence of the ice floe was excited by a time-harmonic force and moment and the resulting motions of the floater were analyzed.

It has been found that below a specific onset frequency the propagating waves are almost fully transmitted into the ice floe and, consequently, the response of the floater remains unaffected by the presence of the ice. The onset frequency has been defined as the frequency at which the amplitude of the reflected propagating wave divided by the amplitude of the incoming propagating wave is less than one percent. This onset

frequency, which is independent of the properties of the floater, has a power-law dependence on the ice thickness. For one-meter thick ice, the onset frequency is about 0.4 rad/s and for two-meter-thick ice, it is about 0.3 rad/s. The onset frequency is insensitive to changes of the Young's modulus in the range of 5 to 10 GPa and to changes in the water depth in the range of 50 to 1000 meters.

Above the onset frequency, it has been found that the waves reflected by the ice have a significant effect on the response of the floater. Frequency ranges exist wherein the length of the gap between the floater and the ice floe is divisible by the frequency-dependent wavelength of the propagating surface wave. When the vessel is excited with a load whose frequency falls in one of those frequency ranges, quasi-standing waves occur within the gap between ice floe and floater. Depending on the phasing between the reflected waves and the floater's motions, resonance or anti-resonance can occur which can significantly amplify or reduce the floater's motions when compared to the case when no ice is present, with changes in the amplitude of up to 20%. For the limit case where there is no gap between ice and floater, the amplitude of the floater can be amplified by 10% and its natural frequency increased by 20%.

In Ch. 4, the effect of hydrodynamics on the bending failure of an elastic ice floe due to the interaction with a downward-sloping floater has been addressed. A novel, semi-analytical 2D ice-slope interaction model has been proposed that is based on the potential theory in conjunction with the nonlinear Bernoulli equation to describe the fluid pressure. The ice has been modeled as a semi-infinite Kirchhoff-Love plate. The predictions of the hydrodynamic model have been compared with those of a hydrostatic ice-slope interaction model, thereby obtaining a quantitative measure of the effect of hydrodynamics on the interaction.

It has been found that the contribution of the rotational inertia of the ice, axial compression and the nonlinear hydrodynamic pressure to the balance of forces within the ice is insignificant, with all three components contributing less than 1%. As the last two components are the source of spatial nonlinearity in the model, being able to ignore those in modeling the interaction is advantageous for numerical analysis. Bending of the ice floe (44 to 47%), linear hydrodynamic pressure (12 to 41%), hydrostatic pressure (42% to less than 1%) and the inertia of the ice floe (1 to 11%), are identified to be essential in modeling ice-slope interaction. The contribution of the fluid's inertia was on average four to ten times that of the inertia of the ice. The study also has revealed that the effect of wave radiation on ice-slope interaction is minimal.

The relation between the temporal development of the contact force and the velocity-dependence of the breaking length has been studied. The study has revealed that the breaking length can fall into two regimes which are separated by a transition velocity. When the ice drift velocity is below the transition velocity, the ice fails during the initial impact with the sloping structure. Alternatively, when the ice velocity is above the transition velocity, the ice floe survives the impact and fails with a breaking length that is close to the static breaking length. The transition velocity of the hydrodynamic model employed in this thesis is much lower than the transition velocity of the hydrostatic model, 0.0725 m/s compared to 0.275 m/s, confirming that hydrostatic models have a limited range of applicability and should not be used for ice velocities exceeding 0.6 times the

transition velocity obtained with the hydrodynamic model. Outside this range, differences up to 100% exist for the predicted breaking length and maximum contact force.

The study in Ch. 4 has underlined the stochastic nature of the breaking length of the ice floe. When the floe fails, a relatively large segment of the floe is, in fact, close to failure. A defect in the ice can locally amplify the stresses, causing the ice to fail at the defect rather than at the location predicted by a model including homogeneous ice properties. As a consequence, the breaking length varies by 10% to 30% when defects are included.

The last chapter of this thesis, Ch. 5, has built on the knowledge gained in Ch. 4 by attempting to create a simple effective fluid model that captures the observed effects of hydrodynamics on ice-slope interaction. An effective fluid model has been proposed based on frequency-independent added mass and damping coefficients. When combined with a hydrostatic ice-slope interaction model, a complete ice-slope interaction model is obtained that contains all four essential components of the interaction as identified in Ch. 4. Two effective fluid models were considered, one with and one without an effective damper at the contact with the vessel.

The optimal value of the unknown added mass and damping coefficients have been found by minimizing the error of the predictions of the effective model compared to the predictions of the full hydrodynamic model that was used in Ch. 4. The error is defined as the root-mean-squared of the difference between the predictions of both models, normalized by the predictions of the hydrodynamic model. Here, the predicted velocity-dependent breaking length and the maximum contact force that occurred during the interaction have been considered. The error of the effective model including the damper is found to be 0.12 and the error of the model without the damper 0.24, compared to 0.91 for the hydrostatic model. The predictions of both models are, therefore, far more accurate than those of a hydrostatic model, when compared to the full hydrodynamic model.

The sensitivity of the two models' predictions to changes in ice thickness, Young's modulus, flexural yield strength, crushing strength, water depth, and hull angle has been studied. It has been found that the error for the model without the damper ranges between 0.22 and 0.29, whereas the error for the model with the damper ranges between 0.11 and 0.22. Overall, the model with the damper is the preferred model as it always performs better than the model without a damper.

The resulting effective ice-slope interaction model is trivial to implement when compared to a full hydrodynamic model while containing the important contributions of hydrodynamics to the interaction between ice and sloping structure. The model will allow for an increase in the adoption of hydrodynamics in numerical studies of ice-slope interaction.

A

DERIVATION OF GREEN'S FUNCTIONS

In this appendix, a set of Green's functions $\tilde{\phi}_\alpha$ is derived that gives the response of a semi-infinite floating Kirchhoff-Love plate, located at $x \leq -l$, to the three types of loading shown in Fig. A.1: 1) the force $F_{\mathrm{GF}}\delta(t)$ applied at the edge of the plate (where $\delta(t)$ is the Dirac delta function), 2) the moment $M_{\mathrm{GF}}\delta(t)$ applied at the edge of the plate and 3) a uniformly distributed vertical force $P_{\mathrm{GF}}\delta(t)$ of width $2\Delta_{\mathrm{x}}$ that is centered around x_α, which is defined as:

$$x_\alpha = \begin{cases} 2\Delta_{\mathrm{x}}(\alpha - 1/2), & \text{if } \alpha > 0 \\ 2\Delta_{\mathrm{x}}(\alpha + 1/2) - l, & \text{if } \alpha < 0 \end{cases} \tag{A.1}$$

$P_{\mathrm{GF}}\delta(t)$ therefore acts on the surface of the ice-covered region if $\alpha < 0$ and on the surface of the open-water region if $\alpha > 0$. There is a gap of width l that separates the two regions.

The inhomogeneous (not invariant in x) problem is solved in two steps. First, the two complimentary homogeneous (invariant in x) problems shown in Fig. A.2 are solved. These problems do not account for the edge force and edge moment and have a homogeneous surface: the problem on the left in Fig. A.2 is completely covered with ice and the problem on the right does not have any ice cover, i.e. open water. Solving these problems results in the Green's function for the ice-covered water $\tilde{\phi}_\alpha^{(\mathrm{i,p})}$ and the open water Green's function $\tilde{\phi}_\alpha^{(\mathrm{o,p})}$, where the subscript "$\alpha$" is related to the location of the distributed vertical force, the superscript "i" refers to the ice-covered region, the superscript "o" to the open water region and the superscript "p" indicates that these functions give the response to the distributed vertical force $P_{\mathrm{GF}}\delta(t)$. $P_{\mathrm{GF}}^{(-)}$ and $P_{\mathrm{GF}}^{(+)}$, shown in Fig. A.2, are introduced to assures that $P_{\mathrm{GF}}\delta(t)$ excites the correct region depending on the value of α:

$$\begin{cases} P_{\mathrm{GF}}^{(-)} = P_{\mathrm{GF}}, & P_{\mathrm{GF}}^{(+)} = 0, \quad \text{if } \alpha < 0 \\ P_{\mathrm{GF}}^{(-)} = 0, & P_{\mathrm{GF}}^{(+)} = P_{\mathrm{GF}}, \quad \text{if } \alpha > 0 \end{cases} \tag{A.2}$$

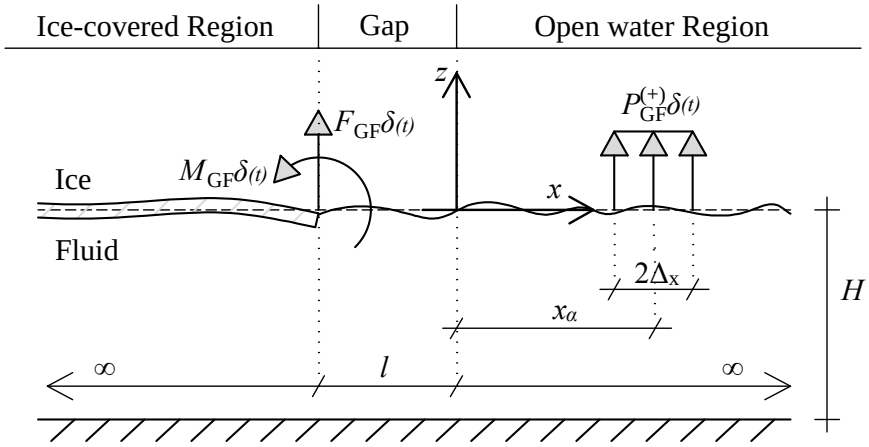

Figure A.1: The problem definition for $\tilde{\phi}_\alpha$. The location of the vertical distributed force $P_{GF}\delta(t)$ depends on α. If $\alpha > 0$ it acts on the fluid and if $\alpha < 0$ it acts on the ice.

During the second step the inhomogeneous problem shown in Fig. A.1 is solved. $\tilde{\phi}^{(i,p)}_\alpha$ is used to describe $x \leq -l$ and $\tilde{\phi}^{(o,p)}_\alpha$ is used for $x > -l$. This assumed solution satisfies all equations except those governing the interface between the two regions located at $x = -l$. Eigenfunction Matching is then used to obtain the final solution $\tilde{\phi}_\alpha$ that satisfies the appropriate interface conditions.

$\tilde{\phi}^{(o,p)}_\alpha$ is derived first in section A.1, followed by $\tilde{\phi}^{(i,p)}_\alpha$ in section A.2. Eigenfunction Matching is then used in section A.3 to obtain $\tilde{\phi}_\alpha$. Certain responses of $\tilde{\phi}_\alpha$ that are used in the main body of the thesis are derived in section A.4. Lastly, in section A.5 the numerical root finding schemes used in the first and second section are explained.

The following Fourier transform $\mathfrak{F}$ and its inverse $\mathfrak{F}^{-1}$ are used in this thesis. Transforming a time-dependent function $f(t)$ as an example:

$$\tilde{f}(\omega) = \mathfrak{F}\left(f(t)\right) = \int_{-\infty}^{\infty} f(t) e^{-i\omega t}\, dt \tag{A.3a}$$

$$f(t) = \mathfrak{F}^{-1}\left(\tilde{f}(\omega)\right) = \frac{1}{2\pi}\int_{-\infty}^{\infty} \tilde{f}(\omega) e^{i\omega t}\, dt \tag{A.3b}$$

where ω is frequency, t is time and i is the imaginary unit. An equivalent transform is used for the transformation from the x-domain to the wavenumber- or k-domain. As all solutions are sought for in the frequency domain, all equations have already been transformed to this domain for brevity.

A.1. GREEN'S FUNCTION FOR OPEN WATER

The open water Green's function $\tilde{\phi}^{(o,p)}_\alpha(x,z,\omega)$ is derived first. This function gives the response of a fluid layer with depth H to the distributed vertical force $P^{(+)}_{GF}\delta(t)$, see Fig. A.2 on the right.

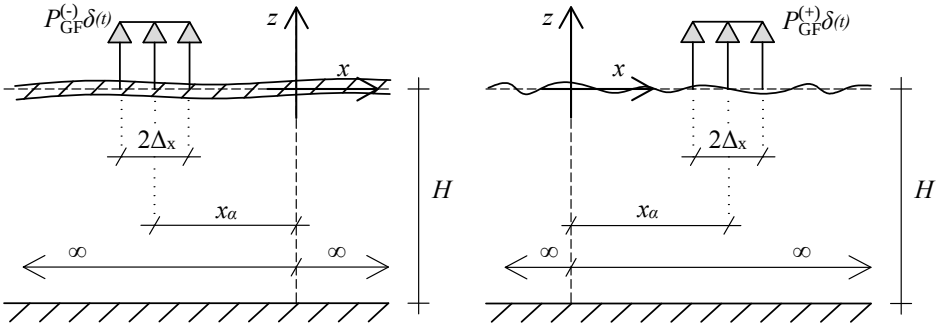

Figure A.2: The problem definition of the two complementary homogeneous infinite problems. Solving the left problem results in the ice-covered Green's function $\tilde{\phi}_\alpha^{(o,p)}$ and the right one results in the open water Green's function $\tilde{\phi}_\alpha^{(o,p)}$.

The fluid is assumed to be incompressible, inviscid and irrotational, i.e. incompressible potential flow is assumed. This allows it to be described by the Laplace equation:

$$\nabla^2 \tilde{\phi}_\alpha^{(o,p)}(x,z,\omega) = 0 \qquad \forall\ x \in (-\infty,\infty)\ \cap\ z \in (-H,0) \tag{A.4}$$

where parentheses denote an open interval and brackets, in formulas to follow, a closed one. The *displacement* potential $\tilde{\phi}_\alpha^{(o,p)}(x,z,\omega)$ is defined by:

$$\vec{u} = \nabla\phi \tag{A.5}$$

where $\vec{u}$ contains the horizontal and vertical displacements of the fluid. A displacement potential (see for instance [139]) is used as it results in a clearer and more standard notation from a structural dynamics point of view.

The governing equation of the fluid must be accompanied by proper boundary conditions. At the lower boundary, $z = -H$, the condition prevents penetration of the fluid into the seabed:

$$\frac{\partial \tilde{\phi}_\alpha^{(o,p)}(x,-H,\omega)}{\partial z} = 0 \qquad \forall\ x \in (-\infty,\infty) \tag{A.6}$$

At the upper boundary, $z = 0$, the fluid pressure $\tilde{p}(x,z,\omega)$ must balance with the external pressure:

$$\tilde{p}(x,0,\omega) = \begin{cases} P_{GF}^{(+)}, & \forall\ x \in (x_\alpha^-, x_\alpha^+] \\ 0, & \text{otherwise} \end{cases} \tag{A.7}$$

where $x_\alpha^- = x_\alpha - \Delta_x$, $x_\alpha^+ = x_\alpha + \Delta_x$, and transforming the uniformly distributed vertical force resulted in $\mathfrak{F}\left(P_{GF}^{(+)}\delta(t)\right) = P_{GF}^{(+)}$. The fluid pressure is calculated according to the *linearized* Bernoulli equation for unsteady potential flow [140]:

$$\tilde{p}(x,z,\omega) = -\rho_w \left(-\omega^2 \tilde{\phi}_\alpha^{(o,p)} + g\left(\frac{\partial \tilde{\phi}_\alpha^{(o,p)}}{\partial z} + z \right) \right) \tag{A.8}$$

where ρ_w is the fluid density and g is the gravitational constant. The first term in Eq. (A.8) introduces linear hydrodynamic effects due to the inertia of the fluid and the second term is responsible for hydrostatic effects. The nonlinear term that accounts for the dynamic pressure was removed by the linearization.

A.1.1. SOLUTION IN THE (k,z,ω)-DOMAIN

The Laplace equation in Eq. (A.4) is transformed to the k-domain:

$$-k^2\tilde{\tilde{\phi}}_\alpha^{(\mathrm{o,p})} + \frac{\partial^2\tilde{\tilde{\phi}}_\alpha^{(\mathrm{o,p})}}{\partial z^2} = 0 \qquad \forall\ z\in(-H,0) \tag{A.9}$$

Solving this ordinary differential equation for $\tilde{\tilde{\phi}}_\alpha^{(\mathrm{o,p})}$ gives:

$$\tilde{\tilde{\phi}}_\alpha^{(\mathrm{o,p})}(k,z,\omega) = c_1\cosh(kz) + c_2\mathrm{i}\sinh(kz) \qquad \forall\ z\in(-H,0) \tag{A.10}$$

Substituting this expression into the boundary condition at the seabed, Eq. (A.6), gives:

$$c_2 = c_1\tanh(kH) \tag{A.11}$$

Substituting this relation back into the expression of $\tilde{\tilde{\phi}}_\alpha^{(\mathrm{o,p})}$, Eq. (A.10), and rewriting one can obtain:

$$\tilde{\tilde{\phi}}_\alpha^{(\mathrm{o,p})}(k,z,\omega) = c_1\frac{\cosh(k(z+H))}{\cosh(kH)} = c_1 Z(k,z) \tag{A.12}$$

To avoid numerical issues, the depth Eigenfunction $Z(k,z)$ is rewritten as:

$$Z(k,z) = \frac{\exp(k(z+H)) + \exp(-k(z+H))}{\exp(kH)+\exp(-kH)} \tag{A.13}$$

Substituting the expression for the fluid pressure, Eq. (A.8), into the surface boundary condition, Eq. (A.7), and transforming to the (k,z,ω)-domain gives:

$$-\rho_w\left(-\omega^2\tilde{\tilde{\phi}}_\alpha^{(\mathrm{o,p})}(k,0,\omega) + g\frac{\partial\tilde{\tilde{\phi}}_\alpha^{(\mathrm{o,p})}(k,0,\omega)}{\partial z}\right) = P_{\mathrm{GF}}^{(+)}\frac{\mathrm{e}^{-\mathrm{i}kx_\alpha^+} - \mathrm{e}^{-\mathrm{i}kx_\alpha^-}}{-\mathrm{i}k} \tag{A.14}$$

Substituting the previously found expression for $\tilde{\tilde{\phi}}_\alpha$, Eq. (A.12), and solving for the unknown amplitude c_1 gives:

$$c_1 = \frac{P_{\mathrm{GF}}^{(+)}}{\rho_w g}\frac{\mathrm{i}}{k}\frac{\mathrm{e}^{-\mathrm{i}kx_\alpha^+} - \mathrm{e}^{-\mathrm{i}kx_\alpha^-}}{a-\lambda(k)} \tag{A.15}$$

where $a = \omega^2/g$ and $\lambda(k) = Z'(k,0) = k\tanh(kH)$. Therefore, the final expression for $\tilde{\tilde{\phi}}_\alpha^{(\mathrm{o,p})}$ in the (k,z,ω)-domain is:

$$\tilde{\tilde{\phi}}_\alpha^{(\mathrm{o,p})}(k,z,\omega) = \frac{P_{\mathrm{GF}}^{(+)}}{\rho_w g}\frac{\mathrm{i}}{k}\frac{\mathrm{e}^{-\mathrm{i}kx_\alpha^+} - \mathrm{e}^{-\mathrm{i}kx_\alpha^-}}{\mathfrak{D}(k)}Z(k,z) \tag{A.16}$$

where $\mathfrak{D}(k)=0$ is the dispersion relation of the open water region with $\mathfrak{D}(k)$ defined as:

$$\mathfrak{D}(k) = a-\lambda(k) \tag{A.17}$$

A.1.2. SOLUTION IN THE (x,z,ω)-DOMAIN

Next, the expression in the (k,z,ω)-domain, Eq. (A.16) is transformed back to the (x,z,ω)-domain:

$$\tilde{\phi}_\alpha^{(\mathrm{o,p})}(x,z,\omega) = \frac{\mathrm{i}P_{\mathrm{GF}}^{(+)}}{\rho_w g}\frac{1}{2\pi}\int_{-\infty}^{\infty}\frac{1}{k}\frac{\mathrm{e}^{\mathrm{i}k(x-x_\alpha^+)}-\mathrm{e}^{\mathrm{i}k(x-x_\alpha^-)}}{\mathfrak{D}(k)}Z(k,z)\,\mathrm{d}k \tag{A.18}$$

This integral is split into two integrals of the following generalized form:

$$\tilde{\Phi}(\hat{x},z,\omega) = \frac{\mathrm{i}P_{\mathrm{GF}}^{(+)}}{\rho_w g}\frac{1}{2\pi}\int_{-\infty}^{\infty}\frac{1}{k}\frac{\mathrm{e}^{\mathrm{i}k\hat{x}}Z(k,z)}{\mathfrak{D}(k)}\,\mathrm{d}k \tag{A.19}$$

The solution to the original problem can then be obtained as:

$$\tilde{\phi}_\alpha^{(\mathrm{o,p})}(x,z,\omega) = \tilde{\Phi}(x-x_\alpha^+,z,\omega)-\tilde{\Phi}(x-x_\alpha^-,z,\omega) \tag{A.20}$$

In order to evaluate the general integral in Eq. (A.19), it is converted into a contour integral. The original integration range is a line (in the complex k-plane) ranging from $-\infty$ to ∞ along the real axis. In order to obtain a closed contour C, a complex semi-circle with infinite radius is added to the original integration range. Using the residue theorem, the counter integral can then be represented as a summation over the residues of the integrand evaluated at the poles enclosed in the contour. Before starting with this procedure, the following definitions are made:

$$\tilde{\Phi}(\hat{x},z,\omega) = \int_{-\infty}^{\infty} I(k)\,\mathrm{d}k = \int_{-\infty}^{\infty}\frac{I_{\mathrm{num}}(k)}{I_{\mathrm{denom}}(k)}\,\mathrm{d}k \tag{A.21}$$

The conversion to a contour integral can only be done if the integral evaluates to zero along the added semi-circle. This requires the integrand $I(k)$ to converge to zero in the limit of $|k|\to\infty$ along the semi-circle. Analyzing $I(k)$ shows that the convergence depends only on the exponential term $\mathrm{e}^{\mathrm{i}k\hat{x}}$. The sign of $\hat{x}$ therefore dictates which half-plane has to be used:

$$\lim_{k\to\infty} I(k) = 0 \;\rightarrow\; \begin{cases} C \text{ closes over UHP} & \text{if } \hat{x}>0 \\ C \text{ closes over LHP} & \text{if } \hat{x}<0 \end{cases} \tag{A.22}$$

where LHP and UHP mean the lower and upper half-plane. Even for the special case when $\hat{x}=0$, the integrand still converges to zero since it is proportional to k^{-2} in the limit of $|k|\to\infty$. This means that the integrand converges unconditionally as long as the correct half-plane is used.

Since the integral converges to zero along the added segment, it can be added to the original integration range without changing the result of the integral. The resulting contour integral can then be evaluated using Cauchy's integral formula (taking into account that all poles are simple):

$$\begin{aligned}\oint_C I(k)\,\mathrm{d}k &= \begin{cases} 2\pi\mathrm{i}\sum_{\text{poles in UHP}}\operatorname{Res} I(k_n), & \text{if } \hat{x}\geq 0 \\ -2\pi\mathrm{i}\sum_{\text{poles in LHP}}\operatorname{Res} I(k_n^-), & \text{if } \hat{x}<0 \end{cases} \\ &= \begin{cases} 2\pi\mathrm{i}\sum_{n=0}^{\infty}\gamma_n\left.\frac{I_{\mathrm{num}}(k)}{I'_{\mathrm{denom}}(k)}\right|_{k=k_n}, & \text{if } \hat{x}\geq 0 \\ -2\pi\mathrm{i}\sum_{n=0}^{\infty}\gamma_n\left.\frac{I_{\mathrm{num}}(k)}{I'_{\mathrm{denom}}(k)}\right|_{k=k_n^-}, & \text{if } \hat{x}<0 \end{cases}\end{aligned} \tag{A.23}$$

where k_n^- are the roots of $I_{\text{denom}}(k)$ located in the LHP, k_n those in the UHP and $I'_{\text{denom}}(k)$ is given by:

$$Q(k) = I'_{\text{denom}}(k) = \frac{\partial(k\mathfrak{D}(k))}{\partial k} = \mathfrak{D}(k) - \left(k^2 H \operatorname{sech}^2(kH) + \lambda(k)\right) \tag{A.24}$$

Since the dispersion relation $\mathfrak{D}(k)$ is an even function in k, see Eq. (A.17), its poles are mirrored in the real and imaginary axis. This implies that its poles in the LHP are minus the poles in the UHP and so $k_n^- = -k_n$. The set of roots k_n is defined as follows:

- k_0: 0,
- k_1: the negative real pole of $D(k) = 0$,
- $k_j \mid j \geq 2$: the positive imaginary roots of $D(k) = 0$ in ascending order.

The numerical scheme used to find these roots is explained in section A.5. k_0 falls on the integration path and so had to be circumvented. The Cauchy principal value of this root contributes only half as much as the other roots that are all located inside the contour and γ_n in Eq. A.23 accounts for this difference:

$$\gamma_n = \begin{cases} 1/2, & \text{if } n = 0 \\ 1, & \text{if } n > 0 \end{cases} \tag{A.25}$$

Combining all these results, the general integral in Eq. (A.19) evaluates to:

$$\tilde{\Phi}(\hat{x}, z, \omega) = -\frac{P_{\text{GF}}^{(+)}}{\rho_w g} \begin{cases} \sum_{n=0}^{\infty} \gamma_n Q^{-1}(k_n) \mathrm{e}^{\mathrm{i}k_n \hat{x}} Z(k_n, z), & \text{if } \hat{x} \geq 0 \\ -\sum_{n=0}^{\infty} \gamma_n Q^{-1}(-k_n) \mathrm{e}^{-\mathrm{i}k_n \hat{x}} Z(-k_n, z), & \text{if } \hat{x} < 0 \end{cases} \tag{A.26}$$

where k_n^- was replaced by $-k_n$. Since both $Q(k)$ (Eq. (A.24)) and $Z(k, z)$ (Eq. (A.12)) are even functions in k, this equation can be simplified to:

$$\tilde{\Phi}(\hat{x}, z, \omega) = -\frac{P_{\text{GF}}^{(+)}}{\rho_w g} \operatorname{sgn}(\hat{x}) \sum_{n=0}^{N_{\text{k}}} \gamma_n Q_n^{-1} \mathrm{e}^{\mathrm{i}k_n |\hat{x}|} Z_n(z) \tag{A.27}$$

where $\lambda_n = \lambda(k_n)$, $Q_n = Q(k_n)$ and the infinite summation was truncated at N_{k} for practical reasons. Using this general result, the solution to the original inverse Fourier integral $\tilde{\phi}_\alpha(x, z)$ can be obtained using Eq. (A.20). This results in:

$$\tilde{\phi}_\alpha^{(\text{o,p})}(x, z, \omega) = -\frac{P_{\text{GF}}^{(+)}}{\rho_w g} \sum_{n=0}^{N_{\text{k}}} \gamma_n Q_n^{-1} I_{\alpha,n}(x) Z_n(z) \tag{A.28}$$

where the x-dependency is captured by $I_{\alpha,n}(x) = I_\alpha(k_n, x)$ with $I_\alpha(k, x)$ defined as:

$$I_\alpha(k, x) = \operatorname{sgn}\left(x - x_\alpha^+\right) \mathrm{e}^{\mathrm{i}k|x - x_\alpha^+|} - \operatorname{sgn}\left(x - x_\alpha^-\right) \mathrm{e}^{\mathrm{i}k|x - x_\alpha^-|} \tag{A.29}$$

Its derivatives with respect to x are given by:

$$\frac{\partial^q I_\alpha(k, x)}{\partial x^q} = (\mathrm{i}k)^q \left(\operatorname{sgn}\left(x - x_\alpha^+\right)^{q-1} e^{\mathrm{i}k|x - x_\alpha^+|} - \operatorname{sgn}\left(x - x_\alpha^-\right)^{q-1} e^{\mathrm{i}k|x - x_\alpha^-|}\right) \tag{A.30}$$

A.2. GREEN'S FUNCTION FOR ICE-COVERED FLUID LAYER

The Green's function $\tilde{\phi}_\alpha^{(\mathrm{i,p})}(x,z,\omega)$ of the ice-covered water is derived in a very similar manner as $\tilde{\phi}_\alpha^{(\mathrm{o,p})}(x,z,\omega)$. Its problem definition is given in Fig. A.2 on the left.

Since the fluid is again described by the Laplace equation and the boundary condition at $z=-H$ again prevents penetration of the fluid into the seabed, the derivation of $\tilde{\phi}_\alpha^{(\mathrm{i,p})}(x,z,\omega)$ can start from Eq. (A.12) that satisfies both of these conditions:

$$\tilde{\tilde{\phi}}_\alpha^{(\mathrm{i,p})}(k,z,\omega) = c_1 \frac{\cosh(k(z+H))}{\cosh(kH)} = c_1 Z(k,z) \tag{A.31}$$

At this point the derivation diverges as the ice-covered region has a different surface boundary condition. Because of the presence of the ice, the fluid pressure $\tilde{p}(x,0,\omega)$ has to balance with the internal stresses in the ice, as well as the distributed vertical force $P_{\mathrm{GF}}^{(-)}\delta(t)$. As the ice is modeled as a Kirchhoff-Love plate the surface boundary condition of the fluid becomes:

$$-\omega^2 \rho_\mathrm{i} h \tilde{w}(x,\omega) + D_\mathrm{i} \tilde{w}''''(x,\omega) = \tilde{p}(x,0,\omega) + \begin{cases} P_{\mathrm{GF}}^{(-)} & \forall\ x \in [x_\alpha - \Delta_\mathrm{x}, x_\alpha + \Delta_\mathrm{x}) \\ 0 & \text{otherwise} \end{cases} \tag{A.32}$$

where ρ_i is the density of the ice, h its thickness, $w(x,t)$ its transverse displacements and the dash denotes a spatial derivative. The plate's bending stiffness is given by $D_\mathrm{i} = Eh^3(12(1-\nu^2))^{-1}$ where E is the ice's Young's modules and ν its Poisson ratio.

To assure a continuity of vertical displacements between ice and fluid, the following interface condition has to be satisfied at $z=0$:

$$\tilde{w}(x,\omega) = \frac{\partial \tilde{\phi}_\alpha^{(\mathrm{i,p})}(x,0,\omega)}{\partial z} \qquad \forall\ x \in (-\infty,\infty) \tag{A.33}$$

Substituting this relation into the surface boundary condition, Eq. (A.32), using Eq. (A.8) for the fluid pressure $\tilde{p}$ and then transforming to the (k,z,ω)-domain gives:

$$\begin{aligned} \left(-\omega^2 \rho_\mathrm{i} h + D_\mathrm{i} k^4\right) \frac{\partial \tilde{\tilde{\phi}}_\alpha^{(\mathrm{i,p})}(k,0,\omega)}{\partial z} = \\ -\rho_w \left(-\omega^2 \tilde{\tilde{\phi}}_\alpha^{(\mathrm{i,p})}(k,0,\omega) + g \frac{\partial \tilde{\tilde{\phi}}_\alpha^{(\mathrm{i,p})}(k,0,\omega)}{\partial z} \right) + P_{\mathrm{GF}}^{(-)} \frac{e^{-\mathrm{i}k(x_\alpha+\Delta_\mathrm{x})} - e^{-\mathrm{i}k(x_\alpha-\Delta_\mathrm{x})}}{-\mathrm{i}k} \end{aligned} \tag{A.34}$$

The expression for the fluid potential, Eq. (A.31), is now substituted into this equation. Using the fact that $Z(k,0) = 1$ and assigning $Z'(k,0) = k\tanh(kH) = \lambda(k)$, Eq. (A.34) simplifies to:

$$\left(-\omega^2 \rho_\mathrm{i} h \lambda(k) + D_\mathrm{i} k^4 \lambda(k) + \rho_w g \lambda(k) - \rho_w \omega^2\right) c_1 = P_{\mathrm{GF}}^{(-)} \frac{e^{-\mathrm{i}kx_\alpha^+} - e^{-\mathrm{i}kx_\alpha^-}}{-\mathrm{i}k} \tag{A.35}$$

Solving for c_1 gives:

$$c_1 = \frac{P_{\mathrm{GF}}^{(-)}}{-\mathrm{i}k} \frac{1}{\lambda(k)} \frac{e^{-\mathrm{i}kx_\alpha^+} - e^{-\mathrm{i}kx_\alpha^-}}{-\omega^2 \rho_\mathrm{i} h + D_\mathrm{i} k^4 + \rho_w g - \rho_w \omega^2 \lambda^{-1}(k)} \tag{A.36}$$

Substituting this expression into the potential, Eq. (A.31), and transforming back to the (x,z,ω)-domain gives:

$$\tilde{\phi}_\alpha^{(\mathrm{i,p})}(x,z,\omega) = \frac{\mathrm{i}}{2\pi} P_{\mathrm{GF}}^{(-)} \int_{-\infty}^{\infty} \frac{1}{k} \frac{1}{\lambda(k)} \frac{e^{\mathrm{i}k(x-x_\alpha^+)} - e^{\mathrm{i}k(x-x_\alpha^-)}}{-\omega^2\rho_{\mathrm{i}}h + D_{\mathrm{i}}k^4 + \rho_w g - \rho_w\omega^2\lambda^{-1}(k)} Z(k,z)\,\mathrm{d}k \tag{A.37}$$

This integral can be rewritten as:

$$\tilde{\phi}_\alpha^{(\mathrm{i,p})}(x,z,\omega) = \frac{\mathrm{i}}{2\pi} \frac{P_{\mathrm{GF}}^{(-)}}{\rho_w g} \int_{-\infty}^{\infty} \frac{1}{k} \frac{1}{\lambda(k)} \frac{e^{\mathrm{i}k(x-x_\alpha^+)} - e^{\mathrm{i}k(x-x_\alpha^-)}}{\bar{\mathfrak{D}}(k)} Z(k,z)\,\mathrm{d}k \tag{A.38}$$

where $\bar{\mathfrak{D}}(k) = 0$ is the dispersion relation of the ice-covered region, with $\bar{\mathfrak{D}}(k)$ defined as:

$$\bar{\mathfrak{D}}(k) = \delta k^4 + 1 - a(\gamma + \lambda^{-1}(k)) \tag{A.39}$$

where $a = \omega^2/g$, $\gamma = h\rho_{\mathrm{i}}/\rho_w$, $\delta = D_{\mathrm{i}}/(\rho_w g)$ and the overbar is used to differentiate terms related to the ice-covered region from those related to the open water. Note that $\lambda(k)$ in the denominator does not generate any poles.

The integral in Eq. (A.36) is evaluated using the same procedure as used in the previous section. This results in the following final expression for $\tilde{\phi}_\alpha^{(\mathrm{i,p})}(x,z,\omega)$:

$$\tilde{\phi}_\alpha^{(\mathrm{i,p})}(x,z,\omega) = -\frac{P_{\mathrm{GF}}^{(-)}}{\rho_w g} \sum_{n=0}^{N_{\mathrm{k}}+2} \gamma_n \bar{Q}_n^{-1} \bar{I}_{\alpha,n}(x) \bar{Z}_n(z) \tag{A.40}$$

where γ_n is defined in Eq. (A.25), the x-dependency is captured by $\bar{I}_{\alpha,n}(x) = I_\alpha(\bar{k}_n, x)$, see Eq. (A.29) and the infinite summation was truncated for practical reasons. The truncation was done at $N_{\mathrm{k}}+2$ to facilitate the Eigenfunction Matching procedure that is applied in the next section. The set of roots of the ice-covered region $\bar{k}_n$ are defined as:

- $\bar{k}_0 = 0$,
- $\bar{k}_1$: the complex root in the first quadrant of $\bar{D}(k) = 0$,
- $\bar{k}_2$: the complex root in the second quadrant of $\bar{D}(k) = 0$,
- $\bar{k}_3$: the negative real root of $\bar{D}(k) = 0$,
- $\bar{k}_n \mid n \geq 4$: the positive imaginary roots of $\bar{D}(k) = 0$ in ascending order.

The numerical scheme used to find these roots is explained in section A.5. $\bar{Q}_n$ in Eq. (A.40) is the derivative of the denominator of Eq. (A.38) with respect to the wavenumber k:

$$\bar{Q}_n = \frac{\partial\left(k\lambda(k)\bar{\mathfrak{D}}(k)\right)}{\partial k} = \bar{\mathfrak{D}}_n\left(2\bar{\lambda}_n + H\left(\bar{k}_n^2 - \bar{\lambda}_n^2\right)\right) + 4\delta\bar{k}_n^4\bar{\lambda}_n + a\left(1 + \frac{H\left(\bar{k}_n^2 - \bar{\lambda}_n^2\right)}{\bar{\lambda}_n}\right), \tag{A.41}$$

where $\bar{\lambda}_n = \lambda(\bar{k}_n)$ and $\bar{\mathfrak{D}}_n = \bar{\mathfrak{D}}(\bar{k}_n)$.

A.3. GREEN'S FUNCTIONS FOR A SEMI-INFINITE ICE COVER

In the third section of this appendix, the final set of Green's functions $\tilde{\phi}_\alpha$ is derived. These Green's functions are a solution to the original inhomogeneous problem shown in Fig. A.1 and are derived using the Eigenfunction Matching procedure. A solution is sought for in the following form:

$$\tilde{\phi}_\alpha(x,z,\omega) = \begin{cases} \tilde{\phi}_\alpha^{(\mathrm{i,p})}(x,z,\omega) + \tilde{\phi}_\alpha^{(\mathrm{i,EM})}(x+l,z,\omega), & \forall\ x \in (\infty,-l] \cap z \in [-H,0] \\ \tilde{\phi}_\alpha^{(\mathrm{o,p})}(x,z,\omega) + \tilde{\phi}_\alpha^{(\mathrm{o,EM})}(x+l,z,\omega), & \forall\ x \in (-l,\infty) \cap z \in [-H,0] \end{cases} \tag{A.42}$$

where $\tilde{\phi}_\alpha^{(\mathrm{i,p})}$ and $\tilde{\phi}_\alpha^{(\mathrm{o,p})}$, which were derived in the previous two sections, account for the distributed vertical force $P_{\mathrm{GF}}\delta(t)$. The two new potentials, $\tilde{\phi}_\alpha^{(\mathrm{i,EM})}$ in the ice-covered region and $\tilde{\phi}_\alpha^{(\mathrm{o,EM})}$ in the open water region, are defined as:

$$\tilde{\phi}_\alpha^{(\mathrm{o,EM})}(x+l,z,\omega) = \sum_{n=1}^{N_\mathrm{k}} a_{\alpha,n} \mathrm{e}^{\mathrm{i}k_n(x+l)} Z_n(z) \qquad \forall\ x \in (-\infty,\infty) \cap z \in [-H,0] \tag{A.43a}$$

$$\tilde{\phi}_\alpha^{(\mathrm{i,EM})}(x+l,z,\omega) = \sum_{n=1}^{N_\mathrm{k}+2} \bar{a}_{\alpha,n} \mathrm{e}^{-\mathrm{i}\bar{k}_n(x+l)} \bar{Z}_n(z) \qquad \forall\ x \in (-\infty,\infty) \cap z \in [-H,0] \tag{A.43b}$$

These potentials are offset by l to assure the numerical stability of the evanescent modes. These two potentials sum over the modes of open water and ice-covered region and, therefore, satisfy all equations presented in sections A.1 and A.2 respectively. As their modal amplitudes $a_{\alpha,n}$ and $\bar{a}_{\alpha,n}$ are unknown, these potentials do not account for any loading. Consequently, k_0 and $\bar{k}_0$ are excluded as these were introduced by the distributed vertical force. The reason why $\tilde{\phi}_\alpha^{(\mathrm{i,EM})}(x,z,\omega)$ contains two extra modes is explained at the end of this section.

The assumed solution in Eq. (A.42) satisfies all the governing equations except those related to the interface between the two region, located at $x=-l$. The conditions that have to be satisfied at this interface are z-dependent. At the ice edge, located at $z=0$, the two boundary conditions of the Kirchhoff-Love plate have to be satisfied while along the water column, $z \in (-H,0)$, the interface conditions of the fluid have to be satisfied.

The two boundary conditions of the plate account for the force $F_{\mathrm{GF}}\delta(t)$ and moment $M_{\mathrm{GF}}\delta(t)$ that act on its edge located at $x=-l$:

$$D_\mathrm{i} \frac{\partial^2 \tilde{w}(-l,\omega)}{\partial x^2} = M_{\mathrm{GF}} \tag{A.44a}$$

$$D_\mathrm{i} \frac{\partial^3 \tilde{w}(-l,\omega)}{\partial x^3} = F_{\mathrm{GF}} \tag{A.44b}$$

Substituting the interface condition between ice and fluid, Eq. (A.33), and substituting the assumed form of the solution, Eq. (A.42), gives:

$$D_\mathrm{i}\left(\frac{\partial^3 \tilde{\phi}_\alpha^{(\mathrm{i,p})}(-l,0,\omega)}{\partial z x^2} + \frac{\partial^3 \tilde{\phi}_\alpha^{(\mathrm{i,EM})}(-l,0,\omega)}{\partial z x^2}\right) = M_{\mathrm{GF}} \tag{A.45a}$$

$$D_\mathrm{i}\left(\frac{\partial^4 \tilde{\phi}_\alpha^{(\mathrm{i,p})}(-l,0,\omega)}{\partial z x^3} + \frac{\partial^4 \tilde{\phi}_\alpha^{(\mathrm{i,EM})}(-l,0,\omega)}{\partial z x^3}\right) = F_{\mathrm{GF}} \tag{A.45b}$$

Substituting the expression of the two potentials, Eqs. (A.28) and (A.43b), into this equation results in:

$$D_\mathrm{i}\left(\frac{P_\mathrm{GF}^{(-)}}{\rho_w g}\sum_{n=0}^{N_\mathrm{k}+2}\gamma_n\bar{Q}_n^{-1}\bar{k}_n^2\bar{I}''_{\alpha,n}(-l)\bar{\lambda}_n-\sum_{n=1}^{N_\mathrm{k}+2}\bar{a}_n\bar{k}_n^2\bar{\lambda}_n\right)=M_\mathrm{GF} \tag{A.46a}$$

$$\mathrm{i}D_\mathrm{i}\left(\frac{P_\mathrm{GF}^{(-)}}{\rho_w g}\sum_{n=0}^{N_\mathrm{k}+2}\gamma_n\bar{Q}_n^{-1}\bar{k}_n^3\bar{I}'''_{\alpha,n}(-l)\bar{\lambda}_n+\sum_{n=1}^{N_\mathrm{k}+2}\bar{a}_n\bar{k}_n^3\bar{\lambda}_n\right)=F_\mathrm{GF} \tag{A.46b}$$

It is important to note that the contribution of k_0 and $\bar{k}_0$ is zero outside the domain of the distributed vertical force that these roots relate to. Since $x=0$ falls outside the domain of the distributed vertical force, see Eqs. (A.7) and (A.32), these wavenumbers should be excluded and so the summations of $\tilde{\phi}_\alpha^{(\mathrm{i,p})}$ and $\tilde{\phi}_\alpha^{(\mathrm{o,p})}$ start at $n=1$. Consequently, γ_n, given by Eq. (A.25), simplifies to 1. After applying these simplifications, the unknown amplitudes $\bar{a}_{\alpha,n}$ in Eqs. (A.46) are isolated, thereby obtaining the final form of the two boundary conditions of the plate:

$$\sum_{n=1}^{N_\mathrm{k}+2}\bar{a}_{\alpha,n}\bar{k}_n^2\bar{\lambda}_n=-\frac{M_\mathrm{GF}}{D_\mathrm{i}}+\frac{P_\mathrm{GF}^{(-)}}{\rho_w g}\sum_{n=1}^{N_\mathrm{k}+2}\bar{Q}_n^{-1}\bar{k}_n^2\bar{I}''_{\alpha,n}(-l)\bar{\lambda}_n \tag{A.47a}$$

$$\sum_{n=1}^{N_\mathrm{k}+2}\bar{a}_{\alpha,n}\bar{k}_n^3\bar{\lambda}_n=\frac{F_\mathrm{GF}}{\mathrm{i}D_\mathrm{i}}-\frac{P_\mathrm{GF}^{(-)}}{\rho_w g}\sum_{n=1}^{N_\mathrm{k}+2}\bar{Q}_n^{-1}\bar{k}_n^3\bar{I}'''_{\alpha,n}(-l)\bar{\lambda}_n \tag{A.47b}$$

Next, the two interface conditions of the fluid assure a continuity of the fluid pressure, Eq. (A.48a), and displacement, Eq. (A.48b), across the interface:

$$\left(\tilde{\phi}_\alpha^{(\mathrm{i,p})}+\tilde{\phi}_\alpha^{(\mathrm{i,EM})}\right)\Big|_{x=-l}=\left(\tilde{\phi}_\alpha^{(\mathrm{o,p})}+\tilde{\phi}_\alpha^{(\mathrm{o,EM})}\right)\Big|_{x=-l}\qquad\forall\, z\in[-H,0] \tag{A.48a}$$

$$\left(\frac{\partial\tilde{\phi}_\alpha^{(\mathrm{i,p})}}{\partial x}+\frac{\partial\tilde{\phi}_\alpha^{(\mathrm{i,EM})}}{\partial x}\right)\Big|_{x=-l}=\left(\frac{\partial\tilde{\phi}_\alpha^{(\mathrm{o,p})}}{\partial x}+\frac{\partial\tilde{\phi}_\alpha^{(\mathrm{o,EM})}}{\partial x}\right)\Big|_{x=-l}\qquad\forall\, z\in[-H,0] \tag{A.48b}$$

In order to handle the z-dependence of these two conditions, the orthogonality property of the depth Eigenfunction $Z_n(z)$ is used. Both sides of Eqs. (A.48a) and (A.48b) are multiplied by $Z_j(z)$ and then integrated along z from $-H$ to 0, where $k_j=k_n\mid j=1\,..\,N_\mathrm{k}$. This procedure is first applied to Eq. (A.48a):

$$\begin{aligned}&-\frac{P_\mathrm{GF}^{(-)}}{\rho_w g}\sum_{n=1}^{N_\mathrm{k}+2}\bar{Q}_n^{-1}\bar{I}_{\alpha,n}(-l)\frac{\bar{\lambda}_n-\lambda_j}{\bar{k}_n^2-k_j^2}+\sum_{n=1}^{N_\mathrm{k}+2}\bar{a}_{\alpha,n}\frac{\bar{\lambda}_n-\lambda_j}{\bar{k}_n^2-k_j^2}=\\&-\frac{P_\mathrm{GF}^{(+)}}{\rho_w g}\sum_{n=1}^{N_\mathrm{k}}Q_n^{-1}I_{\alpha,n}(-l)\frac{\lambda_n-\lambda_j}{k_n^2-k_j^2}+\sum_{n=1}^{N_\mathrm{k}}a_{\alpha,n}\frac{\lambda_n-\lambda_j}{k_n^2-k_j^2}\qquad\forall\, j=1\,..\,N_\mathrm{k}\end{aligned} \tag{A.49}$$

where the resulting integrals over z were substituted with:

$$\int_{-H}^{0}Z_n(z)Z_j(z)\,\mathrm{d}z=\frac{\lambda_n-\lambda_j}{k_n^2-k_j^2} \tag{A.50a}$$

$$\int_{-H}^{0}\bar{Z}_n(z)Z_j(z)\,\mathrm{d}z=\frac{\bar{\lambda}_n-\lambda_j}{\bar{k}_n^2-k_j^2} \tag{A.50b}$$

Since k_0 can be ignored, all remaining N_k modes of $\tilde{\phi}_\alpha^{(\mathrm{o,p})}$ satisfy the open water dispersion relation $\mathfrak{D}(k)=0$. This implies that $\lambda_n=\lambda_j=a$. Using this relation, the right hand side of Eq. (A.50a) simplifies to:

$$\frac{\lambda_n-\lambda_j}{k_n^2-k_j^2}=\begin{cases}0, & n\neq j\\ \left(k_n^2H\operatorname{sech}^2(k_nH)+\lambda_n\right)\left(2k_j^2\right)^{-1}=-Q_j\left(2k_j^2\right)^{-1}, & n=j\end{cases} \tag{A.51}$$

where $Q_j=Q(k_j)$. $k_n^2H\operatorname{sech}^2(k_nH)+\lambda_n$ is indeed equal to $-Q_j$ since k_0 is excluded, implying that $\mathfrak{D}(k)$ in Eq. (A.24) is equal to zero since all k_j satisfy the open-water dispersion relation. Based on this result, Eq. (A.49) can be simplified to:

$$\begin{aligned}\sum_{n=1}^{N_\mathrm{k}+2}\bar{a}_{\alpha,n}\frac{\bar{\lambda}_n-\lambda_j}{\bar{k}_n^2-k_j^2}=\frac{1}{2k_j^2}\left(\frac{P_\mathrm{GF}^{(+)}}{\rho_w g}I_{\alpha,j}(-l)-a_{\alpha,j}Q_j\right)+\\ \frac{P_\mathrm{GF}^{(-)}}{\rho_w g}\sum_{n=1}^{N_\mathrm{k}+2}\bar{Q}_n^{-1}\bar{I}_{\alpha,n}(-l)\frac{\bar{\lambda}_n-\lambda_j}{\bar{k}_n^2-k_j^2}\qquad\forall\ j=1..N_\mathrm{k}\end{aligned} \tag{A.52}$$

The same procedure is now applied to the second interface condition that assures a continuity of displacements, Eq. (A.48b), resulting in:

$$\begin{aligned}-\sum_{n=1}^{N_\mathrm{k}+2}\bar{a}_{\alpha,n}\bar{k}_n\frac{\bar{\lambda}_n-\lambda_j}{\bar{k}_n^2-k_j^2}=\frac{1}{2k_j^2}\left(\frac{P_\mathrm{GF}^{(+)}}{\rho_w g}k_jI'_{\alpha,j}(-l)-a_{\alpha,j}k_jQ_j\right)+\\ \frac{P_\mathrm{GF}^{(-)}}{\rho_w g}\sum_{n=1}^{N_\mathrm{k}+2}\bar{Q}_n^{-1}\bar{k}_n\bar{I}'_{\alpha,n}(-l)\frac{\bar{\lambda}_n-\lambda_j}{\bar{k}_n^2-k_j^2}\qquad\forall\ j=1..N_\mathrm{k}\end{aligned} \tag{A.53}$$

Eq. (A.52) is now multiplied by $-k_j$ and added to Eq. (A.53) to get the final expression that assures continuity of the fluid:

$$\begin{aligned}\sum_{n=1}^{N_\mathrm{k}+2}\bar{a}_{\alpha,n}\frac{\bar{\lambda}_n-\lambda_j}{\bar{k}_n-k_j}=-\frac{P_\mathrm{GF}^{(+)}}{\rho_w g}\frac{I'_{\alpha,j}(-l)-I_{\alpha,j}(-l)}{2k_j}\\ -\frac{P_\mathrm{GF}^{(-)}}{\rho_w g}\sum_{n=1}^{N_\mathrm{k}+2}\bar{Q}_n^{-1}\left(\bar{k}_n\bar{I}'_{\alpha,n}(-l)-k_j\bar{I}_{\alpha,n}(-l)\right)\frac{\bar{\lambda}_n-\lambda_j}{\bar{k}_n^2-k_j^2}\qquad\forall\ j=1..N_\mathrm{k}\end{aligned} \tag{A.54}$$

This equation has to be satisfied for each j, resulting in N_k equations to be satisfied. Together with the two equations from the boundary conditions of the plate, Eqs. (A.44), a total of $N_\mathrm{k}+2$ equations need to be satisfied. Using these equations, values can be computed for the $N_\mathrm{k}+2$ unknown amplitudes of the ice-covered region $\bar{a}_{\alpha,n}$. Afterwards the N_k unknown amplitudes of the open-water region $a_{\alpha,n}$ are readily computed using Eq. (A.52). The two boundary conditions of the plate are therefore the reason why $\tilde{\phi}_\alpha^{(\mathrm{i,p})}$ and $\tilde{\phi}_\alpha^{(\mathrm{i,EM})}$ in Eq. (A.43b) sum over two more modes than $\tilde{\phi}_\alpha^{(\mathrm{o,p})}$ and $\tilde{\phi}_\alpha^{(\mathrm{o,EM})}$.

A.4. AVERAGED RESPONSES

In the main body of this thesis the Boundary Element Method (BEM) is employed to discretize the spatially varying nonlinear dynamic pressure and axial compression. In

order to improve the accuracy of this method, the average response within an element is used rather than point-wise evaluations. The elements wherein the averaged response is computed are indexed with β, have a width of $2\Delta_\mathrm{x}$, and are centered around x_β, which has the same definition as x_α in Eq. (A.1). In this section, the analytical expressions for the averaged horizontal and vertical displacements within these elements are derived. These expressions have been validated against averages computed numerically.

Average horizontal response The averaged horizontal displacement in element β, $\tilde{u}_{\alpha,\beta}$, is given by:

$$\begin{aligned}\tilde{u}_{\alpha,\beta} &= \frac{1}{2\Delta_\mathrm{x}}\int_{x_\beta^-}^{x_\beta^+}\frac{\partial\tilde{\phi}(x,z)}{\partial x}\,\mathrm{d}x \\ &= \frac{1}{2\Delta_\mathrm{x}}\int_{x_\beta^-}^{x_\beta^+}\begin{cases}\frac{\partial\tilde{\phi}_\alpha^{(\mathrm{i,p})}(x,z,\omega)}{\partial x}+\frac{\partial\tilde{\phi}_\alpha^{(\mathrm{i,EM})}(x+l,z,\omega)}{\partial x} & \forall\ \beta<0\\ \frac{\partial\tilde{\phi}_\alpha^{(\mathrm{o,p})}(x,z,\omega)}{\partial x}+\frac{\partial\tilde{\phi}_\alpha^{(\mathrm{o,EM})}(x+l,z,\omega)}{\partial x} & \forall\ \beta>0\end{cases}\mathrm{d}x\end{aligned} \tag{A.55}$$

where $x_\beta^- = x_\beta - \Delta_\mathrm{x}$ and $x_\beta^+ = x_\beta + \Delta_\mathrm{x}$. The integral of $I'_\alpha(k,x)$ can be evaluated as follows:

$$\begin{aligned}I'_{\alpha,\beta}(k) &= \int_{x_\beta^-}^{x_\beta^+}\frac{\partial I_\alpha(k,x)}{\partial x}\,\mathrm{d}x \\ &= \int_{x_\beta^-}^{x_\beta^+}\mathrm{i}k\left(\mathrm{e}^{\mathrm{i}k|x-(x_\alpha+\Delta_\mathrm{x})|}-\mathrm{e}^{\mathrm{i}k|x-(x_\alpha-\Delta_\mathrm{x})|}\right)\mathrm{d}x \\ &= \int_{x_\beta^-}^{x_\beta^+}\mathrm{i}k\begin{cases}\mathrm{e}^{\mathrm{i}k(x-(x_\alpha+\Delta_\mathrm{x}))}, & \forall\ x\geq x_\alpha+\Delta_\mathrm{x}\\ \mathrm{e}^{-\mathrm{i}k(x-(x_\alpha+\Delta_\mathrm{x}))}, & \forall\ x<x_\alpha+\Delta_\mathrm{x}\end{cases}\mathrm{d}x \\ &\quad -\int_{x_\beta^-}^{x_\beta^+}\mathrm{i}k\begin{cases}\mathrm{e}^{\mathrm{i}k(x-(x_\alpha-\Delta_\mathrm{x}))}, & \forall\ x\geq x_\alpha-\Delta_\mathrm{x}\\ \mathrm{e}^{-\mathrm{i}k(x-(x_\alpha-\Delta_\mathrm{x}))}, & \forall\ x<x_\alpha-\Delta_\mathrm{x}\end{cases}\mathrm{d}x \\ &= \mathrm{i}k\begin{cases}\frac{1}{\mathrm{i}k}\left(\mathrm{e}^{\mathrm{i}k(x_\beta+\Delta_\mathrm{x}-(x_\alpha+\Delta_\mathrm{x}))}-\mathrm{e}^{\mathrm{i}k(x_\beta-\Delta_\mathrm{x}-(x_\alpha+\Delta_\mathrm{x}))}\right), & \forall\ x\geq x_\alpha+\Delta_\mathrm{x}\\ \frac{1}{-\mathrm{i}k}\left(\mathrm{e}^{-\mathrm{i}k(x_\beta+\Delta_\mathrm{x}-(x_\alpha+\Delta_\mathrm{x}))}-\mathrm{e}^{-\mathrm{i}k(x_\beta-\Delta_\mathrm{x}-(x_\alpha+\Delta_\mathrm{x}))}\right), & \forall\ x<x_\alpha+\Delta_\mathrm{x}\end{cases} \\ &\quad -\mathrm{i}k\begin{cases}\frac{1}{\mathrm{i}k}\left(\mathrm{e}^{\mathrm{i}k(x_\beta+\Delta_\mathrm{x}-(x_\alpha-\Delta_\mathrm{x}))}-\mathrm{e}^{\mathrm{i}k(x_\beta-\Delta_\mathrm{x}-(x_\alpha-\Delta_\mathrm{x}))}\right), & \forall\ x\geq x_\alpha-\Delta_\mathrm{x}\\ \frac{1}{-\mathrm{i}k}\left(\mathrm{e}^{-\mathrm{i}k(x_\beta+\Delta_\mathrm{x}-(x_\alpha-\Delta_\mathrm{x}))}-\mathrm{e}^{-\mathrm{i}k(x_\beta-\Delta_\mathrm{x}-(x_\alpha-\Delta_\mathrm{x}))}\right), & \forall\ x<x_\alpha-\Delta_\mathrm{x}\end{cases} \\ &= \begin{cases}\mathrm{e}^{\mathrm{i}k(x_\beta-x_\alpha)}\left(1-\mathrm{e}^{-2\mathrm{i}k\Delta_\mathrm{x}}\right), & \forall\ \beta>\alpha\\ \mathrm{e}^{-\mathrm{i}k(x_\beta-x_\alpha)}\left(\mathrm{e}^{2\mathrm{i}k\Delta_\mathrm{x}}-1\right), & \forall\ \beta\leq\alpha\end{cases} \\ &\quad -\begin{cases}\mathrm{e}^{\mathrm{i}k(x_\beta-x_\alpha)}\left(\mathrm{e}^{2\mathrm{i}k\Delta_\mathrm{x}}-1\right), & \forall\ \beta\geq\alpha\\ \mathrm{e}^{-\mathrm{i}k(x_\beta-x_\alpha)}\left(1-\mathrm{e}^{-2\mathrm{i}k\Delta_\mathrm{x}}\right), & \forall\ \beta<\alpha\end{cases} \\ &= \begin{cases}\mathrm{e}^{\mathrm{i}k(x_\beta-x_\alpha)}\left(\left(1-\mathrm{e}^{-2\mathrm{i}k\Delta_\mathrm{x}}\right)-\left(\mathrm{e}^{2\mathrm{i}k\Delta_\mathrm{x}}-1\right)\right), & \forall\ \beta>\alpha\\ \mathrm{e}^{-\mathrm{i}k(x_\beta-x_\alpha)}\left(\mathrm{e}^{2\mathrm{i}k\Delta_\mathrm{x}}-1\right)-\mathrm{e}^{\mathrm{i}k(x_\beta-x_\alpha)}\left(\mathrm{e}^{2\mathrm{i}k\Delta_\mathrm{x}}-1\right), & \forall\ \beta=\alpha\\ \mathrm{e}^{-\mathrm{i}k(x_\beta-x_\alpha)}\left(\left(\mathrm{e}^{2\mathrm{i}k\Delta_\mathrm{x}}-1\right)-\left(1-\mathrm{e}^{-2\mathrm{i}k\Delta_\mathrm{x}}\right)\right), & \forall\ \beta<\alpha\end{cases}\end{aligned} \tag{A.56}$$

$$= \begin{cases} 2\mathrm{e}^{\mathrm{i}k(x_\beta - x_\alpha)}\left(1-\cos(2k\Delta_\mathrm{x})\right), & \forall\ \beta > \alpha \\ \mathrm{e}^{-\mathrm{i}k(x_\beta - x_\alpha)}\left(\mathrm{e}^{2\mathrm{i}k\Delta_\mathrm{x}}-1\right) - \mathrm{e}^{\mathrm{i}k(x_\beta - x_\alpha)}\left(\mathrm{e}^{2\mathrm{i}k\Delta_\mathrm{x}}-1\right), & \forall\ \beta = \alpha \\ -2\mathrm{e}^{-\mathrm{i}k(x_\beta - x_\alpha)}\left(1-\cos(2k\Delta_\mathrm{x})\right), & \forall\ \beta < \alpha \end{cases}$$

$$= \begin{cases} 2\,\mathrm{sgn}(\beta-\alpha)\,\mathrm{e}^{\mathrm{i}k|x_\beta - x_\alpha|}\left(1-\cos(2k\Delta_\mathrm{x})\right), & \forall\ \beta \neq \alpha \\ 0, & \forall\ \beta = \alpha \end{cases} \tag{A.57}$$

Using this result, the four integrals in Eq. (A.55) can be evaluated as:

$$\frac{1}{2\Delta_\mathrm{x}}\int_{x_\beta^-}^{x_\beta^+} \frac{\partial\tilde{\phi}_\alpha^{(\mathrm{i,p})}(x,z)}{\partial x}\,\mathrm{d}x = -\frac{P_\mathrm{GF}^{(-)}}{\rho_w g}\frac{1}{2\Delta_\mathrm{x}}\sum_{n=0}^{N_\mathrm{k}+2}\gamma_n \bar{Q}_n^{-1}\bar{I}'_{\alpha,\beta,n}\bar{Z}_n(z) \tag{A.58}$$

$$\frac{1}{2\Delta_\mathrm{x}}\int_{x_\beta^-}^{x_\beta^+} \frac{\partial\tilde{\phi}_\alpha^{(\mathrm{o,p})}(x,z,\omega)}{\partial x}\,\mathrm{d}x = -\frac{P_\mathrm{GF}^{(+)}}{\rho_w g}\frac{1}{2\Delta_\mathrm{x}}\sum_{n=0}^{N_\mathrm{k}}\gamma_n Q_n^{-1} I'_{\alpha,\beta,n} Z_n(z) \tag{A.59}$$

$$\begin{aligned} \frac{1}{2\Delta_\mathrm{x}}\int_{x_\beta^-}^{x_\beta^+} \frac{\partial\tilde{\phi}_\alpha^{(\mathrm{o,EM})}(x+l,z,\omega)}{\partial x}\,\mathrm{d}x &= \frac{1}{2\Delta_\mathrm{x}}\int_{x_\beta^-}^{x_\beta^+}\sum_{n=1}^{N_\mathrm{k}} a_n(\mathrm{i}k_n)\mathrm{e}^{\mathrm{i}k_n(x+l)}Z_n(z)\,\mathrm{d}x \\ &= \frac{1}{2\Delta_\mathrm{x}}\sum_{n=1}^{N_\mathrm{k}} a_n(\mathrm{i}k_n)\frac{1}{\mathrm{i}k_n}\left(\mathrm{e}^{\mathrm{i}k_n(x_\beta^+ + l)} - \mathrm{e}^{\mathrm{i}k_n(x_\beta^- + l)}\right)Z_n(z) \\ &= \frac{1}{2\Delta_\mathrm{x}}\sum_{n=1}^{N_\mathrm{k}} a_n\left(\mathrm{e}^{\mathrm{i}k_n\Delta_\mathrm{x}} - \mathrm{e}^{-\mathrm{i}k_n\Delta_\mathrm{x}}\right)\mathrm{e}^{\mathrm{i}k_n(x_\beta+l)}Z_n(z) \\ &= \frac{1}{\Delta_\mathrm{x}}\sum_{n=1}^{N_\mathrm{k}} a_n\sinh(\mathrm{i}k_n\Delta_\mathrm{x})\mathrm{e}^{\mathrm{i}k_n(x_\beta+l)}Z_n(z) \\ &= \frac{\mathrm{i}}{\Delta_\mathrm{x}}\sum_{n=1}^{N_\mathrm{k}} a_n\sin(k_n\Delta_\mathrm{x})\mathrm{e}^{\mathrm{i}k_n(x_\beta+l)}Z_n(z) \end{aligned} \tag{A.60}$$

$$\begin{aligned} \frac{1}{2\Delta_\mathrm{x}}\int_{x_\beta^-}^{x_\beta^+} \frac{\partial\tilde{\phi}_\alpha^{(\mathrm{i,EM})}(x+l,z,\omega)}{\partial x}\,\mathrm{d}x &= \frac{1}{2\Delta_\mathrm{x}}\int_{x_\beta^-}^{x_\beta^+}\sum_{n=1}^{N_\mathrm{k}+2} \bar{a}_n(-\mathrm{i}\bar{k}_n)\mathrm{e}^{-\mathrm{i}\bar{k}_n(x+l)}\bar{Z}_n(z)\,\mathrm{d}x \\ &= \frac{1}{2\Delta_\mathrm{x}}\sum_{n=1}^{N_\mathrm{k}+2} \bar{a}_n\left(\mathrm{e}^{-\mathrm{i}\bar{k}_n(x_\beta^+ + l)} - \mathrm{e}^{-\mathrm{i}\bar{k}_n(x_\beta^- + l)}\right)\bar{Z}_n(z) \\ &= \frac{1}{2\Delta_\mathrm{x}}\sum_{n=1}^{N_\mathrm{k}+2} \bar{a}_n\left(\mathrm{e}^{-\mathrm{i}\bar{k}_n\Delta_\mathrm{x}} - \mathrm{e}^{-\mathrm{i}\bar{k}_n(-\Delta_\mathrm{x})}\right)\mathrm{e}^{-\mathrm{i}\bar{k}_n(x_\beta+l)}\bar{Z}_n(z) \\ &= -\frac{1}{\Delta_\mathrm{x}}\sum_{n=1}^{N_\mathrm{k}+2} \bar{a}_n\sinh(\mathrm{i}\bar{k}_n\Delta_\mathrm{x})\mathrm{e}^{-\mathrm{i}\bar{k}_n(x_\beta+l)}\bar{Z}_n(z) \\ &= -\frac{\mathrm{i}}{\Delta_\mathrm{x}}\sum_{n=1}^{N_\mathrm{k}+2} \bar{a}_n\sin(\bar{k}_n\Delta_\mathrm{x})\mathrm{e}^{-\mathrm{i}\bar{k}_n(x_\beta+l)}\bar{Z}_n(z) \end{aligned} \tag{A.61}$$

A

Average vertical response The averaged vertical displacement within element β, $\tilde{w}_{\alpha,\beta}$, is given by:

$$\begin{aligned}\tilde{w}_{\alpha,\beta} &= \frac{1}{2\Delta_x}\int_{x_\beta^-}^{x_\beta^+}\frac{\partial\tilde{\phi}_\alpha(x,z,\omega)}{\partial z}\,\mathrm{d}x \\ &= \frac{1}{2\Delta_x}\int_{x_\beta^-}^{x_\beta^+}\begin{cases}\frac{\partial\tilde{\phi}_\alpha^{(\mathrm{i,p})}(x,z,\omega)}{\partial z}+\frac{\partial\tilde{\phi}_\alpha^{(\mathrm{i,EM})}(x+l,z,\omega)}{\partial z} & \forall\ \beta<0\\ \frac{\partial\tilde{\phi}_\alpha^{(\mathrm{o,p})}(x,z,\omega)}{\partial z}+\frac{\partial\tilde{\phi}_\alpha^{(\mathrm{o,EM})}(x+l,z,\omega)}{\partial z} & \forall\ \beta>0\end{cases}\mathrm{d}x\end{aligned} \tag{A.62}$$

The integral over $I_\alpha(k,x)$, given by Eq. (A.29), can be evaluated to give:

$$\begin{aligned}I_{\alpha,\beta}(k) &= \int_{x_\beta^-}^{x_\beta^+} I_\alpha(k,x)\,\mathrm{d}x \\ &= -4\begin{cases}\mathrm{sinc}(\Delta_x k)\mathrm{e}^{\mathrm{i}\Delta_x k}, & \text{if } \alpha=\beta\\ \mathrm{i}\Delta_x k\,\mathrm{sinc}^2(\Delta_x k)\mathrm{e}^{2\mathrm{i}\Delta_x k|\alpha-\beta|}, & \text{if } \alpha\neq\beta\end{cases} \\ &= -4\begin{cases}\Delta_x\,\mathrm{sinc}\left(\frac{\Delta_x k}{\pi}\right)\mathrm{e}^{\mathrm{i}\Delta_x k}, & \text{if } \alpha=\beta\\ \mathrm{i}\Delta_x^2 k\,\mathrm{sinc}^2\left(\frac{\Delta_x k}{\pi}\right)\mathrm{e}^{2\mathrm{i}\Delta_x k|\alpha-\beta|}, & \text{if } \alpha\neq\beta\end{cases} \qquad \text{(Matlab)}\end{aligned} \tag{A.63}$$

Using this result, the integrals in Eq. (A.62) are evaluated to:

$$\frac{1}{2\Delta_x}\int_{x_\beta^-}^{x_\beta^+}\frac{\partial\tilde{\phi}_\alpha^{(\mathrm{i,p})}(x,z,\omega)}{\partial z}\,\mathrm{d}x = -\frac{P_{\mathrm{GF}}^{(-)}}{\rho_w g}\frac{1}{2\Delta_x}\sum_{n=0}^{N_k+2}\gamma_n\bar{Q}_n^{-1}\bar{I}_{\alpha,\beta,n}\bar{Z}_n'(z) \tag{A.64}$$

$$\frac{1}{2\Delta_x}\int_{x_\beta^-}^{x_\beta^+}\frac{\partial\tilde{\phi}_\alpha^{(\mathrm{o,p})}(x,z,\omega)}{\partial z}\,\mathrm{d}x = -\frac{P_{\mathrm{GF}}^{(+)}}{\rho_w g}\frac{1}{2\Delta_x}\sum_{n=0}^{N_k}\gamma_n Q_n^{-1} I_{\alpha,\beta,n} Z_n'(z) \tag{A.65}$$

where $I_{\alpha,\beta,n} = I_{\alpha,\beta}(k_n)$ and $\bar{I}_{\alpha,\beta,n} = I_{\alpha,\beta}(\bar{k}_n)$. Continuing with the remaining two integrals:

$$\begin{aligned}\frac{1}{2\Delta_x}\int_{x_\beta^-}^{x_\beta^+}\frac{\partial\tilde{\phi}_\alpha^{(\mathrm{o,EM})}(x+l,z,\omega)}{\partial z}\,\mathrm{d}x &= \frac{1}{2\Delta_x}\int_{x_\beta^-}^{x_\beta^+}\sum_{n=1}^{N_k} a_n\mathrm{e}^{\mathrm{i}k_n(x+l)}Z_n'(z)\,\mathrm{d}x \\ &= \frac{1}{2\Delta_x}\sum_{n=1}^{N_k} a_n\frac{1}{\mathrm{i}k_n}\left(\mathrm{e}^{\mathrm{i}k_n(x_\beta^+ +l)}-\mathrm{e}^{\mathrm{i}k_n(x_\beta^- +l)}\right)Z_n'(z) \\ &= -\mathrm{i}\frac{1}{2\Delta_x}\sum_{n=1}^{N_k} a_n k_n^{-1}\left(\mathrm{e}^{\mathrm{i}k_n\Delta_x}-\mathrm{e}^{-\mathrm{i}k_n\Delta_x}\right)\mathrm{e}^{\mathrm{i}k_n(x_\beta+l)}Z_n'(z) \\ &= -\mathrm{i}\frac{1}{\Delta_x}\sum_{n=1}^{N_k} a_n k_n^{-1}\sinh(\mathrm{i}k_n\Delta_x)\mathrm{e}^{\mathrm{i}k_n(x_\beta+l)}Z_n'(z) \\ &= \frac{1}{\Delta_x}\sum_{n=1}^{N_k} a_n\,\mathrm{sinc}(k_n\Delta_x)\mathrm{e}^{\mathrm{i}k_n(x_\beta+l)}Z_n'(z) \\ &= \sum_{n=1}^{N_k} a_n\,\mathrm{sinc}\left(\frac{k_n\Delta_x}{\pi}\right)\mathrm{e}^{\mathrm{i}k_n(x_\beta+l)}Z_n'(z) \qquad \text{(Matlab)}\end{aligned} \tag{A.66}$$

$$\begin{aligned}
\frac{1}{2\Delta_x}\int_{x_\beta^-}^{x_\beta^+}\frac{\partial\tilde{\phi}_\alpha^{(i,EM)}(x+l,z,\omega)}{\partial z}\,dx &= \frac{1}{2\Delta_x}\int_{x_\beta^-}^{x_\beta^+}\sum_{n=1}^{N_k+2}\bar{a}_n e^{-i\bar{k}_n(x+l)}\bar{Z}_n'(z)\,dx \\
&= \frac{1}{2\Delta_x}\sum_{n=1}^{N_k+2}\bar{a}_n\frac{1}{-i\bar{k}_n}\left(e^{-i\bar{k}_n(x_\beta^+ +l)}-e^{-i\bar{k}_n(x_\beta^- +l)}\right)\bar{Z}_n'(z) \\
&= i\frac{1}{2\Delta_x}\sum_{n=1}^{N_k+2}\bar{a}_n\bar{k}_n^{-1}\left(e^{-i\bar{k}_n\Delta_x}-e^{-i\bar{k}_n(-\Delta_x)}\right)e^{-i\bar{k}_n(x_\beta+l)}\bar{Z}_n'(z) \\
&= -i\frac{1}{\Delta_x}\sum_{n=1}^{N_k+2}\bar{a}_n\bar{k}_n^{-1}\sinh(i\bar{k}_n\Delta_x)e^{-i\bar{k}_n(x_\beta+l)}\bar{Z}_n'(z) \\
&= \frac{1}{\Delta_x}\sum_{n=1}^{N_k+2}\bar{a}_n\,\mathrm{sinc}(\bar{k}_n\Delta_x)e^{-i\bar{k}_n(x_\beta+l)}\bar{Z}_n'(z) \\
&= \sum_{n=1}^{N_k+2}\bar{a}_n\,\mathrm{sinc}\left(\frac{\bar{k}_n\Delta_x}{\pi}\right)e^{-i\bar{k}_n(x_\beta+l)}\bar{Z}_n'(z) \qquad \text{(Matlab)}
\end{aligned} \tag{A.67}$$

A.5. ROOT-FINDING ALGORITHMS

In the last section of this appendix, the numerical schemes are explained that were used to find the set of roots k_n that satisfies the open water dispersion equation $\mathfrak{D}(k)=0$ and the set $\bar{k}_n$ that satisfies the ice-covered dispersion equation $\bar{\mathfrak{D}}(k)=0$. The numerical schemes are based on a set of recursive formulas that differ for each type of root. The formulas for each type are listed below. The scheme evaluates the recursive formulas and should converge to the root k_j. The scheme has converged successfully if $|k_j^{(i+1)}-k_j^{(i)}|<\epsilon_{abs}$ where i is the iteration counter that starts at $i=0$. Even with very strict tolerances, for example $\epsilon_{abs}=10^{-12}$ as used in this thesis, the scheme converges in only several iterations (less than 10).

A.5.1. ROOTS FOR THE OPEN WATER REGION

The dispersion equation for open water is given in Eq. (A.17) and is repeated here for convenience:

$$\mathfrak{D}(k)=a-\lambda(k)=\frac{\omega^2}{g}-k\tanh(kH)=0 \tag{A.68}$$

Solving this equation for k results in the set of roots k_n. As explained in section A.1, k_n starts with $k_0=0$, followed by k_1 which is the negative real root of $\mathfrak{D}(k)=0$. All subsequent entries contain the imaginary roots of $\mathfrak{D}(k)=0$ located in the UHP, in ascending order.

Negative real root The negative real root k_1 is found using the following recursive formula that starts with $k^{(0)}=a$:

$$k^{(i+1)}=\frac{a}{\tanh(k^{(i)}H)} \tag{A.69}$$

Imaginary roots in the UHP For finding the imaginary roots located in the UHP, $k_n\ \forall\ n\geq 2$, the dispersion relation is mapped to the imaginary axis. This allows the computation

A

to be done using real numbers which improves the computational speed:

$$\mathfrak{D}(\mathrm{i}k) = a + k\tan(kH) = 0 \tag{A.70}$$

The roots of this equation are found using the following recursive formula:

$$k^{(i+1)} = \frac{1}{H}\left(\operatorname{atan}\left(\frac{a}{k^{(i)}}\right) + \pi\left\lceil\left|k^{(i)}\frac{H}{\pi}\right| - 1/2\right\rceil\right) \tag{A.71}$$

where $\lceil..\rceil$ is the ceiling function that maps a real number to the smallest following integer. The first term is the direct solution of $\mathfrak{D}(\mathrm{i}k) = 0$ and the second term accounts for the multivalued nature of the arctangent. Once a root has been found, it should be multiplied with i to account for the substitution of ik done in Eq. (A.70). Since $\{\tan(kH) \mid k \in [\pi(j-1/2),\ \pi(j+1/2)] \cap j \in \mathbb{N}_0\} \mapsto [-\infty,\infty]$ and a/k is a finite number, $\mathfrak{D}(\mathrm{i}k) = 0$ will have a root between each pair of consecutive poles of $\tan(kH)$. Therefore, the initial guesses are set half-way between each pair of poles:

$$k_j^{(0)} = \frac{j\pi}{H} \ \forall\ j \in \mathbb{N}_0 \tag{A.72}$$

Note that $j = 0$ is not guaranteed to return a root since $\{\tan(kH) \mid k \in [0,\ \pi/2]\} \mapsto [0,\infty]$.

A.5.2. ROOTS FOR THE ICE-COVERED REGION

The dispersion equation of the ice-covered region is given in Eq. (A.39) and is repeated here for convenience:

$$\bar{\mathfrak{D}}(k) = \delta k^4 + 1 - a(\gamma + \lambda^{-1}(k)) = 0 \tag{A.73}$$

Solving this equation for k results in the set of roots $\bar{k}_n$. As explained in section A.2, $\bar{k}_n$ starts with $\bar{k}_0 = 0$, followed by $\bar{k}_1$ and $\bar{k}_2$ which are the complex poles of $\bar{\mathfrak{D}}(k) = 0$ located in the UHP. $\bar{k}_3$ is the negative real root of $\bar{\mathfrak{D}}(k) = 0$ and all subsequent entries contain the imaginary roots of $\bar{\mathfrak{D}}(k) = 0$ located in the UHP, in ascending order.

Complex roots in the UHP The complex conjugated roots $\bar{k}_1$ and $\bar{k}_2$ located in the UHP are found using the following recursive formula:

$$k^{(i+1)} = \sqrt[4]{-\delta^{-1}\left(1 - a\left(\gamma + \lambda^{-1}(k^{(i)})\right)\right)} \tag{A.74}$$

The initial guess is set to the solution of the plate without hydrodynamic effects: $k^{(0)} = \sqrt[4]{\delta^{-1}(a\gamma - 1)}$.

Negative real root The negative real root $\bar{k}_3$ is found using the following recursive formula that starts at $i = 0$:

$$k^{(i+1)} = \frac{1}{\tanh(k^{(i)}H)}\frac{a}{a\gamma - \delta(k^{(i)})^4 - 1} \tag{A.75}$$

with the initial guess $k^{(0)} = k_1$.

Imaginary roots in the UHP The imaginary roots of $\tilde{\mathfrak{D}}(k) = 0$ are found using the following recursive formula that starts at $i = 0$:

$$k^{(i+1)} = \frac{1}{H}\left(\operatorname{atan}\left(\frac{a}{k^{(i)}}\frac{1}{\delta(k^{(i)})^4 + 1 - a\gamma}\right) + \pi\left\lceil\left|k^{(i)}\frac{H}{\pi}\right| - 1/2\right\rceil\right) \tag{A.76}$$

The roots are again located between pairs of consecutive poles of $\tan(kH)$. The initial guesses for Eq. (A.76) are located half-way between each pair of poles:

$$k_j^{(0)} = \frac{j\pi}{H} \;\forall\; j \in \mathbb{N}_0 \tag{A.77}$$

where $j = 0$ is again not guaranteed to return a root.

B

NUMERICAL SCHEME FOR EVALUATING IFTS

In this section, a numerical scheme is introduced for evaluating the Inverse Fourier Transforms (IFTs) that arose in Ch. 4. In order to obtain a scheme that can effectively and efficiently evaluate these IFTs, the problem in Ch. 4 is analyzed, thereby establishing the design specifications for the numerical IFT scheme. This is done in section B.1. Next, the analytical form of the IFTs is optimized in section B.2. The numerical aspects of the scheme are then discussed in section B.3. Lastly, the scheme is validated in section B.4.

B.1. REQUIREMENTS FOR THE IFT SCHEME

Analysis. The numerical scheme will be optimized for the IFTs that arose in Ch. 4. The IFTs to be solved, based on Eq. (4.24) and (4.31), are of the following form:

$$\mathcal{L}_n^{(i)} = \frac{1}{2\pi}\int_{-\infty}^{\infty} \tilde{\boldsymbol{\mathcal{G}}}_i(\omega)\tilde{\mathcal{L}}(\omega)\mathrm{e}^{\mathrm{i}\omega\Delta_\mathrm{t}n}\,\mathrm{d}\omega \tag{B.1a}$$

$$\mathcal{T}_n^{(i)} = \frac{1}{2\pi}\int_{-\infty}^{\infty} \tilde{\boldsymbol{\mathcal{G}}}_i(\omega)\tilde{\mathcal{T}}(\omega)\mathrm{e}^{\mathrm{i}\omega\Delta_\mathrm{t}n}\,\mathrm{d}\omega \tag{B.1b}$$

where Δ_t is the time step, n is the index for time ($t = n\Delta_\mathrm{t}$), $\tilde{\boldsymbol{\mathcal{G}}}_i(\omega)$ is the set of $\hat{N}_q$ Green's functions that contains the frequency-domain response of each state-component in the reduced state-vector $\hat{\mathbf{q}}_n$ (a vector of length $\hat{N}_q$, see Eq. (4.39)) excited by the i^{th} pseudo-force and $\tilde{\mathcal{L}}(\omega)$ and $\tilde{\mathcal{T}}(\omega)$ were introduced by the linearization of the loading within each time step. In total, N_F pseudo-forces act on the system and therefore the total number of Green's functions is $\hat{N}_\mathrm{q} \times N_\mathrm{F}$. For each input-output pair, both IFTs have to be evaluated. The total number of IFTs is thus $2\hat{N}_\mathrm{q} \times N_\mathrm{F}$. If all pseudo-forces are zero at $t = 0$, $\mathcal{L}_n^{(i)}$ is not needed and the total number of IFTs reduces to $\hat{N}_\mathrm{q} \times N_\mathrm{F}$. Eqs. (B.1) are further analyzed in order to assess their implications on the design of the integration scheme.

First, both equations show that adding new integration points requires evaluation of the Green's functions $\tilde{\mathcal{G}}_i(\omega)$ of the system. This is computationally expensive as for each frequency the set of roots $\bar{k}_n$ needs to be computed (see App. A.1 and A.2 for the details). Moreover, for each frequency, as well as for every pseudo-force, the eigenfunction matching procedure in App. A.3 has to be performed in order to find the modal amplitudes of the system, which involves solving a $(N_\mathrm{k}+2)\times(N_\mathrm{k}+2)$ linear problem. As both of these steps are computationally expensive, the numerical scheme should strive to minimize the number of evaluations of the system's Green's functions.

Second, each Green's function sums over the modes of the system and each mode is based on a wavenumber. These wavenumbers are found using a numerical root-finding scheme (see App. A.5) and therefore all Green's functions in $\tilde{\mathcal{G}}_i(\omega)$ are discrete functions. Because of this, the IFTs in Eqs. (B.1) cannot be evaluated exactly and will contain a time-domain error. As the response of the system is obtained by superimposing the response excited by all pseudo-forces, see Eq. (4.33), it is imperative that all IFTs are evaluated with a time-domain error of a similar order of magnitude.

Based on these two properties, the following two specifications are set for the design of the numerical IFT scheme:

1. The scheme should minimize the number of evaluations of the Green's functions, i.e. it should minimize the number of integration points.

2. The scheme should evaluate each IFT with a time-domain error that is of a similar order of magnitude.

These two specifications are the primary drivers for the design of the integration scheme. The remaining design space is used to make the scheme as general as possible and to maximize its computational speed.

Implications. In order to guarantee the second specification, the integration scheme has to be adaptive. This implies that the scheme will be iterative, gradually refining the frequency-domain mesh until the resulting time-domain error meets the specified tolerances. In order to minimize the number of evaluations of the Green's functions, the scheme should reuse all previously computed integration points at each iteration, i.e. the scheme should nest. Therefore, an adaptive, nesting integration scheme is required.

Scope. The scope is limited to discrete Green's functions of real-valued, causal systems that are bounded for all real frequencies, i.e. damped systems.

B.2. SELECTION OF THE ANALYTICAL FORM

To start, Eqs. (B.1) are rewritten into the following general form for clarity:

$$f(t) = \frac{1}{2\pi}\int_{-\infty}^{\infty} \tilde{f}(\omega)\mathrm{e}^{\mathrm{i}\omega t}\,\mathrm{d}\omega \tag{B.2}$$

Since the time-domain response $f(t)$ is real, $\tilde{f}(\omega)$ is an Hermitian function, which means that its real part is symmetric and imaginary part is anti-symmetric. Consequently, the

integral over the imaginary part of $\tilde{f}(\omega)e^{i\omega t}$ evaluates to zero and this equation simplifies to:

$$\begin{aligned} f(t) &= \frac{1}{2\pi}\Re\left(\int_{-\infty}^{\infty}\tilde{f}(\omega)e^{i\omega t}\right)d\omega + \frac{i}{2\pi}\Im\left(\int_{-\infty}^{\infty}\tilde{f}(\omega)e^{i\omega t}\right)d\omega \\ &= \frac{1}{\pi}\Re\left(\int_{0}^{\infty}\tilde{f}(\omega)e^{i\omega t}\,d\omega\right) \\ &= \frac{1}{\pi}\int_{0}^{\infty}\Re\big(\tilde{f}(\omega)\big)\Re\big(e^{i\omega t}\big) - \Im\big(\tilde{f}(\omega)\big)\Im\big(e^{i\omega t}\big)\,d\omega \end{aligned} \tag{B.3}$$

where $\Re$ and $\Im$ imply taking the real and imaginary parts respectively. These forms are preferred over the form in Eq. (B.2) as the integration range has been reduced. Next, since the system is assumed to be causal $\Re\big(\tilde{f}(\omega)\big)\Re\big(e^{i\omega t}\big) - \Im\big(\tilde{f}(\omega)\big)\Im\big(e^{i\omega t}\big) = 0 \;\forall\; t < 0$ and, consequently, $\Re\big(\tilde{f}(\omega)\big)\Re\big(e^{i\omega t}\big) = -\Im\big(\tilde{f}(\omega)\big)\Im\big(e^{i\omega t}\big)$. This relation allows the equation to be further simplified to:

$$f(t) = \frac{2}{\pi}\int_{0}^{\infty}\Re\big(\tilde{f}(\omega)\big)\cos(\omega t)\,d\omega \tag{B.4a}$$

$$= -\frac{2}{\pi}\int_{0}^{\infty}\Im\big(\tilde{f}(\omega)\big)\sin(\omega t)\,d\omega \tag{B.4b}$$

These two forms are analytically equivalent but numerically different. The cosine-based form is more susceptible to catastrophic cancellation for small t which can result in a loss of significant digits, causing large errors in $f(t)$ at small values of t. Minimizing this error is important as the iterative set of equations being solved at each time step, Eq. (4.34), depends on $\mathcal{T}_0^{(i)}$ which, effectively, is the evaluation after only a single time step, i.e. at $t = 1\Delta_t$. As such the sin-based form is chosen.

B.3. NUMERICAL ASPECTS

The numerical aspects of the scheme are explained next. First, the integration range will be truncated in order to obtain a definite integral. Since $\tilde{f}(\omega)$ is assumed to be a discrete function in ω, an interpolation scheme is then introduced to interpolate between these discrete points, thereby obtaining a continuous approximation of $\tilde{f}(\omega)$. Next, the inverse transform is evaluated, thereby obtaining an approximation to $f(t)$. Since $f(t)$ contains an error due to the truncation and interpolation, the adaptive component of the scheme is then introduced to assure that this error $\epsilon(t)$ meets the user-specified tolerances. These steps are explained in detail next.

Integration range truncation. First, the integration range in Eq. (B.4b) is truncated in order to obtain a definite integral:

$$f(t) \approx -\frac{2}{\pi}\int_{0}^{\Omega}\Im\big(\tilde{f}(\omega)\big)\sin(\omega t)\,d\omega \tag{B.5}$$

This truncation introduces an error $\epsilon_\Omega(t)$ which contributes to the overall error of the scheme $\epsilon(t)$. $\epsilon_\Omega(t)$ is defined as:

$$\epsilon_\Omega(t) = -\frac{2}{\pi}\int_{\Omega}^{\infty}\Im\big(\tilde{f}(\omega)\big)\sin(\omega t)\,d\omega \tag{B.6}$$

For now, it is assumed that $\epsilon_\Omega(t)$ can be ignored if Ω is sufficiently large. The exact value of Ω is specified later in this appendix.

B

Interpolation. Next, since $\tilde{f}(\omega)$ is assumed to be a discrete function in ω, an interpolation scheme is needed to interpolate between the discrete points. The resulting continuous interpolation function can then be used to approximate $\tilde{f}(\omega)$. Using this interpolation function, the IFT can then be evaluated, thereby obtaining an approximation of $f(t)$.

First, a decision has to be made on whether or not to discretize $\sin(\omega t)$ in Eq. (B.5). Discretizing this term will increase the time-domain discretization error. Moreover, this additional error will dependent on t. Since $f(t)$ has to meet the same tolerances for all values of t, the adaptive component that assures that $f(t)$ meets the specified tolerances would have to be repeated for each value of t. As this would greatly slow down the scheme, $\sin(\omega t)$ will not be discretized.

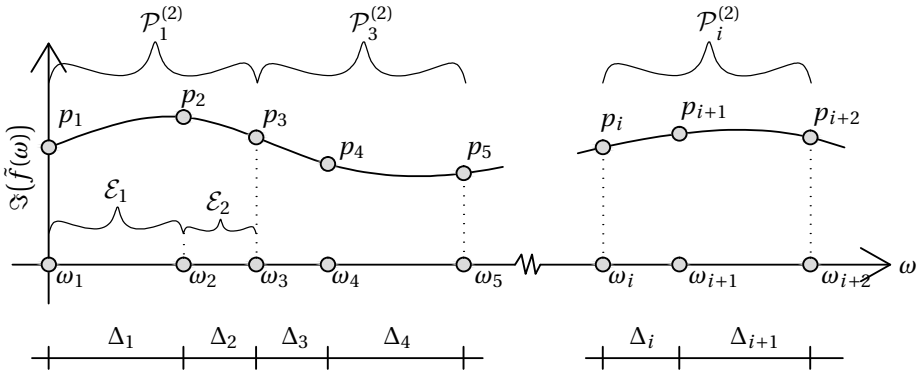

Figure B.1: $\Im\big(\tilde{f}(\omega)\big)$ is approximated using N_p second order polynomials $\mathcal{P}_i^{(2)}$ that are indexed with i. Each polynomials is constructed using the elements $\mathcal{E}_i$ and $\mathcal{E}_{i+1}$ that depend on the set of points $\{p_i, p_{i+1}, p_{i+2}\}$.

Next, the interpolation scheme for $\tilde{f}(\omega)$ is introduced. To facilitate the explanation of the interpolation, it is assumed that $\Im\big(\tilde{f}(\omega)\big)$ has already been evaluated $2N_\mathrm{p}+1$ times (in actual fact, the integration points are added by the adaptive component of the scheme that is explained later). This results in $2N_\mathrm{p}+1$ integration points or $2N_\mathrm{p}$ elements between these points. The scheme is illustrated in Fig. B.1.

Between each pair of adjacent elements, a second order polynomial is constructed, see Fig. B.1. The i^{th} polynomial $\mathcal{P}_i^{(2)}$ is constructed using the set of integration points $\{p_i, p_{i+1}, p_{i+2}\}$ which are the evaluations of $\Im\big(\tilde{f}(\omega)\big)$ at the frequencies $\{\omega_i,\ \omega_{i+1} = \omega_i + \Delta_i,\ \omega_{i+2} = \omega_{i+1} + \Delta_{i+1}\}$. The (2) indicates that this is a second order polynomial. The compact support of $\mathcal{P}_i^{(2)}$ is, therefore, $[\omega_i, \omega_{i+2}] = [\omega_i, \omega_i + \Delta_i + \Delta_{i+1}]$. The resulting set of N_p polynomials is indexed with $i \in \boldsymbol{i}$, with $\boldsymbol{i} = \{1, 3, 5, .., 2N_\mathrm{P} - 1\}$. Together, these polynomials form the interpolation function $\mathcal{P}^{(2)}(\omega)$ that approximates the discrete function $\Im\big(\tilde{f}(\omega)\big)$:

$$\mathcal{P}^{(2)}(\omega) = \sum_{i \in \boldsymbol{i}} \mathcal{P}_i^{(2)}(\omega) \tag{B.7}$$

The compact support of $\mathcal{P}^{(2)}(\omega)$ is $[0,\Omega] = [0,\omega_{2N_p}]$. Based on this definition of $\mathcal{P}^{(2)}(\omega)$, Eq. (B.5) becomes:

$$f(t) \approx -\frac{2}{\pi}\int_0^{\Omega} \mathcal{P}^{(2)}(\omega)\sin(\omega t)\,\mathrm{d}\omega = -\frac{2}{\pi}\int_0^{\Omega}\sum_{i\in\boldsymbol{i}} \mathcal{P}_i^{(2)}(\omega)\sin(\omega t)\,\mathrm{d}\omega$$
$$= -\frac{2}{\pi}\sum_{i\in\boldsymbol{i}}\int_{\omega_i}^{\omega_{i+2}} \mathcal{P}_i^{(2)}(\omega)\sin(\omega t)\,\mathrm{d}\omega \tag{B.8}$$

All N_P integrals are now evaluated analytically:

$$f(t) \approx -\frac{2}{\pi}\sum_{i\in\boldsymbol{i}}\Big(\left(p_{i+2}\cos(\omega_{i+2}t) - p_i\cos(\omega_i t)\right)t^{-1}$$
$$+\left(s_i^{(2)}\sin(\omega_{i+2}t) - s_i^{(1)}\sin(\omega_i t)\right)t^{-2}$$
$$+c_i\left(\cos(\omega_{i+2}t) - \cos(\omega_i t)\right)t^{-3}\Big) \tag{B.9}$$

where the amplitudes are given by:

$$c_i = -4(a_i + b_i) \tag{B.10a}$$
$$s_i^{(1)} = a_i\Delta_i + b_i\left(\Delta_i^{(+)} + \Delta_i\right) \tag{B.10b}$$
$$s_i^{(2)} = a_i\left(\Delta_i^{(+)} + \Delta_{i+1}\right) + b_i\Delta_{i+1} \tag{B.10c}$$

with $\Delta_i^{(+)} = \Delta_i + \Delta_{i+1} = \omega_{i+2} - \omega_i$ and a_i and b_i defined as:

$$a_i = \frac{p_{i+2} - p_{i+1}}{\Delta_i^{(+)}\Delta_{i+1}} \tag{B.11a}$$
$$b_i = \frac{p_i - p_{i+1}}{\Delta_i^{(+)}\Delta_i} \tag{B.11b}$$

Now, consider the summation of the two terms $\propto t^{-1}$. Since the contribution of adjacent polynomials cancels out, the summation of these two terms evaluates to:

$$f(t) \approx -\frac{2}{\pi}\left(p_1\cos(0t) + p_{2N_\mathrm{P}+1}\cos(\omega_{2N_\mathrm{P}}t)\right)t^{-1}$$
$$-\frac{2}{\pi}\sum_{i\in\boldsymbol{i}}\Big(\left(s_i^{(2)}\sin(\omega_{i+2}t) - s_i^{(1)}\sin(\omega_i t)\right)t^{-2}$$
$$+c_i\left(\cos(\omega_{i+2}t) - \cos(\omega_i t)\right)t^{-3}\Big) \tag{B.12}$$

Since $\tilde{f}(\omega)$ is an Hermitian function $p_1 = \Im\left(\tilde{f}(0)\right) = 0$ and the term $\propto p_0$ is always equal to zero. The term $\propto p_{2N_\mathrm{P}+1}$ is adjacent to the upper bound Ω of the truncated integration range and it is, therefore, assumed to be negligible. Consequently, all terms $\propto t^{-1}$ can be removed. Next, the two terms $\propto t^{-3}$ can be rewritten as:

$$f(t) \approx -\frac{2}{\pi}\sum_{i=1}^{N_\mathrm{P}}\Big(\left(s_i^{(2)}\sin(\omega_{i+2}t) - s_i^{(1)}\sin(\omega_i t)\right)t^{-2}$$
$$+c_i\left(\sin\left(\frac{\Delta_i^{(+)}}{2}t\right)\sin\left(\frac{\omega_{i+2}+\omega_i}{2}t\right)\right)t^{-3}\Big) \tag{B.13}$$

This form is preferred as it is solely based on sine functions, which again alleviates precision issues at small t.

Error estimation. The second order polynomials used for the interpolation introduce a time-domain error $\epsilon_{\mathrm{p}}(t)$:

$$\epsilon_{\mathrm{p}}(t) = -\frac{2}{\pi}\int_0^{\Omega}\left(\mathcal{P}^{(2)}(\omega) - \Im\left(\tilde{f}(\omega)\right)\right)\sin(\omega t)\,\mathrm{d}\omega \tag{B.14}$$

Estimating $\epsilon_{\mathrm{p}}(t)$ is computationally expensive as it depends on time. To avoid this issue, an upper bound can be obtained by considering that, since $\epsilon_{\mathrm{p}}(t)$ is a superposition of sine functions, its maximum possible value occurs when all sine functions synchronize and all evaluate to either 1 or -1. This results in the upper bound ϵ_{p}^*:

$$|\epsilon_{\mathrm{p}}(t)| \leq \epsilon_{\mathrm{p}}^* = \frac{2}{\pi}\int_0^{\Omega}\left|\mathcal{P}^{(2)}(\omega) - \Im\left(\tilde{f}(\omega)\right)\right|\mathrm{d}\omega = \frac{2}{\pi}\sum_{i\in\boldsymbol{i}}\int_{\omega_i}^{\omega_{i+2}}\left|\mathcal{P}^{(2)}(\omega) - \Im\left(\tilde{f}(\omega)\right)\right|\mathrm{d}\omega \tag{B.15}$$

The absolute value is now moved outside the integral:

$$\epsilon_{\mathrm{p}}^* \approx \frac{2}{\pi}\sum_{i\in\boldsymbol{i}}^{N_{\mathrm{P}}}\left|\int_{\omega_i}^{\omega_{i+2}}\mathcal{P}^{(2)}(\omega) - \hat{\mathcal{P}}^{(q)}(\omega)\,\mathrm{d}\omega\right| \tag{B.16}$$

This equation gives the same results as Eq. (B.15), except at zero-crossings of $\Im\left(\tilde{f}(\omega)\right)$. The error of the polynomial wherein the zero-crossing falls will be estimated wrongly as the contributions from its positive and negative domains will be subtracted from one another, rather than added. However, this additional error is accepted in lieu of programming an exception.

Next, since $\Im\left(\tilde{f}(\omega)\right)$ is assumed to be discrete, it again has to be approximated by a continuous interpolation function $\hat{\mathcal{P}}^{(q)}(\omega)$ that consists of a superposition of compactly supported q^{th}-order polynomials:

$$\epsilon_{\mathrm{p}}(t) \approx -\frac{2}{\pi}\int_0^{\Omega}\left(\mathcal{P}^{(2)}(\omega) - \hat{\mathcal{P}}^{(q)}(\omega)\right)\sin(\omega t)\,\mathrm{d}\omega \tag{B.17}$$

where the hat is used to differentiate it from $\mathcal{P}^{(2)}(\omega)$. Ideally, q is as large as possible to assure that ϵ_{p}^* reflects the discretization error introduced by $\mathcal{P}^{(2)}(\omega)$ and not the error introduced by $\hat{\mathcal{P}}^{(q)}(\omega)$. However, already when $q = 3$ the analytical expressions of ϵ_{p}^* consists of a very large number of terms, which would make evaluating ϵ_{p}^* too expensive. For this reason $q = 2$ has to be used and, consequently, the accuracy of $\epsilon_{\mathrm{p}}(t)$ as an estimator of the time-domain error introduced by $\mathcal{P}^{(2)}(\omega)$ is reduced. Despite this, $\epsilon_{\mathrm{p}}(t)$ will still be of the correct order of magnitude, allowing it to be used as a measure by which convergence of the adaptive scheme can be assessed.

Since $q = 2$, $\hat{\mathcal{P}}^{(2)}(\omega)$ cannot use the exact same definition as $\mathcal{P}^{(q)}(\omega)$ as otherwise $\epsilon_{\mathrm{p}}(t)$ would always be equal to zero. As such, it is constructed using the same integration points as $\mathcal{P}^{(2)}(\omega)$ but all its polynomials are shifted one element to the right, i.e. its first polynomial starts at ω_2 rather than ω_1. The contribution of element i to ϵ_{p}^*, ϵ_i, is then

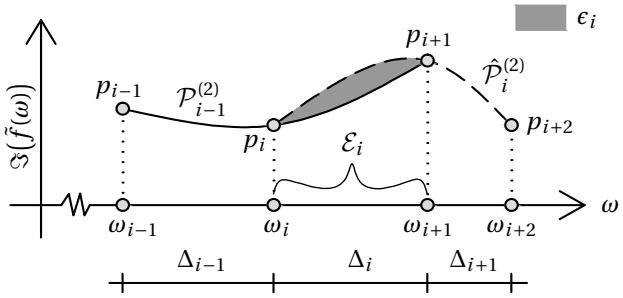

Figure B.2: The error within element i, ϵ_i, is estimated as the gray area between $\mathcal{P}_{i-1}^{(2)}(\omega)$, depicted by the solid line, and $\hat{\mathcal{P}}_i^{(2)}(\omega)$, depicted by the dashed line.

computed as the absolute difference in area between $\hat{\mathcal{P}}^{(2)}(\omega)$ and $\mathcal{P}^{(2)}(\omega)$ within element i, as visualized in Fig. B.2. This results in the following expression for ϵ_i:

$$\epsilon_i = \frac{\Delta_i^2}{6}\left|\Delta_i^{(\pm)}\left(\frac{p_i}{\Delta_{i-1}\Delta_i^{(+)}} - \frac{p_{i+1}}{\Delta_{i+1}\Delta_i^{(-)}}\right) + \Delta_i\left(\frac{p_{i+2}}{\Delta_{i+1}\Delta_i^{(+)}} - \frac{p_{i-1}}{\Delta_{i-1}\Delta_i^{(-)}}\right)\right| \qquad \forall\ i = 2\,..\,2N_\mathrm{P}-1 \tag{B.18}$$

where $\Delta_i^{(-)} = \Delta_{i-1} + \Delta_i$, $\Delta_i^{(\pm)} = \Delta_{i-1} + \Delta_i + \Delta_{i+1}$ and $\Delta_i^{(+)} = \Delta_i + \Delta_{i+1}$. This approach is not possible for the first and last element, i.e. for $i = 1$ and $i = 2N_\mathrm{P}$. For these two elements, the error will be estimated using $q = 1$. This results in the following definitions for ϵ_1 and ϵ_{2N_P}:

$$\epsilon_1 = \frac{\Delta_1^2}{6}\left|p_1\frac{1}{\Delta_1^{(+)}} - p_2\frac{1}{\Delta_2} + p_3\frac{\Delta_1}{\Delta_1^{(+)}\Delta_2}\right| \tag{B.19a}$$

$$\epsilon_{2N_\mathrm{P}} = \frac{\Delta_{2N_\mathrm{P}}^2}{6}\left|p_{2N_\mathrm{P}-1}\frac{\Delta_{2N_\mathrm{P}}}{\Delta_{2N_\mathrm{P}}^{(-)}\Delta_{2N_\mathrm{P}+1}} - p_{2N_\mathrm{P}}\frac{1}{\Delta_{2N_\mathrm{P}+1}} + p_{2N_\mathrm{P}+1}\frac{1}{\Delta_{2N_\mathrm{P}}^{(-)}}\right| \tag{B.19b}$$

These lower order estimators are acceptable as the magnitude of $\tilde{f}(\omega)$ is small in these frequency ranges since $p_1 = \Im\big(\tilde{f}(0)\big) = 0$ and $p_{2N_p} = \Im\big(\tilde{f}(\Omega)\big) << 1$. Moreover, the adaptive nature of the scheme assures that the natural frequencies of $\tilde{f}(\omega)$ will not be near either of these bounds, meaning that the curvature of $\tilde{f}(\omega)$ close to the bounds is very small and, therefore, even linear polynomials will give good a approximation. Finally, the estimate of ϵ_p^* can be obtained by summing the contributions of all $2N_\mathrm{P}$ elements:

$$\epsilon_\mathrm{p}^* = \sum_{j=1}^{2N_\mathrm{P}} \epsilon_j \tag{B.20}$$

Adaptive nesting quadrature. The adaptive component of the integration scheme is introduced next. This component assures that all IFTs are evaluated with a time-domain error of a same order of magnitude, independently of the particular Green's functions being evaluated. To achieve this, the scheme will iterate, adding integration points in the frequency-domain until ϵ_{p}^* satisfies the specified tolerances. Moreover, the scheme should nest, meaning that each iteration should reuse all previously computed integration points. In this manner, the number of integration points can be minimized.

The scheme starts with the following set of three frequencies: $\boldsymbol{\omega} = \{0,\ \Omega/2,\ \Omega\}$. Therefore, the scheme starts with two elements between which a single second order polynomial is constructed. The contribution of both elements to ϵ_{p}^* is then computed using Eqs. (B.19). These contributions are then summed according to Eq. (B.20), thereby obtaining ϵ_{p}^*. ϵ_{p}^* has to meet the following tolerance criterion:

$$\epsilon_{\mathrm{p}}^* \leq \max\left(\left\{\epsilon_{\mathrm{abs}}, \epsilon_{\mathrm{rel}} f^*\right\}\right) \tag{B.21}$$

where f^* is the maximum possible response which is estimated as follows, again excepting any additional errors due to zero-crossings:

$$f^* \approx \frac{2}{\pi} \sum_{i=1}^{N_{\mathrm{P}}} \left| \int_{\omega_{2i-2}}^{\omega_{2i}} \mathcal{P}_i^{(2)}(\omega)\, \mathrm{d}\omega \right| \tag{B.22}$$

As long as this criterion is not met, the scheme will keep iterating. During each iteration, the element with the largest contribution to ϵ_{p}^*, i.e. the largest ϵ_j, is split in half by placing a new integration point in the middle of the element, see Fig. B.3. This new frequency is added to $\boldsymbol{\omega}$. The two integration points of the original element can be reused after the split, implying that the scheme nests. After splitting, the error estimates of the affected elements, see Fig. B.3 on the right, are recomputed using Eq. (B.18) and Eqs. (B.19). Thereafter, ϵ_{p}^* is updated and the tolerance criterion in Eq. (B.21) is reevaluated. This process continues until Eq. (B.21) is satisfied.

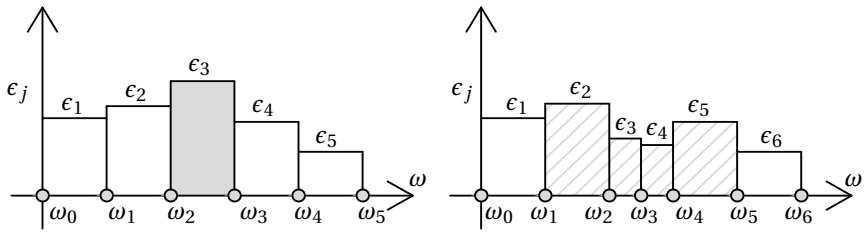

Figure B.3: An illustration of the element placement and how it affects the error contributed by element being split. The element with the largest contribution, ϵ_3, is split by placing a new integration point half-way the element. This results in the new situation shown on the right. The error estimates ϵ_j of the four hatched elements are affected by the split and have to be (re)computed.

Since new points are always placed in the middle of each element and since the initial frequency range is the same for all IFTs being evaluated, it is very likely that there is a large overlap in the frequency set used when evaluating multiple IFTs of the same system. This systematic placement of integration points allows certain frequency-dependent

terms, such as wavenumbers and modal amplitudes, to be stored and reused. This greatly reduces the computation time.

The facilitate the repeated halving of the elements, the upper bound frequency Ω is rounded to the next power of two:

$$\Omega = 2^{\lceil \log_2(2\pi/\Delta_t) \rceil + \epsilon_2} \tag{B.23}$$

where ϵ_2 was set to +2 in this thesis. This definition minimizes the loss of significant digits due to floating-point arithmetics while repeatedly splitting elements in two, improving the accuracy of terms such as $\Delta_i^{(-)}$, $\Delta_i^{(\pm)}$ and $\Delta_i^{(+)}$, which, in turn, improves the accuracy of ϵ_p^*. By relating Ω to the time step Δ_t, all the relevant natural frequencies of the system will be included as long as the time step is chosen correctly by the user. While this approach for setting Ω is not very robust, increasing ϵ_2 by 1 or 2 only increases the total number of integration points by several percents and, therefore, does not have a significant impact on the performance of the solver. For this reason, alternative approaches, like estimating $\epsilon_\Omega(t)$ or adaptively increasing Ω, were not implemented.

The adaptive scheme performs as expected under most conditions. However, when a low accuracy is required, implying that both ϵ_{abs} and ϵ_{rel} are set to relatively lenient values, and Ω is much larger than the natural frequencies of the system, the scheme can converge with a mesh that is too coarse and, therefore, does not capture the fidelity of $\Im\big(\tilde{f}(\omega)\big)$, meaning the peaks at its natural frequencies will not be properly discretized. This results in a time-domain response $f(t)$ that has no physical meaning. To avoid this issue, a minimum refinement level is enforced:

$$\min(\boldsymbol{\omega}') \leq \frac{2\pi}{T_{sim}} \tag{B.24}$$

where the prime denotes taking the difference between adjacent entries of the set $\boldsymbol{\omega}$ that contains all used frequencies in ascending order. This minimum refinement level forces the scheme to continue until at the very least a coarse outline of $\Im\big(\tilde{f}(\omega)\big)$ is achieved. Once this coarse outline has been established, the criterion in Eq. (B.21) takes over and will assure that $\mathcal{P}^{(2)}(\omega)$ is further refined until it captures the fidelity of $\Im\big(\tilde{f}(\omega)\big)$ up to the specified tolerance. The check of this criterion can be disabled once it has been met.

Lastly, two notes are in order. Firstly, while performing the convolution, $\boldsymbol{\mathcal{L}}_n^{(i)}$ and $\boldsymbol{\mathcal{T}}_n^{(i)}$ are scaled by the loads acting on the system, see Eq. (4.39). This scaling has to be taking into account by the user when specifying the absolute tolerance ϵ_{abs}. Second, when multiple loads act on the system, the time-domain error generated by each load will be superimposed when computing the state-components. This increase in error is not taken into account.

B.4. VALIDATION

The scheme was used to solve the following ODE for $x(t)\ \forall\ t \in [0, 100]$ s:

$$\ddot{x} + \frac{1}{2}\dot{x} + x = 1,\ x(0) = \dot{x}(0) = 0 \tag{B.25}$$

Since the load is constant in time, the convolution scheme does not introduce any errors as it is exact up to the first order. This means that any error in $x(t)$ is introduced by the

IFT scheme. The predictions of the proposed scheme are compared against the analytical solution. The absolute and relative errors of the displacement $x(t)$ are shown in Fig. B.4 for three tolerances. The frequency range was $[0, 2^{14}] = [0, 16384]$ rad/s for all three tolerances shown. In order to meet the three specified tolerances, a total of 47, 208 and 1134 integration points were used respectively. The figure shows that the solver is able to achieve errors of the desired order of magnitude for all t.

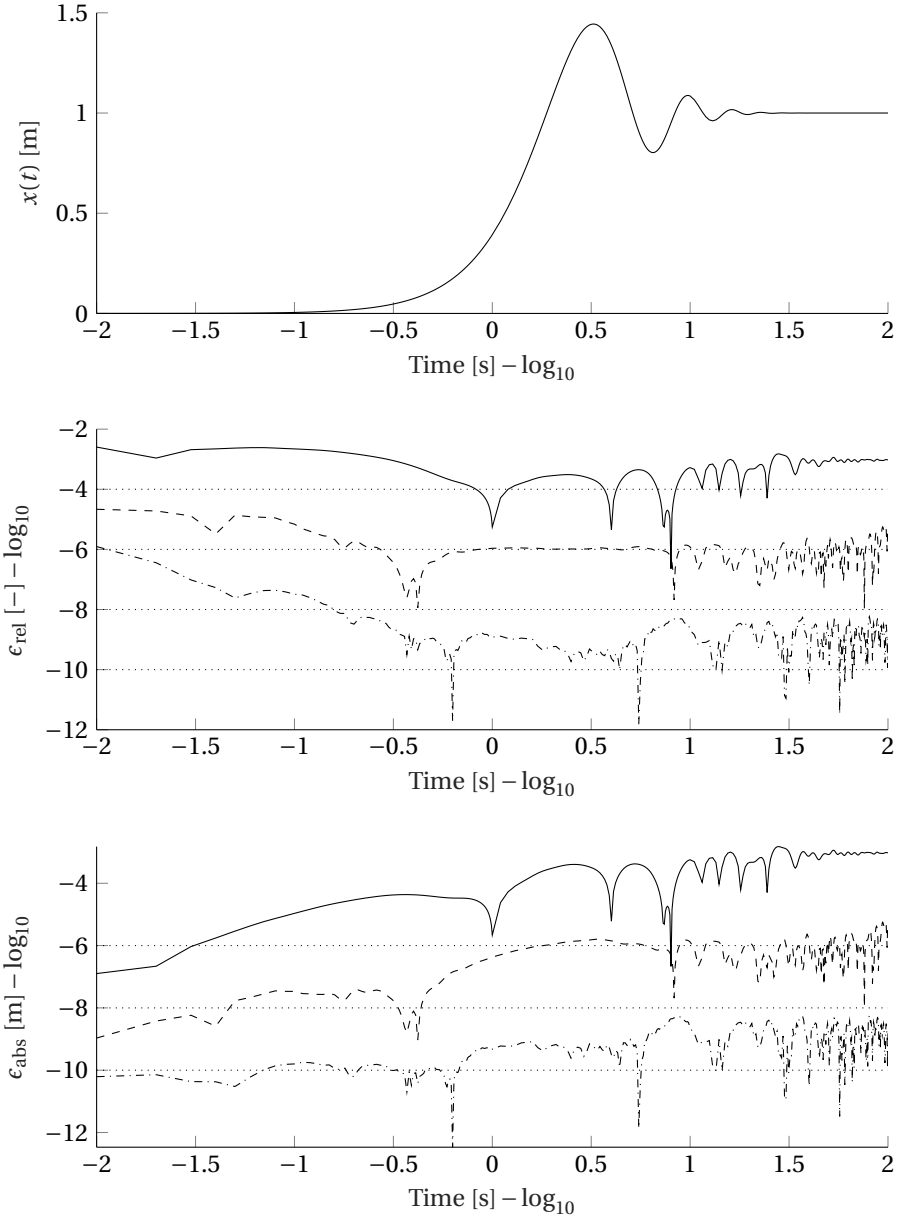

Figure B.4: The displacement $x(t)$ for three sets of tolerances: $\{\epsilon_{\text{rel}} = 10^{-2}, \epsilon_{\text{abs}} = 10^{-4}\}$ solid line, $\{\epsilon_{\text{rel}} = 10^{-4}, \epsilon_{\text{abs}} = 10^{-6}\}$ dashed line, $\{\epsilon_{\text{rel}} = 10^{-6}, \epsilon_{\text{abs}} = 10^{-8}\}$ dash-dot line.

C

DERIVATION OF THE STATIC BREAKING LENGTH

The contact model used in Chapter 4 accounts for the tip moment and this has a minor effect on the static breaking length. In this appendix, an analytical expression for the static breaking length $l_{\text{br,s}}$ is derived that accounts for this tip moment.

In the static limit the equation of motion of the ice given by Eq. (4.4) reduces to:

$$D w''''(x) + \rho_w g w(x) = 0 \qquad \forall x \in (-\infty, 0] \tag{C.1}$$

The general solution to this ODE that account for the proper behavior at $x \to -\infty$ is:

$$w(x) = c_1 \exp(r_1 x) + c_2 \exp(r_2 x) \tag{C.2}$$

where $D = E(1-\nu^2)^{-1} h^3/12^{-1}$, c_1 and c_2 are unknown integration constants, $r_1 = (-1-\text{i})\sqrt{2}l/2$ and $r_2 = (-1+\text{i})\sqrt{2}l/2$ with $l = \sqrt[4]{\delta}$, where $\delta = D/(\rho_w g)$ is defined in Eq. (4.11). To complete the problem statement, two boundary conditions are needed. The boundary conditions account for the contact force and moments that act on the edge of the plate:

$$D w'''(0) = \sigma_{cr} \left(V_{\text{ice}} t \tan(\theta) - w(0)\right) \cos(\theta) \tag{C.3}$$

$$D w''(0) = -h/2 \sigma_{cr} \left(V_{\text{ice}} t \tan(\theta) - w(0)\right) \sin(\theta) \tag{C.4}$$

The contact force is assumed to act at the top of the cross-section of the ice. The arm of the horizontal component of the contact force with respect to the neutral axis is assumed to be constant and equal to $h/2$.

These two boundary conditions can be used to find expressions for the unknown constants c_1 and c_2. The breaking length can be found by determining the location where the bending stress, given by the first term in Eq. (4.7), is maximum. This results in the following expression for the static breaking length:

$$l_{\text{br,s}} = \sqrt{2} l \operatorname{atan}\left(\frac{\sqrt{2}l}{\sqrt{2}l - h\tan(\theta)}\right) \tag{C.5}$$

D

CONVERGENCE OF THE ITERATIVE SCHEME

In Chapter 4, an iterative scheme is used to solve the implicit equation, Eq. (4.34), that allows the time-integration scheme to advance to the next time step. In this appendix, the convergence rate of that recursive scheme is derived. To this end, Eq. (4.34) is rewritten in a simpler form under the assumption that there is only a single pseudo-force $F(q)$, noting again that the iteration counter j starts at 0:

$$q^{[j+1]} \approx q^{[0]} + cF(q^{[j]}) \tag{D.1}$$

where $c = \mathcal{T}_0 << 1$ with $\mathcal{T}_0$ being the factor of proportionality between a load that acts on the system during the current time step and the response this load has excited by the end of the time step. First, the pseudo-force $F(q)$ is expanded in a Taylor series around the state $q^{[0]}$ that contains the response excited by the load during all previous time step:

$$F(q) = F\left(q^{[0]}\right) + \left(q - q^{[0]}\right) F'\left(q^{[0]}\right) + \frac{\left(q - q^{[0]}\right)^2}{2} F''\left(q^{[0]}\right) + O\left(\left(q - q^{[0]}\right)^3\right) \tag{D.2}$$

Evaluations of F and its derivatives at $q^{[0]}$ will be indicated with the subscript 0 for brevity:

$$F(q) = F_0 + (q - q^{[0]})F_0' + \frac{(q - q^{[0]})^2}{2} F_0'' + O\left((q - q^{[0]})^3\right) \tag{D.3}$$

Substituting the expansion into Eq. (D.1) and evaluating the first iteration ($j = 0$) one obtains:

$$q^{[1]} = q^{[0]} + cF(q^{[0]}) = q^{[0]} + cF_0 \tag{D.4}$$

Since $q^{[1]} - q^{[0]} = cF_0$, the second iteration ($j = 1$) gives:

$$\begin{aligned}
q^{[2]} &= q^{[0]} + c\left(F\left(q^{[1]}\right)\right) \\
&= q^{[0]} + c\left(F_0 + \left(q^{[1]} - q^{[0]}\right)F_0' + \frac{\left(q^{[1]} - q^{[0]}\right)^2}{2}F_0'' + O\left(\left(q^{[1]} - q^{[0]}\right)^3\right)\right) \\
&= q^{[0]} + c\left(F_0 + (cF_0)F_0' + \frac{(cF_0)^2}{2}F_0'' + O(c^3)\right) \\
&= \left(q^{[0]} + cF_0\right) + \left(c^2F_0F_0' + \frac{c^3}{2}F_0^2F_0'' + O(c^4)\right) \\
&= q^{[1]} + \left(c^2F_0F_0' + \frac{c^3}{2}F_0^2F_0'' + O(c^4)\right)
\end{aligned} \tag{D.5}$$

Since $q^{[2]} - q^{[0]} = c\left(F(q^{[1]})\right)$, the third iteration ($j = 2$) gives:

$$\begin{aligned}
q^{[3]} &= q^{[0]} + c\left(F\left(q^{[2]}\right)\right) \\
&= q^{[0]} + c\left(F_0 + \left(q^{[2]} - q^{[0]}\right)F_0' + \frac{\left(q^{[2]} - q^{[0]}\right)^2}{2}F_0'' + O\left(\left(q^{[2]} - q^{[0]}\right)^3\right)\right) \\
&= q^{[1]} + c\left(q^{[2]} - q^{[0]}\right)F_0' + \frac{c}{2}\left(q^{[2]} - q^{[0]}\right)^2F_0'' + cO\left(\left(q^{[2]} - q^{[0]}\right)^3\right) \\
&= q^{[1]} + c^2F\left(q^{[1]}\right)F_0' + \frac{c^3}{2}F\left(q^{[1]}\right)^2F_0'' + O\left(c^4\right) \\
&= q^{[1]} + c^2\left(F_0 + cF_0F_0' + \frac{c^2}{2}F_0^2F_0'' + O\left(c^3\right)\right)F_0' \\
&\quad + \frac{c^3}{2}\left(F_0 + cF_0F_0' + \frac{c^2}{2}F_0^2F_0'' + O\left(c^3\right)\right)^2F_0'' + O\left(c^4\right) \\
&= q^{[1]} + \left(c^2F_0F_0' + c^3F_0(F_0')^2 + O\left(c^4\right)\right) + \left(\frac{c^3}{2}F_0^2F_0'' + O\left(c^4\right)\right) + O\left(c^4\right) \\
&= q^{[2]} + c^3F_0(F_0')^2 + O\left(c^4\right)
\end{aligned} \tag{D.6}$$

This derivation shows that $q^{[1]} - q^{[0]} = O(c)$, $q^{[2]} - q^{[1]} = O(c^2)$ and $q^{[3]} - q^{[2]} = O(c^3)$. So, the error after j iterations is $O(c^{[j+1]})$, meaning the recursive scheme thus converges at a rate of $c = \mathcal{T}_0$.

ACKNOWLEDGEMENTS

I am very happy that after six years my thesis has finally come to a positive conclusion. It was a long and arduous process. It was an experience that was very different than I initially assumed, having more in common with a complete master than simply a very long master thesis. What I value the most from this experience is the knowledge that I have gained, the friends that I made along the way and the great trips we all had together. In a semi-particular order, I would like to thank the following people.

First, I would like to thank Andrei. You taught me a lot about regarding dynamics, maths and scientific writing. Regarding supervision, you showed me what to do but also what not to do. While you certainly could have made the process easier, I would not have been able to finish the PhD without your help.

Second, I would like to thank Hayo. Over the years we had many great trips together, starting with the first week of my PhD when we attended the awesome safety course in Svalvard and ending (so far at least) on a high note with karaoke in Korea. Towards the end you also started to become involved with the actual PhD. You helped me a lot, first by assisting with the second journal paper and in the last year by helping me with the structure and writing of the thesis itself. Thanks a lot for your help and support, I could not have finished it without you!

Third, I would like to thank all my office mates over the years. The original Arctic room crew, Hayo, Marnix and Renate, and the next-generation Arctic room members, Andrei and Yaxi, thanks a lot for your icy discussion and feedback on my ideas and thoughts!

Four, I would like to thank all other colleague for their kindness, ideas, discussion and shared trips. The conferences we attended together were extremely “educational”.

Next, I would like to thank the SAMCoT project for the sponsoring they provided for my PhD and all the SAMCoT members for given me the critical feedback needed to guide my thesis towards novelty.

Lastly, I would like to thank my personal support line, a.k.a., my parents for always being there to support me during the last six years, not only for my PhD-related struggles, but for everything. I also want to thank the rest of my family and friends for helping me stay positive and supporting me over the years.

CURRICULUM VITÆ

Chris KEIJDENER

5 March 1987 — Born in Heerlen, Netherlands.

EDUCATION

2005–2009 — Bachelor of Science
Civil Engineering
Hogeschool Zuyd, Heerlen

2009–2012 — Master of Science (*cum laude*)
Offshore & Dredging Engineering
Thesis: *Dynamics of JBF Arctic drilling unit moored in ice*
Faculty of Mechanical, Maritime and Materials Engineering
Delft University of Technology

2013–2018 — Ph.D. Research
Thesis: *The effect of hydrodynamics on the interaction between floating structures and ice floes*
Delft University of Technology
Department of Structural Mechanics
Faculty of Civil Engineering and Geosciences

AWARDS

2013 — KIVI NIRIA award for best thesis in Offshore Engineering during the academic year 2011–2012.

List of Publications

Journal publications

1. **C. Keijdener**, J. M. de Oliveira Barbosa, and A. V. Metrikine, *The influence of level ice on the frequency domain response of floaters*, Cold Regions Science and Technology 143, 112 (2017).

2. **C. Keijdener**, H. Hendrikse, and A. Metrikine, *The effect of hydrodynamics on the bending failure of level ice*, Cold Regions Science and Technology 153, 106 (2018)

Conference publications

3. **C. Keijdener**, E. Arens, and A. Bereznitski, *Time domain analysis of a MODU moored in ice*, in Proceedings of OTC Arctic Technology Conference (The Offshore Technology Conference, 2012).

4. **C. Keijdener** and A.Metrikine, *The effect of ice velocity on the breaking length of level ice failing in downward bending*, Proceedings of 22nd IAHR International Symposiumon Ice (2014), 10.3850978-981-09-0750-1 1262.

5. **C. Keijdener** and A.Metrikine, *An efficient method for computing the time domain response of a floating ice block including hydrodynamics*, in Proceedings of the 23nd International Conference on Port and Ocean Engineering under Arctic Conditions (2015).

6. **C. Keijdener** and A.Metrikine, *A simple numerical model of a geometrically nonlinear Timoshenko beam*, in APM Proceedings (2015).